

PHYSICAL PROPERTIES OF CONCRETE MODIFIED WITH SUPERABSORBENT POLYMERS

Von der Fakultät für Bau- und Umweltingenieurwissenschaften der Universität Stuttgart
zur Erlangung der Würde eines Doktor-Ingenieurs (Dr.-Ing.) genehmigte Abhandlung

Vorgelegt von
Dipl.-Ing. Alexander Assmann
aus Backnang

Hauptberichter: Prof. Dr.-Ing. Prof. h.c. Dr.-Ing. E.h. Hans-Wolf Reinhardt
Mitberichter: Prof. Dr.-Ing. Pietro Lura

Tag der mündlichen Prüfung:
27.05.2013

Institut für Werkstoffe im Bauwesen der Universität Stuttgart
2013

Danksagung

Die vorliegende Dissertation entstand während meiner Tätigkeit als wissenschaftlicher Mitarbeiter am Institut für Werkstoffe im Bauwesen (IWB) der Universität Stuttgart. Finanziert wurde die Arbeit durch zwei Forschungsvorhaben der Deutschen Forschungsgemeinschaft (DFG), die sich im Allgemeinen mit der Anwendbarkeit von salzstabilen Superabsorbentpolymeren als Betonzusatz und im Besonderen mit ihrem Einfluss auf die Dauerhaftigkeitseigenschaften von Beton beschäftigten. Daher gilt mein Dank an dieser Stelle der DFG, ohne deren Finanzierung diese Arbeit nicht möglich gewesen wäre.

Mein besonderer Dank gilt Herrn Prof. Hans-Wolf Reinhardt für seine vertrauensvolle Unterstützung, seine Diskussions- und seine stets freundliche Hilfsbereitschaft und die hervorragende Betreuung meiner Arbeit. Herrn Prof. Pietro Lura danke ich für sein Interesse an dieser Arbeit, seine Bereitschaft den Mitbericht zu übernehmen und die wertvollen Anregungen und Diskussionen bei der Abfassung der Dissertationsschrift.

Ganz herzlich bedanken möchte ich mich auch bei meinen studentischen Hilfskräften Alexander Schief, Christian Schwab und Norbert Vita, meinen Diplomanden Mona Wiesinger und Martin Voigt und unserem Gastwissenschaftler Herrn Dr. Kazuo Ichimiya, für die tatkräftige Unterstützung. Bei Herrn Dr. Vladimir Knjasev bedanke ich mich sehr für die Durchführung der Kernspinresonanz-Messungen und die anschließenden Diskussionen der Ergebnisse. Frau Corina Luz danke ich für die Einarbeitung im Analyselabor und Frau Monika Werner danke ich für die bibliothekarische Hilfestellung. Des Weiteren gilt mein Dank dem Leiter des Instituts, Herrn Prof. Harald Garrecht, und all meinen Kolleginnen und Kollegen für das freundliche Miteinander und die entgegengebrachte Unterstützung. Den Mitarbeiterinnen und Mitarbeitern der Materialprüfungsanstalt Universität Stuttgart, insbesondere der Abteilung für Mineralische Baustoffe, sei herzlichst für die sehr gute Zusammenarbeit und die große Hilfsbereitschaft gedankt.

An dieser Stelle möchte ich mich auch bei den Mitgliedern des RILEM Technischen Komitees 225-SAP für die wertvollen Erfahrungen die ich im Rahmen der Mitarbeit sammeln durfte, bedanken. Den Herren Dr. Stefan Friedrich, Dr. Gregor Herth und Dr. Jürgen Bokern von der BASF Construction Chemicals GmbH in Trostberg danke ich für die freundliche Kooperation, die vielfältige Unterstützung und die Bereitstellung von Polymer-Mustern.

Dank gilt auch meinem Diplombetreuer Dr. Sven Mönning, ohne den ich den Weg der Promotion wahrscheinlich nicht eingeschlagen hätte.

Für das gründliche Korrekturlesen dieser Arbeit bedanke ich mich recht herzlich bei den Herren Dennis Kittel und Andreas Karden.

Meinen Eltern Gabi und Werner Assmann danke ich für das mir geschenkte Vertrauen, die großzügige Unterstützung und die Freiheit, meinen eigenen Weg zu gehen.

Meiner Partnerin Diana Wilhelm danke ich für ihr großes Verständnis und die moralische Unterstützung, diese Arbeit fertigzustellen.

Backnang, Februar 2013

Alexander Assmann

Abstract

This dissertation deals with the effect of a new concrete additive, called salt-insensitive superabsorbent polymer, on the physical properties of normal and high strength concrete. Superabsorbent polymers, short SAP, are special polymers that are able to absorb many times more water than their own weight within short time. They can even store water when exposed to gentle mechanical stress. When added dryly to the concrete mix, they absorb a specific part of the mixing water. In doing so, they swell and form finely distributed internal water reservoirs with diameters of about 50 to 1000 μm . During cement hydration, the stored water is released back and air-filled macropores remain in the hardened matrix. The supply of water due to internal reservoirs is called internal curing. Recently, internal curing by SAP is investigated in the field of high-strength concretes at low water-to-cement (w/c) ratio. The intention is to mitigate self-desiccation and self-desiccation shrinkage, respectively, in order to prevent early-age cracking of restraint concrete structures.

The superabsorbent polymers examined in this thesis were tested with respect to their ability for internal curing in Portland cement pastes and silica fume modified high performance mortars. Autogenous shrinkage tests, continuous monitoring of the dynamic elastic material parameters and measurements on the change in internal relative humidity were performed. The results show that not only the amount of entrained water but also the three dimensional distribution of the water reservoirs significantly influences the efficiency of internal curing. Due to measurements with nuclear magnetic resonance relaxometry, the emptying of the initially water-filled SAP pores in hardening cement paste was observed. Thermogravimetry measurements revealed that curing water provided by SAP does not influence hydration much different compared to the same amount of ordinarily added water. A similar trend was found for the influence of internal curing water on the development of compressive strength. Only in case of mixtures produced at low w/c ratio it could be shown that internal curing leads to a slight increase of compressive strength when compared to mixtures without internal curing but same total water content.

One of the main topics of this work is the redistribution of capillary water into larger SAP pores. This approach has the target to significantly enhance the concrete's durability by a specific change of the pore structure. For instance, it is shown that the gas and water permeability and the capillary water absorption of concrete can be reduced due to addition of SAP. This effect is more pronounced when the particle size distribution of the used SAP is increased. Further, it is demonstrated that the air pores, which remain after the polymers have dried out, can be used to improve the freeze-thaw resistance of concrete. The presented results substantiate the assumption that a certain SAP pore volume with $d_{50} > 150 \mu\text{m}$ can improve the frost-resistance of concrete (according to the CDF-test method) similar to the same volume of air pores generated by traditional air-entraining agents, although the SAP pores are initially water-filled. So far, the void spacing factor has been used as reliable parameter for the characterization of the pore system. However, it was found that the correlation between total pore volume and concrete scaling is much better than the correlation between void spacing of SAP pores and scaling. A big advantage of air-entrainment by SAP is the ability to control the characteristics of the pore volume by the dosage and the size of the dry SAP particles.

A so far completely unknown effect was observed in case of tensile creep measurements on SAP-modified concrete. It was found that addition of SAP reduces tensile creep down to a level

of a reference concrete without SAP addition, which has a water content comparable to the water content of the SAP-modified concrete while neglecting the water stored in SAP. Further, it was found that tensile creep of concrete is less sensitive to changes in ambient relative humidity compared with shrinkage of concrete.

Kurzfassung (German abstract)

Die vorliegende Dissertation beschäftigt sich mit dem Einfluss von salzstabilen Superabsorbierenden Polymeren als neuem Betonzusatz auf die physikalischen Eigenschaften von normal- und hochfestem Beton. Superabsorbierende Polymere, kurz SAP, sind Spezialkunststoffe, die in der Lage sind innerhalb weniger Minuten ein Vielfaches ihres Eigengewichts an Wasser oder wässriger Lösung aufzunehmen und unter Druck zu speichern. Dem Beton trocken zugemischt, entziehen sie einen vordefinierten Teil des Anmachwassers und quellen dabei zu feinverteilten, inneren Wasserreservoirs mit Durchmessern von zirka 50 bis 1000 μm auf. Während der Hydratation des Zements geben sie das Wasser wieder ab und verbleiben als luftgefüllte Poren im Zementstein zurück. Dieser Vorgang, auch innere Nachbehandlung genannt, wird seit kurzem im Bereich hochfester Betone erforscht, um der inneren Austrocknung dieser Betone und dem damit einhergehenden autogenen Schwinden, welches zur frühen Rissbildung im Bauteil führen kann, entgegenzuwirken.

Die in dieser Arbeit verwendeten Superabsorber wurden ebenfalls hinsichtlich ihrer Eignung zur inneren Nachbehandlung in Portlandzementleimen und in mit Silikastaub modifizierten Hochleistungsmörteln untersucht. Es wurden Messungen zum autogenen Schwinden, zur Entwicklung der dynamischen elastischen Materialparameter und zum Verlauf der inneren Feuchte vorgenommen. Dabei konnte gezeigt werden, dass nicht nur die Menge an eingebrachtem Wasser, sondern auch die räumliche Verteilung der Wasserquellen einen maßgebenden Einfluss auf die Effektivität der inneren Nachbehandlung ausübt. Anhand hochauflösender Kernspinresonanzmessungen an Zementleimproben wurde die Entleerung der anfangs wassergefüllten SAP-Poren über den Hydratationsverlauf beobachtet. Mittels Thermogravimetrie wurde nachgewiesen, dass sich das von den SAP zur Verfügung gestellte Wasser hinsichtlich des Hydratationsverlaufs nur marginal von einer vergleichbaren Menge an frei zugegebenem Wasser unterscheidet. Ähnlich verhält es sich mit dem Einfluss der SAP-Poren auf die Druckfestigkeit. Hier konnte lediglich bei Mischungen mit niedrigen Wasser-Zement-Werten gezeigt werden, dass durch die inneren Wasserquellen die Druckfestigkeit im Vergleich zur gleichen Menge an gewöhnlich zugegebenem Wasser leicht gesteigert werden kann.

Ein wesentlicher Bestandteil dieser Arbeit stellt die Herausarbeitung der Auswirkungen einer Umverteilung von Kapillarwasser in größere SAP-Poren dar. Ziel dieses Ansatzes ist es, durch gezielte Änderungen der Porenstruktur die Dauerhaftigkeitseigenschaften des Betons erheblich zu verbessern. So konnte beispielsweise gezeigt werden, dass durch den Einsatz von SAP die Gas- und Wasserpermeabilität sowie die kapillare Wasseraufnahme des Betons reduziert werden können. Dieser positive Effekt nimmt mit steigender Partikelgröße der verwendeten SAP zu. Des Weiteren wurde die Eignung der nach Austrocknung im Zementstein verbleibenden SAP-Poren zur Steigerung der Frost-Tausalzbeständigkeit des Betons untersucht. Die dargelegten Ergebnisse bekräftigen die Annahme, dass ein bestimmtes Volumen an SAP-Poren bei ausreichender Größe der einzelnen Poren von $d_{50} > 150 \mu\text{m}$, trotz ihrer anfänglichen Wassersättigung, den Frost-Tausalz widerstand (CDF-Verfahren) in ähnlicher Weise steigern kann, wie ein vergleichbares Volumen an herkömmlich eingebrachten Luftporen. Dabei zeigte sich eine bessere Korrelation zwischen Gesamtporenvolumen und Abwitterungsmenge als eine entsprechende Korrelation mit dem Porenabstandsfaktor, der bisher als geeigneter Parameter für die Beschreibung des Frost-

Tausalz widerstandes galt. Ein wesentlicher Vorteil der Verwendung von SAP besteht in der Zuverlässigkeit, mit der ein entsprechendes stabiles Porensystem im Beton angelegt werden kann.

Ein bisher völlig unbekannter Effekt trat bei der Untersuchung des Einflusses der SAP auf das Zugkriechverhalten von Beton in Erscheinung. Hier wurde festgestellt, dass sich durch Zugabe von SAP das Zugkriechen auf ein Maß reduzieren lässt, das dem eines Referenzbetons ohne SAP entspricht, dessen Zugabewasser um die in SAP gespeicherte Wassermenge reduziert wurde. Des Weiteren wurde festgestellt, dass das Zugkriechen von Beton deutlich weniger empfindlich auf Änderungen der Umgebungsfeuchte reagiert als das Schwinden von Beton.

Table of contents

LIST OF SYMBOLS	III
LIST OF ABBREVIATIONS	VI
1 INTRODUCTION	1
1.1 Scope.....	1
1.2 Motive.....	1
1.3 Objective and organization	2
2 FUNDAMENTALS	4
2.1 Introduction.....	4
2.2 Cement hydration and formation of microstructure	4
2.3 Volume changes and autogenous phenomena	9
2.4 Internal curing.....	16
2.5 Deformation of concrete under constant load.....	18
2.6 Durability of concrete	22
2.7 Transport processes in concrete.....	25
2.8 Freeze-thaw damage of concrete with de-icing salts	29
2.9 Superabsorbent polymer (SAP)	33
3 BASIC PRINCIPLES OF USING SAP IN CONCRETE TECHNOLOGY	37
3.1 Introduction.....	37
3.2 Internal curing.....	37
3.3 Redistribution of capillary water.....	42
3.4 Further applications of SAP in concrete construction.....	44
3.5 Additional remarks	48
4 CHARACTERIZATION OF USED SAP MATERIAL.....	49
4.1 Introduction.....	49
4.2 SAP material investigated	49
4.3 Methods for determining the water absorption capacity	51
4.4 Formation of artificial macropore inclusions	52
4.5 Summary	59
5 OBSERVATIONS ON SEALED HYDRATION OF PORTLAND CEMENT	60
5.1 Introduction.....	60
5.2 Materials and methods	60
5.3 Results and discussion.....	67
5.4 Conclusion and outlook.....	75
6 AUTOGENOUS PHENOMENA STUDIED ON CEMENT PASTE	76
6.1 Introduction.....	76
6.2 Materials and methods	76

6.3	Results and discussion	81
6.4	Modelling of self-desiccation shrinkage	95
6.5	Conclusion and outlook	98
7	INTERNAL CURING OF HIGH PERFORMANCE MORTAR	100
7.1	Introduction	100
7.2	Materials and methods	100
7.3	Results	101
7.4	Discussion.....	102
7.5	Conclusion and outlook	109
8	SHRINKAGE AND TENSILE CREEP OF CONCRETE.....	110
8.1	Introduction	110
8.2	Materials and methods.....	110
8.3	Results and discussion	113
8.4	Conclusion.....	122
8.5	Outlook.....	123
9	PERMEABILITY AND TRANSPORT COEFFICIENTS	125
9.1	Introduction	125
9.2	Materials and methods.....	125
9.3	Results and discussion	130
9.4	Conclusion.....	138
9.5	Outlook.....	138
10	ENHANCED FREEZE-THAW RESISTANCE.....	139
10.1	Introduction	139
10.2	Materials and methods.....	139
10.3	Results	143
10.4	Discussion.....	150
10.5	SAP vs. traditional AEA.....	155
10.6	Conclusion.....	155
10.7	Outlook.....	156
11	FINAL CONCLUSION AND FUTURE RESEARCH.....	157
11.1	Final conclusion.....	157
11.2	Future research	158
	REFERENCES.....	160
	APPENDIX.....	181

List of symbols

Greek letters:

α	Degree of hydration
$\alpha_{c,T}$	Thermal expansion coefficient
α_{max}	Maximum degree of hydration
β	Contact angle
γ	Surface tension of pore fluid
$\Delta\gamma$	Change in surface energy
Δc	Concentration gradient
Δb	Pressure of liquid
Δl	Length change
$\Delta l_{c,T}$	Length change caused by thermal action
Δm	Absorbed mass of liquid
Δm_c	Loss on ignition of plain cement
Δm_s	Weight loss of test sample
Δp	Differential pressure
ΔT	Thermal action
ΔT_f	Freezing point depression
ε_{as}	Autogenous shrinkage strain
ε_c	Creep strain
ε_{CP}	Free autogenous shrinkage of cement paste
ε_{cf}	Elastic delayed strain
ε_{ci}	Plastic set
ε_{el}	Initial elastic strain at loading
ε_s	Shrinkage strain
ε_{tot}	Total strain
η	Viscosity of test gas
θ_A	Volume fraction of aggregates
λ	Coefficient of proportionality
μ	Magnetic moment
μ_{dyn}	Dynamic Poisson's ratio
ρ_c	Density of cement
ρ_{CP}	Density of cement paste
ρ_{SAP}	Density of SAP
ρ_w	Density of water
σ	Stress
σ_{cap}	Capillary tension in the pore fluid
τ	Magnetogyric ratio
ν	Angular velocity (Larmor frequency)
φ_c	Creep coefficient
χ	Water absorption capacity
ω	Nuclear precession frequency

Latin letters:

a_{cube}	Edge length of cube
A	Test surface of sample
A^1, A^2	Stretching factors
A_{ϕ}	Average cut pore surface
B_0, B_1	Magnetic flux density
c	Amount of cement
c_0	Chloride concentration in the test solution
c_d	Critical chloride concentration
c_{air}	Concentration of carbon dioxide in air
c_c	Concentration of carbon dioxide needed for carbonation
c_{cl}	Concentration of chloride ions
d	Diameter
d_1	Delay time
d_{ϕ}	Average pore diameter
D	Diffusion coefficient
e	Cryoscopic constant
E	Modulus of elasticity
F	Farraday constant
f_c	Compressive strength
f_{cm}	Compressive strength measured on cylinders
f_{ct}	Flexural strength
f_{SAP}	Amount of SAP
G	Shear modulus
h_0	Effective thickness of specimen
H	Heat development in an adiabatic system
H_0	Molar enthalpy of fusion
i	Hydraulic gradient
I	Magnetization density
I_x	One-dimensional diffusion flow
k	Empirical parameter
k_w	Specific permeability coefficient of water
K	Bulk modulus
K_g	Specific permeability coefficient of gas
l	Length
L	Length of specimen
m	Mass
M	Molar mass
n	Number of pores
n^d_{SAP}	Number of dry SAP particles
p	Initial porosity
p_{intr}	Intrudable mercury volume
p_i	Inlet pressure

p_o	Outlet pressure
P	Angular momentum
Q	Swelling capacity
Q_g	Flow rate of gas
r	Kelvin radius
r_{SAP}^d	Radius of SAP particle in dry condition
r_{mod}	Mode radius
r_{Pore}	True average pore radius
r_{SAP}^s	Radius of SAP particle in saturated condition
R	Ideal gas constant
RH	Relative humidity
S	Saturation degree
S_s	Specific internal surface
t	Time or age
t_d	Age at begin of drying
t_f	Age at unloading
t_0	Time zero
T	Absolute temperature
T_f	Freezing temperature
T_{f0}	Freezing temperature of bulk water
T_{Pore}	Line segment of cut pore
T_{Solid}	Line segment of solid matter
T_{tot}	Sum of all line segments
T_1	Longitudinal relaxation time
T_2	Transverse relaxation time
u	Perimeter of specimen
U	Potential difference
v_f	Filter velocity
v_p	Velocity of pressure wave
v_s	Velocity of shear wave
V_{Air}	Volume of air
V_C	Volume of cement
V_{CW}	Volume of capillary water
V_{GS}	Volume of gel solid
V_{GW}	Volume of gel water
V_{UC}	Volume of unhydrated cement
V_W	Volume of water
VS	Void spacing factor
w	Amount of water
w_{ch}	Amount of chemically bound water
W	Water absorption coefficient
x_d	Average intrusion depth
x_w	Water intrusion depth
X_l	Molar mass fraction of water in pore fluid
z	Charge of ions

List of abbreviations

AAC	Autoclave aerated concrete
AEA	Air-entraining agent
CCD	Charge-coupled device
CDF	Capillary suction of de-icing solution and freeze-thaw test
CH	Calcium hydrate
CIF	Capillary suction, internal damage and freeze-thaw test
CPMG	Carr-Purcell-Meiboom-Gill
CSH	Calcium silicate hydrate
DSC	Differential scanning calorimetry
ESEM	Environmental scanning electron microscope
FID	Free induction decay
HCP	Hexagonal close packing
HPM	High performance mortar
HSC	High strength concrete
IA	Imaging analysis
IC	Internal curing
IR	Infra-red
LG	Laser granulometry
LVDT	Linear variable differential transformer
LWA	Lightweight aggregate
MIP	Mercury intrusion porosimetry
MRSE	Multi-ring-sensor-electrode
NMR	Nuclear magnetic resonance
NSC	Normal strength concrete
OPC	Ordinary Portland cement
PCE	Polycarboxylate ether
PP	Polypropylene
RH	Relative humidity
RILEM	International union of laboratories and experts in construction materials, systems and structures
RCM	Rapid chloride migration
RF	Radio frequency
RRT	Round Robin Test
SAF	Superabsorbent polymer fibres
SAP	Superabsorbent polymer
SHCC	Strain-hardening cement-based composites
SRA	Shrinkage reducing agents
TGA	Thermo gravimetric analysis
UHPC	Ultra-high performance concrete
US	Ultrasound
VS	Void spacing (factor)
XRD	X-ray diffraction

1 Introduction

1.1 Scope

In the present chapter the motive and objective of the dissertation will be addressed. It describes briefly the general idea of using superabsorbent polymers (SAP) in concrete construction and provides a short introduction to the main objects and goals of this research. Finally, the organization of the dissertation is explained.

1.2 Motive

Great advances in concrete technology have appeared in the last decades due to the development of new chemical additives which, although added in only small quantities, can lead to significant improvements concerning properties of concrete in its fresh and/or hardened state. One example is the use of superplasticizers on the basis of polycarboxylate ethers. Their application allowed the design of new types of concrete, such as self-compacting and ultra-high-strength concrete.

Recently, efforts are made in the field of salt-insensitive superabsorbent polymers (SAP) used as concrete additive for gaining water control in concrete. SAP is a special material that is able to absorb many times more water than its own weight, within short time. Added in dry condition to the mixture, water absorption changes the rheology of fresh concrete, reduces the tendency of bleeding and segregation, and may be advantageous in case of shotcreting. However, the most appropriate application of SAP in concrete so far is the purpose of internal curing (IC). IC means the provision of extra water by internal water reservoirs, which is freely available for hydration. Especially high performance concrete with low water-to-cement (w/c) ratio suffers from self-desiccation when the free water is consumed by hydration and the dense pore structure inhibits the transport of external curing water from the surface to the interior. This self-desiccation is accompanied by so-called autogenous shrinkage, which primarily occurs at early age and causes high cracking susceptibility if the concrete structure is restraint. IC water released by SAP may prevent self-desiccation and, therefore, autogenous shrinkage cracking. Compared to saturated lightweight aggregates and other materials used for incorporation of curing water, water entrainment by SAP is considered to be the most straightforward IC method at the moment.

One of the major challenges in modern concrete technology is still to fit concrete structures with sufficient durability against all kinds of actions and threats possible for the expected service life. However, nearly all concrete deterioration mechanisms only become operative, if water, dissolved harmful substances or gases can enter the concrete interior. Since the transport processes that trigger concrete deterioration are facilitated by the presence of interconnected capillary pores, another intention of adding SAP to concrete is redistribution of capillary water to artificial water-filled macropore inclusions. The characteristics of the imposed SAP pore system in the hardened concrete, such as size, shape and number of pores, depends on the properties of the dry SAP material, e.g. its water absorption capacity, which are defined by polymer chemistry, production method and processing. The aim is to manipulate the pore structure of the concrete in a way that its durability is improved. The use of durable concrete helps the environment by conserving natural resources and reducing wastes and environmental impacts from repair and replacement. An

example that illustrates the practicability of durability enhancement by SAP is the still persistent problem of concrete deterioration caused by freezing and thawing in combination with de-icing agents. At the latest when SAP pores are drained due to hydration or by evaporation, air-filled macropores remain. These pores act similarly as air pores generated by traditional air-entraining agent (AEA), and achieve high freeze-thaw resistance. In doing so, the addition of SAP is expected to show an immense profit compared with the use of traditional AEA: While the method of AEA is sensitive to environmental impacts, the SAP pore system is stable enough to sustain transport, compaction and changes in temperature.

Research on the application possibilities for SAP as concrete additive has increasingly becoming popular in the last years. Comprehensive information on the application of SAP in concrete construction is provided by the recently available state of the art report of the RILEM Technical Committee 225-SAP [Rilem 2012]. However, most research published up to now deals with the use of SAP for the purpose of internal curing. The study of the effects of SAP addition on the physical properties of concrete is a new task, being extensively investigated in this dissertation.

1.3 Objective and organization

The dissertation provides first comprehensive data on the application of SAP as concrete additive for the enhancement of durability of concrete and mortar produced with w/c ratios in the range 0.30 to 0.50. Fundamentals that are essential for the understanding of the research topics dealt within this work are provided by **CHAPTER 2**. The idea behind addition of SAP for the two main purposes, i.e. provision of extra water for internal curing of concrete and redistribution of capillary water in order to manipulate the concrete's pore structure, is described in **CHAPTER 3**. In addition, further application possibilities for SAP in concrete construction are discussed briefly.

Chapters 4 to 10 report on individual experimental series that can be regarded separately. Basically, various types of SAP were investigated to account on the sensitivity of the test results to the specifications of the SAP material in use. To ease the comparability among the test results obtained from various SAP, only one type of cement was used, viz CEM I 42.5 R. In order to highlight the effects of SAP addition on the concrete properties, by contrast with ordinarily added water, each mixture containing SAP is compared to two control mixes without SAP addition: The first control mix has the same total amount of added water whereas the second control mix has less water content, i.e. equal to the water content of the SAP-modified mixture while neglecting water initially absorbed by SAP. The amount of initially absorbed water varied between 0.04 and 0.14 on a w/c ratio basis, corresponding to SAP contents of 0.25 to 0.58% by mass of cement.

This concept of water entrainment implies the use of the best possible estimate of the water absorption capacity as a basis. Thus, **CHAPTER 4** was intended to characterize the dry polymer material, for example by laser granulometry, as well as its water absorption capacity in cementitious environment. The latter was studied by comparative mortar spread tests and computer-based imaging analysis of microsections.

Water release of SAP during sealed hydration is the subject matter of **CHAPTER 5**. Drainage of SAP was indirectly observed on cement pastes due to measurements with nuclear magnetic resonance (NMR) relaxometry. Further, the effect of IC water on the development of hydration was investigated and compared with ordinarily added water. In doing so, the non-evaporable water content was determined as a function of age of cement paste by thermogravimetric analysis.

Naturally, this work cannot afford to miss investigating the ability of the used SAP material as admixture for internal curing. In fact, mitigation of autogenous shrinkage can indisputably enhance the durability of concrete due to prevention of possible cracking. Thus, **CHAPTER 6** is aimed on the effects of the used SAP types on autogenous phenomena of cement paste, such as change in internal relative humidity and free autogenous deformation. Unfortunately, stresses that would occur if autogenous shrinkage was restraint could not be measured, nor the susceptibility to cracking could be observed. However, the performance in the free autogenous deformation test provides a suitable benchmark for the ability of SAP material as admixture for internal curing. The determination of the dynamic elastic material parameters due to non-destructive ultrasound transmission testing was another part of the series. The results were compared with statically determined values. Furthermore, the self-desiccation shrinkage of reference pastes was calculated in analogy with a refined modelling approach that was originally introduced by Lura [Lura 2003].

In **CHAPTER 7** free autogenous shrinkage of a fine-grained high-performance mortar is investigated and the results are compared to findings of cement paste measurements. To clarify the reasons of ineffective curing that was found to occur despite sufficiently high amounts of entrained curing water, the travel distance of water in the hydrating matrix is estimated, as well as the spacing of SAP inclusions. The latter estimate bases on results obtained from imaging analysis.

The effect of SAP addition on creep of concrete under constant tension loading is the main topic of **CHAPTER 8**. Creep is relevant for durability of concrete since it causes loss of pre-stress in case of pre-stressed concrete structures, and, increase of deformation and deflections. The last two may especially impair the serviceability of concrete structural elements subjected to bending. But, high creep capability can also have positive effects. In case of restraint shrinkage at early age, i.e. when the young material is particularly weak, creep reduces detrimental stress. However, in case of SAP-modified concrete, which is expected to prevent autogenous shrinkage at early age, creep behaviour at higher age is of interest. The specimens were loaded 28 days after casting by 60% of the mean tensile strength. The measurements ended 5 months later.

The effects of redistribution of capillary water on the transport properties of concrete is reviewed and evaluated in **CHAPTER 9**. Knowledge of the transport properties is of paramount interest to assess the resistance of concrete against various attacks. The experimental series comprises the determination of the water absorption coefficient, oxygen and water permeability measurements and tests on chloride migration and carbonation. The question is whether redistribution of capillary water can increase the durability of concrete, even though the total porosity remains the same. Most of the concretes designed for this investigation possessed high w/c ratio of 0.42 or 0.50. This means that the results can be safely transferred to systems with low w/c ratios where internal curing may additionally enhance the durability due to further densification of the matrix. Last but not least, the effect of water entrainment on the 28 days compressive strength in dependence on the storage condition is emphasized and the pore structure is characterized by mercury intrusion porosimetry.

CHAPTER 10 considers the question whether a given volume of initially water-saturated SAP pores increases the frost resistance of concrete as efficient as the same volume of pores entrapped by traditional air-entraining agent. Further, the method of air entrainment due to SAP is used to study the influence of pore size and spacing on the frost resistance. In doing so, the particle size of SAP is varied while the total pore volume is kept constant.

The main achievements and open questions resulting from this research are summarized in **CHAPTER 11**. For reasons of completeness, several appendices are attached to this work. They are listed chronologically in the last section, designated **APPENDIX**.

2 Fundamentals

2.1 Introduction

The intention of this chapter is to provide a theoretical background for the comprehension of the main topics dealt within this dissertation. Only the fundamentals that are essential for the understanding are discussed briefly in the following:

- hydration and microstructure formation of Portland cement
- mechanisms causing volume change
- autogenous phenomena and internal curing
- deformation of concrete under constant load
- durability of concrete
- transport processes in concrete
- freeze-thaw damage of concrete with de-icing salts
- superabsorbent polymers.

2.2 Cement hydration and formation of microstructure

2.2.1 Portland cement hydration

Cement is a hydraulic binder which hardens independently when mixed with water. All reactions of the cement constituents with water are summarized under the term “hydration”. Once reacted, either in air or even under water, it remains solid but changes its material properties over time. These changes are dependent on the environmental conditions, e.g. availability of free water.

Ordinary Portland cement (OPC) that was used for all experiments of this thesis has generally a fraction of 95 to 100% by mass of Portland cement clinker. It is produced by sintering of the principal constituents calcium oxide CaO , silicon dioxide SiO_2 , aluminium oxide Al_2O_3 and hematite Fe_2O_3 . Minor constituents are free lime CaO and periclas MgO . The fraction of each clinker can be calculated on the basis of equations developed by Bogue [Bogue 1955]. During hydration, the cement clinker reacts with water molecules forming various complex hydrates. The speed of reaction as well as the heat quantity released during hydration depends on the clinker phase composition. According to [Locher et al. 1976] and [Jennings et al. 1981] the hydration of Portland cement can be divided into three stages, see Figure 2.1:

- 1) Early period: Immediately after getting in contact with water, the cement grains start to react. This reaction period lasts only a few minutes and is called pre-induction phase. The main reaction component is calcium aluminate C_3A and gypsum $\text{CaSO}_4 \cdot 2\text{H}_2\text{O}$. As a result, ettringite is formed and Ca^{2+} ions start to evolve. The concentration of Ca^{2+} ions can reach up to 30 mmol/l within a few minutes [Rajabipour et al. 2008]. In particular with regard to the swelling of SAP in fresh cement paste, Ca^{2+} ions are important as they act as additional crosslinkers reducing the absorption capacity of SAP in pore solution, cf. chapter 2.9. The pre-induction phase is followed by a period of reduced reaction velocity, called dormant stage. It can be explained by the formation of a layer of reaction products that covers the surface of the cement grain. When the pressure inside, applied by further evolving hydration products, is sufficient enough, the layer breaks. Ludwig and Pence

[Ludwig & Pence 1956] supposed that the protecting layer repeatedly cracks and heals again until the sulphate is consumed and the dormant stage ends.

- 2) Middle period: The tricalcium silicate, C_3S , and the dicalcium silicate, C_2S , react with water forming amorphous calcium silicate hydrate, CSH, and crystalline calcium hydroxide, CH. In this period, long CSH needles are formed that fill the space between the cement grains and lead to the first strength development. It marks the end of workability (setting) as the viscosity is changed irreversibly. From the reaction of the aluminates, C_3A and C_4AF , and the sulphates further ettringite emerges that is later converted into monosulphate. Since all clinker minerals do react, the heat production is rapidly increasing.
- 3) Late period: In the late period, also called hardening, the hydration products form a dense structure inside the original boundaries of the cement grains. The reaction rate and the heat release decrease as hydration is controlled by diffusion of water molecules and ions through the layer of hydration products becoming more and more dense. While the concentration of Ca^{2+} ions decreases progressively within the first 3 days, the amount of OH increases, resulting in an alkaline environment of approximately $pH > 12.5$.

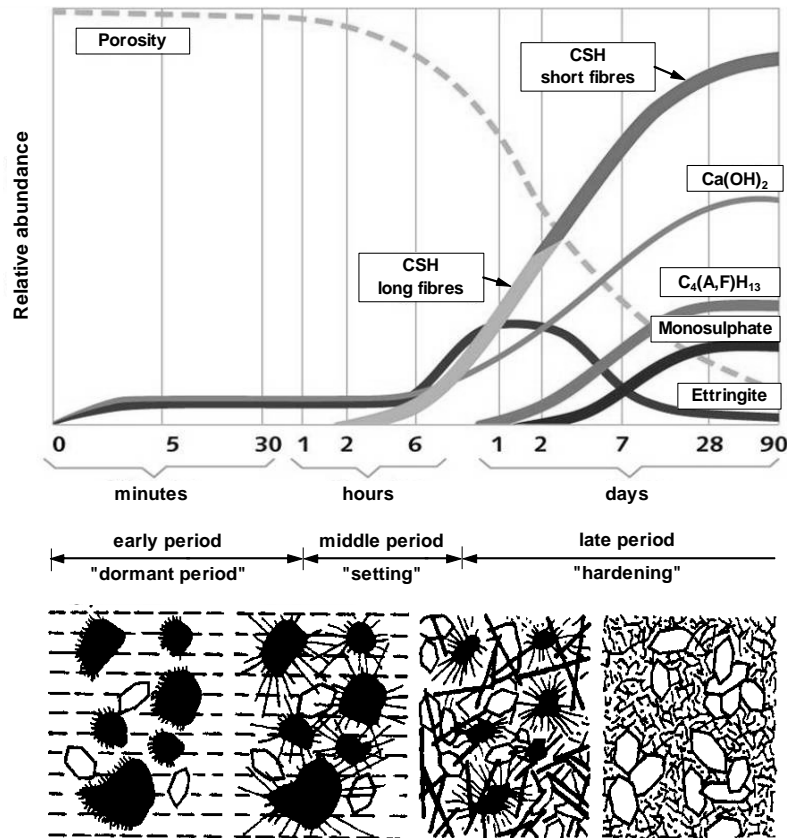


Figure 2.1: Stages of hydration [Locher et al. 1976].

2.2.2 Degree of hydration

The degree of hydration α [-] is defined as the quotient of $c_{reacted}(t)$ [kg/m^3], the cement reacted until time t , to c [kg/m^3], the total amount of cement initially present in the mixture:

$$\alpha(t) = \frac{c_{reacted}(t)}{c} \quad 0 \leq \alpha(t) \leq 1 \quad (2.1)$$

Besides the definition above, which is referred to in the present thesis, there are different other definitions published in literature. All have in common the observation of a characteristic “X” that is developing closely related to hydration, e.g. heat development in an adiabatic system H [J/(s m³)], amount of chemically bound water w_{cb} [g/g], compressive strength f_c [MPa] or specific internal surface S_v [cm²/g]. In all these cases the degree of hydration is defined as the quotient of $X(t)$, the specific characteristic at time t to X_{max} , its maximum possible stage of development at full hydration. The maximum achievable degree of hydration a_{max} depends on the amount of water available during hydration and the pore space that can be occupied by the reaction products. The stoichiometric amount of water that is needed to obtain full hydration in a closed system corresponds to w/c ratio of 0.42 [Powers & Brownnyard 1948]. Closed (also called sealed) means no exchange of water between the cement paste and the surrounding during hydration. In an open system, where water can penetrate into the hardening cement paste, the w/c ratio to obtain full hydration is reduced to 0.36 as explained below.

2.2.3 Powers’ model

One of the most important empirical models describing the volumetric phase distribution of a hardening cement paste is the so-called Powers-Brownnyard model¹. It bases on a widely discussed theory developed from Powers and Brownnyard [Powers & Brownnyard 1948]. The fundamentals are detailed studies on water vapour sorption isotherms and chemically bound water of cement paste during hardening. According to the model, the hardened cement paste is divided into unhydrated cement, hydration products and pores. There is no further distinction between the various hydration products as they are all referred to as cement gel, consisting of gel solid and gel water. Powers found the volume of the hydrates to be about 2 times the volume of the original cement. Further he described the cement gel as a porous substance interspersed with micropores as the hydration products occupy less space than the volumes of water and cement unreacted. This reduction in volume is called chemical shrinkage and was found to yield approximately 6 to 7 ml per 100 g of Portland cement reacted. Besides gel porosity present as gel water and micropores created by chemical shrinkage, the cement gel is interspersed with coarser pores, the so-called capillary pores. At onset of hydration, the capillary porosity is equal to the initial porosity represented by the water component. During hydration the water in the capillary pores is consumed and the capillary porosity becomes less in favour of cement gel (cf. Figure 2.3 on page 7).

According to Powers’ model, the water existing in a hydrating cement paste system can be classified into three water phases, cf. Figure 2.2 on page 7:

- 1) Chemically bound water: It is the water that has already reacted with cement. Thus it is an integral part of the structure of the gel solid, also known as non-evaporable water as it can only be driven off at temperatures far above 105 °C.
- 2) Physically bound water: It is the water that is absorbed on the surface of the gel solid, referred to as gel water. It has a range of binding energies depending on the RH of the pore system and can be driven off at temperatures of 105 °C.
- 3) Free water: It is the water in the coarse capillary pores that is freely accessible for cement hydration. It is also called capillary water and can be dried at temperatures below 105 °C.

Powers’ measurements showed that one gram of fully hydrated Portland cement can bind approximately 0.23 g of water chemically and 0.19 g of water physically. Hence, in sealed condition, complete hydration is possible only for w/c > 0.42. Sealed condition refers to a closed,

¹ Powers slightly modified the model later [Powers 1960], which is why it is referred to as Powers’ model nowadays.

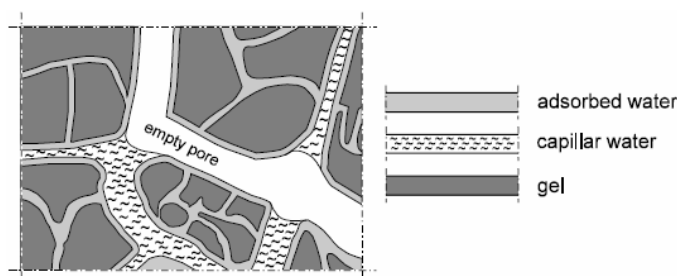


Figure 2.2: Schematic view of water phases in the hardening cement paste [van Breugel 1991].

isothermal system not subjected to external forces [Jensen & Hansen 2001a]. In an open system, complete hydration is possible even in the range $0.36 < w/c < 0.42$, provided that external curing water is available and the sample observed is small enough to facilitate water intake. In doing so, the air-filled space created from chemical shrinkage is replaced by water. Figure 2.3 shows the volumetric phase distribution of two sealed hardening cement pastes at w/c ratio of 0.50 (left) and 0.30 (right) calculated according to Powers. The equations are reported in appendix 2.

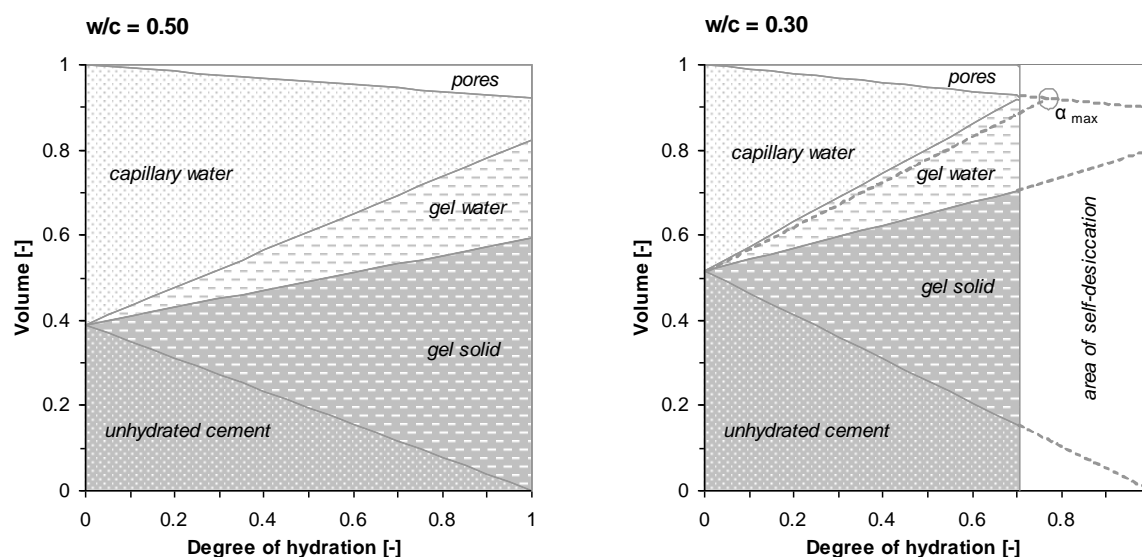


Figure 2.3: Volumetric phase distribution of cement paste as a function of degree of hydration at w/c ratio of 0.50 (left) and 0.30 (right). The diagrams apply to sealed hydration.

In case of w/c of 0.50 the cement can hydrate completely since an excess of free water is available. Further, the excess water maintains the relative humidity (RH) in the pore structure to be 100%, neglecting the RH-depression due to salts dissolved in the pore solution. At w/c of 0.30 on the contrary, hydration is significantly retarded when all the capillary water is consumed, i.e. the cement attempts to react with the harder bound gel water. As a result, the cement paste self-desiccates and hydration stops although a certain amount of cement remains unreacted. The growth of hydration products is restricted at this stage due to lack of free water and the minimum gel porosity. The latter is about 26 to 28% by volume of the cement gel. Of course, the maximum degree of hydration decreases with decreasing w/c ratio. In contrast, the capillary porosity at maximum degree of hydration is higher when increasing the w/c ratio provided that $w/c > 0.42$. Brouwers [Brouwers 2004] revealed that the minimum w/c ratio necessary to obtain complete hydration is actually lower for CEM I produced nowadays, i.e. around 0.39. Nevertheless, in the present thesis the calculations refer to values predicted by Powers, which were found to be more in line with the values of the used Portland cement.

Another model for hydrated cement paste was developed by Feldman and Sereda [Feldman & Sereda 1968]. It was deduced from sorption measurements on water vapour and nitrogen. The cement gel is described as layered irregular structure illustrated as crumpled sheets. The model distinguishes between chemically bound water, surface-absorbed water and interlayer water. The last named is considered to be partially bound in hydrates and is therefore accounted as solid phase. Gel water, capillary water and interlayer water are assumed to be driven off at 105°C.

A third model is presented in [Tzschichholz et al. 1996]. They modelled the cement hydration by describing the dissolving and crystallization processes mainly of the tricalciumsilicate.

2.2.4 Microstructure and porosity

As a consequence of hydration the initial suspension of cement and water is transformed into a porous solid. Powers and Brownyard found only minor differences in the characteristics of the cement gel due to variation of the w/c ratio and the degree of hydration. They assumed the average diameter of the gel pores to be 2 nm. On the contrary, the capillaries get narrowed during hydration as the water is consumed and new hydration products form in the pore space [Aligizaki 2006]. A simplified illustration of the cement gel as proposed by Powers is presented below.

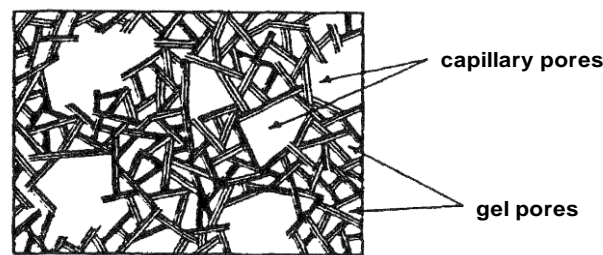


Figure 2.4: Schematic structure of cement gel as proposed by Powers [Stark & Wicht 2000].

In literature, various pore size classifications can be found, cf. appendix 2 on page 182. Stark and Wicht [Stark & Wicht 2000] classified the individual pore sizes as follows: Gel pores have a radius of up to 10 nm, capillary pores have a size between 10 nm and 10 to 100 μm , where the highest frequency is between 10 and 100 nm, and air voids range between 1 μm and 1 mm. Air-filled micropores that emerge from chemical shrinkage have sizes about 10 nm. The pore size classification considered in the thesis at hand refers to this data as reported in Figure 2.5.

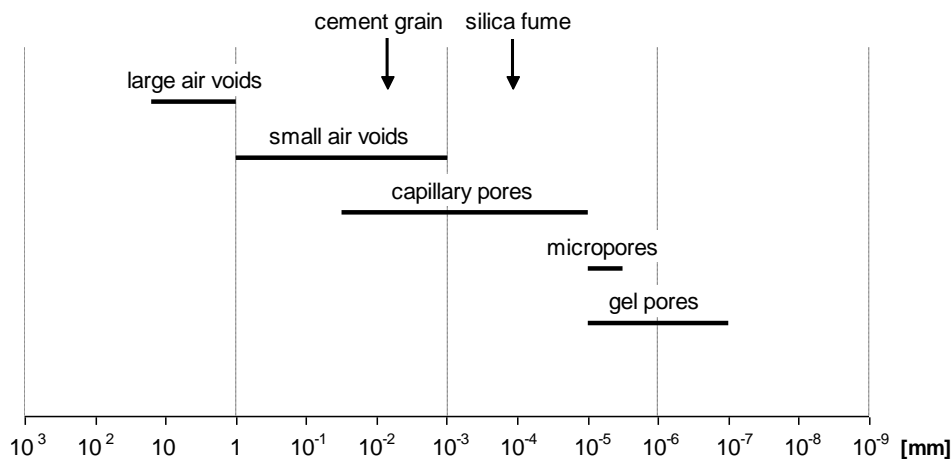


Figure 2.5: Size of various concrete pores compared to size of cement and silica fume.

2.2.5 Silica fume

Silica fume used as concrete additive according to [DIN EN 13263-1 2009] is also referred to as micro-silica or condensed silica fume. It is a by-product of the manufacture of silicon and ferro-silicon alloys made from high-purity quartz and coal. The exhaust gas SiO oxidizes and condensates in form of extremely fine particles of amorphous silica (SiO_2), which is filtered from the submerged-arc electric furnace. The effect of silica fume on the microstructure of concrete is twofold. First, the pozzolanic reaction: it is the reaction of silica fume with water and calcium hydroxide formed during hydration of Portland cement. Silica fume has a specific surface of 19 to 25 m^2/g [Alfes 1989] and is highly reactive. Self-desiccation and chemical shrinkage are increased if Portland cement is replaced by silica fume, see chapter 3.2. Due to consumption of the calcium hydroxide the addition of silica fume is limited to a maximum of 11% by mass of cement in order to maintain the high alkalinity of concrete required for protection of the reinforcing steel against corrosion, see section 2.6.3. Second, the filler-effect: It means that the spherical silica fume particles of 0.1 μm average size enter the space between the cement grains and thus improve packing. This second effect leads to reduced total porosity [Kahn et al. 2000] and pore refinement resulting in higher strength [Malier 1992]. The porosity in the interfacial transition zone between matrix and aggregates is reduced as even confirmed by numerical simulation [Bentz & Garboczi 1991a]. Besides the filler-effect, the addition of silica fume improves workability of the fresh concrete and mitigates bleeding [Neville 1995], i.e. no bleed water is trapped beneath coarse aggregates, cf. section 2.3.6. In consequence, the transition zone is no longer particular weak, neither in terms of strength, nor in terms of permeability.

2.3 Volume changes and autogenous phenomena

2.3.1 Volume changes of concrete - an overview

The total deformation of a concrete construction is the sum of stress-dependent and stress-independent deformations. The latter are of hygroscopic nature, are caused by chemical reactions or result from changes in temperature. Stress-dependent volume changes may be instantaneous, e.g. if elastic material behaviour is considered, occur due to cyclic loading or depend on time as well, i.e. strain increases with time when concrete is subjected to sustained loading. Table 2.1 presents an overview on the different volume changes of concrete classified according to the mechanism. The bold printed types of deformation are investigated in the thesis at hand.

Table 2.1: Volume changes of concrete - classification due to mechanism

Stress-independent	Time-dependent	Autogenous deformation
		Plastic shrinkage
		Drying shrinkage & expansion
		Carbonation shrinkage
Stress-dependent	Time-dependent	Creep & relaxation
		Instantaneous
	Plastic compaction	
	Cyclic	Reversible deformation
		Irreversible deformation

A brief introduction to stress-independent deformations is presented in the next sections. The mechanisms behind autogenous deformation and the autogenous phenomena involved are discussed in detail in paragraphs 2.3.3 to 2.3.5. Further, an empirical approach for the estimation of concrete shrinkage is reported and the consequences of restraint shrinkage are paid attention to. The basics on stress-dependent deformation mechanisms, primarily mechanisms causing creep of concrete under constant load, are addressed in chapter 2.5.

2.3.2 Stress-independent deformations

The effects involved in stress-independent deformation are still under discussion but there is broad consensus about the general mechanisms [Müller et al. 2012]. In contrast, the terminology found in literature is inconsistent in some cases, especially with regard to autogenous deformation. The nomenclature of the term “autogenous deformation” in this dissertation will be adopted from [Jensen & Hansen 2001a]. It bases on definitions of physical chemistry:

- Autogenous deformation: The bulk deformation of a closed, isothermal, cementitious material system not subjected to external forces. It includes chemical shrinkage, which is the internal volume reduction associated with the cement hydration reactions as already introduced in chapter 2.2.3. In addition, self-desiccation shrinkage is the autogenous deformation of a set cementitious material system caused by chemical shrinkage.

The following definitions base on the terminology given in [Neville 1995]:

- Plastic shrinkage: The contraction of concrete due to evaporation of water from the surface while the concrete is still in plastic state (fluid or semi-fluid).
- Drying shrinkage: The shrinkage of concrete caused by the withdrawal of water when stored in unsaturated air.
- Carbonation shrinkage: The contraction of concrete resulting from carbonation.
- Thermal deformation: The deformation of concrete caused by thermal action.

Common causes for plastic shrinkage of concrete are insufficient curing, see section 2.3.7, and lack of protection of the concrete surface exposed to severe conditions, i.e. strong wind, high temperatures and low humidity. Wittmann [Wittmann 1976] has shown experimentally that plastic shrinkage is caused by the physical process of capillary tension build-up in the mixing water present in the fresh concrete after the surface is exposed to drying. The capillary pressure is related to the connectivity between the solids of a drying suspension [Radocea 1992]. Once the water film covering the concrete surface vanishes, a complicated system of menisci develops and the tensile capillary pressure of the liquid is increased to a maximum rate which Wittmann calls “break-through pressure”. The increase is inverse proportional to the radius of the formed meniscus. As a result, the solid particles are subjected to contracting interparticular forces resulting in shrinkage, in both, horizontal (surface) and vertical (depth) direction [Cohen et al. 1990]. Plastic shrinkage cracking can occur if the amount of water lost exceeds the amount of water brought to the surface e.g. by bleeding, cf. section 2.3.6, which is needed to bridge the gaps between the solid particles by formation of water menisci.

The change in volume of drying concrete is due to removal of adsorbed water on the surface of the gel particles. It was found that the change in volume of unrestrained hardened cement paste equals approximately the volume of the water layer dried from the surface of the gel particles [Powers 1959]. In return, absorption of water, i.e. due to storage in water or moist air, leads to swelling of concrete, that means drying shrinkage is reversible to some extent. The irreversible part of shrinkage of ordinary concrete was found to be in the range of 0.3 to 0.6 of the

drying shrinkage [L'Hermite 1960]. The gel particle size has an influence on the amount of drying shrinkage since the use of cement with high specific surface shows higher concrete shrinkage. The loss of free water drained from large capillary pores, which takes place prior to loss of physically bound water, causes little or no shrinkage. In general, decreasing the capillary porosity due to decreasing the w/c ratio leads to reduction of drying shrinkage. Further, increasing the ambient humidity leads to reduction of drying shrinkage. While the ambient air humidity is in equilibrium with the concrete moisture at area close to the surface after quite a short time, the time to achieve equilibrium with the internal relative humidity of concrete may last several decades. The required period increases with increasing thickness of the concrete member exposed to drying. The free shrinkage strain along the cross-section correlates with the humidity profile resulting in eigenstresses, i.e. tensile stresses at the surface and compressive stresses in the lower depths. Surface cracking of concrete will occur if the tensile stresses reach the tensile strength.

In practice, drying shrinkage of ordinary Portland cement (OPC) concrete with normal strength includes shrinkage caused by autogenous volume change and carbonation. The latter has a share in total shrinkage when the RH ranges between 25% and <100%. It is a secondary effect caused by the binding of carbon dioxide in hydration products, cf. section 2.6.3. Actually, this comes along with an increase of mass of the hydration products and the concrete, respectively. Shrinkage is caused by the dissolving of $\text{Ca}(\text{OH})_2$ crystals while under compressive stresses (imposed by drying of concrete) and the depositing of CaCO_3 formed in spaces free from stress [Houst 1993]. As a first approximation, free concrete shrinkage ranges in total between 0.1 and 1.0 mm/m and can be assumed to be proportional to the matrix content [Neville 1995].

Thermal deformation is mainly caused by the development of heat of hydration at early age or by heat treatment. The length change of concrete $\Delta l_{c,T}$ [-] caused by thermal action ΔT [K] is:

$$\Delta l_{c,T} = \alpha_{c,T} \cdot \Delta T \cdot l \quad (2.2)$$

where $\alpha_{c,T}$ [1/K] is the thermal expansion coefficient of concrete. It is in the range 14.2×10^{-6} to 5.4×10^{-6} /K [Dettling 1962] and depends on composition, moisture and age of concrete.

2.3.3 Problems resulting from autogenous phenomena

Autogenous deformation is the self-created deformation of a closed cementitious system. That means it occurs devoid of environmental impacts such as changes in temperature and humidity or external loads. It is a phenomenon known from the beginning of the 20th century [Neville & Jones 1928] but not much noticed since for ordinary concrete autogenous deformations are negligible compared to e.g. drying shrinkage [Davis 1940]. Only when the first high performance concretes (HPC) were developed in the 1980s, autogenous shrinkage has achieved increasing practical relevance [Jensen & Hansen 1996]. HPC is characterized by low w/c ratios (far below 0.40) and, at the same time, the use of superplasticizer to maintain workability and micro-fillers to further increase strength. In the process, capillary porosity is reduced dramatically and thus impermeability is increased. As a result, conventional water curing (section 2.3.8) is not applicable as penetration of water from the external surface is limited to small cross-sections only [Schrage 1994]. Self-desiccation occurs in the interior of concrete due to chemical water binding as a consequence of hydration resulting in high autogenous shrinkage, primarily at very early age, i.e. when the matrix has small stiffness (section 2.3.4). However, autogenous shrinkage should be limited since it may induce micro-, macro- or even through-cracking of concrete if restraint (section 2.3.8) and may extensively impair the quality of concrete structures [Paillère et al. 1989].

2.3.4 Mechanisms causing autogenous shrinkage

Most literature published in recent years emphasizes capillary tension in the pore fluid to be the prominent mechanism causing self-desiccation shrinkage [Fontana 2007]. It correlates well with the drop in internal relative humidity which is indicating self-desiccation. In [Lura et al. 2003] various other mechanisms suggested for the description of autogenous shrinkage are intensively discussed. A summary of the main mechanisms debated by Lura is presented in the following. Besides the capillary tension approach, these are the disjoining pressure and the change in surface tension of the solid gel particles.

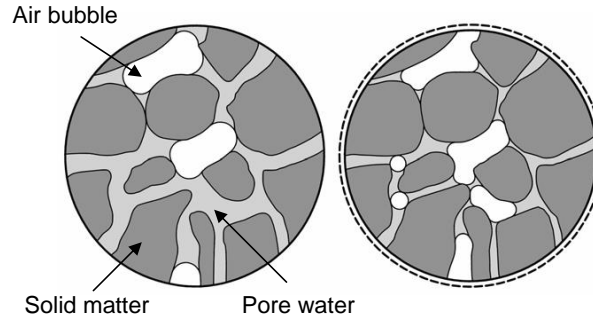


Figure 2.6: Schematic representation of a cross-section of hydrating cement paste at low degree of hydration (left) and at high degree of hydration (right) [Jensen & Hansen 2001a].

As long as the cement paste is a fluid suspension, i.e. before setting, the internal volume reduction due to chemical shrinkage may be completely converted into a bulk deformation of the system, also called setting shrinkage [Jensen & Hansen 2001a]. Thus, setting shrinkage is a constituent part of the autogenous deformation and amounts to about 1% of the total shrinkage. With begin of setting that means when the cement paste starts to form a solid skeleton, the paste system gains stiffness and is able to sustain this external volume change. As a result small air bubbles arise as illustrated by Figure 2.6. The small air bubbles form water-air menisci causing the relative humidity to drop. The drop in internal RH is related to the radius of the water-air meniscus, r [m], according to Kelvin's law:

$$r = \frac{-2\gamma \cdot V_w \cdot \cos \theta}{\ln RH \cdot RT} \quad (2.3)$$

where γ [N/m] is the surface tension of the pore fluid, V_w [m³/mol] the molar volume of water, i.e. 18.02×10^{-6} , R [J/mol K] the ideal gas constant, i.e. 8.314, T [K] the absolute temperature and θ [-] the contact angle between water and solids, with $\cos \theta \approx 1$ in case of perfect wetting.

Self-desiccation starts in larger pores and passes on to smaller pores. The radius of the largest pore filled with water as a function of the RH is reported in Figure 2.7 (left). In doing so, γ was assumed as 0.073 N/m. The capillary tension in the pore fluid σ_{cap} [MPa] is given by Laplace's law:

$$\sigma_{cap} = -\frac{2\gamma}{r} \quad (2.4)$$

Both Kelvin's law and Laplace's law apply to the assumption of circular cylindrical pores. Theoretically, the maximum surface tension at 75% RH is -38.4 MPa, as reported in Figure 2.7 (right). At the same time pores of diameter > 3.8 nm are already emptied due to self-desiccation.

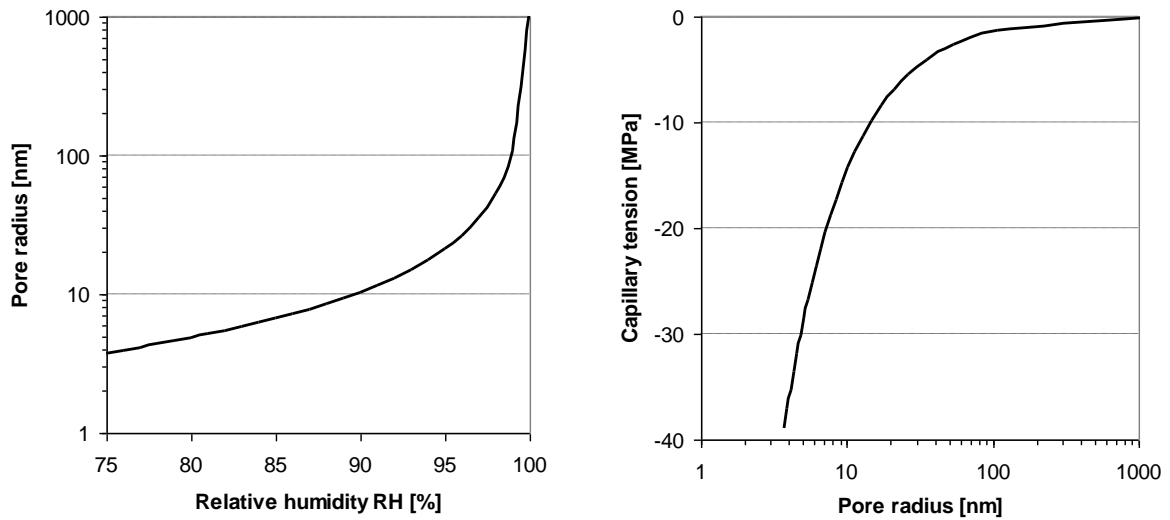


Figure 2.7: Pore radius as a function of internal RH (left) and capillary tension as a function of the radius of water-filled pores (right).

The fact that shrinkage reducing agents (SRA) successfully diminish autogenous shrinkage by lowering the surface tension of the pore fluid [Bentz et al. 2001], underlines the importance of the capillary tension approach. Nevertheless, as further consequence of the RH drop, the layer thickness of adsorbed water on the gel solid particles is decreased. This leads to changes in the surface tension of the solid particles and the disjoining pressure between these particles as well.

The surface tension approach goes back to Bangham [Bangham & Fakhoury 1931]. It states that shrinkage and expansion are driven by changes in the surface tension of the gel solid particles caused by adsorption and desorption of water, respectively. The surface tension results in hydrostatic pressure acting on the colloidal solids leading to compaction of the whole system. Adsorption of water lowers the surface tension resulting in expansion whereas desorption of water leads to shrinkage. Bangham studied this phenomenon on coal. He proposed the relation of swelling to the change in surface tension by the following equation:

$$\frac{\Delta l}{l} = \lambda \cdot \Delta \gamma_{solid} \quad (2.5)$$

where l [m] is the length, Δl [m] the length change, λ [s²/kg] a coefficient of proportionality and $\Delta \gamma_{solid}$ [N/m] is the change in surface tension of the solid particles.

The change in thickness of the water layers covering the solid particles influences the surface tension only minor if more than three water layers are absorbed [Wittmann 1977]. This will be the case for RH above 40% [Ferraris & Wittmann 1987]. In other words, surface tension of the solid gel particles does not play a major role in terms of self-desiccation shrinkage where normally, the RH does not drop below 75% [Jensen & Hansen 1995].

In regions of hindered adsorption, i.e. where water of less than two times the thickness of an adsorbed layer is inbetween two solid particles, cf. Figure 2.8 (p. 14), the so called disjoining pressure comes into effect. According to [Ferraris & Wittmann 1987] the disjoining pressure between solid particles is the result of attracting forces, i.e. van der Waals forces, and repelling forces, i.e. electrostatic double layer repulsion and structural forces. Due to drop in RH, the disjoining pressure is decreasing and consequently the paste system contracts. In [Wittmann 1977] it is proposed that the disjoining pressure contributes to hygroscopic deformation at RH above 40%.

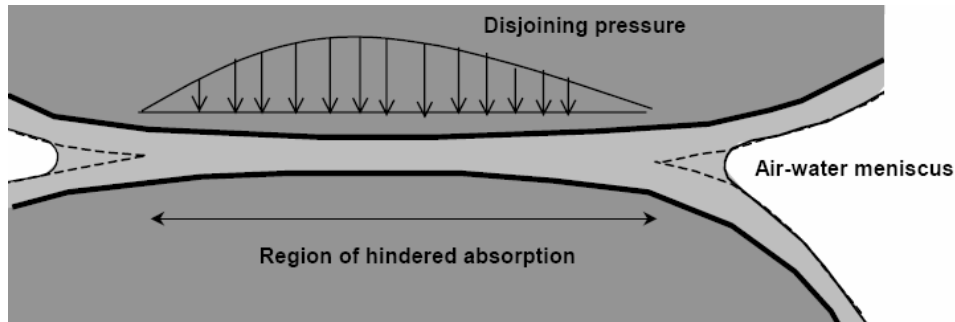


Figure 2.8: Region of hindered adsorption and distribution of disjoining pressure [Lura 2003].

2.3.5 Mechanisms causing expansion

It is well known that concrete with high w/c ratio shows expansion during hardening even when sealed storage is applied [Grube 1991]. It was Le Chatelier who already found in 1900 that cement paste stored in saturated condition expands during hydration although it undergoes chemical shrinkage at the same time [Le Chatelier 1900]. The source of the observed expansion is different from the mechanisms causing expansion of cement paste which is dried prior to re-wetting, q.v. chapter 2.3.2. Powers explained autogenous expansion of cement paste by the absence of capillary pressure, which in drying conditions would counteract expansion by imposing shrinkage [Powers 1935]. According to [Bažant & Wittmann 1982] autogenous expansion is caused by growth of hydration products in the set cement paste. Indeed, the hydration products have less net volume than the reactants, but they occupy more space as they form a spatial network.

In [Lura 2003] further possible mechanisms causing autogenous expansion are discussed. An important factor is the disjoining pressure acting on surfaces of hindered adsorption, see Figure 2.8. As the total surface of hydration products is larger than of the reactants they emerge from, the region of hindered adsorption is increasing as hydration proceeds [Wittmann 1977]. As a result, expansion may occur. Crystallization processes, e.g. formation of ettringite and portlandite are also indicated as principal cause of autogenous expansion [Baroghel-Bouny & Kheirbek 2001]. Lura partially attributed the temporary expansion observed on blast furnace slag cement paste within the acceleration period of hydration to this phenomenon. On the other hand, subsequent conversion of ettringite to monosulphate seems to cause intensified shrinkage [Han et al. 2000].

Mohr and Hood [Mohr & Hood 2010] observed only small influence of ettringite growth on expansion at early age. The same was found for thermal dilation caused by heat release due to hydration. They showed the primary cause for early age expansion to be bleed water reabsorption.

2.3.6 Settlement and bleeding

Due to clear distinction between density of water and solid components, the latter, i.e. aggregates and cement particles, start to settle in fresh concrete [Müller et al. 2012]. As a result, excess mixing water is forced upward. The accumulation of mixing water on the surface of fresh concrete is called bleeding. This process stops either when the matrix sets or the solids are bridging. The latter case leads to internal bleeding if settlement of cement particles continues and consequently water segregates beneath aggregates or reinforcing steel. Addition of supercritical amounts of superplasticizer increases the risk of bleeding [Spanka et al. 1998]. In general, bleeding reduces the w/c ratio leading to higher density of the concrete but also causes optical impairment. At last, settlement and bleeding result in external volume change.

2.3.7 Empirical approach for modelling shrinkage of concrete

In general, models estimating the shrinkage strain of concrete have to consider effects of creep leading to time-dependent reduction of stresses induced when restraint. An empirical approach to predict autogenous shrinkage ε_{as} [μstrain] and drying shrinkage ε_{ds} [μstrain] of concrete as a function of concrete age t [days] and concrete age at begin of drying t_t [days] is presented in [Müller et al. 2012]. It is:

$$\varepsilon_{as}(t) = \varepsilon_{as,\infty} \cdot \left[1 - e^{(-0.2\sqrt{t})} \right] \quad (2.6)$$

$$\varepsilon_{ds}(t, t_t) = \varepsilon_{ds,\infty} \cdot \sqrt{\frac{t - t_t}{H \cdot h_0^2 + t - t_t}} \quad \text{with:} \quad h_0 = \frac{2A}{u} \quad (2.7)$$

where H is 3.5, an empirical coefficient, h_0 [cm] is the effective thickness of the specimen, A [cm] its cross-section and u [cm] its perimeter exposed to drying. Further $\varepsilon_{as,\infty}$ [μstrain] is the final autogenous shrinkage coefficient and $\varepsilon_{ds,\infty}$ [μstrain] is the final drying shrinkage coefficient. Both depend on f_{cm} [MPa], the 28 days compressive strength measured on cylinders, and the type of cement. Further $\varepsilon_{ds,\infty}$ depends on the ambient RH. For the cement of type CEM I 42.5 R, as used in this thesis, both coefficients can be approximated by equation (2.8) and equation (2.9), respectively:

$$\varepsilon_{as,\infty} = -\gamma_{as} \left(\frac{f_{cm}}{60\text{MPa} + f_{cm}} \right)^{2.5} \cdot 10^{-3} \quad \text{with:} \quad \frac{f_{cm}}{f_c} = 0.85 \quad (2.8)$$

$$\varepsilon_{ds,\infty} = -\gamma_{ds} \cdot e^{\left(\frac{0.12 \cdot f_{cm}}{10\text{MPa}} \right)} \cdot 10^{-3} \quad (2.9)$$

where γ_{as} is 0.6, γ_{ds} is ≈ 1.0 at 65% ambient RH and f_c is the 28 days cube compressive strength.

2.3.8 Restraint shrinkage and relevance of curing of concrete

In the above description of volume changes, load-dependent and load-independent actions were regarded decoupled. Actually, load independent deformations are accompanied by stresses - be it eigenstresses in the cross-section of a concrete member due to temperature or drying gradient, or be it stresses due to restraint support conditions or due to deformations imposed in any other manner. In practice, restraint of a concrete member can be caused externally, e.g. by adjoining structures, or internally either by reinforcement or by aggregates [Dela 2000]. Restraint shrinkage leads to tensile stresses in the concrete, whereas restraint expansion results in compressive stresses. The result of changes in temperature depends on whether a decrease or an increase of temperature is considered. The latter occurs e.g. at early age due to development of heat of hydration resulting in compressive stresses. When the concrete structure cools down at later age, i.e. after a certain gain in stiffness has arisen and hydration slows down, the restraint concrete tries to contract and may crack if the tensile stress reaches the concrete's tensile strength. In doing so, external restraint causes through-cracking, while internal restraint leads to micro-cracking.

Compared to changes in temperature, shrinkage of concrete is normally related to higher risk of cracking if restraint. Extent and fraction of each type of shrinkage depend on the type of concrete: Drying shrinkage is dominant in case of ordinary concrete, but autogenous shrinkage may be constitutive in case of high performance concrete (HPC) [Müller et al. 1999]. Both types

of shrinkage should be limited, i.e. by conventional curing in terms of drying shrinkage, or by internal curing in terms of autogenous shrinkage (chapter 2.4). Conventional, external curing can be provided in two ways [Rilem 2007], either by water curing, i.e. ponding or spraying the surface with water, respectively, or by preventing loss of moisture from the concrete. The latter, which is also called sealed curing, is achieved e.g. by:

- leaving formwork in place
- covering the concrete with impermeable membrane
- application of suitable chemical curing agents.

In practice, there are often used combinations of the above curing procedures. External curing is further recommended in order to prevent plastic shrinkage. Plastic shrinkage may occur even without being externally restraint. It is particularly harmful since it may cause early age through-cracking of mainly flat concrete members with cracks ranging in width of up to 3 mm [Neville 1995]. Complete prevention of evaporation immediately after casting eliminates plastic shrinkage cracking [Ravina & Shalon 1968].

To summarize, sufficient curing is needed in order to prevent early age cracking and therefore can be seen as key to produce durable concrete construction.

2.4 Internal curing

2.4.1 Idea of internal curing

Internal curing (IC) means incorporation of a component to the concrete mixture which serves as curing agent [Rilem 2007]. IC can be classified in two categories as proposed by Rilem:

- 1) Internal water curing, which includes the incorporation of a curing agent that serves as an internal water reservoir. This method is also called water entrainment.
- 2) Internal sealing, which introduces a curing agent to the concrete with the intention to delay or prevent the system from water evaporation.

The latter category is not relevant for the thesis at hand. The first definition, which is internal water curing or water entrainment, respectively, is referred to as internal curing in the following.

The basic principle behind IC is the provision of internal water sources to prevent concrete, i.e. HPC, from self-desiccation on the one hand and, on the other hand, to promote hydration. Self-desiccation can be eluded by water movement from the internal water source into pore space created by chemical shrinkage. This way, the formation of water-air menisci is mitigated and the drop in RH is reduced or even prevented. Consequently, the risk of early age cracking caused by self-desiccation shrinkage is dramatically reduced. Since internal curing water is considered as extra water which is accessible for hydration, IC leads to an increase of the degree of hydration.

In literature, several techniques are reported that can be used for incorporation of internal water reservoirs. The most prominent technique is using saturated lightweight aggregates (LWA). More recently, superabsorbent polymers (SAP) are investigated for water entrainment. But also other materials are suggested for this purpose as reported in the next sections.

2.4.2 General prerequisites for internal curing

Appropriate internal curing requires unrestricted supply of water from the internal water source to the cementitious reaction. The thermodynamic availability of water is decreasing with lowering its equilibrium relative humidity, i.e. $< 100\%$. As mentioned previously, cf. Figure 2.7 on page 13,

pure water held in circular cylindrical pores of a porous body will have an equilibrium RH of approximately 99% if the meniscus formed has a diameter of about 200 nm. That means that only substances with water-saturated pores of larger than 200 nm in diameter are recommended for appropriate IC. Further, the kinetic availability of water determines the effectiveness of IC. Thus, another prerequisite for appropriate IC is that water from the internal source is transported to all areas of the self-desiccating matrix. Kinetic availability is eased by spatial distribution of the water sources i.e. due to increasing the specific surface. Nevertheless, water release may be described as a competition for water between internal water source and hydrating cement paste [Mönnig 2009]. Simulations reported in [Bentz & Snyder 1999] showed that the effective distance water can travel in ultra-high performance concrete (UHPC) is limited to approximately 200 μm .

Several potential techniques for incorporation of internal curing water in concrete are presented in [Jensen & Lura 2006]. The various materials were distinguished by the mechanism of water storage, i.e. substances with:

- chemically bound water, e.g. crystalline water in ettringite
- physically adsorbed water, e.g. water in SAP
- physically held water, e.g. capillary water in fine pores of LWA
- unbound water, e.g. water in micro-encapsulations.

For SAP and some suitable lightweight aggregates, material pricing and costs per one kg curing water incorporated are listed in Table 2.2. The data should be seen as a rough guide only. Data of SAP refer to the materials used in this thesis, see chapter 4.

Table 2.2: Pricing and cost efficiency of IC materials (*)²

Material	Water content [kg water/kg]	Material price [€/kg material]	IC water price [€/kg IC water]
SAP	10-40	6	0.15-0.6
Liapor*	0.17	0.1	0.6
Pumice*	0.27	0.06	0.2
Perlite*	4.5	0.3	0.07
Stalite*	0.06	0.04	0.7

2.4.3 Internal curing with lightweight aggregates

LWA having high open porosity added pre-saturated to the concrete mix can effectively counteract autogenous shrinkage as demonstrated e.g. in [Hammer 1992]. Extra water stored in large pores of LWA is drawn into smaller pores of the hydrating cement paste, which is called “autogenous curing” [Weber & Reinhardt 1997]. The difficulties that occur when using LWA, i.e. controlling the consistency of fresh concrete and reduction of mechanical properties of hardened concrete due to poor mechanical properties of the water source, are minimized by the use of SAP.



Figure 2.9: LWA of different size (mm) made of expanded clay (Liapor) [Mönnig 2009].

² (*): Average values adopted from [Jensen & Lura 2006].

2.4.4 Internal curing due to SAP

Macropore inclusions with SAP particles (see chapter 2.9) provide “water-entrainment in its purest form” [Jensen & Hansen 2001b]. SAP can either be added dryly to the mix or in water-saturated condition. In this thesis, the first approach was conducted, i.e. SAP were dryly pre-mixed with cement/binder. In doing so, swelling as illustrated by Figure 2.10 starts as soon as SAP are getting in contact with water. Due to high alkalinity of the pore solution, the swelling capacity in concrete is reduced compared to tap water. The volume increase due to uptake of mixing water amounts to circa 2 to 3.5 times the volume of the dry particles. The basic principles of using SAP in concrete construction, for the purpose of IC in particular, are reported in chapter 3.



Figure 2.10: SAP particles in dry condition (left) and the same amount of SAP after absorption of tap water [Schwarz 2005] as cited in [Mönnig 2009].

2.5 Deformation of concrete under constant load

2.5.1 Introduction

The total strain of concrete in constant environment exposed to constant uniaxial loading is divided into three additive components: shrinkage ε_s , initial elastic strain at loading ε_{el} and creep ε_c , see equation (2.10). Both instantaneous strain at loading and creep strain are the subject matters of this section, in particular with respect to loading in tension. The principles of shrinkage were extensively described in section 2.3.

$$\varepsilon_{tot}(t) = \varepsilon_s(t, t_d) + \varepsilon_{el}(t_0) + \varepsilon_c(t, t_0, t_d) \quad (2.10)$$

Figure 2.11 illustrates qualitatively the components of total concrete strain $\varepsilon_{tot}(t)$ at any time t in case of uniaxial compression loading (left) and tension loading (right). The constant stress σ is applied at time t_0 . Drying starts before, viz at time t_b and the time of unloading is called t_f . In the compression case, the shrinkage strain is in the same direction with creep and in the tension case creep is directed opposite to shrinkage. The elastic strain at loading $\varepsilon_{el}(t_0)$ is always in the direction of creep but is fully reversible, that means the elastic strain at unloading $\varepsilon_{el}(t_f)$ amounts the same. Creep reflects the viscoelastic character of concrete and therefore is only partly reversible, cf. Table 2.3. It is defined as time-dependent response of strain due to constant loading and, thus, does not include load-free volume changes that occur at the same time. The irreversible part of creep that occurs instantaneously at loading is rather small and is known as plastic set $\varepsilon_{ei}(t_0)$. The time-dependent irreversible part of creep is known as viscous deformation and the third part of creep is the elastic-delayed strain $\varepsilon_{ej}(t, t_f)$. The latter is time-dependent as well but fully recoverable on unloading. It reduces the total creep strain after unloading to the final creep ratio of $\varepsilon_c(t=\infty)$.

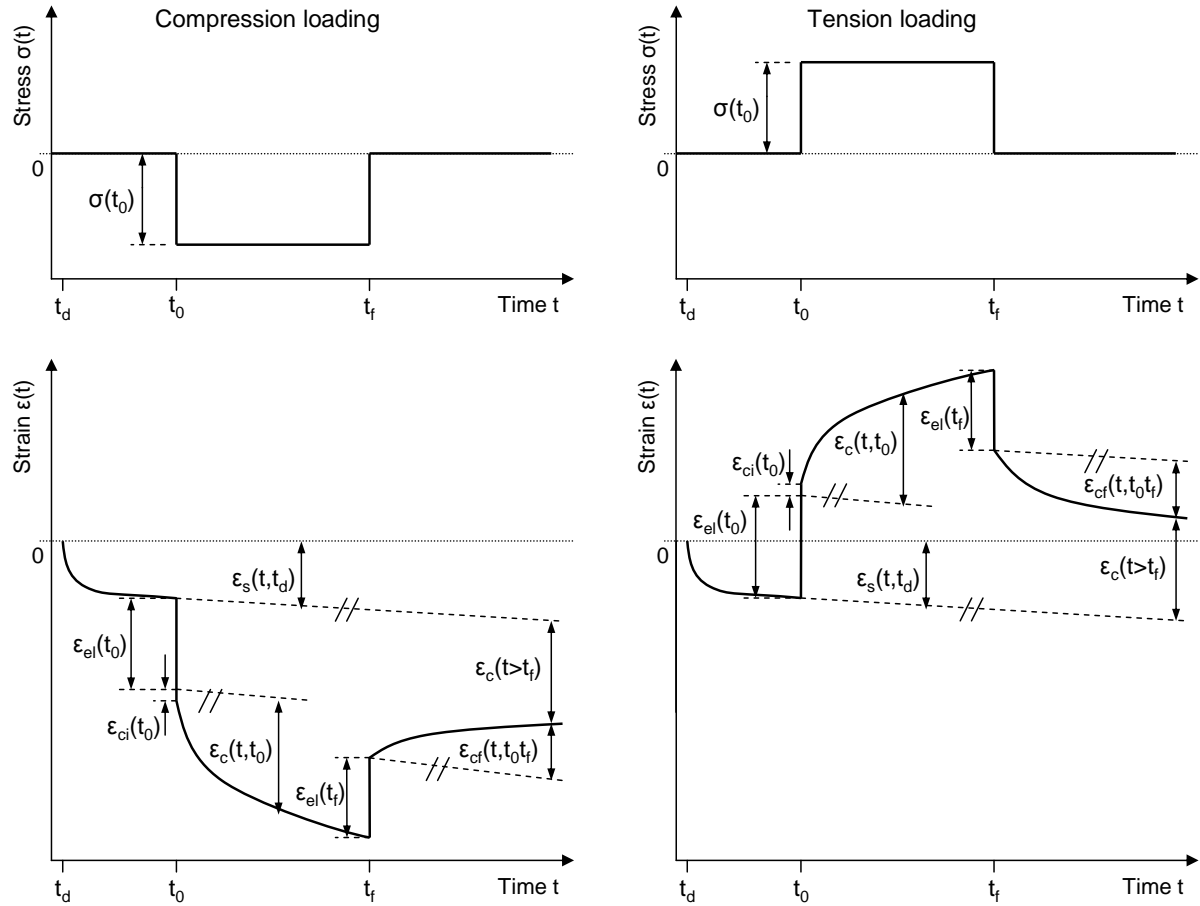


Figure 2.11: Definition of strain components of uniaxially loaded and unloaded concrete.

There is dispute whether creep under loading for an indefinite time period will ever end or not. However, this issue is not relevant in practice since the increase in creep strain becomes smaller with time. Table 2.3 summarizes the phenomenological types of deformation that all, except the instantaneous strain at loading, contribute to concrete creep. To characterize creep, the so-called creep coefficient φ_c is introduced as quotient of creep strain ε_c to elastic strain at loading ε_{el} . At this point it should be noted that uniaxial loading of a concrete specimen of course not only results in longitudinal strain in the direction of the applied load but, at the same time, produces a lateral strain of opposite sign. The factor of lateral to longitudinal strain is referred to as Poisson’s ratio.

$$\varphi_c(t, t_0) = \varepsilon_c(t, t_0) / \varepsilon_{el}(t_0) \tag{2.11}$$

Indeed, equation (2.11) is accepted for stress-strength ratios of < 0.40 only. At above loading rates, creep is disproportionately increasing with stress and at loading rates $> 75\%$ of the tensile strength, rapid failure may occur [Rinder 2002]. Already at 50% of the tensile strength, micro-cracks occur in the interfacial transition zone between matrix and aggregate. In the crack tips, high stresses provoke crack propagation. Due to inhomogeneities like air voids, cracks are branched but still progress until they reach the concrete surface and cause failure [Blaschke 1993].

Table 2.3: Stress-dependent strain components [Neville 1995]

Type of deformation	Instantaneous	Time-dependent
Reversible	Elastic*	Delayed-elastic
Irreversible	Plastic set	Viscous

(*): not part of creep strain

2.5.2 Pickett's effect

In the above-made description the total concrete strain is the sum of elastic, creep and shrinkage strain. In this view, creep and shrinkage are asserted as separable phenomena where creep is defined as the total strain of a loaded specimen minus the initial elastic strain and the shrinkage as measured on an unloaded companion specimen. But the principle of superposition may underestimate the total strain. This observation is referred to as Pickett's effect [Pickett 1942]. It states that during simultaneous creep and shrinkage, the total time-dependent strain ε_{tot} does not equal to the sum of the separate strain of loaded concrete prevented from drying ε_{bc} and the strain of load-free companion specimen exposed to drying ε_{ds} , but differs by an extra strain called drying creep ε_{dc} , as illustrated by Figure 2.12. It is:

$$\varepsilon_{dc} = \varepsilon_{tot} - \varepsilon_{ds} + \varepsilon_{bc} \quad \text{with} \quad \varepsilon_c = \varepsilon_{bc} + \varepsilon_{dc} \quad (2.12)$$

In literature the creep strain of concrete loaded in sealed condition, i.e. under conditions of no moisture exchange with the environment, is called basic creep ε_{bc} and drying creep ε_{dc} is defined as additional creep in excess of basic creep when the loaded concrete is allowed to dry. In case of concrete produced with low w/c ratio, i.e. w/c < 0.42, concrete suffers from internal, probably uniform drying and therefore basic creep in its proper sense cannot be measured. To overcome confusion, Atrushi [Atrushi 2003] introduced the notion "sealed creep". The term sealed creep implies drying creep from self-desiccation that occurs at sealed condition.

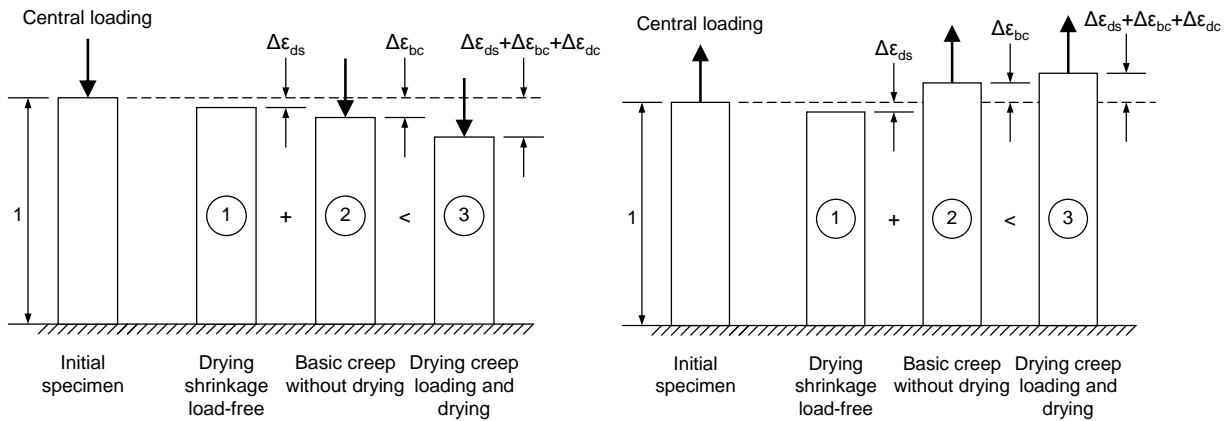


Figure 2.12: Pickett's effect in centric loading in compression (left) and in tension (right). Based on [Bažant & Xi 1994].

In most literature, two major mechanisms are cited that cause Pickett's effect, viz micro-cracking [Wittmann 1982] and stress-induced shrinkage [Bažant & Chern 1985]. In compression, micro-cracking as a result of eigenstresses in the specimen caused by non-uniformity moisture distribution (tension at surface exposed to drying and compression in the moist interior) is compensated. Therefore, the drying shrinkage of a non-loaded companion specimen is smaller than the real shrinkage as micro-cracks cannot close in consequence of inelastic material behaviour when the eigenstresses fade. From this point of view it is not correct to call the extra drying deformation a creep strain [Altoubat & Lange 2002a]. In case of tension loading the tensile stress in the drying surface zone is increased and promotes micro-cracking. Therefore it is rather to speak of reduced shrinkage strain instead of increased creep strain. The outcome of this approach implies that total strain is always increased in the direction of load and, thus, in the direction of creep.

With increasing the weight loss due to drying while the specimen is under load, up to five times larger creep deformations were measured compared to basic creep strain [Acker & Ulm 2001]. But Wittmann's theory can only partially explain such immense increase in strain. Further, the development of tensile strength protects concrete from excessive micro-cracking at later age. Hence, micro-cracking in concrete skin as cause of extra drying creep strain was called into question [Kovler 1995].

The stress-induced shrinkage approach provides a different explanation. It states that during drying, moisture diffusion transports water from micropores to larger capillary pores (micro-diffusion). While macro-diffusion in the large capillaries does not affect deformation, the movement of water through the gel pores causes the breakage of bonds and again the formation of new CSH-bonds. However, there are also some doubts about the correctness of this concept [Kovler 1999]. Some researchers even promote the idea of shrinkage-induced creep as potential cause of drying creep strain [Kovler 2001]. But, in the course of investigations on tensile creep of high-strength concrete [Reinhardt & Rinder 2006] it was found that loaded specimens dry more, shrink more and hydrate more than non-loaded specimens. The fact that shrinkage even exceeded the creep strain supports the idea of stress-induced shrinkage as cause of drying creep. Rossi [Rossi et al. 2012] even proposes basic creep to be mainly an additional self-drying shrinkage under stress.

An attempt to experimentally separate the effects of micro-cracking and stress-induced shrinkage on drying creep was invented by [Bažant & Xi 1994]. They examined the curvature creep of beam specimens exposed to the same bending moment but different eccentric loadings. The stress-induced shrinkage was found to increase continuously whereas micro-cracking contributed more intensively to creep at early age and then reduced its influence over time. According to [Bažant et al. 1988] the part of creep increase per unit stress due to cracking is larger for tension than for compression, while the part of stress-dependent shrinkage is about the same. Comparative experiments on uniaxial tension loaded beam specimens revealed the influence of micro-cracking to be almost non-existent in case of fibre-reinforced concrete, while the stress-induced shrinkage was found to yield the same with plain control concrete [Altoubat & Lange 2002b]. It was concluded that preventing the apparent drying creep caused by micro-cracking, i.e. due to fibre-reinforcement, reduces the creep strain and enhances stress relaxation.

Since creep and relaxation capability decrease with time [Kordina 1999] it is useful to investigate the early-age behaviour of concrete under constant loading. Especially creep in tension needs to be concerned when the possibility of cracking due to shrinkage and thermal stress is high.

2.5.3 Creep mechanisms

Several theories have been elaborated to explain the mechanisms of creep. As cited in [Lange & Altoubat 2003] the main creep mechanisms as proposed by [ACI 209R 1992] are:

- 1) Viscous flow of cement paste caused by sliding or shearing of the gel particles lubricated by layers of absorbed water.
- 2) Consolidation of gel due to seepage in the form of absorbed water or the decomposition of interlayer hydrate water.
- 3) Delayed elastic deformation due to the cement paste acting as a restraint on the skeleton formed by the aggregates and gel crystals.
- 4) Permanent deformation caused by micro-cracking as well as re-crystallization and formation of new physical bonds.

Although these mechanisms are still under discussion, it is generally agreed that viscous flow and seepage are the main causes of creep. The viscous flow hypothesis [Ruetz 1968] states that few layers of absorbed water are appropriate to ensure shearing of CSH particles. The Seepage theory [Powers 1968] postulates that creep is caused by change of internal vapour pressure that results in change of gel water content. In regions of hindered absorption, seepage of gel water under pressure into regions of unhindered absorption causes decrease in the disjoining pressure, cf. section 2.3.4. From this viewpoint, creep is a time-dependent removal of a swollen state of the gel solid. Further theories are the interlayer theory [Feldman & Sereda 1968] and the thermal activation theory [Wittmann 1982]. However, each theory considered individually is not able to explain all creep phenomena. A comprehensive discussion on creep mechanisms is given in [Bažant & Chern 1985]. Besides, relaxation is expected to refer to the same mechanisms as creep of concrete and means the time-dependent stress reduction under imposed constant deformation.

2.5.4 Parameters influencing creep

As stated in [Müller & Kvitsel 2002], it is well known from systematical investigations on creep of concrete that the creep strain:

- increases with increasing loading time and increasing stress-strength ratio,
- is greater the higher the cement content or the matrix volume,
- decreases with decreasing porosity, with exceeding hydration and lowering the w/c ratio,
- increases with faster weight loss due to drying, and
- is on the increase if temperature rises but is constant during loading.

So far, no investigation about the effect of SAP addition on tensile creep of concrete exists.

2.5.5 Measure of tensile creep

Measuring creep under uniaxial tensile loading can be performed either by the direct measuring method where the concrete specimen is subjected to a constant load (conventional test) or tensile creep is indirectly measured from a restraint shrinkage test [Kovler et al. 1999]. In the second method, the strain is incrementally pulled back to zero (restraint condition) after shrinkage occurred and has approached a pre-defined level. The creep plus shrinkage strain is obtained by adding the incremental strains over time. The conventional method was applied in this thesis (chapter 8).

2.6 Durability of concrete

2.6.1 Introduction

The mechanical properties of concrete are of outstanding importance for the stability of concrete structures, but they alone will not be sufficient to describe the serviceability. Concrete structures have to withstand all kinds of actions and threats possible for the expected service life, i.e. the material properties must not change inadmissibly. Actions are directed either to cause corrosion of the reinforcing steel or of the concrete itself. The resistance of concrete structures against both classes of action are subsumed under the term durability of concrete.

In the following, an overview on the mechanisms causing deterioration of concrete is given and the classification of risk of deterioration is addressed. As durability of concrete in the vast majority of cases is related to transport of gas, water or deleterious substances, the mechanisms behind are discussed in chapter 2.7. A special topic, the impact of freezing and thawing associat-

ed by the action of dissolved salts, is the subject matter of chapter 2.8. An outline of the durability aspects edited in the dissertation at hand will follow in chapter 3.

2.6.2 Exposure classes

Environmental and ground conditions are classified as exposure classes in [DIN EN 206-1 2001] for both the attack of concrete and the corrosion of reinforcement. Table 2.4 provides a general overview. The set of exposure classes reflects the chemical and physical environmental conditions the concrete and the reinforcement, respectively, are exposed to. A more detailed description of the exposure classes including informative examples for concrete structural elements is provided in appendix 2 on page 182. The number in the class designation indicates the risk potential. The higher the number the higher the risk indicated.

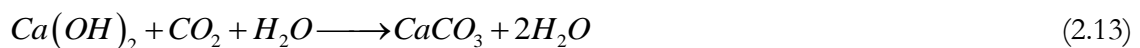
Table 2.4: Exposure classes of structural concrete according to DIN EN 206-1/DIN 1045-2

Classification of risk of concrete attack		Classification of risk of corrosion of reinforcement	
Class designation	Class description	Class designation	Class description
X0	No risk of attack	X0	No risk of corrosion
XF (XF1 ... XF4)	Freeze thaw attack	XC (XC1 ... XC4)	Corrosion induced by carbonation
XA (XA1 ... XA3)	Chemical Attack	XD (XD1 ... XD3)	Corrosion induced by chlorides
XM (XM1 ... XM3)	Mechanical Abrasion	XS (XS1 ... XS3)	Corrosion induced by chlorides
W0, WF, WA, WS	Alkali-Silica Reaction		from sea water

For a given structural element, different surfaces might be exposed to different environmental actions. If concrete is subject to more than one of the actions described in Table 2.4, the environmental conditions are expressed as a combination of exposure classes.

2.6.3 Corrosion of reinforcement

Corrosion of steel reinforcement is prevented by the passivity layer of iron oxide formed in the alkaline environment of hardened cement paste. Corrosion takes place if the passivation is lost by carbonation or a critical concentration of chloride ions is present and, at the same time, water and oxygen are available. Carbonation is the chemical reaction of the hydrated cement paste with carbon dioxide molecules diffusing from air into concrete, see section 2.7.3. Equation (2.13) depicts the main reaction where OH⁻ ions are consumed and calcium carbonate is formed causing the pH value to drop. Once the pH value drops below 9, the steel reinforcement is depassivated.



Chloride induced corrosion of reinforcing steel is the most important degradation process for reinforced concrete structures [Tang & Zhu 2007]. The two main sources for chlorides to penetrate into concrete are seawater and de-icing agents. Chlorides enter the concrete dissolved in water, but the mechanisms behind chloride ingress are not fully understood. In dependence on the cement composition, the temperature and the alkali concentration, chlorides are bound by the matrix to a certain extent [Tang 1996]. Only when a critical concentration of free chloride ions reaches the reinforcement, depassivation occurs. In [Richartz 1969] the amount of chlorides bound in hardened Portland cement was found to yield 0.4% by mass of cement. It is in agreement with the limit value for chlorides in reinforced concrete fixed by the standard [DIN 1045-2 2008]. Further information on corrosion of reinforcing steel is compiled e.g. in [Slater 1983].

2.6.4 Concrete attack

Actions causing concrete deterioration can be of mechanical, chemical or physical nature. Mechanical damage is caused by impact, erosion, cavitation or abrasion. High abrasion resistance is required if the concrete surface is exposed to e.g. moving traffic, bed load or floating debris. A good indication for the hydroabrasion resistivity of concrete is the product of compressive strength and dynamic modulus of elasticity [Vogel 2011]. The higher the factor, the higher the expected resistivity is. In general, higher concrete strength means lower surface abrasion.

Chemical causes of deterioration can be distinguished between internal causes including alkali-silica and alkali-carbonate reactions, and external causes. Alkali-silica reaction is an expansive chemical reaction between the alkaline solution of concrete and reactive minerals (amorphous silicic acid) in the concrete aggregates. The reaction product is a gel which occupies much more space than the reactants, as already observed by Stanton [Stanton 1941]. As a result, cracks may start to emerge out of the aggregate surface. Preventive measures are the choice of aggregates of less potential reactivity and cements with low alkali content. External chemical causes are mainly due to attack of aggressive ions like sulphates as well as of natural and industrial liquids and gases. Main sources of sulphate ions in groundwater are soils containing sodium, potassium, magnesium and calcium sulphate [BRE 1996]. Formation of ettringite, thaumasite and gypsum as a result of sulphate attack cause expansion and disruption of concrete structures. Besides expansive attacks, solvent attacks caused by the action of acids may degrade concrete heavily. Acids like carbon dioxide enriched groundwater convert calcium silicate hydrates to soluble products. This process is also called decalcification. As a result, the pH value drops, the porosity is increased, the microstructure is progressively opened to further forms of attack and the strength is dramatically reduced [Monteny et al. 2000]. Further solvent attack is caused by soft water, interchangeable salt ions, plant and animal oils and greases.

In general, the chemical resistance of concrete depends significantly on the intrusion velocity of water and harmful substances dissolved, see chapter 2.7.

Physical causes of deterioration are high temperature treatment accompanied by differences in thermal expansion of concrete components (see section 2.3.2) and the effects of alternating freezing and thawing as discussed in chapter 2.8.

Physical and chemical deterioration processes can act in a synergetic manner which is why it is difficult to assign damage to single factors. As a rule of thumb, high quality of concrete means high durability. Improperly produced concrete, e.g. insufficient curing (see section 2.3.8), and change of use of concrete construction accompanied by a change in exposure class may lead to dramatically increased risk of deterioration.

Detailed information on concrete attack is provided e.g. in [Stark & Wicht 2001].

2.6.5 Guidance for the design of concrete construction

For each exposure class, guidance is given by the standard [DIN EN 206-1 2001] with respect to mix design, properties of hardened concrete and nominal concrete cover. The requirements to be fulfilled by the mix design to guarantee adequate protection refer to:

- minimum compressive strength class of concrete
- maximum w/c ratio and w/b ratio, respectively
- minimum content of cement
- minimum air content
- frost-resistance of aggregates.

2.7 Transport processes in concrete

2.7.1 Introduction

The durability of concrete structures strongly depends on the physical properties of concrete. Except mechanical abrasion and attack by high temperatures, deterioration processes come along with the penetration of gas, water and harmful dissolved substances in concrete: Water permeability governs the ingress of deleterious substances such as chlorides; gas diffusion and gas permeability is responsible for carbonation and corrosion of reinforcing steel; water supply triggers alkali-silica reaction and leaching; and freeze-thaw problems occur with higher water saturation. The resistance of concrete against penetration, i.e. its impermeability, is of paramount interest when considering durability of concrete and requires an understanding of the transport phenomena involved. In the following, the basic mechanisms behind transport of fluid in concrete are introduced. In detail these are permeation, diffusion and capillary suction. Freely available for transportation are capillary pores, pores in the contact zone between aggregates and matrix and micro-cracks. Besides total porosity, size distribution of pores and degree of inter-connection are important factors influencing the impermeability. Pore discontinuity is achieved by low w/c ratios and at the same time high degrees of hydration [Bentz & Garboczi 1991b].

2.7.2 Permeation

Permeation means flow of liquids and gases through porous media as a consequence of pressure applied. It is characterized by the specific permeability coefficient k_w [m/s] in case of liquids, i.e. water, and K_g [m²] in case of gases, respectively. Hagen-Poiseuille's law describes the flow rate of gas Q_g [m³/s] through porous solids which possess narrow capillaries under consideration of the compressibility of the test gas as follows:

$$Q_g = K_g \cdot \frac{A}{\eta \cdot L} \cdot \frac{(p_i - p_o) \cdot (p_i + p_o)}{2p} \quad (2.14)$$

where A [mm²] is the test surface, L [mm] is the specimen's height, p_i and p_o [10^5 N/m²] is the inlet and the outlet pressure, respectively, p [10^5 N/m²] is the atmospheric pressure and η [10^5 Ns/m²] is the viscosity of the test gas.

The atmospheric pressure depends on the altitude above zero and the viscosity of the test gas depends on the ambient temperature. Equation (2.14) leads to constant permeability coefficients solely in case of laminar flow which is verified by the following condition:

$$Q_g \sim (p_i^2 - 1) \quad (2.15)$$

Permeation of liquids is described by d'Arcy's law which is derived from flow in pipes. It is:

$$Q_w = k_w \cdot \frac{A \cdot \Delta h}{L} \quad \text{with} \quad \Delta h = (p_i - p_o) \quad (2.16)$$

where Q_w [m³/s] is the flow rate of liquid, k_w [m/s] is the permeability coefficient of liquid and Δh [m] is the pressure of liquid expressed in meter water column.

Equation (2.16) is present in equation (2.14) if liquid (water) is considered as incompressible:

$$p = \frac{p_i + p_o}{2} \quad (2.17)$$

Equation (2.16) conceals the well-known correlation between filter velocity v_f [m/s], also known as Darcian velocity, and hydraulic gradient i [m/m]:

$$v_f = k_w \cdot i \quad \text{with} \quad v_f = \frac{Q_w}{A} \quad \text{and} \quad i = \frac{\Delta h}{L} \quad (2.18)$$

In accordance with Valenta [Valenta 1969] the water intrusion depth x_w [m] in dependence of time t [s] can be estimated by integration of the following equation:

$$x_w^n \cdot dx_w = k_w \cdot \Delta h^n \cdot dt \quad (2.19)$$

where v_f and i from equation (2.18) were replaced as follows:

$$v_f = \frac{dx_w}{dt} \quad \text{and} \quad i = (\Delta h / x_w)^n \quad (2.20)$$

As a result, the approximated water intrusion depth x_w is obtained by the following equation:

$$\frac{x_w^{n+1}}{n+1} + c = k_w \cdot \Delta h^n \cdot t \quad (2.21)$$

where in agreement with Darcy it is $n = 1$ and $c = 0$:

$$x_w = \sqrt{2k_w \cdot \Delta h \cdot t} \quad (2.22)$$

Unfortunately, the high capillary activity of concrete is not considered in this approach. It can be assumed that the water permeability coefficient is not constant but rather decreases with time and persistent moisture penetration, respectively. The reason is twofold: first, the reactivity of water with unhydrous cement and, second, the swelling of the concrete itself densify the matrix.

2.7.3 Diffusion

Diffusion takes place if transport of water, vapour, gas or dissolved substances, ions and atoms, respectively, is the result of a concentration gradient and not of a pressure differential. The resistance of a porous solid against diffusion is described by the diffusion coefficient D [m²/s] according to Fick's first law:

$$I_x = -D \cdot \frac{dc}{dx} \quad (2.23)$$

where I_x [g/m²s] is the one-dimensional diffusion flow of molecules or ions driven by molecular motion and change in concentration dc [g/m³] along the infinitesimal length dx [m]. For steady-state diffusion in homogenous material with isotropic behaviour it is:

$$D = I_x \cdot \frac{L}{\Delta c} \quad (2.24)$$

where L [m] is the specimen's thickness and Δc [g/m³] is the concentration gradient.

For concrete structures, diffusion has practical relevance when considering, e.g. desiccation rates, carbonation as a consequence of penetration of carbon dioxide from air, chloride migration and oxygen penetration resulting in corrosion of embedded steel. The diffusion coefficient of gas is inversely proportional to the square root of its molar mass. That means it is possible to calculate the diffusion coefficient of one gas from experimental data on another gas.

For concrete stored in constant environment, the carbonation depth d_{car} [m] can be described by the laws of diffusion as a function of time t according to equation (2.25):

$$d_{car} = \sqrt{2D_{CO_2} \cdot \frac{c_{air}}{c_c} \cdot t} \quad (2.25)$$

where D_{CO_2} [m²/s] is the diffusion coefficient of carbon dioxide in carbonated concrete, c_{air} [g/m³] is the concentration of CO₂ in air and c_c [g/m³] is the amount of CO₂ needed for carbonation of one unit volume of concrete.

The concentration of CO₂ in air is in the range 0.03 to 1.0% by volume. The relation of c_{air} to c_c can be estimated by 8×10^{-6} [CEB 2003]. Besides these two parameters, the carbonation depth d_{car} is influenced by the diffusion coefficient D_{CO_2} which mainly depends on the capillary porosity, the degree of hydration, the w/c ratio and the surface quality determined by the curing regime applied. Of course, diffusion is lower the denser the concrete and the higher its moisture content is. However, in very dry concretes, i.e. RH below 25%, and in water-saturated concretes, carbonation is almost zero. Further, alternating watering and drying of the concrete surface leads to limited carbonation depth.

In addition to the diffusion of gases, i.e. oxygen and carbon dioxide, it is the diffusion of ions of aggressive character like chlorides and sulfates that move by diffusion in pore water. This process can be described by Fick's second law for non-steady state processes, e.g. for chlorides:

$$\frac{\partial c_{cl}}{\partial t} = D_{cl} \cdot \frac{\partial^2 c_{cl}}{\partial x^2} - \frac{\partial c_{cl}^b}{\partial t} \quad (2.26)$$

where c_{cl} [g/m³] is the concentration of total chloride ions at time t and place x , t [s] is the duration of chloride penetration, x [m] is the coordinate, c_{cl}^b [g/m³] is the amount of chlorides bound in the matrix and D_{cl} [m²/s] is the diffusion coefficient for chlorides in pore solution.

The second term in equation (2.26) stands for the amount of chlorides that are bound by the matrix. By insertion of D_{cl}^{eff} [m²/s] instead of D_{cl} , this phenomenon is accounted for:

$$\frac{\partial c_{cl}^{free}}{\partial t} = D_{cl}^{eff} \cdot \frac{\partial^2 c_{cl}^{free}}{\partial x^2} \quad (2.27)$$

where it is c_{cl}^{free} [g/m³] the concentration of free chloride ions in the pore solution.

On the one hand D_{cl}^{eff} depends on the capillary porosity and density of the matrix, and on the other hand it depends on the binding capacity of the matrix, i.e. the type of cement [Brodersen 1982]. In particular the use of blast furnace slag cement reduces D_{cl}^{eff} effectively [Smolczyk 1984].

In real conditions chloride ions enter rarely the concrete by diffusion only. Most times transport is managed by capillary suction in combination with diffusion. This happens if concrete is treated by salt-solutions and, at the same time, its surface is allowed to dry periodically.

2.7.4 Capillary absorption

Among all transport processes in concrete, capillary absorption is the fastest. It is the transport of water or other wetting liquids due to capillary forces. The pore volume can be determined by adsorption, but it is not necessarily related to the ease with which the liquid can penetrate it. Absorption is usually determined by immersing a specimen in water or liquid after it was dried to a constant mass previously, and measuring the mass ingress as a percentage of dry mass. The absorption process is assumed to follow a square root of time law as stated by equation (2.28):

$$\Delta m = W \cdot \sqrt{t} \cdot A \quad (2.28)$$

where Δm is the absorbed mass of liquid at time t [s], W [$\text{g}/\text{m}^2\text{s}^{-1/2}$] is the water absorption coefficient and A [m^2] is the test surface.

The test results may be widely different due to various procedures used, i.e. the temperature applied for drying or the immersion conditions [Lea 1970].

2.7.5 Influence of moisture on transport processes

The equations above describing the transport mechanisms in concrete are quite similar, i.e. the transport coefficients underlie the same parameters which are influenced first and foremost by environmental conditions. In general, higher temperatures accelerate transportation processes in concrete [Jooss & Reinhardt 2002]. In addition, the speed of water and gas penetration, and hence, the coefficients k_w , K_g , D and S , are increased with increasing the capillary porosity and the level of micro-cracking, respectively. Further, the penetration depth depends on the moisture content of concrete. With increasing moisture content the permeability of gas as well as the water absorption are remarkably reduced and even reach a negligible level in case of water saturation [Kropp & Hilsdorf 1995]. The influence on diffusion needs to be looked at more differentiated as it depends on the media transported. For example, diffusion of gas decreases strongly by increasing the moisture content, whereas the diffusion of ions and vapour will be facilitated.

A model for the description of moisture transport in a porous solid like concrete was developed by Rose [Rose 1965]. It bases on the previously introduced transport mechanisms. In agreement with the model there are 6 stages of water movement in the pore system as reported in Figure 2.13. From stage 1 to stage 6 the water content in the pore structure is increasing. In dry porous media, cf. stage 1, the vapour intruding the pore will be absorbed on the surface of the pore walls. As far as the pore walls are covered by one or more layers of water molecules, vapour can diffuse the pore space, cf. stage 2. The thickness of the absorbed water film is in equilibrium with the ambient relative humidity and increases with increasing RH. In stage 3 the smaller pore channels are filled with liquid water as a result of capillary condensation. Consequently, water movement encounters less resistance, whereas in the larger pores water movement is still managed by diffusion. The thickness of the water layer in stage 4 allows continuous water transport as distinct from diffusion by higher effectiveness. Stage 5 provides unsaturated flow described by Krischer's law [Krischer & Kast 1974]. The air bubble enclosed is assumed to be afloat. In stage 6, complete water-saturation is achieved and water transport proceeds acc. to Darcy's law.

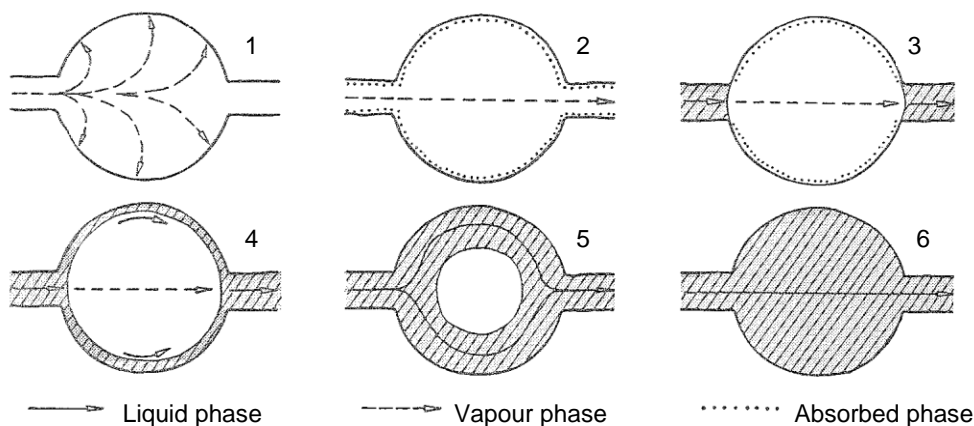


Figure 2.13: Model for moisture transport in porous media [Lutz et al. 2002].

2.8 Freeze-thaw damage of concrete with de-icing salts

2.8.1 Introduction

Due to its mix design, structural concrete that is sufficiently cured has generally a high durability, even with regard to freeze-thaw attack. However, damage may occur when the concrete is exposed to severe conditions e.g. low temperatures in combination with constant water impact, de-icing salts and frequently arising cycles of freezing and thawing. The mechanisms behind freeze-thaw damage of concrete belong to two categories: macroscopic phenomena and processes that pass off on the micro- and sub-micro scale, respectively. In the following, the relevant mechanisms of both categories are addressed. Further, this subchapter discusses methods that are usually applied to enhance the freeze-thaw resistance of concrete, i.e. the use of air-entraining agents, and provides a short introduction into the testing methods quantifying the damage.

2.8.2 Mechanisms causing freeze-thaw damage

Freeze-thaw damage of concrete is directly linked to the formation of ice on the surface of concrete and/or in its pore structure. The change in phase state of water when freezing comes along with a volumetric expansion of approximately 9%. With this in mind, Powers postulated the working hypothesis of hydraulic pressure [Powers 1945]: Macroscopic ice growth in the capillary pores expels water away from the ice leading to hydraulic pressure in the pore system. In simple terms concrete damage will occur if its breaking strain is exceeded in this process. The pressure build-up depends on the length of the pore channels equivalent to the distance between air voids where the pressure can relieve. As a result of his investigations, Powers introduced the critical spacing factor [Powers 1949]. It is equal to the longest distance water can travel in the capillaries without causing deterioration of the concrete. The magnitude of this factor was initially estimated to yield about 200 μm . On the basis of Powers' hypothesis, Fagerlund [Fagerlund 1973] assessed a critical degree of saturation above which freeze-thaw attack causes damage of concrete without artificial air pores. However, the hypothesis about the hydraulic pressure and the critical degree of saturation are not sufficient to entirely explain freeze-thaw damage with de-icing salts.

2.8.3 Further microscopic phenomena

Water in porous media like concrete can coexist stably as liquid, solid and vapour [Setzer 2001]. The temperature at which water freezes in concrete mainly depends on the concentration of dissolved salts and the binding forces that act between the pore solution and the pore wall. The freezing point depression ΔT_f is proportional to the concentration of the dissolved substances:

$$\Delta T_f = e \cdot \frac{m_2 \cdot s}{M_2 \cdot m_1} \quad (2.29)$$

where e is the cryoscopic constant, m_1 is the mass of liquid, m_2 and M_2 are the mass and the molar mass of the dissolved substance, respectively, and s is its degree of dissociation.

The temperature depression due to binding forces depends on the hydraulic pore radius r_h . The relation between radius and temperature depression is given by equation (2.30) [Setzer 1977]:

$$\ln(T_f / T_{f0}) = \frac{-2 \cdot \Delta \varphi \cdot V_m}{H_0 \cdot r_h} \quad (2.30)$$

where T_{f0} is the freezing temperature of the bulk water, T_f is the freezing temperature of the pore with radius r_b , $\Delta\phi$ is the change in the surface energy, V_m and H_0 are the molar volume of ice and its molar enthalpy of fusion, respectively. For cylindrical pores r_b is about one quarter of the pore diameter. More exact approximations are presented in [Stockhausen 1981].

As a consequence of temperature depression the water present in the microstructure of concrete is only partly freezing even at very low temperatures. Freezing starts in the larger capillary pores and expands to smaller capillaries if the temperature drops further. Already Powers found that some of the gel pores are too small that water cannot freeze at temperatures above -78°C . In general, water at temperatures below 0°C has higher Gibbs free energy than ice. According to the laws of thermodynamics, which state the diffusion from high to low free energy, water will flow from gel to capillary pores along the free energy gradient in order to freeze. Pressure will develop if further ice accretion is hindered by the pore wall. This mechanism is called capillary effect and mainly depends on the cooling rate. Besides the hydraulic pressure the capillary effect is the most prominent mechanism causing freeze-thaw damage of concrete.

2.8.4 Micro-ice-lens model

When the water present in the microstructure is alternating freezing and thawing, not only global expansion of the concrete is measured but also temporary global shrinkage. Setzer [Setzer 2002] developed the micro-ice-lens model in order to explain both phenomena using the laws of mechanical thermodynamics and physico-chemical effects.

Figure 2.14 shows the temperature and strain of concrete as a function of time during freezing and thawing. Further it presents a schematic illustration of the related microscopic damage mechanisms. To this end the concrete is modelled as cement matrix with gel pores embedding the larger capillary pores. The temperature depression due to binding forces prevents the formation of ice inside the microstructure although the temperature drops below 0°C (cf. state 1 and 2). Further water from the interior of the concrete moves along the free energy gradient in order to freeze on the top. As a result, the concrete shrinks since the matrix is non-infinitely rigid.

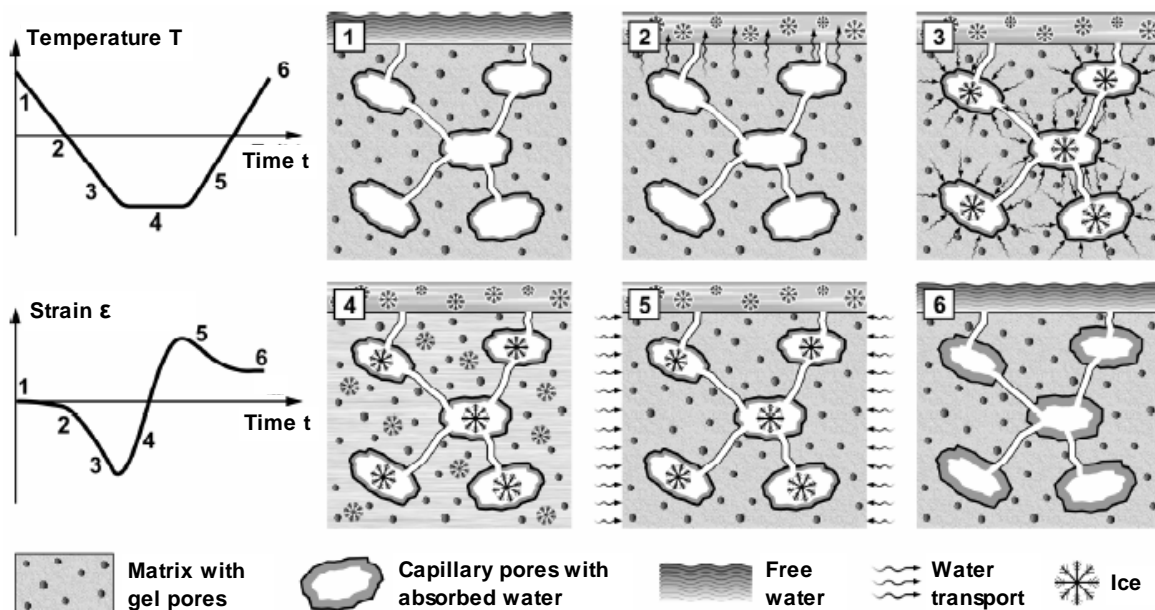


Figure 2.14: Schematic illustration of the mechanisms causing damage of concrete during freezing and thawing [Haist et al. 2009].

This shrinkage is called frost shrinkage and is extended by a further drop in temperature since the negative pressure build-up between liquid water and ice grows by 1.22 MPa per K undercooling [Stark & Wicht 2001]. Due to further decrease of temperature water in the capillary pores is freezing and consequently, the gel pores are drained (cf. state 3).

At temperatures of approximately -25°C the water in the smaller capillaries and the larger gel pores is freezing. Since frost shrinkage has already finished, the ice formation causes first changes of the microstructure while the matrix expands (cf. state 4). During the following thawing period, the negative pressure (capillary effect) relieves as thawing begins in the gel pores and the smaller capillaries whereas the water in the larger pores remains frozen (cf. state 5). As a result, free water is attracted by the gel pores in order to keep the system in equilibrium. This effect is called frost suction. Since thawing is a non-stationary process, water released by thawing of the ice-lenses is provided with delay. On this account, the free water attracted is primarily, if available, external water, i.e. water from the top of the concrete that is treated with de-icing agents. According to Setzer, this mechanism is called micro-ice-lens pump. In consequence, the degree of saturation of the pores is increased accompanied by the macroscopic expansion of the concrete. If the saturation is completed, i.e. enough freeze-thaw cycles were assessed, global expansion dominates and the concrete strain remains above the initial level (cf. state 6).

It is the air-filled pore structure that ensures the frost-resistance of concrete. This free pore space is generated either by the use of air-entraining agents, by self-desiccation during hydration, or by drying of initially water-filled pores due to appropriate environmental conditions. Only once the saturation of the pore space has exceeded a critical value and the breaking strain during alternating shrinkage and expansion processes has reached its limit, freeze-thaw damage occurs. In general, the damage results in visible surface scaling or internal damage, e.g. leading to reduced modulus of elasticity.

2.8.5 The role of dissolved salts

Considerable amounts of chloride ions, i.e. dissolved in the surface water treated with de-icing salt, are able to enter the concrete by means of the micro-ice-lens pump during thawing. Because ice is free of any dissolved substances, the ions accumulate in the unfrozen gel water [Setzer 2009]. When increasing the concentration of the dissolved substances in the pore solution, the electrostatic part of the disjoining pressure between solid particles of the hardened cement paste is reduced, cf. chapter 2.3.4. As a result, the frost shrinkage is increased. However, due to electro-osmosis and chromatography the penetration of ions is restricted to the surface close area and affects surface scaling more than internal damage. Investigations of Auberg [Auberg 1998] have shown that even the quality of the used tap water significantly influences the scaling of concrete.

2.8.6 Methods for quantifying freeze-thaw damage

Concrete of high quality survives freeze-thaw attack for a rather long time, which is why the established test methods prescribe the application of many freeze-thaw cycles e.g. the ASTM standard 300 [ASTM C666-08], the slab test 56 [DIN EN 12390-9 2009], the CDF-test 28 [Rilem 1996] and the CIF-test method 56 [Rilem 2004]. To maintain the comparison of laboratory test results with practice, the boundary conditions of the test methods have to reproduce the real conditions as closely as possible. Both, the CDF and the CIF test method meet this requirement the most [Setzer 2009]. On this account, in the present thesis the decision was made in favour of a combination of both test methods in order to examine the effect of SAP on the freeze-thaw

resistance of concrete, cf. chapter 10.2.3. The CDF-test method determines the surface scaling of the test samples and postulates a limit value of 1500 g/m² after 28 freeze-thaw cycles. The CIF test method measures the ultrasonic transit time of an US wave travelling through the test sample. A decrease in the ultrasonic velocity with increasing number of freeze-thaw cycles is an indication for internal damage (leading to reduced lifetime of the concrete) as internal cracks reduce the velocity of the US wave. After the 56th cycle, the relative dynamic modulus of elasticity - calculated on the basis of the US-wave velocity - must not drop below 80%.

2.8.7 Requirements for improved freeze-thaw-resistance of concrete

The design of concrete with high frost resistance has to follow general rules:

- The pore structure has to be influenced in a way that capillary water transport is mitigated.
- The matrix has to sustain the pressure build-up by ice formation; therefore the tensile strength of the matrix has to be maximized.
- The aggregates used have to show sufficient resistance against freeze-thaw attack.

To achieve these requirements, the following measures are available:

- Reduction of the w/c ratio and selection of an appropriate type of cement/binder.
- Entrainment of artificial air voids.

The w/c ratio is one of the main parameters determining the frost resistance of concrete. With decreasing w/c ratio, capillary water transport is reduced and strength as well as frost-resistance is increased. Because of its dense microstructure formed during hydration, blast furnace cement is recommended when the concrete member is protected against carbonation. Otherwise the porosity is increased and the long-term resistance against freeze-thaw attack is even reduced [DAfStB 2005]. The use of fly ash has shown positive effects on the frost-resistance of concrete [Brameshuber & Schießl 2000]. In contrast, the use of silica fume can increase the internal damage of concrete [Feldrappe & Müller 2004].

Air pores entrapped in the matrix enhance the frost-resistance of concrete the most effective. They do not only provide space for expansion of expelled water (hypothesis of hydraulic pressure), they also provide space for ice accretion (capillary effect) and interrupt water transport by capillary suction. The void spacing (VS) factor, compare Figure 2.15, is still the decisive parameter for the design of frost-resistant concrete today. It is defined as the distance between the centroid of three equally afar air voids to the pore wall by assuming equal size and distribution of the air voids. Keeping the limit value of $VS \leq 0.20$ mm recommended for frost-resistant concrete [DIN EN 480-11 2005] implies the use of air-entraining agents.

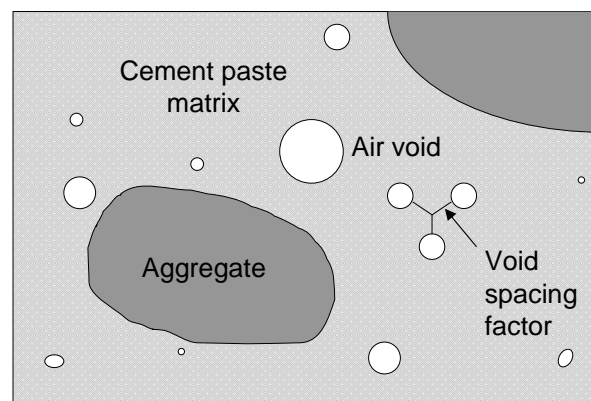


Figure 2.15: Schematic illustration of the VS factor based on [Jungwirth et al. 1986].

2.8.8 Air-entraining agents

Air-entraining agents (AEA) generate a large number of small air voids of about 300 μm in diameter in the fresh concrete during mixing. AEA are admixtures that belong to the group of surface-active agents also known as tensides. The characteristic all tensides have in common is their hydrophobic/hydrophilic molecular structure, cf. Figure 2.16. They consist of a covalent hydrophobic hydrocarbon chain and a hydrophilic polar carboxyl group. The latter may also be a sulphate or sulphonate group. The hydrophilic part reduces the surface tension of the pore water which results in a liquefying effect. The hydrophobic part has a water repellent effect causing the creation of stable air voids. AEA base primarily on soaps made from natural resin. Synthetic active ingredients have been used in the last years increasingly as well.

The interactions of the active ingredients forming air voids, the influence of the mixing regime, the temperature, the consistency of the concrete and the amount added to the fresh mix are poorly understood so far. To compensate the inadequate knowledge, initial testing and testing during construction work have to be exercised in detail. Further the interaction with superplasticizer containing defoaming agents has to be carefully considered. An alternative to AEA is provided by the application of synthetic microspheres [Sommer 1978].

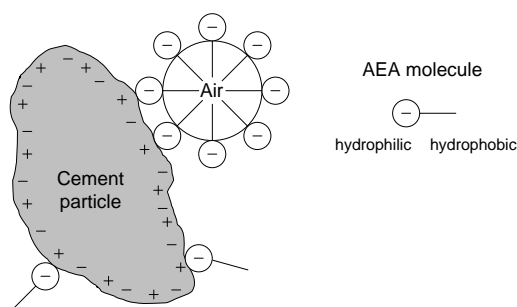


Figure 2.16: Schematic illustration of the acting mechanism of air-entraining agents.

A promising new technology for air entrainment of concrete is provided by the use of superabsorbent polymers as concrete admixture. This task is extensively being dealt with in chapter 10. The basic principle behind this new technology is explained in chapter 3.3.

2.9 Superabsorbent polymer (SAP)

2.9.1 General information

Polymer materials that are able to absorb many times more water or aqueous solution than their own weight belong to the group of superabsorbent polymers (SAPs). One gram of these polymers can absorb and retain more than 1000 g of water and up to 100 g of dilute salt solution without dissolving [Buchholtz & Graham 1998]. SAPs were developed in the late 1980s and were used primarily as urine absorber in baby diapers.

Chemically speaking SAPs are cross-linked polyelectrolytes. In [Buchholtz & Graham 1998] SAPs are classified according to their ionic and non-ionic nature. SAPs of the ionic group, which are generally used in this dissertation, can be subdivided further into anionic and cationic polymers. The commercially important types of SAP are covalently cross-linked polyacrylates and copolymerized polyacrylamides/polyacrylates [Jensen & Hansen 2001b]. SAP produced for the hygiene industry usually bases on copolymers of acrylic acid partially neutralized with sodium [Friedrich 2012], see Figure 2.17.

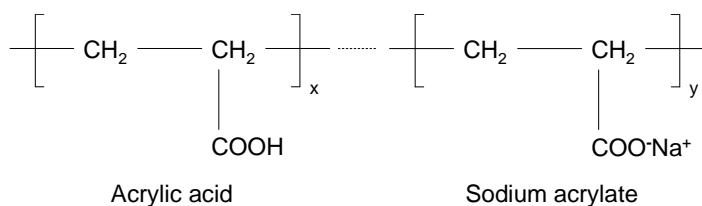


Figure 2.17: Basic components of SAP produced for the hygiene industry.

2.9.2 Swelling

SAPs can be seen as crosslinked networks of flexible polymer chains which start to swell upon contact with water or aqueous solutions forming a hydrogel. The crosslinks keep the polymer network from dissolving. In general, SAPs show isotropic swelling due to disordered crosslinking. As a result, the shape of the SAP particle after swelling remains the same as before. The degree of crosslinks and the salinity of the fluid highly influence the swelling capacity, which is defined as relation between absorbed fluid and dry polymer. With increasing fraction of crosslinked polymer chains the swelling capacity and thus the absorption capacity is decreasing. Di- and trivalent ions in the swelling medium, e.g. Ca^{2+} and Al^{3+} , reduce the absorption capacity of polyacrylates dramatically since they act as additional crosslinkers. Externally applied forces, e.g. shear and compressive forces, can significantly reduce the absorption capacity of SAP as well. Generally, the mechanical properties of the gel become poorer with increasing the water content and the degree of saturation, respectively. Figure 2.18 provides an illustration of the free water absorption of a single spherical SAP particle (left) and a schematic representation of the SAP network (right).

Different mechanisms control the motion of water into the SAP particle. The driving force is an osmotic pressure which is proportional to the ions in the swelling medium. As the concentration of ions outside the polymer is increased, the osmotic pressure inside the gel is decreased. Ionisable groups that are trapped within the polymer chain attract water molecules in order to reduce the pressure by diluting the charges. Further, water solvation of hydrophilic polymer chains hosting dissociated, ionic functional groups contributes to increase the swelling. On the other hand, retractive forces due to elastic free energy counteract swelling of the SAP. Until the competitive balance of all forces is even, swelling is in equilibrium [Friedrich 2012].

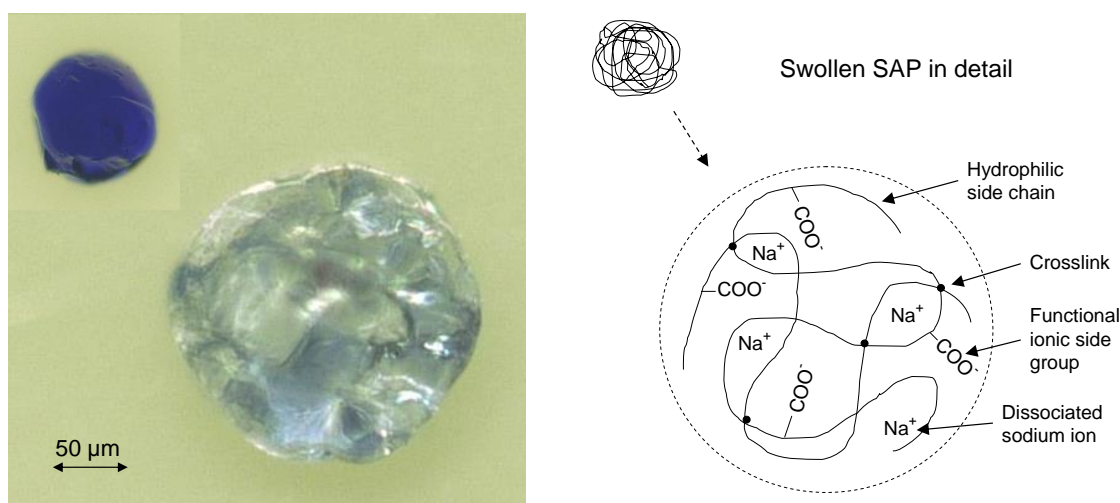


Figure 2.18: Picture of a spherical SAP particle coloured with blue ink in dry and water saturated state (left) and schematic representation of a crosslinked SAP network (right).

2.9.3 Production

The annual world production of SAP amounts to ca. 1 Mio t. About 95% of the SAP production accounts for the application in baby diapers. The most commonly available SAP configurations are hard, dry, granular powders with a particle size range of approximately 100 to 1000 μm . They are either produced by gel-polymerization or inverse suspension polymerization. In case of gel-polymerization, also known as solution polymerization, the production of SAP starts with an aqueous monomer solution, prepared from acrylic acid, water and a crosslinking monomer. The monomer mix is cooled down to 0 to 10°C and transferred to a reaction vessel. The reactor is either an endless belt reactor [Chmelir & Pauen 1988] or a kneader [Irie et al. 1996]. By adding free-radicals, i.e. sodium persulfate, the monomer mix begins to polymerize forming a gel. In case of the endless belt reactor, the rubber-like gel is cut at the end of the belt by an extruder. Using a kneader, polymerization and cutting are done in one step. The broken gel is then dried and prepared by grinding and screening to obtain the desired particle size distribution. The dry particles made by this production method have an irregular shape and show sharp edges [Friedrich 2012].

Inverse suspension polymerization is employed when spherical shaped particles are demanded. In this process droplets of the monomer mix are suspended in an organic solution. This can either be hexane or cyclohexane, blended with suspension aids stabilizing the droplets. At temperatures between 50 and 70°C the polymerization starts and is turned off when the particles are grown to the desired size. Finally, the water is separated by azeotropic distillation and the particles are dried. The production of SAP by inverse suspension polymerization is limited to small volumes since the costs are higher compared to gel-polymerization [Friedrich 2012].

Superabsorbent fibres (SAF) represent another configuration of superabsorbent polymer material. SAF, as used in this dissertation, can be produced by dry-spinning from an essentially linear co- or terpolymer of acrylic acid, methyl acrylate and hydroxyl containing monomers e.g. hydroxyethyl acrylate. The latter component is used to form crosslinks during a heat treatment step. Methyl acrylate is implemented as an internal plasticizer. The dispersion is spun into filaments through a spinneret at temperatures of 90 to 100°C. Afterwards, the water is evaporated by drying in an air bath at ca. 150°C and the filaments are wound to yield a fibre of about 30 μm in diameter. The fibre length is adjustable by cutting. The bulk density of fibres is typically lower than that of granules and their capability to retain fluid under an externally applied pressure is less. Due to the low production rate of SAF, the present cost exceeds by several times the costs of granular superabsorbents [Buchholtz & Graham 1998].

Figure 2.19 presents images of granul, spherical and fibre shaped dry SAP particles recorded by environmental scanning electron microscope (ESEM).

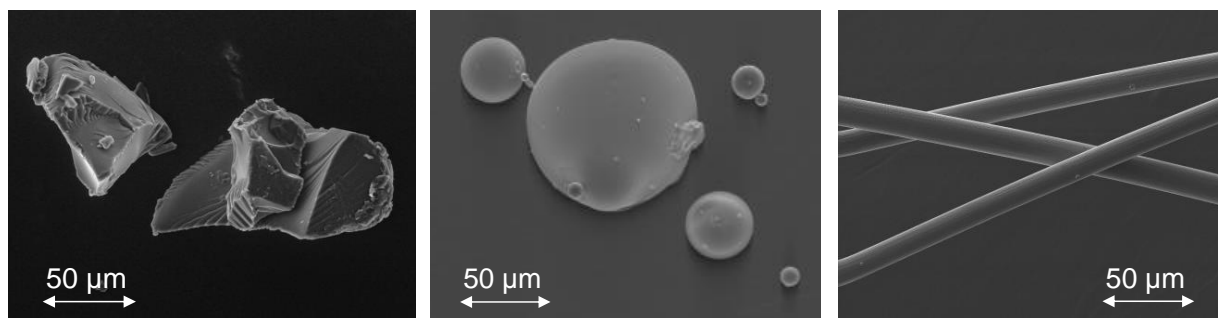


Figure 2.19: gel-polymerized particles (left), suspension polymerized particles (center) and dry-spun fibres (right) recorded by ESEM.

2.9.4 Applications

The market for SAP is split between the hygiene industry and the technical applications. The first market, the hygiene industry, is still the main market for SAP today [Friedrich 2012]. Besides the application in diapers, SAPs are used in several cosmetic formulations and adult care products i.e. to control the consistency or to contribute to a soft, dry feel. The rest of the market consists of all applications apart from hygiene products e.g. (cf. also [Buchholtz & Graham 1998]):

- Agricultural and horticultural applications such as soil additives helping to retain moisture and to control the release of water in the soil as conditions become drier; or even to improve the air content of the soil due to expansion and contraction during the cycles of moisture absorption and evaporation.
- Controlled release of substances that are initially trapped within the polymer, such as pesticides, fertilizers or pharmaceuticals.
- Electronics and cabling protected from water damage due to water-blocking tape containing SAP or polyester tape coated with SAP-modified resin. Any water that penetrates the covering of the cable encounters the protective layer and swells the SAP to seal the crack or perforation in the covering material.
- Food packaging systems making use of SAP as liquid absorber. Even chilled SAP gels are used as a dry-cooling medium since the water is retained when thawing begins.
- Aqueous waste management with the aim to reduce the potential of environmental contamination using SAP in order to make waste easier to handle by gelling it into a rubbery material or a solid phase.

In the field of construction applications the focus is put on water-absorbing construction materials using the volume increase of the gel to form a barrier to further water flow. Various sealing composites made by blending SAP into a rubber material were developed for sealing around joints of miscellaneous building materials. Further, SAPs are used as component in water-blocking back-filler materials e.g. for tunnel constructions, or serve as soil stabilizer for wet soils.

The promising and still young application technology of SAP used as concrete admixture forms a basis to the present thesis. The principles behind this technology that are essential for the understanding of this work are extensively described in the next chapter.

3 Basic principles of using SAP in concrete technology

3.1 Introduction

This chapter will provide an introduction of the basic principles behind the use of SAP as concrete admixture. In the last years, research conducted for the application of SAP in concrete construction has become popular among experts all over the world. Most research is underway in order to follow the overall aim of gaining control over the water balance in concrete. However, there is a wide range of application methods for SAP in cementitious materials to be investigated in future. Currently, two promising applications for SAP in concrete construction stand out:

- 1) Water entrainment for the purpose of internal curing.
- 2) Redistribution of capillary water to artificial water-filled macropore inclusions of pre-designed size, shape, spacing and volume.

The first purpose aims on the mitigation of self-desiccation and self-desiccation shrinkage. Using SAP seems to be the most straightforward technology to apply IC of concrete today. The second purpose targets on the manipulation of the pore structure in order to improve the durability of concrete. At the latest when SAP pores are emptied due to hydration or drying, air-filled macropores remain that act similar to air pores generated by traditional AEA. From this point of view, the application of SAP can be seen as a new method for air entrainment in concrete.

Both topics are addressed further on and their relevance for the thesis at hand is highlighted. In the last part of this chapter, new fields of application for SAP in concrete construction will be addressed. Besides several conceivable applications proclaimed by literature, two own approaches are presented: the use of superabsorbent fibres (SAF) in order to prevent explosive spalling of concrete exposed to fire and the application of SAP in lightweight concrete with porous matrix.

3.2 Internal curing

3.2.1 Theoretical background

A first concept for internal curing of hardening cement-based materials by using fine SAP particles was presented by Jensen & Hansen [Jensen & Hansen 2001b]. They formulated a re-interpretation of Powers' model [Powers & Brownyard 1948] in order to explain the phenomenon of self-desiccation (see section 2.2.3) and the basics of water entrainment (see section 2.6).

Figure 3.1 presents the volumetric phase distribution as a function of the degree of hydration at sealed condition of a plain cement paste with w/c of 0.36 in comparison to a water-entrained cement paste with w/c of 0.36+0.06. The add-on part of the designation refers to the amount of entrained water, e.g. $(w/c)_e$ of 0.06. The w/c ratio by neglecting water stored in SAP is called basic w/c ratio, i.e. $(w/c)_{\text{basic}}$. While hydration of a plain paste system at low w/c ratio stops when all capillary water is consumed, hydration of the water-entrained paste system proceeds as IC water is considered "on top". In case of w/c = 0.36+0.06 hydration up to $a_{\text{max}} = 1$ is possible. Several positive effects of water entrainment by SAP are expected or even demonstrated so far:

- The degree of hydration is increased compared to plain cement paste with same $(w/c)_{\text{basic}}$.
- No air-filled micropores occur as the space is taken up by further hydration products; pre-designed, air-filled macropores remain instead.

- Self-desiccation, self-desiccation shrinkage and, consequently, cracking due to restraint autogenous shrinkage are prevented.

The latter point is particularly important as autogenous deformations take place at early age where thermal deformations superpose. It is obvious that at this stage of hydration, even small stresses acting on the system lead to large deformations as the resistivity of the paste is quite low.

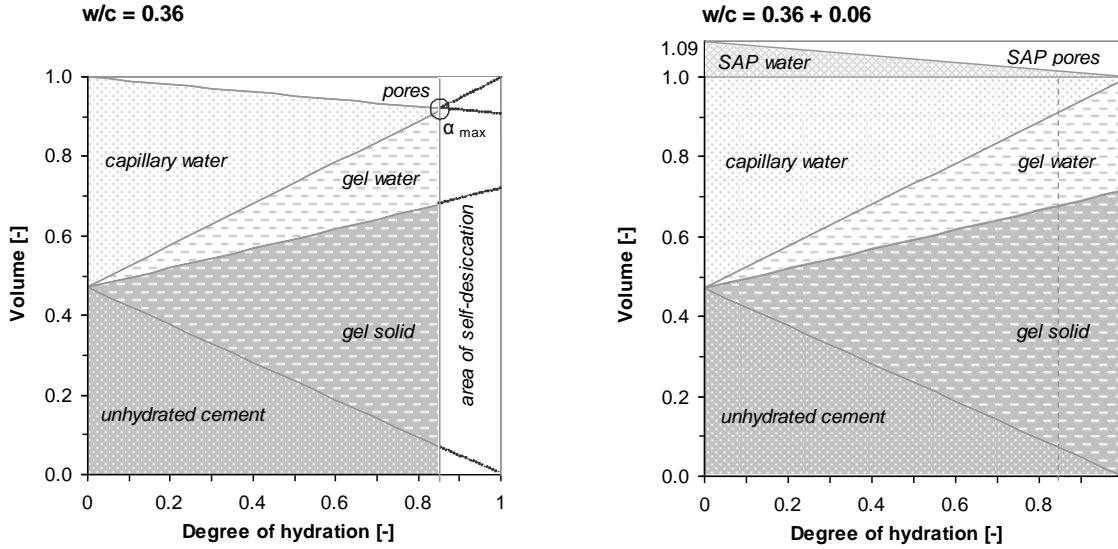


Figure 3.1: Volumetric phase distribution as function of degree of hydration: plain cement paste at w/c of 0.36 (left) and water-entrained cement paste at w/c of 0.36+0.06 (right).

The amount of entrained water that is theoretically needed to avoid self-desiccation of a plain cement paste can be calculated in agreement with Powers, see appendix 3. It is assumed that the maximum degree of hydration is reached when all the space is taken up by the volumes of gel solid V_{GS} , gel water V_{GW} and unhydrated cement V_{UC} :

$$V_{GS} + V_{GW} + V_{UC} = 1 \quad \text{for } \alpha = \alpha_{\max} \quad (3.1)$$

As a result, the amount of entrained water equals the chemical shrinkage of the cement paste at the maximum degree of hydration. The necessary condition to obtain α_{\max} is:

$$(w/c)_e = 0.18 \cdot (w/c) \quad \text{for } (w/c) < 0.36 \quad (3.2)$$

For $w/c > 0.36$ the amount of entrained water necessary to reach complete hydration is less:

$$(w/c)_e = 0.42 - (w/c) \quad \text{for } 0.36 \leq (w/c) \leq 0.42 \quad (3.3)$$

Figure 3.2 provides an illustration of the minimum entrained w/c ratio $(w/c)_e$ needed to obtain α_{\max} at sealed hydration as a function of the basic w/c ratio $(w/c)_{\text{basic}}$. The derivation of the equations used for calculation is reported in appendix 3. It goes back to considerations of Jensen and Hansen [Jensen & Hansen 2001b] and was extended to paste systems including silica fume of 10% by the weight of cement (see appendix 3). Replacement of cement by silica fume results in high chemical shrinkage of about 22 ml per 100 g silica fume reacted [Jensen & Hansen 2001b]. On this account, silica fume-modified cement pastes show much greater self-desiccation and autogenous shrinkage than plain Portland cement pastes [Jensen & Hansen 1996] leading to greater micro-cracking if restraint [Dela 2000]. As a consequence, more entrained water is needed to prevent complete self-desiccation of paste systems modified with silica fume.

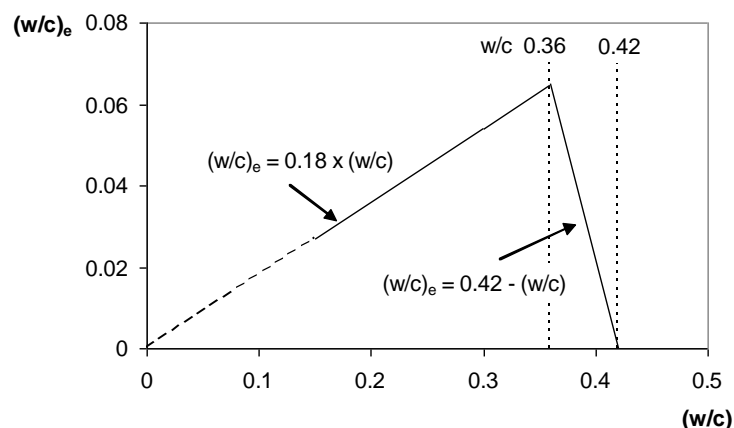


Figure 3.2: Amount of entrained water theoretically needed to avoid self-desiccation of plain Portland cement paste as a function of basic w/c ratio.

3.2.2 Literature review on IC due to SAP

First experimental observations on water entrainment by SAP were published by Jensen and Hansen [Jensen & Hansen 2002]. They examined Portland cement pastes with respect to autogenous deformation and autogenous RH change and mortars with respect to cracking susceptibility by using an instrumented ring [ASTM C1581-09]. The SAP content amounted to 0.3 to 0.6% by mass of cement and the basic w/c ratio was 0.30. It was shown that it is possible to avoid self-desiccation, autogenous shrinkage and cracking during restrained hardening by means of SAP as water-entraining admixture. Furthermore, they suggested the optimum size of swollen SAP for internal curing to yield 100 μm . Their first measurement results were confirmed in other studies using the same type of SAP, e.g. [Igarashi & Watanabe 2006] and [Lura et al. 2006a] and were even extended to high strength concretes (HSC) [Braam et al. 2006]. In parallel to free autogenous shrinkage, Igarashi and Watanabe investigated the development of tensile stresses due to restraint shrinkage. The test device used was a computer-controlled uniaxial restraint shrinkage testing machine as recommended by Kovler [Kovler 1994]. At 0.7% SAP, which was the amount where complete elimination of autogenous shrinkage was found, they measured no tensile stresses. For concrete without SAP, tensile stresses of 0.7 to 1.1 MPa were found at the age of 7 days. Addition of half the amount of SAP, i.e. 0.35%, led to tensile stresses of 0.3 MPa after 7 days.

Recently, several investigations on IC of concrete and HSC using other SAP material were published, e.g. [Wang et al. 2009], [Dudziak & Mechtcherine 2008], [Mechtcherine et al. 2009]. The results are in good agreement with findings of Jensen and Hansen. Further investigations on restrained shrinkage were performed on SAP-modified UHPC [Dudziak & Mechtcherine 2009].

In comparison to other IC materials, the method of water entrainment by SAP is asserted to be the more straight-forward technology. The undesirable addition of mechanically poor aggregates is avoided and, instead, free design of pore shape and size distribution is enabled. With regard to mitigation of autogenous shrinkage, Geiker [Geiker et al. 2004] demonstrated on cement/silica fume mortars with w/b of 0.35 that addition of a small amount of Jensen's SAP particles is as efficient as the replacement of a significant amount of sand by LWA. A detailed comparison of SAP and LWA with respect to IC, can be found in [Mönnig 2009]. Piérard et al. [Piérard et al. 2006] verified that SAP can prevent autogenous shrinkage more effectively than traditional SRA. They stated that only CaO-based expansive agents achieve similar good results.

In [Schroefl et al. 2012] it is reported that there are substantial differences in the effectiveness of IC in dependence on the type of SAP used. This issue will be discussed later on in conjunction with own measurement results presented in chapter 6. However, it should be admitted at this point that the performance of SAP obviously is influenced by the polymer chemistry and the interaction of SAP with the cementitious environment.

Further current papers on IC due to SAP are composed e.g. in [Jensen et al. 2010].

3.2.3 Further consequences of water entrainment

The majority of research underway is still focussed on mitigation of autogenous shrinkage and cracking due to restraint shrinkage of high performance paste, mortar or concrete compositions, i.e. with w/b ratios far below 0.40. However, water entrainment affects properties of fresh and hardened concrete in many ways. Some crucial findings of research conducted for the study of the side-effects of water entrainment by SAP are summarized in the following:

1) Effect of SAP on workability and fresh concrete properties:

Even though only few results are available in literature that concern the influence of SAP in fresh concrete, it is out of the question that SAP addition considerably changes the concrete's rheology. It was observed that adding SAP is equivalent to removal of free water from the system resulting in reduced spread flow [Mönnig 2005]. If no extra water is added to compensate this tendency, yield stress and plastic viscosity are increasing as shown by rheometer measurements [Toledo Filho et al. 2012]. The thickening effect of SAP in fresh concrete as first observed in [Jensen & Hansen 2002] may be advantageous for special practical applications such as pumping.

2) Effect of SAP on mechanical properties:

In general, incorporation of large volumes of water sources may affect the mechanical properties of hardened concrete and its durability as well. On this account, it is recommended to only entrain the amount of water that is needed to prevent or acceptably limit self-desiccation and self-desiccation shrinkage, respectively. On the other hand, SAP promotes a higher degree of hydration as long as low enough w/c ratios are considered. In [Lura et al. 2006b] it is reported that IC by SAP has no significant influence on compressive strength of high performance mortars, whereas for cement paste the compressive strength was reduced by 20% at early age and by 10% at later age. This observation was explained by the limiting effect of interfacial transition zones and weaker aggregates present in mortar. In [Assmann 2008] the minimum impairment of strength of mortar prisms at cement content of 575 kg/m³ in the range $0.40 < w/c < 0.64$ that were cured in water was proposed for swollen SAP of about 110 µm in radius. Smaller and larger polymers increased the impact on compressive strength. The suggested radius corresponds with the prediction of de Larrard and Belloc [De Larrard & Belloc 1997] who found a relation between paste thickness and compressive strength. An explicit study on mechanical properties of SAP-modified concrete was conducted by Hasholt, who investigated the effect of SAP on development of compressive strength [Hasholt et al. 2010a] and modulus of elasticity [Hasholt et al. 2010b]. According to their test data, mix design and age make decision whether SAP has a negative or positive effect on mechanical properties. At high w/c ratio (> 0.45) SAP addition had no significant influence on hydration, and therefore strength was reduced. The same was found for low w/c ratios at early age, and if the amount of SAP was too large. In these cases the strength-increasing effect due to increased degree of hydration could not counterbalance the strength-reducing effect of the volume of SAP voids. It was further shown that SAP addition can at the same time increase the compressive strength and lower the modulus of elasticity.

3) Effect of SAP on other types of shrinkage, i.e. plastic and drying shrinkage:

Tests presented in [Dudziak & Mechtcherine 2010] indicated a decrease of capillary pressure build-up in cement pastes containing SAP. Plastic shrinkage measured under severe drying conditions was lower compared to the reference mix with same basic w/c ratio of 0.30, whereas the settlement deformation was higher. The latter phenomenon coincided with retarded setting. The effect of SAP addition on early age cracking susceptibility of concrete plates with dimensions of 160 x 60 x 8 cm³ exposed to severe drying in a ventilated tunnel were investigated in terms of a diploma thesis [Sárosi 2007]. Besides the reduction of plastic shrinkage it was indicated that SAP reduce bleeding and contribute to a high surface quality. The number of cracks was not reduced by SAP addition, but it is probably true that average and maximum crack width were smaller in case of SAP-modified concrete. However, some findings were contradictory, which is why no final conclusion could be drawn. First results concerning the effect of SAP on drying shrinkage of cement paste were already published in [Jensen & Hansen 2002]. Previous to drying, the specimens were stored sealed for the first days of hydration. Drying shrinkage increased for the water-entrained pastes but did not affect the total deformation since autogenous deformation was drastically reduced. Measurements on concrete starting at 24 hours after casting showed that addition of SAP reduces total deformation at w/c of 0.42 comparable to the effect of LWA addition [Reinhardt & Mönnig 2006]. In [Mechtcherine et al. 2009] shrinkage measurements on fine-grain UHPC at 20°C and 65% RH, executed from one day after casting, are reported. When the total w/b ratio of basically 0.19 was increased due to addition of SAP and extra curing water, the measured deformation was higher compared to the reference mix. An increase in IC water, of course, led to an increase in total deformation. But in this study as well, the increase in drying shrinkage caused by IC water was less pronounced than the decrease in autogenous shrinkage, which occurred mainly within the first day of hydration.

4) Much more effects of SAP, e.g. on the development of microstructure are present but marginal research exists so far.

A comprehensive discussion of the above mentioned topics is given by the recently available state of the art report of the RILEM TC 225-SAP, “application of superabsorbent polymers in concrete construction” [Rilem 2012]. Chapter 9 of the report includes results made available by the dissertation at hand.

3.2.4 Relevance of internal curing for the present dissertation

The application of SAP in order to prevent autogenous shrinkage may improve the durability of concrete by reducing the risk of crack formation at early age. Therefore the prevention of autogenous shrinkage is a main topic of this thesis, see Figure 3.3 on the following page. Although the crack formation due to restraint autogenous deformation was not observed directly, the influence of SAP on sealed cement hydration and free, unrestricted shrinkage of paste, mortar and concrete were examined: Observations on the effect of SAP on the hydration of sealed Portland cement paste is reported in chapter 5. The effect of SAP on autogenous shrinkage of cement paste is studied in chapter 6. Further, a model for calculating autogenous shrinkage of cement paste on the basis of an approach developed by Lura [Lura 2003] is presented. Chapter 7 reports about an investigation on autogenous shrinkage of high strength mortar and concerns the effectiveness of IC in dependence on type and dosage of SAP. Chapter 8 deals with autogenous shrinkage of normal strength concrete and the impact on creep of concrete under constant tensile load. Mechanical properties of water-entrained concrete are discussed in chapter 8 and 9 as well.

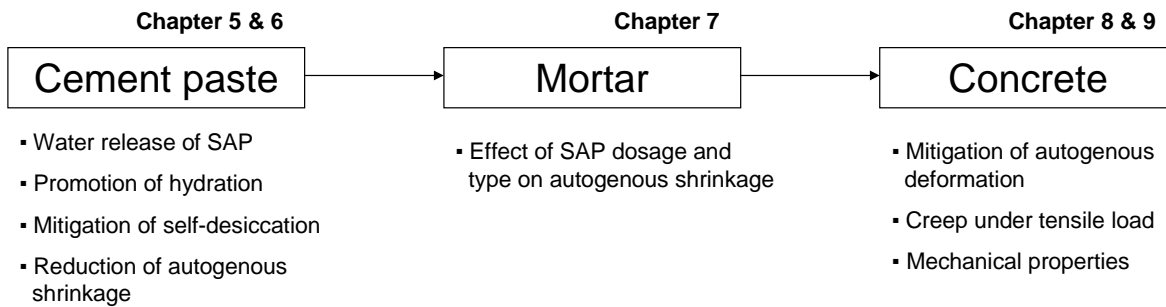


Figure 3.3: Trace of the idea of internal curing by SAP followed in the dissertation.

Although research on internal curing by SAP became increasingly popular in the last years, some questions of outstanding importance have remained unanswered yet, e.g.:

- Does IC water (SAP) influence the cement hydration differently compared to free water? According to Powers' theory, plain cement paste and water-entrained cement paste with same total amount of water have the same maximum degree of hydration at sealed condition.

- What is the key to adjust high effectiveness of internal curing?

The type of SAP has a great influence on the effectiveness of IC independent on the total volume of water entrained. The reasons behind this observation are not clarified so far.

- Is the curing effect on strength of SAP-modified concrete significant enough?

Up to now there is not enough data where different curing conditions are applied and compared in the same study.

The thesis at hand tries to contribute to a better understanding of the functioning of SAP with regard to manipulation of the water balance in the cement hardening process. The investigations are conducted for answering the above-listed questions and for helping to understand several other problems and issues related. Brief descriptions of the tasks being dealt within the single chapters are presented in the respective introductions.

3.3 Redistribution of capillary water

3.3.1 Theoretical background

Addition of dry SAP to the fresh concrete in the mixing process leads to redistribution of free water, acutally anticipated to form capillary pores, in pre-designed macropore inclusions of much larger size, called SAP pores. The characteristics of the imposed SAP pore system, such as shape, size and number of pores, depend on the characteristics of the dry SAP material. Shape, size and swelling capacity of dry SAP particles are defined by polymer chemistry, production method and processing (see section 2.9.3). SAP pores are initially water-saturated in the fresh state and remain as partially air-filled pores due to drying in hardened concrete. The drying process may be driven by chemical shrinkage during sealed hydration or by evaporation in case of an open system.

Figure 3.4 illustrates the idea of redistribution of capillary water by SAP on the basis of the volumetric phase distribution of a hardening cement paste at w/c of 0.50 during sealed hydration. The water initially absorbed by SAP equals to $(w/c)_e$ of 0.08. This water is not considered "on top" as in case of IC at low w/c ratio systems (see Figure 3.1), but rather considered as "lost" from the volume of free capillary water in systems with $w/c > 0.40$. As shown in the right diagram, it is expected that the water-entrained cement paste has a capillary pore system similar to a non-water-entrained cement paste with $(w/c)_{\text{basic}}$ of 0.42.

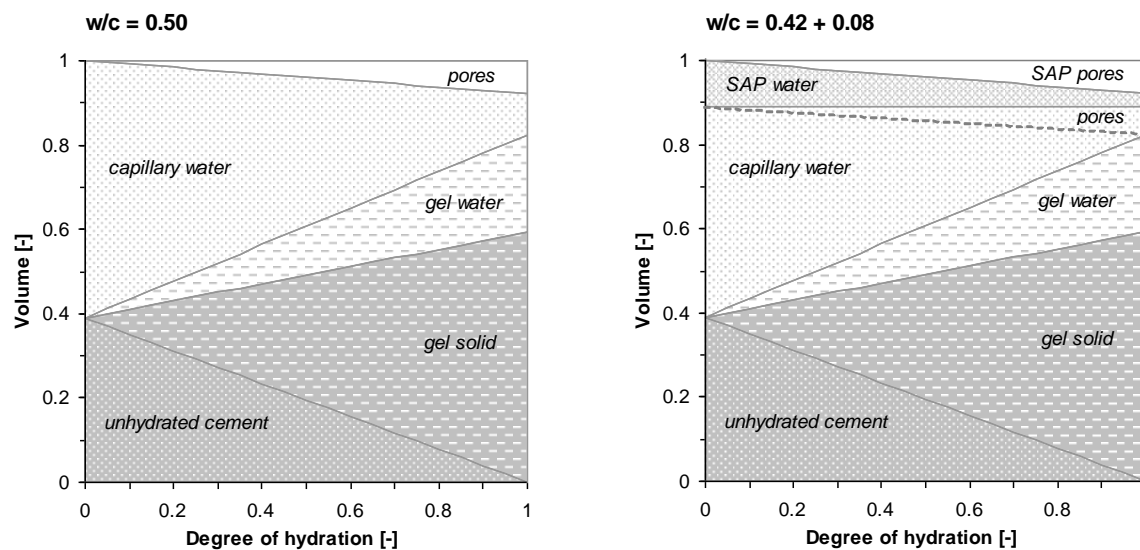


Figure 3.4: Substitution of capillary water illustrated on the basis of the volumetric phase distribution of a hardening cement paste at total w/c of 0.50 under sealed hydration.

Redistribution of free water, of course, results in loss of workability, that means e.g. superplasticizer has to be used for compensation. On the other hand, mechanical properties and hydration should be unaffected to the greatest extent.

3.3.2 Relevance for durability of concrete

As mentioned in section 2.6.5, most deterioration mechanisms causing damage of concrete and concrete structural elements, respectively, will only become operative if water, dissolved harmful substances or gases can enter the concrete interior. The transport processes are eased by capillary pores forming an interconnected pore structure. Due to this background, it is expected that redistribution of capillary water by SAP will greatly influence the transport processes in concrete and its durability in consequence. The main question is whether this effect is strong enough to exceed the contribution of SAP pores to the total pore volume, which is possibly relevant for transport of gas, moisture and liquid in a similar magnitude. Further it is conceivable that SAP directly intervene transport of water due to physical effects, e.g. water absorption. This consideration comprises a possible influence of the degree of saturation of SAP pores. However, experimental data on the influence of SAP on transport processes in concrete do not exist so far.

Pore space provided by SAP pores when partially air-filled may act in a similar manner as natural air pores or pores entrained by traditional AEA. With respect to freeze-thaw resistance of concrete, SAP pores may offer several benefits compared to the method of using AEA. Since external influences like ambient temperature or compaction energy applied during placing have a huge impact on the efficiency of AEA, the success of this method is difficult to control. In contrast, artificial SAP pores are pre-designed within production related limits of the SAP material. This is expected to be the most important advantage for the method of air entrainment in concrete by SAP. First efforts indicating positive effects of SAP addition on the freeze-thaw resistance of concrete were made at the University of Stuttgart. Some preliminary test results were published in [Reinhardt et al. 2008]. The questions that did arise since then are as follows:

- Are initially water-saturated SAP pores as effective as the same volume of pores generated by traditional AEA?

- How do SAP particle size and spacing influence the frost resistance?
- What is the main factor influencing frost resistance: void spacing or total pore volume?

3.3.3 Specific aspects of durability dealt within this thesis

In this thesis, focus is put on the effect of SAP addition on durability aspects of concretes with w/c ratios in the range 0.36 to 0.50. For concretes at low w/c ratio, i.e. far below 0.40, IC effects are present which may improve durability by the common rule that higher density of concrete is regarded as positive for durability. Higher degrees of hydration and less air-filled micropores will be noted on the asset side as a result of IC water considered “on top” as specified in chapter 3.2. Viewed in this way, SAP pore volume is present instead of micropores contributing to increase of total pore volume, which is considered as negative for durability, except in case of freeze-thaw attack. Further, mitigation of autogenous shrinkage and prevention of early age micro- and macro-cracking when under restraint will strongly enhance durability. At high w/c ratio, as studied in terms of durability aspects here, IC effects are not operative. That means that results presented can safely be transferred to low w/c systems. The specific durability issues processed in this thesis are listed below:

- The effect of SAP on transport processes, i.e. permeability of gas and water, capillary absorption, migration of chlorides and CO₂ and weight loss due to evaporation (chapter 9)
- The effect of SAP on the freeze-thaw deterioration processes (chapter 10)
- The effect of SAP on the mechanical abrasion resistance (chapter 10).

Outstanding importance is accounted for the investigations on transport properties as they form the basis for concrete deterioration mechanisms. Transport of chlorides and CO₂ in concrete is measured indirectly due to chloride migration testing and measurements on carbonation depth. Direct measurements on damage of concrete caused by physical and mechanical attack are conducted for the determination of freeze-thaw resistance with de-icing salts and abrasion resistivity.

The aim of this work is the provision of first test data in order to promote the potential of SAP as admixture to increase the durability of concrete. Findings presented later on in the text will refer to research recommended to do in future.

3.4 Further applications of SAP in concrete construction

3.4.1 Crack-healing

The dependency of the water absorption capacity on alkalinity and pH value of the absorbed liquid allows the application of SAP for water-blocking cracks in concrete. Tsuji et al. [Tsuji et al. 1998], [Tsuji et al. 1999] reported on the use of a special type of SAP that can, on the one hand, hardly absorb alkaline water, i.e. pore solution in fresh concrete. On the other hand, this SAP is able to absorb large quantities of neutral or acidic water, i.e. external water intruding the concrete through cracks. When cracks expose entrapped SAP particles to external water supply, swelling starts and leads to water-blocking. This healing effect was proved by permeability measurements.

3.4.2 Surface curing

Poor and insufficient surface curing can lead to reduced durability of the concrete surface caused by high evaporation rate accompanied with plastic shrinkage cracking. The idea of using SAP for

surface curing was implemented by different strategies, but none has been established yet. One application triggers water supply to the concrete surface by using a water-soaked gel-layer protected from desiccation by a latex rubber coating as proposed by the Onoda Cement Company Ltd., Japan, as cited in [Cusson et al. 2012]. Another application was suggested by Harrison [Harrison 1991]. He placed flexible SAP sheetings in conventional formwork which he called controlled-permeability formwork. The sheetings were impermeable to air and could absorb up to 200 times their weights of water. During placing the concrete, water from the surface zone was sucked up, resulting in decrease of the w/c ratio. In doing so, the surface zone showed improved concrete durability.

3.4.3 Shotcreting

Addition of SAP to concrete during mixing leads to a significant change in rheology. This change is caused by lowering of the free water content. In general, the addition of SAP has to be compensated by the use of superplasticizer or the addition of extra water to maintain workability. If not, then the reduction in w/c ratio by e.g. 0.06 will cause the yield stress of the fresh concrete with initial w/c ratio of 0.4 to triple and the plastic viscosity to increase by 25% [Banfill 2006], as cited in [Jensen 2008]. According to Jensen, this thickening effect may be useful for the application in shotcrete. Shotcreting by the wet process requires a good flowability of the fresh material, i.e. a high slump during pumping. On the other hand, a low slump is required when placing the concrete in order to minimize rebound and to guarantee stability of the material's thickness built up during shotcreting. This problem is usually counteracted by the addition of set-accelerating agents added in the nozzle, which obviously reduce the compressive strength of the hardened material [Jolin & Beaupré 2003]. The addition of dry SAP particles instead may avoid this problem and further may cause positive effects due to internal curing, mitigation of autogenous shrinkage or even improved freeze-thaw resistance. In [Jensen 2008] it is reported about first successful pre-tests on the use of SAP in shotcrete. Mechtcherine [Mechtcherine 2012] reports about a first test application of SAP-modified shotcrete used for the rehabilitation of a water reservoir of a pumped-storage power plant.

3.4.4 Recycling of returned concrete

One of the most important issues for concrete sustainability is recycling of concrete. Even returned concrete, which is unused ready-mixed concrete that comes back from the construction site to the concrete plant as excess material, should be recycled. Globally, the annual production of returned concrete is assumed to be about 125 tonnes [WBCSD 2009]. These figures raise awareness of the burden for ready-mix plants accompanied with high costs for disposal and consequently high impact on the environment. Ferrari and Brocchi developed a new recycling method for returned concrete using SAP [Ferrari & Brocchi 2012]. The proposed approach is based on four steps. First, an amount of 0.2 to 0.6 kg of SAP per one m³ of returned concrete is added into the drum of the truck. The stiffness of the concrete mix is increased due to absorption of the free water. After four minutes of mixing, returned concrete is converted into a granular material. In doing so, most of the grains consist of the original aggregate in the core, surrounded by a thick composite layer made of hydrating cement paste, fines aggregate and polymer hydrogel. In the second step, about 4 to 8 kg of set accelerator are added to the granular material. It is an inorganic compound which forms ettringite as soon as it comes in contact with water. As a result the granular material is further dried and gains strength. In the third step, the granular

material is discharged and stored in bulk. Due to its strength, compaction and re-agglomeration are resisted. At last, curing is needed like any other cementitious material requires. The authors recommend the only precaution to move the granules once within the first 24 hours in order to break the weak bonds between the hydrating cement paste layers surrounding the individual grains. This last step guarantees the handling as normal aggregate without risk of agglomeration.

Two eminent outcomes could be promoted:

- The interior of the drum of the truck is quite clean as all of the cement and fines aggregates are stuck together by SAP.
- The aggregates obtained from recycling of returned concrete can be reused fully for the production of new concrete with almost the same characteristics.

3.4.5 Explosive spalling

Spalling of concrete is defined as violent or non-violent breaking off of layers or pieces of a concrete member from its surface when exposed to high and rapidly rising temperatures. There are four categories: explosive, surface, aggregate and corner spalling [Khoury & Anderberg 2000].

Explosive spalling of concrete exposed to fire is related to two phenomena: first, restraint thermal dilation leads to biaxial compressive stresses parallel to the heated surface. As a result, tensile stresses occur in the perpendicular direction. And second, the pressure build-up as a consequence of vaporization of capillary water leads to tensile loads in the microstructure of the heated concrete. The latter phenomenon is considered to have the highest influence on spalling [Hertz 2003]. Thus, permeability of concrete, which affects the rate of vapour release, is expected to be the main parameter regulating spalling [Zeiml et al. 2008]. Due to addition of polypropylene (PP) fibres, the spalling behaviour of concrete can be significantly improved: Subjected to fire, the fibres show melting at temperatures of about 170°C and, finally, vaporization at about 360°C. In consequence, the permeability of concrete is increased due to provision of additional pore space and explosive spalling of concrete is defused.

The addition of superabsorbent polymer fibres (SAF) is expected to gain positive effects on the spalling behaviour of concrete as well. Even though water absorption of SAF leads to densification of the matrix, the pore channels that remain after the initially water-saturated fibres have dried out may act similarly to pore space provided by PP fibres after melting. The crucial prerequisite for the well-functioning of both methods is an existent inter-connection of the pore channels, indicated by the percolation threshold. Indeed, the pore structure created by SAF allows the transport of harmful substances into the concrete structure and therefore may affect its durability. But, nevertheless, the SAF method is expected to show two advantages compared to PP fibres. First, the dispersion is easier to manage since SAF can be added pre-saturated with water. Second, the concrete's strength is less reduced since SAF provides internal curing if low w/c ratio is applied. In combination with the potential of SAF as regulating agent in shotcrete, its application e.g. in protective concrete layers for tunnel constructions is theoretically possible.

Preliminary tests including two reference concretes and two mixtures with SAP and SAF, respectively, were performed on cylindrical specimen with 150 mm in diameter and 300 mm in height [Assmann 2009]. Before the specimens were heat-treated in groups of four in the furnace according to the standard temperature curve [DIN EN 1991-1-2 2010], they were exposed to different storage conditions: oven-drying (60°C), standard climate (20°C / 65% RH) and indoor storage. This procedure had the purpose to maintain different moisture contents in the pore structure of the specimen. Unfortunately, the location of each specimen in the furnace during

testing had a significant influence on its performance and it was not possible to distinguish between real explosive spalling and concrete damage due to thermal expansion. Further, the number of specimen tested had been too small and just one dosage of SAF was examined. Consequently, no final conclusion on the effect of SAF on the prevention of explosive spalling has been drawn.

3.4.6 Strain hardening cement-based composites

Multiple cracking of strain hardening cement-based composites (SHCC) results in ductile response with a strain capacity of up to 5% when subjected to uni-axial tensile loading. Crack bridging is provided by short, well-distributed fibres. Entrapped SAP pores are expected to act as micro-defects which ease multiple cracking, as demonstrated in [Bruedern & Mechtcherine 2010].

3.4.7 Lightweight concrete with porous matrix

Sustainable construction means, among others, a proper heat insulation of the exterior walls of buildings. Germany has edited the new Energy Saving Directive (EnEV 2012) with severe legal requirements, which can only be fulfilled with a layered insulation system of a bearing wall and an additional lightweight organic or mineral material. Facing the challenge to develop a cementitious material which is strong enough and has, at the same time, sufficiently low heat conductivity, the application of SAP in order to aerate the matrix of concrete for further weight reduction was put into practice [Reinhardt & Assmann 2010a]. The design of the developed concrete mixtures with porous matrix started from a concrete mixture with a dense microstructure (RefM) using expanded glass granulate as lightweight aggregate. The volume fraction of sand and cement paste was replaced in three steps (10, 20 and 30%) by either adding water saturated SAP (MSAP) or stable protein foam (MF). As a result, the oven-dry densities of the obtained lightweight concretes decreased down to 300 kg/m³. Besides that, thermal conductivity and strength properties are similar to the one of autoclave aerated concrete (AAC). Figure 3.5 shows an excerpt of the test results. More information on the mixture composition is available in appendix 3.

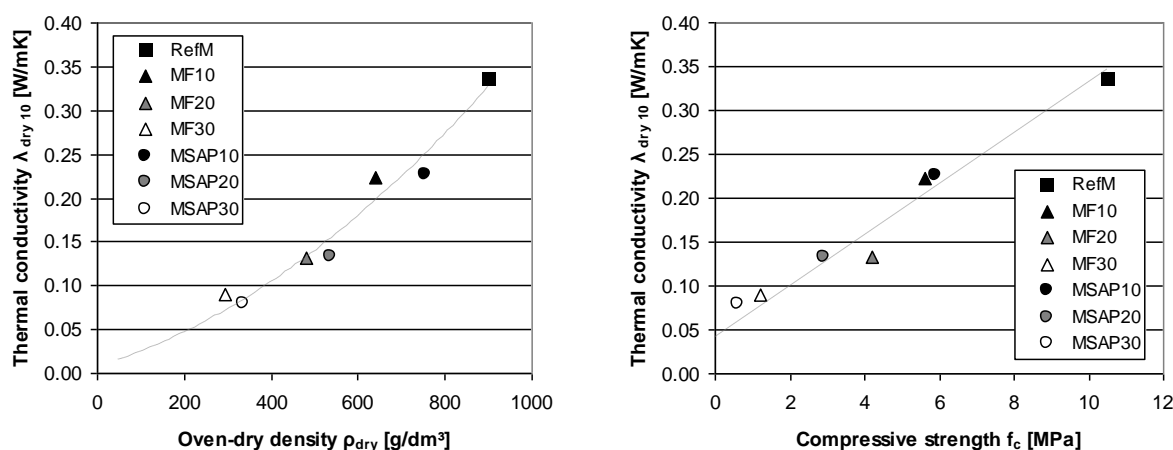


Figure 3.5: Thermal conductivity vs. oven-dry density (left) and thermal conductivity vs. 28 days compressive strength (right) [Reinhardt & Assmann 2010a].

The method of weight reduction due to addition of saturated SAP is feasible, but involves a number of limitations compared to traditional methods, i.e. using foam. The major problem is that the hardening of SAP-modified lightweight concrete requires conditions for an adequate desiccation of the entrained extra water, e.g. well-ventilated storage at 20°C and 65% RH.

3.5 Additional remarks

Although superabsorbers possess a wide application potential, which has already been noticed by the scientific community and the construction chemistry as well, no SAP material is certificated as concrete additive up to now. Despite that, a first demonstration building made of SAP-modified UHPC - the FIFA World Cup Pavillon in Kaiserslautern - has been put into practice. The pavillon was designed as “filigree, thin-walled structure with slender columns and no conventional reinforcement” [Mechtcherine et al. 2006]. It is expected that more case studies will follow soon.

By now, most research underway is still dealing with the application of SAP for the purpose of internal curing at low w/c ratio. This fact could be misinterpreted to mean that other topics are of lesser importance. Yet, the opposite is the case: among experts, there is broad consensus about the necessity of advanced investigations on the effect of SAP on long term properties of concrete and its durability, respectively. Currently, a Round Robin Test (RRT) prepared by Rilem TC 225-SAP is addressing this issue: in a first part, the potential of SAP for mitigation of autogenous shrinkage is investigated [Mechtcherine et al. 2013], whereas in a second part, the focus will be put on the method of air entrainment by SAP for enhanced freeze-thaw resistance of concrete.

At last it should be stated again that the performance of SAP will strongly depend on the type of SAP, i.e. polymer chemistry associated with the cementitious environment. On this account, in the thesis at hand special emphasis is put on the characteristics of the SAP material used. The next chapter will solely deal with properties of the used SAP. For the sake of comparability and reproducibility, all tests in this thesis were performed with Portland cement of type CEM I 42.5 R produced by Schwenk KG Allmendingen. Only one publication was available where another type of cement was used [Klemm & Sikora 2012].

4 Characterization of used SAP material

4.1 Introduction

The present chapter serves as the characterization of the SAP material used. It focuses on the determination of the main properties of SAP, which are the swelling capacity in cementitious environment (CEM I 42.5 R) and the size distribution of SAP particles in dry condition and after swelling. For the estimation of the water absorption capacity under mixing conditions, comparative mortar spread tests were conducted. Further, volume and distribution of SAP pores in hardened pastes were determined by imaging analysis carried out on polished microsections. At last, a calculation approach is presented that provides an estimation of the SAP pore spacing on the basis of the hexagonal close packing. Water desorption by SAP is addressed in chapter 5.

4.2 SAP material investigated

4.2.1 Provision of SAP

The superabsorbent polymer materials investigated in this thesis were made available by different producers, see Table 4.1. SAP A and SAP B were development products provided by the BASF Construction Chemicals GmbH, Trostberg. SAP C was produced by SNF Floerger, Andrézieux Cedex, and was shipped by the chairman of the RILEM TC 225-SAP to the participants of the RRT on autogenous shrinkage [Mechtcherine et al. 2013]. Chemically speaking SAP C is made of the main monomers acrylic acid and acrylamide. SAP D was developed by Prof. Jensen at the Technical University of Denmark (DTU). It is a suspension-polymerized covalently crosslinked acrylamide/ acrylic acid copolymer [Jensen & Hansen 2001b] which has already been used by different other researchers. SAF is a commercially available superabsorbent polymer fibre produced by the company Technical Absorbents, UK. It is made of cross-linked acrylate co-polymers partially neutralised to the sodium salt and is mainly used in products of the personal care industry. SAP A, SAP B and SAP D are “salt-stable”, that means they were developed for special use in high alkaline environment such as cementitious suspension.

Table 4.1: Superabsorbent polymer material investigated

Designation	Classification	Producer
SAP A	gel-polymerized	BASF Construction Chemicals GmbH
SAP B	suspension-polymerized	BASF Construction Chemicals GmbH
SAP C	gel-polymerized	SNF Floerger
SAP D	suspension-polymerized	Technical University of Denmark
SAF	dry-spun polymer fibre	Technical Absorbents

4.2.2 Properties of dry SAP

The dry granular particles of SAP A and SAP C were characterized by lasergranulometry (LG) [EDANA 2002a], as were the spherical particles of SAP B. By using a screen tower, the production related Gauss distribution of SAP A particles was subdivided into the particle size ranges $<63 \mu\text{m}$, $63\text{-}125 \mu\text{m}$ and $125\text{-}250 \mu\text{m}$. The size distributions obtained by LG are presented in Figure 4.1 on the next page. SAP D particles were characterized by air jet sieving, see appendix 4.

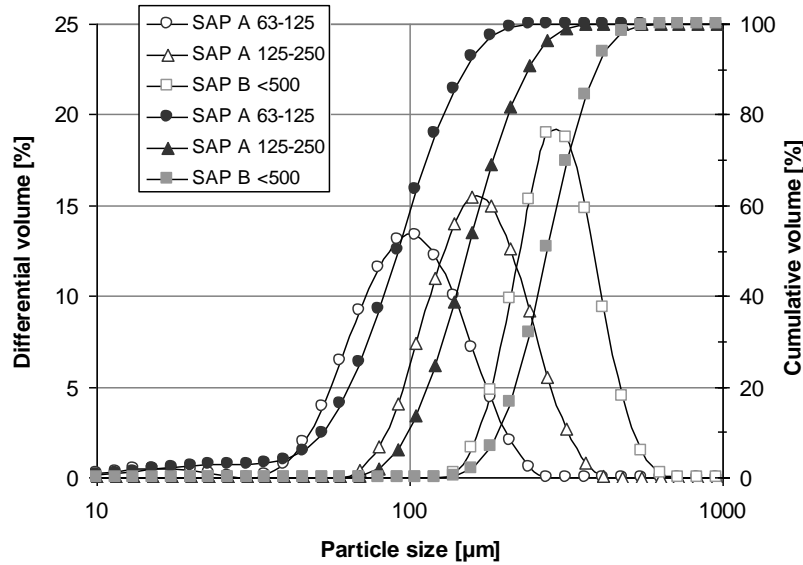


Figure 4.1: Size distribution of dry SAP found by lasergranulometry.

Table 4.2 lists the corresponding d10, d50 and d90 values. The average length of the polymer fibres SAF was 5.8 mm according to the manufacturer's specification. The average thickness was measured due to light optical microscope and was found to yield approximately $21 \pm 1 \mu\text{m}$.

Table 4.2: Main data obtained from LG (SAP A, B, C) and air jet sieving (SAP D)

		SAP A	SAP A	SAP A	SAP B	SAP C	SAP D
Size range	[μm]	< 63	63-125	125-250	< 500	< 1500	< 250
Shape	-	granular	granular	granular	spherical	granular	spherical
d10	[μm]	15	50	100	190	300*	90
d50	[μm]	40	90	150	270	590*	130
d90	[μm]	80	150	250	390	1100*	200

*: value provided by TU Dresden

4.2.3 Addition of SAP in concrete

As mentioned in chapter 2.4.4, SAP can either be added pre-saturated with water or dryly pre-mixed with cement or binder, respectively. The second method was used in this thesis in case of granule and spherical SAP particles to gain homogenous distribution and to avoid gel-blocking. The latter is a phenomenon especially of very small particles. Immediately after getting in contact with water, the particles stick together due to absorption on the surface. Once the particles are merged, they do not disaggregate anymore. Gel-blocking is an effect desired for the application of SAP as sealing material [Buchholtz & Graham 1998]. Experiments showed that 30 seconds of pre-mixing dry SAP with cement is enough to successfully prevent gel-blocking in concrete.

4.2.4 Durability of SAP material

Heat development due to hydration does not impair functioning of SAP, nor do sub-zero temperatures. Only when the temperature exceeds 200°C , hydrolysis will lead to decomposition of polyacrylates. Fracture of polymer chains may also be caused by longterm exposure to ultra-violet radiation. SAP embedded in concrete is spared from that risk. But it is anticipated that even salt-stable types of SAP will be affected by the high alkalinity of the pore solution over time. This influence is not yet quantified in detail.

4.3 Methods for determining the water absorption capacity

4.3.1 Definition of term

The water absorption capacity χ is defined as relation between the mass of swelling medium absorbed until weight equilibrium is reached and the initial dry polymer mass. The unit is [g water/g dry polymer] or shortened [g/g].

4.3.2 Standardized test procedures

Standardized test methods for the characterization of SAP are provided by EDANA, the roof organisation for the European nonwovens industry. The recommended standard test for the quantitative study of the absorption behaviour is the so-called “teabag method” [EDANA 2002b]. To this end, SAP of known amount is filled in a paper bag and put in the test solution. The paper bag has to be pre-wetted in the test solution before beginning the test. After individually chosen periods of time, the paper bag is removed and hung up to exclude excess water and then weight. After the weight ingress has approached a limit value, the absorption capacity is determined.

If the absorption against external pressure has to be determined, the so-called absorption against pressure (AAP) test [Kellenberg 1993] or the absorption under load (AUL) test [Azad et al. 2003] is commonly used. These test methods may potentially be suitable for simulating environmental conditions during mixing and placing, since swelling against an external pressure is measured. However, in this dissertation, only non-standardized test methods were used.

4.3.3 Mortar spread tests

A non-standardized test procedure that should provide a realistic estimation of the water absorption capacity in concrete was developed by Mönnig [Mönnig 2005]. He called it slump-flow test method, referred to as mortar spread test in the following. The method considers the impact of external forces during mixing and the impact resulting from the net weight of the concrete constituents. The idea is to compare the spread of a mortar mixture containing a specific amount of SAP with the spread of mortars without SAP but variable water content. In doing so, the spread of each mixture is measured according to [DIN EN 459-2 2010] in intervals of 6 minutes, whereof the first two minutes of each interval are considered as additional mixing time. The absorption capacity is determined on the assumption that water absorbed by SAP does not contribute to spread formation. Therefore, the spread curve of the reference mortar is in demand that comes closest to the spread curve of the SAP-modified mortar. The difference in total water content is considered to be absorbed by SAP. The water absorption capacity χ [g/g] results from the following equation [Mönnig 2009]:

$$\chi = \frac{m_{\text{water}}^{\text{added}} - m_{\text{water}}^{\text{available}}}{m_{\text{SAP}}^{\text{added}}} \quad (4.1)$$

where m_{water} [g] is the mass of water and m_{SAP} [g] is the mass of SAP in the mix. The mass of available water is the amount of free water that remains after water absorption by SAP and equals the water content of the reference mortar with closest spread curve.

4.3.4 Computer-based evaluation of microsections

A new approach for determining the water absorption capacity of SAP in cement paste is provided by computer-based evaluation of microsections. To this end, microsections of hardened SAP-modified cement paste prisms with a base area of 40 x 40 mm² and a thickness of 30 μm were manufactured according to [DIN EN 12407 2007] at the age of one week. The cement pastes had a basic w/c ratio of 0.36. The amount of added SAP should correspond to (w/c)_e of 0.06. Three microsections of each prism were scanned by a slide scanner using a resolution of 4000 dpi. Subsequently, the digital images were evaluated by imaging software Leica LAS Image Analysis. In the process, the unit of pixels was calibrated to the real scale of the image (1 pixel = 6.35 μm). Due to differences in colour and shape, the actually present area segments of cement paste matrix, air voids and SAP pores were automatically separated by software. As the relative area segments can be regarded as volume fractions, the results were used for calculating the absorption capacity. Unfortunately, the method is not applicable in case of spherical particles, since the software is not able to distinguish between air voids and spherical SAP pores.

A potential source of error is in the contrast adjustment that governs the automatic distinction between pore surface and solid. This boundary zone is blurred when the microsections are screened, i.e. when the slides are taken. To defuse the inaccuracy of the pore boundary determination, especially of small pores, the thickness of the microsections should be decreased in future.

4.4 Formation of artificial macropore inclusions

4.4.1 Ca²⁺ ion concentration

As mentioned in section 2.2.1, Ca²⁺ ions may lead to undesired additional crosslinking of polymer chains resulting in reduced absorption capacity. In order to roughly investigate this tendency, ion chromatographic analysis was carried out on eluates of two SAP-modified cement pastes (SAP A, SAP D) and one reference paste. To this end, about 500 g of the fresh paste were filtered two hours after mixing by means of a water-jet pump to extract pore solution. At this age, the water absorption of SAP was expected to be finished. Table 4.3 reports on the ion concentration found.

Table 4.3: Concentration of Ca²⁺ ions in pore solution 2 hours after mixing

Cement paste		Polymer		Ca ²⁺
w/c _{tot} [-]	w/c _e [-]	Type	SAP/c [%]	[mmol/l]
0.36	-	-	-	22
0.36	0.06	SAP A	0.25	11.2
0.36	0.06	SAP D	0.55	16.5

The highest Ca²⁺ concentration was found for the reference paste without SAP. For both SAP-modified pastes, the concentration of Ca²⁺ was lower. This leads to the assumption that the polymer chains of both SAP types increased their degree of crosslinking due to binding of Ca²⁺ ions or exchange with Na⁺ ions, respectively. Although the SAP/c ratio is higher for SAP D, the Ca²⁺ concentration is not reduced as much as in case of SAP A. This leads to the assumption that SAP A tends to bind more Ca²⁺. In [Rajabipour et al. 2008], the maximum concentration of Ca²⁺ ions in pore solution emerged within the first 10 hours after mixing was 60 mmol/l. Fujii [Fujii et al. 1970] found the highest Ca²⁺ concentration in plain Portland cement paste one minute after mixing. During the pre-induction phase of hydration the Ca²⁺ concentration generally decreases

as calcium sulphate dissolves and forms ettringite. During the subsequent dormant stage the chemical composition of the pore solution was found to remain almost stable, even though further ettringite, calcium hydroxide and first calcium silicate hydrates (CSH) are formed.

Schröfl et al. [Schroefl et al. 2012] reported that SAP with very high anionic functional group density takes up synthesized pore solution quickly and releases it back to a large extent during the first three hours after mixing. In contrast, SAP with lower anion density is able to store the liquid for a long time. Once absorbed, they measured no desorption of the liquid within the first three hours, independently of the crosslinking density. They traced back this finding to the less pronounced interaction between the anionic functional groups with Ca^{2+} ions in the pore solution in case of polymers with lower anion concentration.

4.4.2 Water absorption capacity and parameters involved

Results of mortar spread tests for SAP B and SAP D are shown in Figure 4.2. The corresponding results of SAP A testing while varying the particle size ($<63 \mu\text{m}$, $63\text{-}125 \mu\text{m}$ and $125\text{-}250 \mu\text{m}$) is reported in appendix 4. In some diagrams the spread curves of the plain mortars used for comparison are identical. The basic ingredients of the mortars were 1350 g of sand according to [DIN EN 196-1 2005] and 450 g of CEM I 42.5 R. The SAP-modified mortars contained either 1.5 g of SAP A plus 275 g of water or 1.5 g of SAP B plus 290 g of water or 3 g of SAP D plus 270 g of water. The plain mortars used for comparison had less water. They are designated by the amount of water reduced per g of SAP added in the corresponding SAP-modified mix.

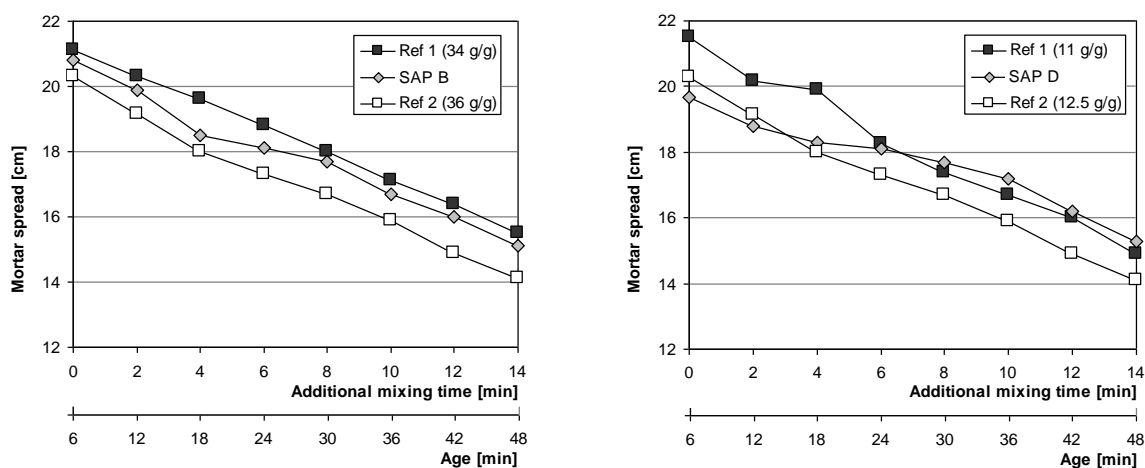


Figure 4.2: Results of mortar spread tests for SAP B (left) and SAP D (right).

The resulting water absorption capacities χ [g water/g SAP] were estimated from the mortar spread tests as Table 4.4 shows, see following page. The spread curves were generated from 9 measurements conducted over a period of 48 minutes. It is assumed that within this test period, the polymer achieves weight equilibrium. By using the teabag method, Jensen [Jensen & Hansen 2002] showed that water absorption of SAP D (corresponding to type A in his paper) reaches about 95% of the final weight after half an hour. Other types of SAP are known that finish water absorption even after a few minutes [Buchholtz & Graham 1998]. Figure 4.2 (right) indicates that SAP D might dispense a specific amount of initially absorbed pore fluid during testing. After 20 minutes the water absorption levels off at circa 11 g/g. Similar observations on other SAPs were reported in [Schroefl et al. 2012]. It is a phenomenon certainly related to the molecular structure of the polymer and its interactivity with the continually changing pore fluid.

Table 4.4: Water absorption capacity estimated by mortar spread tests

	SAP A <63	SAP A 63-125	SAP A 125-250	SAP B <500	SAP D <250
Water absorption [g/g]	23	24	25	35	11

At first sight, water absorption seems to be a material constant, but it is influenced by e.g. the particle size. In case of the investigated size fractions of SAP A, this influence is only a minor: the mortar spread tests produced values for χ of 23 g/g for the small size fraction of SAP A and up to 25 g/g for the large size fraction. The tendency of increasing water absorption capacity with increasing size of dry particles might be explained by the severity of ions to diffuse in larger depth of the polymer structure and the cross-link structure of the particles itself. Esteves who used Jensen's polymers found a non-linear relationship between particle size and absorption capacity [Esteves 2010a]. In his study the size increase of individual SAP particles due to absorption of synthetic pore fluid was observed by an optical microscope. The composition was in detail [mmol/l]: $\text{Na}^+ = 200$, $\text{K}^+ = 200$, $\text{Ca}^{2+} = 1$, $\text{SO}_4^{2-} = 15$ and $\text{OH}^- = 672$. The swelling capacity was found to yield 10 g/g for the smallest dry particles of 50 μm in diameter and up to 16 g/g for dry particles of 500 μm in diameter. Further, Esteves verified the influence of dry particle size on the speed of absorption. The surface to volume ratio increases with decreasing the diameter of dry particles, resulting in higher speed of absorption. He described the absorption kinetics of the polymers on the basis of the first order of Fick's second law of diffusion as follows:

$$Q(t) = Q_{\max} (1 - e^{-kt}) \quad (4.2)$$

where Q and Q_{\max} are the swelling capacities at any time t and at equilibrium, respectively.

For the empirical parameter k , expressing the swelling rate constant, the following dependency on ϕ , the diameter of SAP D particles, is proposed:

$$k = 2.76 \cdot 10^3 \cdot \phi^{-1.567} \quad (4.3)$$

Again, it is worth noting that the experiments of Esteves were executed in absorption medium of stable chemical composition, therefore the model presented is idealized.

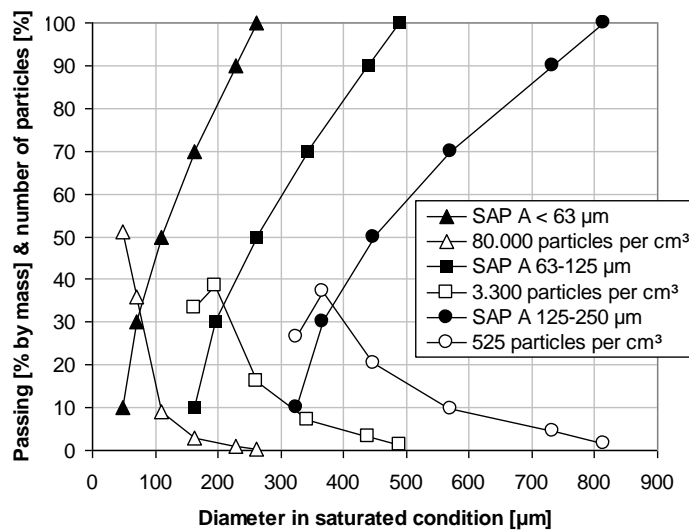


Figure 4.3: Expected size distribution of saturated SAP A particles and deduced distribution of particle number in 1 cm³ concrete. The diagram applies to χ of 24 g/g. The given total number of particles refers to the addition of 1 kg SAP A per 1 m³ concrete.

Figure 4.3 presents the expected particle size distribution of SAP A particles after absorption of pore fluid, i.e. in saturated condition. For the sake of simplicity, here and in the following, the absorption capacity of SAP A is chosen to be 24 g/g, independent of the particle size. The radius of SAP in saturated condition r_{SAP}^s [cm] was calculated from the dry polymer radius r_{SAP}^d [cm] obtained from lasergranulometry according to equation (4.4), see also appendix 4. It is ω [-] the swelling factor and ρ_{SAP}^s and ρ_{SAP}^d [g/cm³] are the densities of SAP in dry and saturated condition, respectively.

$$r_{SAP}^s = r_{SAP}^d \cdot \sqrt[3]{\frac{\rho_{SAP}^d}{\rho_{SAP}^s} \cdot (1 + \chi)} = r_{SAP}^d \cdot \omega \quad (4.4)$$

The density of dry SAP A particles was assumed to be 1.4 g/cm³ as stated by the manufacturer. The density of saturated SAP particles can be calculated due to equation (4.5), where ρ_w is the density of water, i.e. 1.0 g/cm³.

$$\rho_{SAP}^s = (1 + \chi) / \left(\frac{1}{\rho_{SAP}^d} + \frac{\chi}{\rho_w} \right) \quad (4.5)$$

The number of particles was derived from the pore volume of each size fraction of SAP A multiplied with the saturated density, i.e. 1.0135 g/cm³, multiplied with the total number of pores per mass unit of dry SAP A, i.e. the reciprocal of the dry density of SAP A, cf. appendix 4.

The value for the water absorption capacity of SAP C was provided by TU Dresden. It was found to yield 10 g/g. The tests performed at TU Dresden based on the teabag method applied in extracted pore solution using the same type of cement but blended with 1/10 silica fume.



Figure 4.4: Micrograph of polymer fibre SAF in dry condition (left) and after saturation with tap water (right).

The water absorption capacity of SAF was determined by light optical microscope as illustrated by Figure 4.4. The diameter of the fibres was measured in dry condition and after absorption of extracted pore fluid. The estimated difference in diameter was transformed numerically into the water absorption capacity by simplified equation(4.6). χ_{SAF} was found to yield about 19 g/g.

$$\chi_{SAF} = \frac{\pi (d_{SAF}^s - d_{SAF}^d)^2}{4 \cdot \rho_w} \bigg/ \frac{\pi (d_{SAF}^d)^2}{4 \cdot \rho_{SAF}^d} \quad (4.6)$$

where d_{SAF}^d and d_{SAF}^s are the diameter of SAF in dry and saturated condition, respectively.

4.4.3 Characterization of macropores by imaging analysis

Figure 4.5 on the next page presents details of three microsections produced at total w/c ratio of 0.42 varying in size fraction of added SAP A. It is conspicuous that at constant pore volume the number of pores formed decreases with increasing the size fraction of dry SAP A particles.



Figure 4.5: Microsections ($27 \times 20 \text{ mm}^2$) of hardened cement pastes containing 0.25% SAP A of different size fraction: $<63 \mu\text{m}$, $63\text{-}125 \mu\text{m}$ and $125\text{-}250 \mu\text{m}$ (from left to right).

For each mix, microsections with a total surface of 4800 mm^2 were analyzed by imaging software. The settings of the software allowed categorizing between air voids, SAP pores and matrix. By neglecting chemical shrinkage during hydration, the latter is equal to the volume fraction of cement V_c plus free water V_w that is initially present in the mix:

$$V_{\text{Matrix}} = V_w + V_c = \frac{c + w}{c / \rho_c + w / \rho_w} \quad (4.7)$$

where $\rho_c = 3.124 \text{ kg/dm}^3$ is the density of cement and $\rho_w = 1.0 \text{ kg/dm}^3$ is the density of water.

For cement paste containing a certain amount of SAP f_{SAP} , the mass fractions of cement c [kg/dm^3] and water w [kg/dm^3] can be calculated by the following equations:

$$c = \frac{1 - V_{\text{Air}}}{1 / \rho_c + (w / c) / \rho_w + f_{\text{SAP}} / \rho_{\text{SAP}}^d} \quad (4.8)$$

$$w = (w / c) \cdot c \quad (4.9)$$

where $f_{\text{SAP}} = 0.0025$ is the amount of added dry SAP [% by weight of c], $\rho_{\text{SAP}}^d = 1.4 \text{ kg/dm}^3$ is the density of dry SAP and V_{Air} [-] is the volume fraction of air voids equal to the relative area segment of air voids determined by software.

The actual volume fraction of SAP pores V_{SAP} [-], equal to the relative area segment of SAP pores obtained by IA, leads to the actual water absorption capacity χ_{actual} [g/g]:

$$\chi_{\text{actual}} = \frac{V_{\text{SAP}}}{\rho_w \cdot f_{\text{SAP}} \cdot c} - \frac{1}{\rho_w \cdot \rho_{\text{SAP}}^d} \quad (4.10)$$

Table 4.5 reports on the volume fractions V_{Matrix} , V_{Air} and V_{SAP} , equal to the relative area segments of cement paste matrix, air voids and SAP pores, obtained by computer-based evaluation of the microsections. Further χ_{actual} is compared to the nominal value of water absorption capacity χ_{nominal} , derived from mortar spread tests. It can be seen that both values are close together, although the particle size effect on the absorption capacity is more pronounced in case of χ_{actual} . Nevertheless, the absorption capacity of SAP A will stick to the value of 24 g/g .

Table 4.5: Results of computer-based evaluation of microsections

Cement paste	SAP _{dry} [μm]	χ nominal [g/g]	Measured values [V.-%]			χ actual [g/g]
			V_{Matrix}	V_{Air}	V_{SAP}	
SAP A 0.36+0.06	< 63	23	90.26	1.59	8.15	23.9
SAP A 0.36+0.06	63-125	24	90.30	0.55	9.15	26.6
SAP A 0.36+0.06	125-250	25	88.71	1.50	9.79	28.8

The size distribution of SAP A pore surfaces obtained from IA was converted into the cumulative distribution of SAP A pore volume, see Figure 4.6 (left). The d50 values of the curves are presented in Table 4.6. The right diagram shows the cumulative distribution of the number of counted SAP A pores. It is conspicuous that the median pore size d_{med} [μm] is almost independent of the particle size fraction. Further, the largest size fraction produced a large number of fine pores, i.e. smaller than 50 μm . Reasons might be found in the breakage of large particles during mixing or in the detachment of small particles sticking on the surface of larger particles that have not been removed during sieving. It is also possible that swollen particles break in fresh concrete since the mechanical properties get poorer with increasing the water content and size, respectively. According to [Buchholtz & Graham 1998] the volume of the swollen particles is inversely proportional to the shear modulus of the gel. Principally, breakage of SAP should come into effect for granular particles, i.e. SAP A and SAP C.

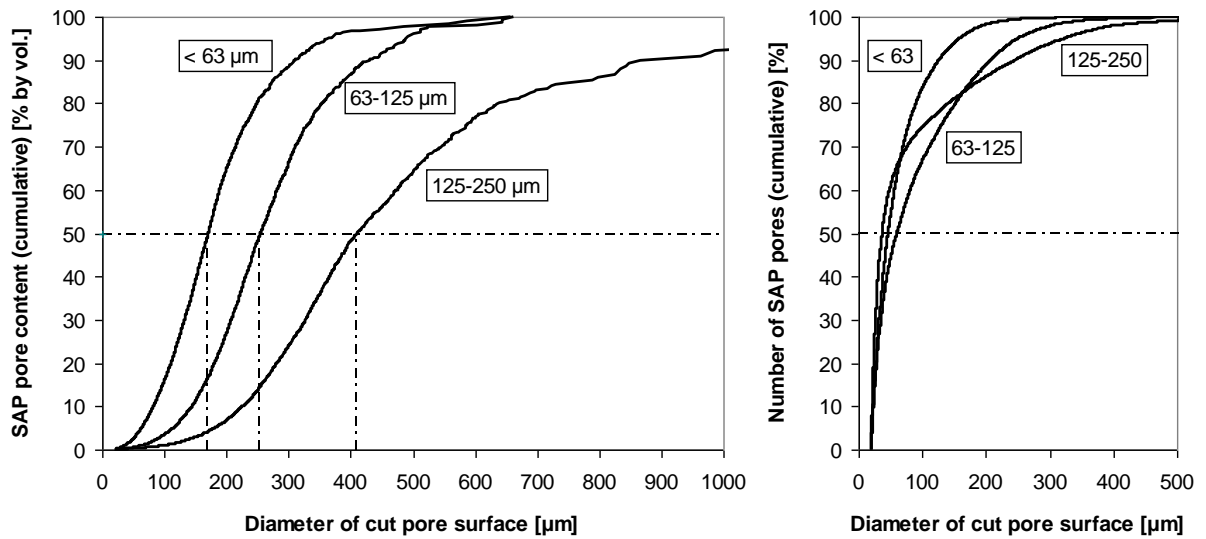


Figure 4.6: Cumulative distribution of SAP A pore size by volume (left) and by number (right), obtained from computer-based evaluation of cut pore surfaces.

Assuming spherical shape, the true average SAP pore radius r_{Pore} [μm] can be predicted on the basis of a probability calculation using equation (4.11), where A_{Pore}^O [μm^2] and r_{Pore}^O [μm] are the average cut pore surface and radius, respectively, according to equation (4.12). The approach implies the probability that the measured radius is the radius of a spherical pore cut at its center.

$$A_{Pore}^\phi = \frac{1}{\pi/2} \cdot \int_0^{\pi/2} \pi (r_{Pore} \cdot \sin \alpha)^2 \cdot d\alpha = \pi/2 \cdot r_{Pore}^2 \quad (4.11)$$

$$A_{Pore}^\phi = \frac{A_{Pore}}{n} \quad (4.12)$$

where A_{Pore} [μm^2] is the sum of all counted SAP pore surfaces and n [-] is their total number. As a result, r_{Pore} is obtained from the following relation:

$$r_{Pore} = \sqrt{\frac{2 \cdot A_{Pore}^\phi}{\pi}} = \sqrt{2} \cdot r_{Pore}^\phi \quad (4.13)$$

The true average pore diameter d_{Pore} [μm] is $\sqrt{2}$ times the average diameter d_{Pore}^O [μm] from IA. Table 4.6 on the following page lists IA results in comparison to d50 value obtained from LG.

Table 4.6: Pore data derived from IA in comparison to d50 values obtained from LG

	Results from LG [μm]	Calc. pore data [μm]	Results from IA [μm]			
	d50	d50	d50	d_{med}	d_{Pore}^O	d_{Pore}
SAP A <63	40	130	170	46	75	110
SAP A 63-125	90	290	255	60	120	170
SAP A 125-250	150	480	410	37	140	195

4.4.4 Light optical micrographs

Figure 4.7 shows images of concrete cross-sections with different SAP, recorded by light optical microscope. The test samples used had been prepared for pore counting presented in chapter 10. The boundaries of the SAP pores are clearly visible. Although granular particles form irregular shaped pores, they might be assumed as spherical as well. Both SAP A and SAP D pores contain residual pieces of the polymer sticking on the pore walls. In case of SAF, the cut surface of the fibre is clear to see. In general, it is expected that re-wetting results once again in swelling. If the alkalinity of the re-absorbed medium is lower than the pore fluid, i.e. acidic water has access to the pores, swelling may cause internal pressure on the pore walls and block further water ingress.

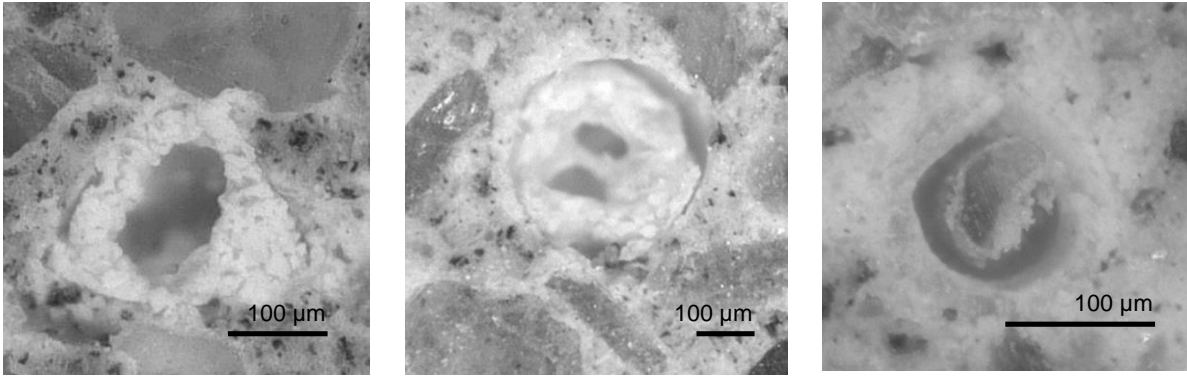


Figure 4.7: Microsection of macropore inclusion in concrete formed by gel-polymerized SAP A (left), suspension-polymerized SAP D (center) and fibre-shaped type SAF (right).

4.4.5 Model for the spacing of SAP pores

For calculating the void spacing VS [μm] of SAP A pores, the average pore radius r_{Pore} according to equation (4.13) can be used as input. The present calculation approach bases on the idealized distribution of spherical pores equal in size. It is anticipated that the equally sized SAP pores are located in the center of imaginary spheres arranged in the hexagonal close packing (HCP) formation. Here, VS is defined as the distance between the centroid of three equally afar pores to the pore wall. It is given by equation (4.14). A schematic illustration of the HCP formation and the derivation of equations (4.14) and (4.15) is provided in appendix 4.

$$VS = 1/\sqrt{3} \cdot \left(\sqrt{2} \cdot n_{EZ} \right)^{-1/3} - r_{Pore} \quad (4.14)$$

n_{EZ} [-] is the number of unit cells per $1 \mu\text{m}^3$ of cement paste according to:

$$n_{EZ} = \left(f_{SAP} \cdot n_{SAP}^d \right) / 2 \cdot 10^{18} \quad (4.15)$$

where f_{SAP} [kg/m^3] is the amount of added SAP per m^3 cement paste and n_{SAP}^d [-] is the number of particles in 1 kg dry SAP. One unit cell of HCP formation contains two pores.

4.5 Summary

Table 4.7 provides a summary of the main characteristics of the investigated dry polymer material and of the pores formed after water absorption in cement paste. The realistic estimate of the water absorption of SAP in cement-based materials is a difficult task. The continually changing chemical composition of the absorption fluid and further influences like external forces acting during mixing, transportation and placing can hardly be mapped by established experimental setup. In this study, non-standardized test methods have been used for characterization of water absorption. The following conclusions could be drawn:

- Both comparative mortar spread tests and imaging analysis are appropriate methods for estimating the absorption capacity of granular and spherical SAP in cement based materials. The water absorption capacity of the investigated SAP types was found in the range 10 (SAP C) to 35 g/g (SAP B).
- The particle size seems to slightly change the swelling capacity and the speed of absorption. For reasons of simplification this effect is neglected in the following.
- Pores formed by granular particles of SAP A are estimated as spheres.
- An approach for calculating the void spacing of SAP pores was presented on the basis of the hexagonal close packing (HCP) of equally sized spheres using the true average diameter derived from IA as input.

A more straightforward method to visualize the phenomena of water absorption and desorption processes in fresh cement paste after mixing might be testing with x-ray micro-tomography. This technique has already been applied for the study of internal structures of natural building stones, e.g. by [Cnudde & Jacobs 2003].

Table 4.7: Properties of dry SAP and pores formed in cement paste (CEM I 42.5 R)

Properties of dry particles	SAP A	SAP A	SAP A	SAP B	SAP C	SAP D	SAF
Size range [μm]	<63	63-125	125-250	<500	<1500	<250	-
d50 by vol. [μm]	40	90	150	270	590*	130	-
Density [kg/m^3]	1.4	1.4	1.4	1.4	1.5	1.5	1.5
Absorption capacity	SAP A	SAP A	SAP A	SAP B	SAP C	SAP D	SAF
Mortar spread tests [g/g]	23	24	25	35	-	11	-
Imaging analysis [g/g]	23.9	26.6	28.8	-	-	-	-
Chosen value [g/g]	24	24	24	35	10*	11	19**
Swelling factor [-]	3.26	3.26	3.26	3.68	2.52	2.60	-
Pore characteristics from IA	SAP A	SAP A	SAP A	SAP B	SAP C	SAP D	SAF
d50 [μm]	170	255	410	-	-	-	-
dmed [μm]	46	60	37	-	-	-	-
Average pore diameter [μm]	75	120	140	-	-	-	-
True average pore diameter [μm]	110	170	195	-	-	-	-

*: value provided by TU Dresden; **: value estimated from microscope experiments

5 Observations on sealed hydration of Portland cement

5.1 Introduction

This chapter deals with the effect of SAP on sealed hydration of Portland cement. Plain cement pastes and water-entrained cement pastes were compared with respect to degree of hydration, chemical shrinkage, formation of pore volume and water phase distribution. Thermo gravimetry (TG), mercury intrusion porosimetry (MIP) and nuclear magnetic resonance (NMR) are the key methods applied. The investigation tries to provide answers on two main questions:

- Is there a difference in hydration of plain cement paste compared to water-entrained cement paste provided that the total amount of added water is the same?
- How does the quantitative emptying of the water-filled macropore inclusions look like?

As a first approximation it was assumed that water-saturated SAPs are emptied due to motion of water from SAP into pore space created by chemical shrinkage. Therefore chemical shrinkage rates were adopted from literature and compared to own measurements. In a second step, the retention of water in SAP at early age was determined indirectly by NMR spectrometry.

Information on the degree of hydration and the saturation of pores was further used for modelling of the self-desiccation shrinkage of cement paste presented in chapter 7.

5.2 Materials and methods

5.2.1 Portland cement

Table 5.1 reports on the phase distribution of the used Portland cement of type 42.5 R from Schwenk KG, Allmendingen. The values were obtained by chemical analysis (Bogue) and X-ray diffraction (XRD). Basically, the sum of minor constituents in Portland cement is limited to 5% by mass. Appendix 5 on page 189 reports on the XRD results in detail.

Table 5.1: Phase distribution of used Portland cement

Clinker phase		C ₃ S	C ₂ S	C ₃ A	C ₄ AF	Rest
Bogue	[% by mass]	58	11.8	9.3	8.9	12.0
XRD	[% by mass]	65.1	7.7	8.4	7.9	10.9

The cement had a density of 3124 kg/m³ and a specific surface by Blaine of 337 m²/kg. The maximum amount of chemically bound water $(w_n/c)_{\max}$ was calculated on the basis of the phase distribution determined by XRD. The used equation refers to [Hansen 1986]:

$$(w_n/c)_{\max} = 0.230 \cdot (C_3S) + 0.320 \cdot (C_2S) + 0.317 \cdot (C_3A) + 0.368 \cdot (C_4AF) \quad (5.1)$$

It was found that one g of fully hydrated cement can bind approximately 0.23 g of water chemically. This result is in good agreement with values reported in [Taylor 1997]. Further, it was assumed that one g of fully hydrated cement binds approximately 0.19 g of water physically [Stark & Wicht 2000]. The loss on ignition of the plain cement between 105°C and 1050°C was found to yield 2.25%. All analysis results are to be understood as average values of two cement samples tested.

5.2.2 Preparation of cement paste

Table 5.2 lists all cement pastes investigated within the present experimental series. Mixing was done by a 5 l epicyclic mixer. SAPs were added dryly pre-mixed with 1500 g of cement. The scheduled amount of tap water was added during 90 s of mixing with a speed of 170 rpm. Subsequently, agglomerates were scrapped from the wall of the bowl and mixing was continued for 120 s, whereof for the first 60 s the speed was increased to 360 rpm.

Table 5.2: Specifications of tested Portland cement pastes

Cement paste	(w/c) _{basic} [-]	(w/c) _e [-]	SAP size _{dry} [μm]	SAP [m.-% by c]	Air [Vol.-%]	ρ_{CP} [kg/dm ³]
Ref 0.50	0.50	-	-	-	0.6	1.84
SAP A 0.42+0.08	0.42	0.08	63-125	0.33	0.7	1.83
Ref 0.42	0.42	-	-	-	0.4	1.91
SAP A 0.36+0.06	0.36	0.06	63-125	0.25	0.5	1.90
Ref 0.36	0.36	-	-	-	0.3	1.99
SAP A 0.30+0.06	0.30	0.06	63-125	0.25	1.2	1.97
SAP D 0.30+0.06	0.30	0.06	< 250	0.55	0.8	2.02
Ref 0.30	0.30	-	-	-	0.5	2.08

After mixing, the fresh cement paste was filled in test glasses with a diameter of 12 mm clamped to the vibrating table turned on. The filled test glasses were plugged and stored in a water bath at $20 \pm 0.2^\circ\text{C}$. After achieving the required age, the hardened cement paste was removed by breaking the glass. The sample was crushed in a mortar and was either tested immediately by thermo gravimetry or prepared by oven-drying at 105°C for mercury intrusion porosimetry.

In case of NMR-spectrometry the fresh cement paste was injected into a special glass tube with an inner diameter of 10 mm. This was done by the use of a flexible hosepipe with 9 mm outer diameter mounted on a 50 ml plastic syringe stuffed with the fresh paste.

5.2.3 Thermo gravimetry (TG) and differential scanning calorimetry (DSC)

Thermo analytical techniques are methods used to study physical properties of materials during changes in temperature. The device used in this series was a Netzsch STA 409 PC. It consists of the following main parts: control unit, furnace, high-precision balance and sample holder with thermocouples including pans. The device allows combined measurements of two methods: differential scanning calorimetry (DSC) and thermo gravimetry (TG). The DSC method determines the heat flow required to increase the temperature of the sample compared to an inert reference as a function of temperature. The required heat flow correlates with the calorific output of the furnace measured as electrical power. Changes in the morphology of the sample are detected by peaks in the recorded DSC signal. Exothermic processes, e.g. crystallization, are indicated by negative peaks as they require more heat flowing to the sample to increase its temperature at the same rate as the reference. By contrast, endothermic processes, e.g. melting, cause positive peaks. The TG method determines the weight loss of a sample applied to a controlled temperature program in relation to an inert reference. The tests performed were simultaneous DSC/TG-measurements aimed on the determination of chemically bound water in hardened cement paste. Table 5.3 reports on the setting of the applied temperature program developed for this purpose. It was assumed that the chemically bound water is driven off at temperatures between 105 and 1050°C . The recorded weight loss within this range was used to calculate the degree of hydration.

Table 5.3: Setting of temperature program

Temperature sequence [°C]	Heating rate [K/min]	Duration [min]	Total time [min]
20 - 85	10	6	6
85 - 105	1	20	26
105	-	60	86
105 - 1050	10	94	180
1050	-	10	190

For each cement paste, measurements were performed at ages of 6, 12, 24, 48, 72 hours and 4, 5, 6, 7, 14, 28, 56, 91 days respectively. About 80 mg of the crushed test material was filled into a corundum pan placed in the sample holder. A second, blank pan was used as reference. During testing, nitrogen gas was supplied to the furnace in order to maintain an inert atmosphere.

5.2.4 Method for the determination of chemical shrinkage

Chemical shrinkage of the reference pastes with w/c ratios of 0.30 and 0.42 was measured according to procedure A described in [ASTM C1608-07]. The technique behind the standardized method was developed by Geiker [Geiker 1983]. About 5 g of fresh cement paste were placed on the bottom of a glass vial with 25 mm in diameter and 75 mm in height. The cement paste was covered with a thin layer of water and the vial was filled with paraffin oil free from air bubbles. A rubber stopper with an inserted capillary tube was used to seal the vial. The level of paraffin oil in the graduated capillary tube was observed to the nearest 2.5 μl over a time period of 14 days. The chemical shrinkage rate was calculated by the measured change in volume in relation to the mass of initial cement in the sample. For each measurement two replicate specimens were prepared.

5.2.5 Introduction to nuclear magnetic resonance (NMR) spectrometry

Nuclear magnetic resonance (NMR) spectrometry is an essential analytical method used in the context of structural chemistry. It is based on the nuclear magnetism of atomic nuclei which possess nuclear spins with a spin quantum number not equal to zero, e.g. ^1H or ^{13}C atoms. NMR experiments can be described as a series of radiofrequency (rf) pulses used to manipulate the nuclear spins to provide qualitative and/or quantitative information on the composition of matter [Claridge 1999]. In case of cementitious materials NMR experiments can be used to study water balance during hydration as already demonstrated by Blinc [Blinc et al. 1978].

A nucleus carries charge and, when spinning, possesses a magnetic moment μ according to equation (5.2) where P is the angular momentum and τ is the magnetogyric ratio, which is a constant for any given nuclide. Both μ and P are vector quantities having magnitude and direction.

$$\mu = \tau \cdot P \quad (5.2)$$

When located in an external static magnetic field with magnetic flux density B_0 , the angular momentum of a spin-half nucleus, such as a proton, takes up two possible orientations, either parallel or antiparallel with respect to the static field, the former being of lower energy. As a result of the static magnetic field applied, the nucleus is caused to precess. In doing so, the spin about its own axis depends on the magnetogyric ratio τ and the precession of this axis about the direction of the field is defined by the angular velocity ν , known as Larmor frequency of the nucleus:

$$\nu = \frac{-\tau \cdot B_0}{2\pi} \quad (5.3)$$

Figure 5.1 schematically illustrates the nucleus motion referred to Cartesian co-ordinate frame. NMR occurs when the nucleus changes its spin state due to electromagnetic radiation applied with a frequency that matches with its Larmor frequency. The precessing spin-half nucleus will have a component of its magnetic moment along the z-axis viz the longitudinal component and an orthogonal component in the x-y plane viz the transverse component. After excitation, the magnetization approaches equilibrium condition according to the so-called Boltzmann distribution, i.e. excess of nuclei orientated parallel to the applied field due to lower energy state is achieved. The time that passes until the longitudinal component of the magnetic moment (z-axis) has returned to equilibrium is characterized by the so-called relaxation time T_1 . In fact, T_1 is not a direct measure of time, but rather is the first-order time constant that describes the recovery of magnetization following exponential behaviour. So the relaxation time constant of the transversal component (x-y plane) is designated T_2 .

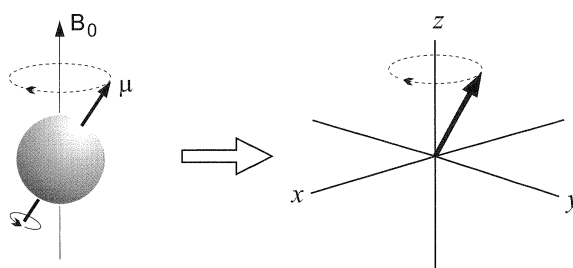


Figure 5.1: Nucleus spinning about its own axis caused to precess about the direction of a static magnetic field applied along the z-axis [Claridge 1999].

In pulsed NMR experiments a time-dependent magnetic field (B_1 field) using radiofrequency (rf) pulses oscillating at the Larmor frequency is applied to induce transitions between energy levels causing NMR to occur. After excitation by rf pulse from the transmitter coil in the direction of the x-axis or the y-axis, respectively, the receiver coil detects all signals emitted from the nuclei. This detected NMR signal is a time-dependent oscillating voltage called free induction decay (FID) and fades as the nuclear spins relax back towards equilibrium. The data acquired is a time domain representation $f(t)$ of the nuclear precession frequencies ω within the sample that needs to be transferred into the frequency domain $f(\omega)$ by Fourier transformation of the general form:

$$f(\omega) = \int_{-\infty}^{+\infty} f(t) \cdot e^{i\omega t} dt \quad (5.4)$$

Figure 5.2 (left) illustrates this procedure. The resonance peak is broader the faster the FID decays and the higher the inhomogeneity of the sample is. The transverse relaxation time T_2 is one of the factors that determine the half-height line width $\Delta\nu_{1/2}$ of the resonance according to equation (5.5), cf. Figure 5.2 (right). The width of the NMR resonance is inversely proportional to T_2^* where T_2 is due to natural transverse relaxation process (spin-exchange factor) and $T_2(\Delta B_0)$ is due to static magnetic field inhomogeneity (inhomogeneity factor).

$$\Delta\nu_{1/2} = 1/\pi T_2^* \quad \text{with:} \quad 1/T_2^* = 1/T_2 + 1/T_{2(\Delta B_0)} \quad (5.5)$$

The inhomogeneity factor is more critical for the higher frequencies and often dominates the line-width of viscous liquids. For ideal liquids both T_1 and T_2^* are even the same. But for porous

solids T_2^* is shorter than T_1 in the vast majority of cases. Integration of the resonance leads to the magnetization intensity I . This signal intensity corresponds with the number of the respective spinning nuclei. Observation of I over sample age reveals possible quantitative change.

At this point it should be noted that longitudinal relaxation causes loss of energy from the spins which is transferred into the surroundings in form of heat and, thus, is an enthalpic process. In contrast, transverse relaxation is entropic since it is caused by swapping of energy between neighbouring spins changing their orientation.

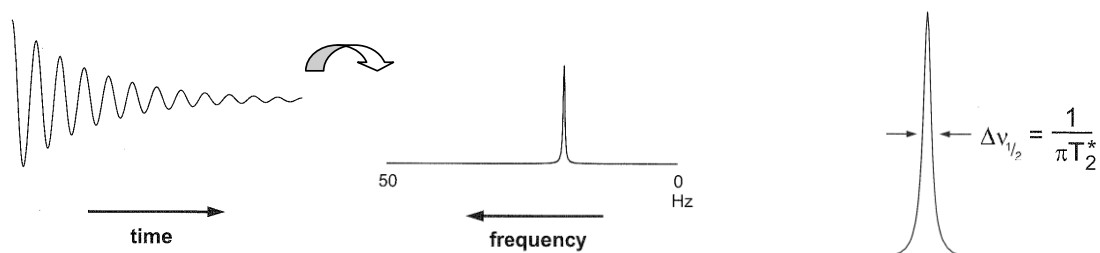


Figure 5.2: Fourier transformation of time domain FID into frequency domain (left) and definition of the half-height linewidth of a resonance (right) [Claridge 1999].

To give quantitative statements on water balance in cementitious material, ^1H atoms are excited and relaxation is observed, e.g. [Nestle et al. 2002]. Fortunately, the relaxation time depends on the binding state of water, i.e. free (capillary) and physically bound (gel) water are distinguishable from chemically bound water. The NMR signal can be made blind to the latter since its relaxation time is much shorter. The observation of the signal intensity and the values of T_1 and T_2 during cement hydration provides information on water consumption and change in pore structure.

In literature some studies on detection of IC water are available. The prerequisite for quantifying IC water is that an ^1H -NMR signal from the water inside the internal reservoir is detectable and even more it differs in its relaxation time from the signal of free and physically bound water coexisting in the cement matrix. Following this idea, transition of water from various internal reservoirs into the hydrating cement matrix was studied by low-field NMR relaxometry: In [Friedemann et al. 2006] alginate gel used as IC agent was investigated, in [Friedemann et al. 2008] water-saturated lightweight aggregates were examined and in [Friedemann et al. 2009] the application of carboxylates and sulfates of polysaccharides for IC was evaluated. In these studies the recorded magnetization decay curves were analyzed using inverse Laplace transformation yielding the transverse relaxation time distributions. The mean transverse relaxation times were obtained separately for both free and physically bound water and IC water. Shiftings of the T_2 values over time were interpreted as indication for densification of the pore-structure in analogy with [Halperin et al. 1994] and revealed water transition from the internal source to the matrix. Similarly, IC due to acrylic acid-based SAP was studied by low-field NMR relaxometry in [Nestle et al. 2009]. The results are addressed further on in the context of discussion of own NMR results.

5.2.6 Description of own NMR measurements

In this thesis, high-resolution relaxometry measurements were performed at room temperature (about 25°C) using the device Bruker AVANCE DPX 300. The static magnetic flux density B_0 yielded 7.275 Tesla, which corresponds to a proton resonance frequency of 300 MHz. The longitudinal relaxation time T_1 was monitored using the inversion recovery pulse sequence illustrated in Figure 5.3. The sequence starts with a first π -pulse that is applied to invert the initial spin population by 180° . The magnetization vector therefore is aligned with the negative z -axis, shrinks

gradually back towards the x-y plane, passes this plane and turns into full recovery position along the positive z-axis. Unfortunately, magnetization along the z-axis is not directly observable. To account on this, a 90° pulse follows the initial inversion in order to place the vector back into the x-y plane after variable delay time. Repeating this measurement with increasing delay, starting from zero delay, one is allowed to observe relaxation of the spins. At delay of 5 times T_1 longitudinal magnetization recovery is 99.3% [Claridge 1999], i.e. the maximum signal will be detected again (this time positive).

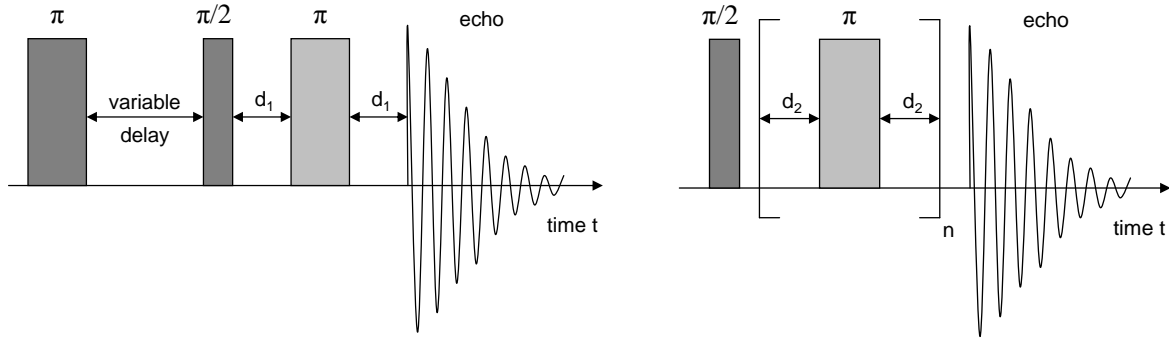


Figure 5.3: Pulse sequence used for detection of free water plus water absorbed by SAP (left) and CPMG-pulse sequence applied for isolating the signal of water in SAP (right).

The second part of the pulse sequence is a so-called spin-echo sequence [Hahn 1950]. It was applied in order to exclude chemically bound water from the NMR signal due to delayed data acquisition. In doing so, some of the magnetization vectors will locally move ahead of the mean vector after the 90° pulse is applied, i.e. during the first delay time d_1 , while some others will lack behind. Due to the following 180° pulse the vectors are rotated back towards the $-y$ -axis in order to fully refocus after the second period of d_1 . This approach will remove the contribution of magnetic field inhomogeneity $T_2(\Delta B_0)$ from the transverse relaxation time T_2^* and leads to the natural relaxation time constant T_2 , cf. equation (5.5). In pre-tests the optimal d_1 delay was found to yield $50 \mu\text{s}$. So the pulse width of the π -pulse was set to $34 \mu\text{s}$ and to $17 \mu\text{s}$ for the half- π pulse.

In case of plain pastes 10 variable delays of up to 3 s were adjusted to determine the magnetization recovery curve as shown exemplarily by Figure 5.4 (left). Each data point represents the average of 8 measurements. The right diagram reports on the 10 respective frequency domains obtained from Fourier transformation. To observe slower relaxing SAP water, 16 variable delays of up to 7 s were applied in case of SAP-modified paste. As a result, the time resolution of the NMR experiment was 12 min for reference paste and 16 min for SAP-modified paste. T_1 was obtained from multi-exponential fitting of the signal intensities according to equation (5.6) for plain paste and equation (5.7) for water-entrained paste. The second addend in equation (5.7) is due to the signal of water in SAP and overlays the component from pore water. It is:

$$I(t) = I_0^1 \cdot (1 - 2 \cdot e^{-t/T_1}) \quad (5.6)$$

$$I(t) = I_0^1 \cdot (1 - A^1 \cdot e^{-t/T_1^1}) + I_0^2 \cdot (1 - A^2 \cdot e^{-t/T_1^2}) \quad (5.7)$$

with $-1 < I < 1$, where I_0^1 and I_0^2 [-] correspond to equilibrium magnetization, A^1 and A^2 [-] are stretching factors and T_1^1 and T_1^2 [μs] is the relaxation time of longitudinal magnetization of free and physically bound water and water in SAP, respectively.

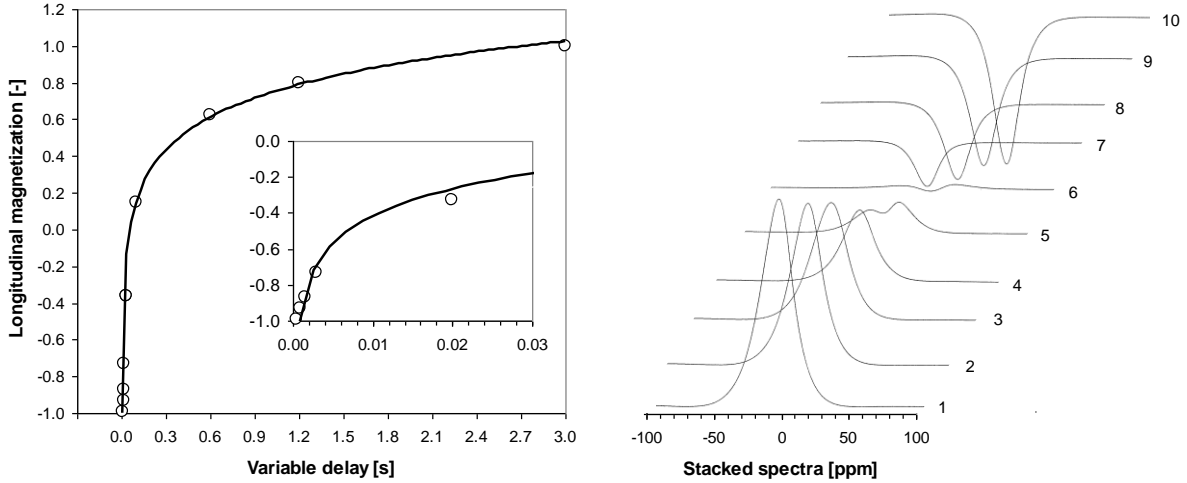


Figure 5.4: Longitudinal magnetization as a function of variable delay of plain cement paste (left) and corresponding frequency domains obtained from Fourier transformation (right).

The stretching factors should equal 2 since recovery starts from inverted magnetization but can be made variable to account for experimental imperfections. These are inaccurate recording of equilibrium magnetization and imperfect initial inversion caused by inaccurate π -pulse application.

Fitting was done by a so-called SIMPLEX optimization algorithm. With regard to T_1 determination the algorithm was found to be stable. However, it was unstable with regard to determination of I . So the first idea that the relation between the signal intensities of the first and the second component of equation (5.7) leads to the ratio of free and physically bound water to water in SAP was discarded. But, an alternative experimental setup made it possible to separately study the intensity of the signal emitted from water in SAP and further to deduce the saturation of SAP as a function of age. To this end, the Carr-Purcell-Meiboom-Gill (CPMG) sequence in analogy with Figure 5.3 (right) was applied. The sequence consists of a 90° pulse followed by a train of n spin-echos with delay d_2 . Large d_2 causes error from diffusion of spins into neighbouring regions that are subjected to slightly different field magnetization during the sequence and therefore cannot be fully refocused. To minimize the effect of diffusion on T_2 determination, d_2 was kept rather short, i.e. $50 \mu\text{s}$. It should be noted here that T_2 of free and physically bound water was found to yield about 0.8 to 8 ms, which is in good agreement with values reported in literature [Nestle et al. 2007]. In contrast, T_2 of water in SAP was found to yield about 100 ms. Further, it is assumed that 5 times T_2 assures complete magnetization recovery. Thus, it can be estimated that a total delay of 20 ms, that is 200 repetitions of the single echo, is sufficient to completely mask the signal component of free and physically bound water.

Unfortunately, also the transverse magnetization intensity I could not be used for quantitative statement on the relation between free and physically bound water and water in SAP. There is loss of phase coherence by natural transverse relaxation during delay that cannot be refocused by spin-echo. That means at onset of data acquisition, the intensity of the observed magnetization of free and physically bound water will have decayed according to the natural T_2 time constant, independent on field inhomogeneity. Even at shortest delay possible ($n = 1$) the signal loss of transverse relaxation from free and physically bound water is about 10% according to:

$$\frac{I(t = 2 \cdot d_2)}{I_0} = e^{-\left(\frac{2 \cdot d_2}{T_2}\right)} = e^{-\left(\frac{100}{1000}\right)} \approx 0.90 \quad \text{with} \quad I(t) = I_0 \cdot e^{-\left(\frac{t}{T_2}\right)} \quad (5.8)$$

5.3 Results and discussion

5.3.1 Non-evaporable water content and degree of hydration

Figure 5.5 shows an excerpt of the DSC-TG results of paste SAP A 0.42+0.08. The TG curves are presented in the left diagram and the corresponding DSC signals are shown in the right diagram. The first peak in the DSC signal belongs to the loss of free and physically bound water, i.e. the area enclosed correlates with the recorded weight loss. The peak is decreasing with increasing the age of the test sample. In return, the second peak is higher the older the sample is. It indicates the decomposition of calcium hydroxide formed during hydration which passes off in the range 420 to 490°C:



At temperatures between 550 to 950°C calcium carbonate is decomposed according to equation (5.10). The corresponding weight loss should be the same independent of the test sample's age since no carbon dioxide from air is able to form carbonates during sealed hydration. But it is the decomposition of carbon dioxide initially present in the dry cement powder that contributes to weight loss.



The hold time of 60 min at 105°C was implemented in the applied temperature program to ensure that free and physically bound water are dried out completely before temperature increase proceeds. The content of non-evaporable water was assumed to be equivalent to the recorded weight loss Δm_s of the test sample between 105 and 1050°C. By considering the loss on ignition of the plain cement Δm_c , the mass fraction of cement c in the sample and the maximum amount of chemically bound water, i.e. 0.23 g/g, the degree of hydration a was calculated as follows:

$$\alpha = [(\Delta m_s - \Delta m_c \cdot c) / 0.23] / c \quad (5.11)$$

At the end of test, i.e. after 190 minutes, the residual mass is more or less equal to the relative mass fraction of cement in the sample, which is about 65% in case of paste SAP A 0.42+0.08. Further information on thermoanalytical data of reacted cement is reported in [Taylor 1997].

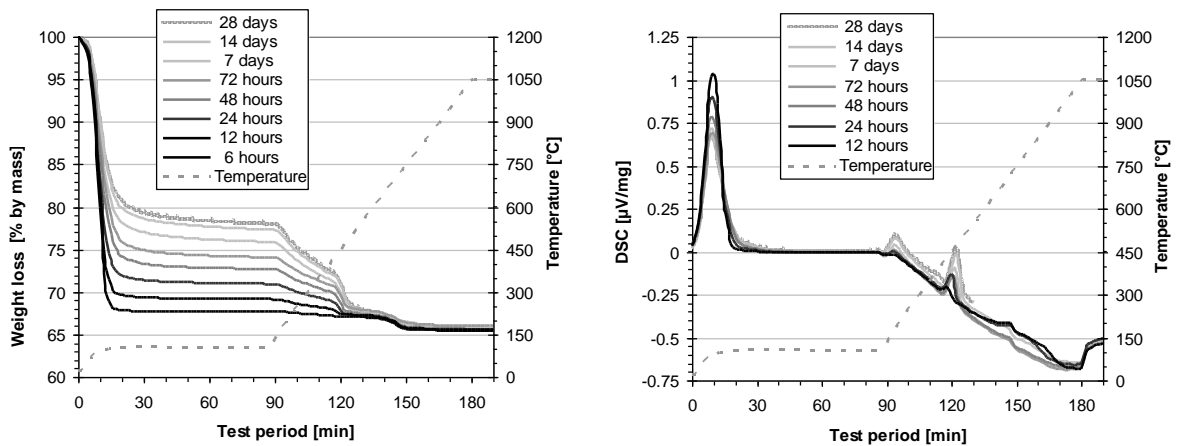


Figure 5.5: DSC-TG test results of cement paste SAP A 0.42+0.08. Left: Weight loss of test samples vs. test period. Right: Corresponding DSC signals vs. test period.

Figure 5.6 reports on the degree of hydration calculated according to equation (5.11). For reasons of clarity, the results are split in two diagrams. The left diagram provides the degree of hydration of pastes with total w/c ≤ 0.36 and the right diagram shows results of pastes with total w/c ≥ 0.36 . Within the first two days hydration is almost the same for all pastes. Afterwards, hydration proceeds slower the lower the w/c ratio is. It is the lack of free water that slows down hydration as the speed of hydration is controlled by diffusion of free water molecules through the layer of hydration products covering the reacting cement grains. The curves of pastes Ref 0.42 and Ref 0.50 drift apart after the first three days have passed. The discrepancy between reference pastes is

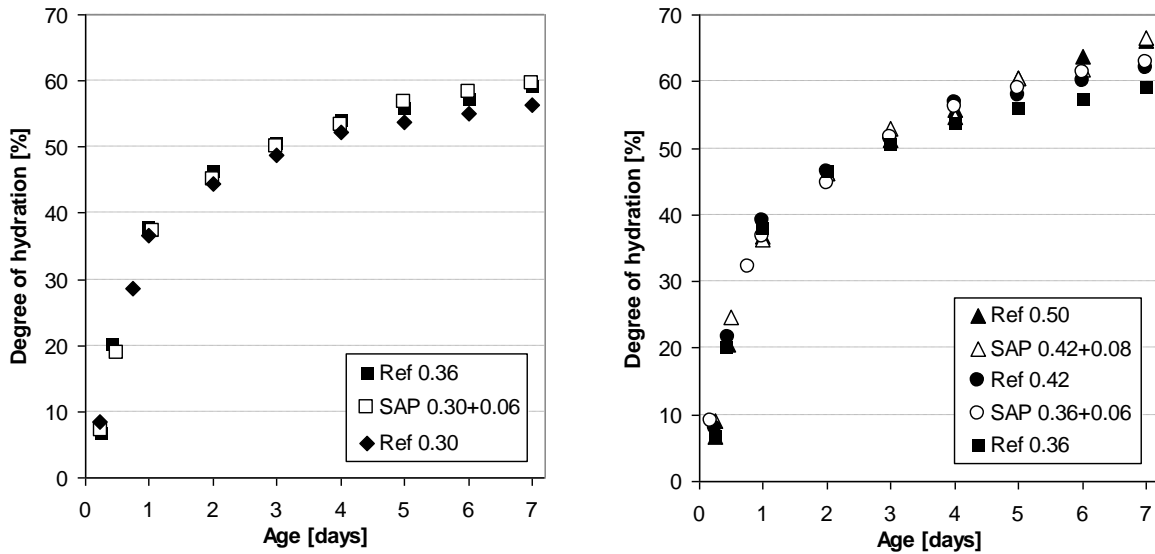


Figure 5.6: Degree of hydration up to 7 days. The diagrams apply to sealed hydration at 20°C.

more pronounced at higher age. After 91 days the degree of hydration is about 86% for w/c of 0.50, 80% for w/c of 0.42 and 71% for w/c of 0.36, cf. Figure 5.7. The diagrams show that for both reference pastes and water-entrained cement pastes hydration is more or less the same provided that the total amount of added water is the same. That means, concerning cement hydration, it is not relevant whether the water comes from SAP or was ordinarily added. This finding is in good agreement with Powers' theory [Jensen & Hansen 2001b]. However, a closer look reveals

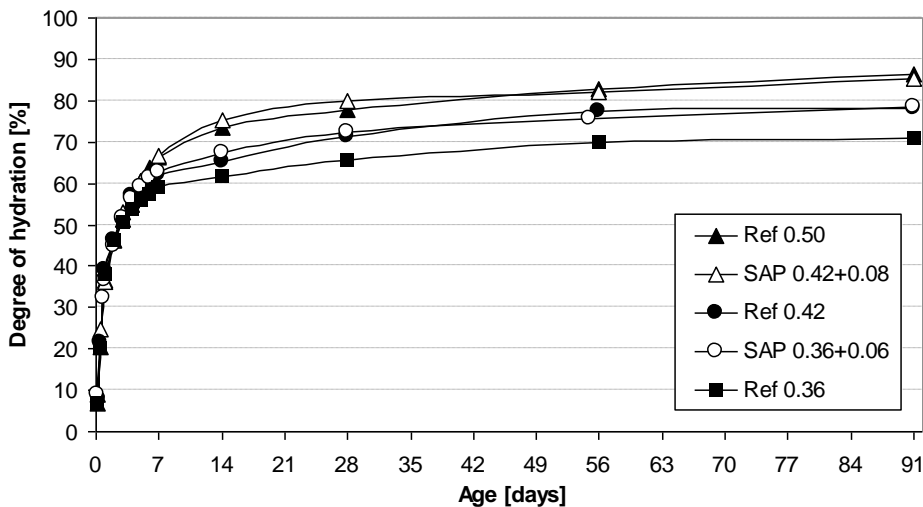


Figure 5.7: Degree of hydration up to 91 days. The diagram applies to sealed hydration at 20°C.

that water entrainment may slightly promote hydration in the first 4 weeks. Afterwards the degree of hydration of reference pastes seems to be slightly increased compared to corresponding SAP-modified pastes. This leads to the assumption that water supply by SAP A works well at early age, but loses efficiency as the degree of saturation becomes less.

5.3.2 Chemical shrinkage

Figure 5.8 shows the chemical shrinkage of pastes Ref 0.30 and Ref 0.42 measured by the glass vial method. It should be pointed out that the presented values apply to water storage of an open system and provide only a rough estimate of the development of chemical shrinkage at sealed condition. The value of 0.035 ml per g cement measured after 10 days for Ref 0.30 is in good agreement with results reported in literature, e.g. [Esteves 2009]. The difference to paste Ref 0.42 might be explained by insufficient water uptake due to the denser microstructure of paste Ref 0.30, i.e. reduced ability of water to penetrate the sample at higher age. If the degree of hydration of sample Ref 0.42 at 14 days is considered to be 80% instead of 68% measured at sealed storage, the chemical shrinkage at complete hydration will amount to ca. 6.1 ml per 100 g cement. This value corresponds with a global volume reduction of 8.7%.

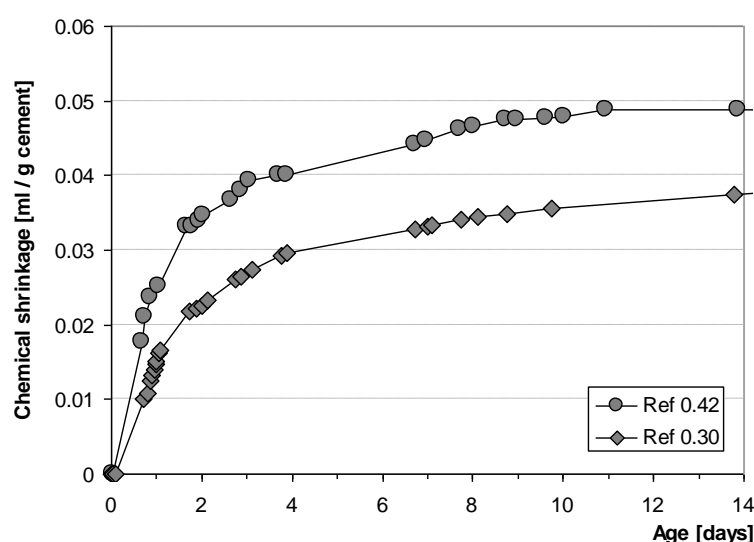


Figure 5.8: Chemical shrinkage of Ref 0.30 and Ref 0.42 measured acc. to [ASTM C1608-07].

In Table 5.4 the chemical shrinkage is reported separately for each clinker phase at the state of complete reaction as given by Fontana [Fontana 2007]. In terms of the clinker phase composition obtained from chemical analysis and X-ray diffraction presented in Table 5.1 on p. 60, chemical shrinkage amounts to 5.9 and 5.8 ml/100 g cement reacted, respectively. However, the calculation does not take into account chemical shrinkage of the remaining mass-share of 12.0% and/or 10.9%, see Table 5.1. But it is known that the reaction of minor constituents causes chemical shrinkage as well as e.g. the formation of ettringite. On this account, in the following the chemical shrinkage of the used cement is referred to Powers' value, i.e. 6.4 ml/100 g cement reacted.

Table 5.4: Chemical shrinkage of clinker [Fontana 2007]

Clinker phase	C ₃ S	C ₂ S	C ₃ A	C ₄ AF
[ml / 100g]	4.8	3.6	17.5	11.5

5.3.3 Expected saturation of SAP pores

As a first approximation it was expected that SAPs are emptied due to chemical shrinkage by the “demand-supply” mechanism: pore space created from hydration is instantaneously filled with IC water since water consumption in the paste is always from big pores to small pores according to the thermodynamic principles. For this purpose, the measured amount of chemically bound water was used to calculate the volumes of gel water, capillary water, water in SAP and chemical shrinkage on the basis of Powers’ theory, see appendix 3. In doing so, the sealed cement paste is regarded as an open system with low w/c ratio where the maximum degree of hydration a_{max} [-] is given by equation (5.12), where p [-] is the initial porosity, i.e. the volume share of mixing water:

$$\alpha_{max} = \frac{p}{1.12 \cdot (1-p)} \quad (5.12)$$

In consequence, a_{max} is 0.852 for SAP 0.30+0.06 and 1.0 for SAP 0.36+0.06, respectively. According to the concept of Jensen & Hansen [Jensen & Hansen 2001b], the amount of entrained water necessary to obtain a_{max} equals the volume of chemical shrinkage V_{CS} [-] at a_{max} :

$$V_{CS}(\alpha = \alpha_{max}) = \rho_c \cdot 6.4 \cdot 10^{-5} \cdot (1-p) \cdot \alpha \quad (5.13)$$

where ρ_c [kg/dm³] is the density of cement, i.e. 3.124.

The volume of chemical shrinkage $V_{CS}(a_{max})$ corresponds to w/c of 0.054 in case of SAP 0.30+0.06 and to w/c of 0.064 in case of SAP 0.36+0.06, respectively. To simplify matters, the amount of entrained water was assessed to be the same for both pastes, viz $(w/c)_e = 0.06$. That means that, on the one hand, all the IC water of paste SAP 0.30+0.06 is consumed before hydration stops. On the other hand, paste SAP 0.36+0.06 spares IC water even when the cement has reacted completely as illustrated by Figure 5.9. Since it can be assumed that a_{max} will not be reached in practice, the volume of entrained water seems to be overdimensioned in both pastes. There is to say nothing of paste SAP 0.42+0.08 which, of course, has higher volume of SAP pores than pore space created from hydration.

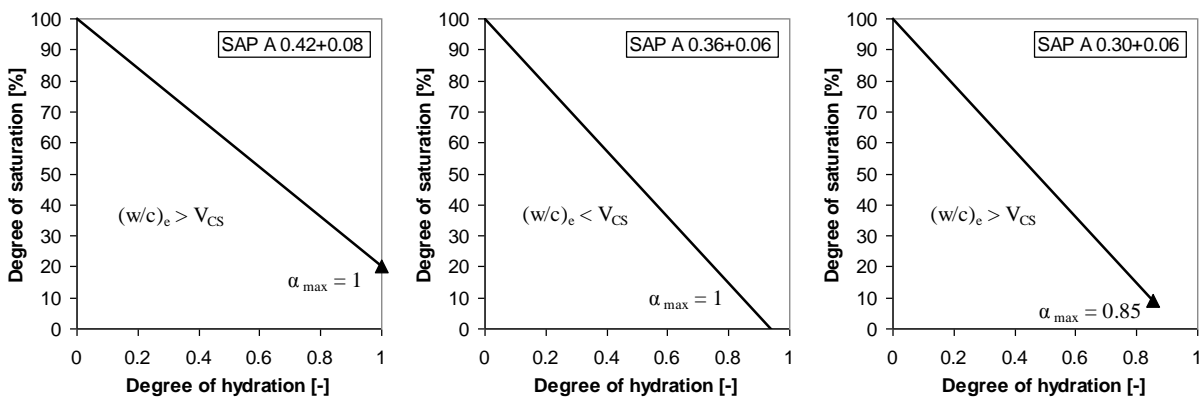


Figure 5.9: Expected saturation of SAP pores as a function of degree of hydration.

Figure 5.10 reports on the volumetric distribution of water phases, chemical shrinkage and water in SAP up to an age of 7 days. The expected saturation of SAP pores is also shown in the diagrams. After 7 days of sealed hydration the saturation of SAP pores ranges between 47% for paste SAP A 0.42+0.08 and 33% for paste SAP A 0.36+0.06. The volume of air voids in the fresh cement paste is neglected in the calculation.

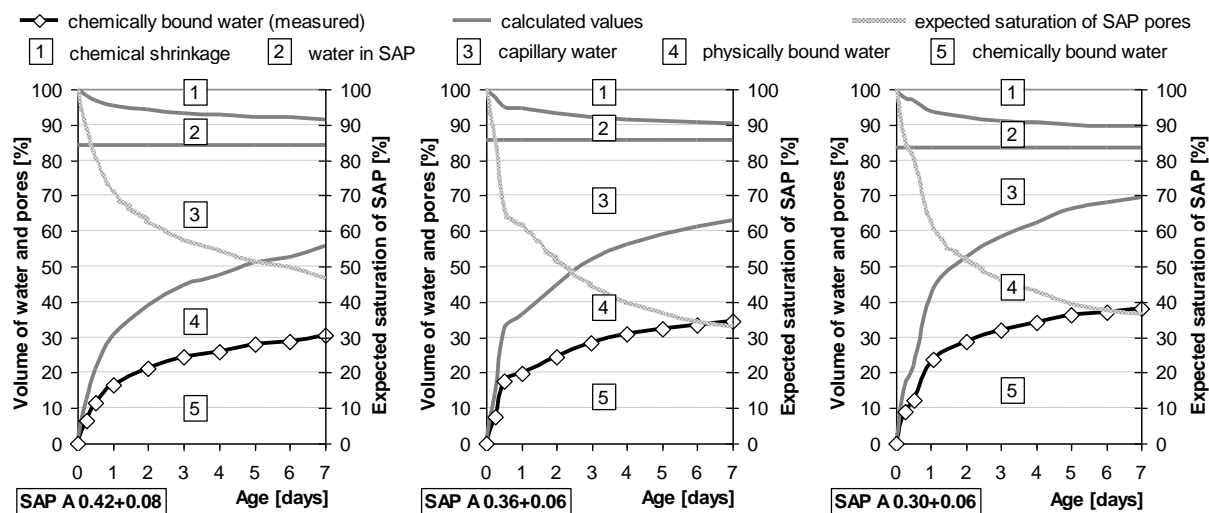


Figure 5.10: Volumetric distribution of water phases in water-entrained cement pastes up to an age of 7 days of sealed hardening at 20 °C and expected saturation of SAP A pores.

Compared to simulation results of Wyrzykowski [Wyrzykowski et al. 2011] who modelled water migration in CEM I mortar at w/c of 0.30+0.04, the saturation degree of SAP A 0.30+0.06 at age of 7 days is rather high. But, as mentioned already, the entrained water content of $(w/c)_e$ of 0.06 is far too high provided that practical hydration degrees are considered.

5.3.4 NMR experiments

A logarithmic representation of the T_1 relaxation time of free and physically bound water as a function of age is reported in Figure 5.11 (left). The T_1 values found in the range 30 to 50 ms at very early age and < 10 ms at the age of 24 hours correspond well with values cited in literature, e.g. [Nestle et al. 2007], even though T_1 is about a factor of 3 to 10 shorter at low proton NMR frequencies of < 1 MHz. A decrease in w/c ratio leads to a decrease in T_1 , indicating smaller pore size or, more precisely, smaller water layer thickness surrounding the cement grains. SAP-modified pastes were fitted by two-exponential regression. However, the T_1 relaxation time constant determined for free and physically bound water is quite similar to all SAP-modified pastes.

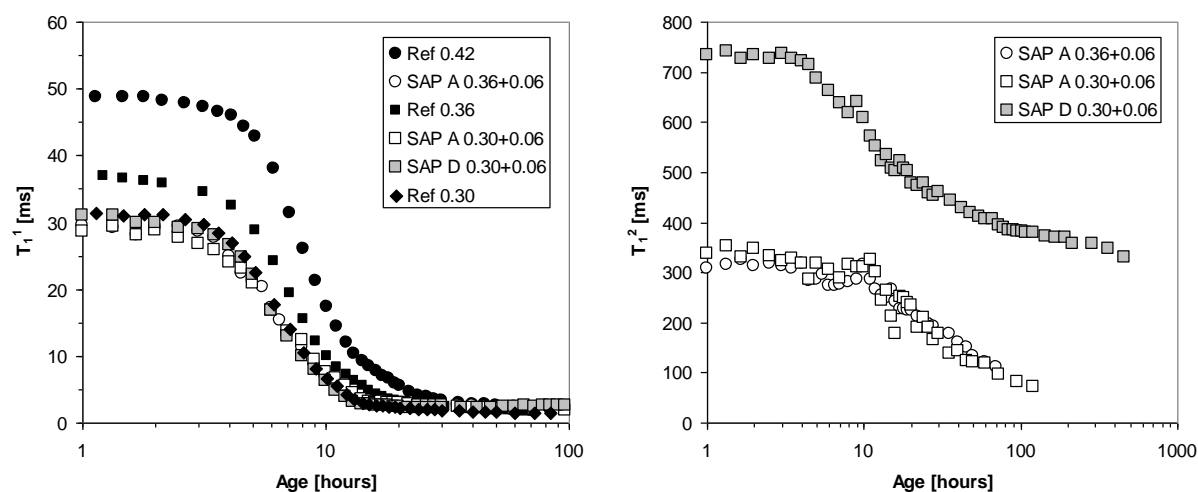


Figure 5.11: Logarithmic representation of longitudinal relaxation time constant of free and physically bound water (left) and water in SAP (right).

The T_1 values of the signal emitted from water in SAP, see Figure 5.11 (right), are one order of magnitude higher and decrease slower with age compared to T_1 of free and physically bound water. T_1 of water in SAP D is double that of water in SAP A. It is a result of larger particle size of SAP D. The T_1 relaxation time curves exhibit bending after initial period of constant values. So do the magnetization curves of the brutto signal normalized to the intensity of the first measurement at the age of 30 min presented in Figure 5.12 (left). The crucial point where the tangents of the flat part and the steep part of the logarithmic curve intersect marks the end of the dormant stage, and, thus, the onset of accelerated hydration. When decreasing the w/c ratio the intersection point occurs earlier. It was found to range between 3.5 hours for paste Ref 0.30 and 6 hours for paste Ref 0.42. Indeed, the occurrence of the intersection point is in good accordance with the setting times of the pastes reported later in chapter 6.

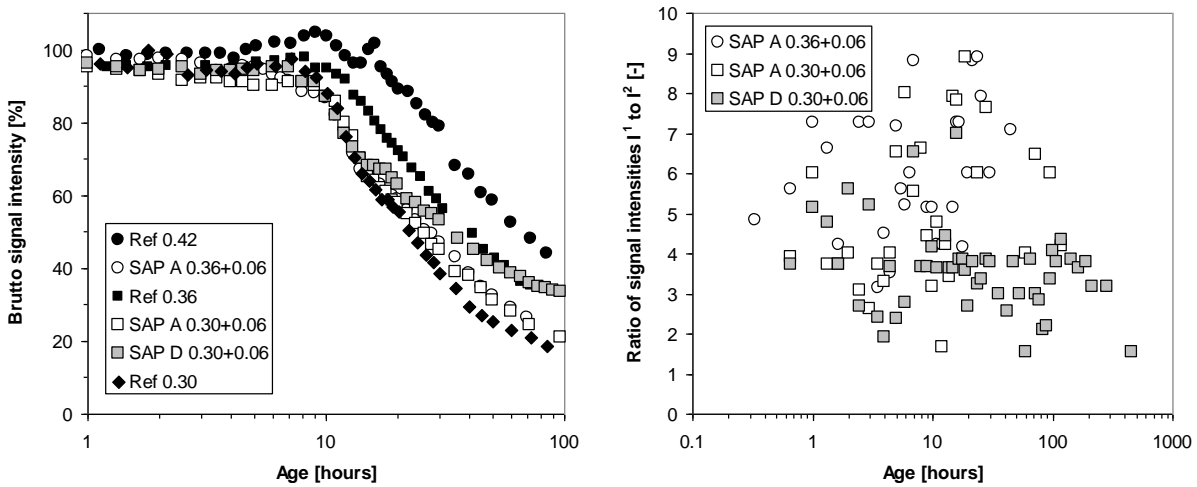


Figure 5.12: Normalized brutto signal intensity of longitudinal relaxation (left) and ratio of signal intensity of free and physically bound water to IC water (right) as a function of age.

Appendix 5 provides information on the T_1 and the normalized magnetization intensity curve of paste Ref 0.36 obtained due to application of inversion recovery pulse sequence with and without spin-echo sequence. It can be seen that both T_1 and signal intensity are smaller if excitation was executed without spin-echo. As a result, initial values of T_1 were found to yield up to 30% less. The difference is caused by attenuation of the signal from magnetic field inhomogeneity removed by refocusing locally displacements of the magnetization vector due to spin-echo.

As mentioned already, the used SIMPLEX optimization algorithm was not stable enough to determine the longitudinal magnetization intensity. Further, signal of faster relaxing free and physically bound water is partly lost during delay to onset of data acquisition. It is in analogy with the error of transverse magnetization intensity proposed by equation (5.8) on page 66. This weakness in experimental setup causes error in the quantitative prediction of the ratio of signal fraction from free and physically bound water to signal fraction from water in SAP. The ratio should equal 5 in case of w/c of 0.30+0.06 and 6 in case of w/c of 0.36+0.06. Actual values scatter much as can be seen from Figure 5.12 (right). Further, the drop in normalized signal intensity is falsified. For example in case of Ref 0.36 it drops below 40% in the first three days. This would correspond to hydration degree of $> 100\%$, which is of course an impossible value. For this reason the second part of the NMR study was addressed to filter the magnetization signals from the FID in order to separate the signal emitted from water in SAP. The results of this approach are presented in the following.

5.3.5 Water release of SAP

Figure 5.13 reports on the transverse magnetization intensity of paste Ref 0.36 in dependence on the total delay produced by the CPMG sequence that consisted of n spin-echos with single delay d_2 of $50 \mu\text{s}$. The intensity is normalized to the value of first measurement found at total delay of 0.1 ms , corresponding to $n=1$. Even at delay of 0.3 ms , more than 50% of the signal intensity is lost. The total inter-echo time of 5 ms is sufficient to mask almost all the signal produced by free and physically bound water. Consequently, data acquisition of the filtered SAP signal started with total delay of 5 ms to the 90° excitation pulse.

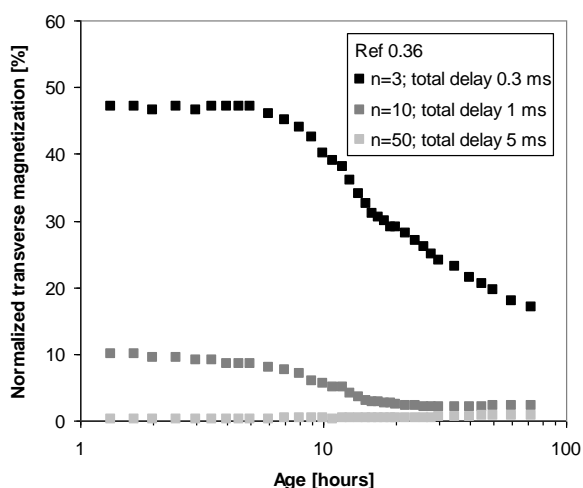


Figure 5.13: Transverse magnetization intensity (Ref 0.36) in dependence on n , number of spin-echos applied through CPMG sequence, normalized to initial signal intensity at $n=1$.

Figure 5.14 reports on the filtered transverse magnetization intensity of water in SAP for pastes SAP A $0.30+0.06$ and SAP D $0.30+0.06$. The intensity values are normalized to the first signal intensity obtained 30 min after water addition. Of course, the absolute mass of water absorbed is not provided by the experiment, but the curves represent the saturation degree of SAP. Since T_2 of water in SAP was about 100 ms , the transverse magnetization loss during the delay of 5 ms to onset of data acquisition is expected to be rather small as can be seen from appendix 5.

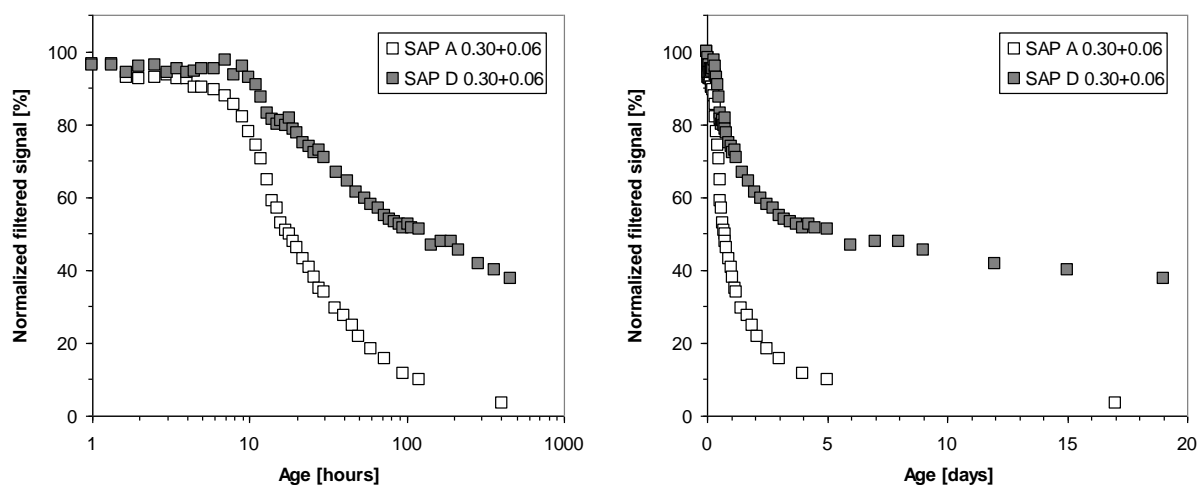


Figure 5.14: Transverse magnetization intensity of isolated signal emitted from water in SAP A and SAP D as a function of age in hours as log scale (left) and days (right).

Obviously, water release of SAP A and SAP D is different. After 7 days the signal intensity of water in SAP D is reduced down to 50%. However, the expected saturation degree is about 37%, as evident from Figure 5.10. There are two possible explanations: either SAP D absorbed more water than expected, i.e. > 11 g/g, or the chemical shrinkage is less than expected, i.e. < 6.4 ml per 100 g cement reacted. In any case, SAP D entrained too much water. In contrast, saturation degree of SAP A is much less compared with expected values. After 7 days signal intensity was only 10%. At the age of 17 days the signal was 3%. Later on no signal was detectable anymore.

Assuming the volume of chemical shrinkage according to Figure 5.10 and drainage of SAP pores according to the demand-supply mechanism, SAP A absorbed less water than the amount of 24 g/g estimated in chapter 4. In case of SAP A 0.30+0.06, water absorption rather corresponds to $(w/c)_e$ of 0.043, which is equal to an absorption capacity of SAP A of 17 g/g. The difference may result from a possible dependency of water absorption on the w/c ratio. But it is a fact that mortar spread tests, which were performed at w/c of 0.50, overestimated the water absorption of SAP A in paste produced at low w/c ratio. Indeed, the value of 24 g/g was confirmed by imaging analysis performed on microsections produced from pastes with w/c of 0.42, but the analysis might be prone to error from contrast adjustment, see section 4.3.4.

In [Nestle et al. 2009] water release of SAP into hydrating cement matrix made of Portland cement (CEM I 52.5 R) at w/c of 0.30+0.04 was faster compared with results presented in this dissertation. The transfer of water from SAP into matrix was finished at least after 2 days. Curve fitting of the measured magnetization decay was achieved by a sequential regression due to superposition of a Gaussian and four exponential components. They postulated that there are two different water populations in SAP related to wall relaxation and diffusive exchange of water inside SAP and the matrix.

Another method for quantifying water release of SAP is neutron tomography. In [Trtik et al. 2010] this method was applied on Portland cement (CEM I 42.5 R) paste made at w/c of 0.25. The emptying process of two single SAP particles, each of about 2 mm in swollen state, was monitored during the first days of hydration. After 20.5 hours the SAP particle was nearly empty.

5.3.6 Weaknesses of the NMR experiment

The main experimental imperfections that impair the significance of the test results are listed in the following:

- 1) Due to high frequency width of excitation the monitored signal of water component shows broad amplitude. It is a weak point specific to the experimental setup used here. High resolution NMR (B_0 was 300 MHz) is usually applied for structural analysis of matter. For the study of water components in cement paste, low-field NMR with high rf-performance is preferable since the signal of water is sharper.
- 2) As mentioned already, inaccurate pulse application leads to imperfect initial inversion of magnetization. This source of error is closely related with error from inaccurate recording of equilibrium magnetization.
- 3) Diffusion of spins into neighbouring regions that are affected by slightly different field magnetizations during the measurement which cannot be refocused by spin-echo.
- 4) Magnetic field variations inside the sample are intensified due to paramagnetic or even ferromagnetic particles present in OPC [McDonald et al. 2005]. This is why usually white Portland cement produced from low-iron raw materials is used in most NMR experiments.

5.4 Conclusion and outlook

In this chapter sealed hydration of OPC was investigated on plain and water-entrained pastes produced at w/c of 0.30 to 0.50 using thermogravimetric analysis, chemical shrinkage test and NMR relaxometry measurement. Thermogravimetry was applied to determine the non-evaporable water content for estimation of the development of hydration degree. The following conclusions can be drawn:

- 1) The hydration degree was found to develop universally the same for the first 24 hours, whatever the w/c ratio was. Afterwards, hydration slowed down with decreasing the w/c.
- 2) SAP seems to promote hydration, if at all, at early age. At higher age the plain control mix with same total water content even possessed slightly higher degree of hydration.

In simple terms, hydration is nearly the same for both plain and water-entrained cement paste provided that the total amount of water is the same. That means water supplied by SAP A does not influence hydration differently from ordinarily added water.

The high-resolution relaxometry measurements were aimed on the observation of water release from SAP into the hydrating cement matrix. To this end, a CPMG pulse sequence was applied that filtered the signal emitted from SAP. In doing so, the time lag between excitation of spins and onset of data acquisition was 5 ms. The results produced another important finding:

- 3) Drainage of SAP A was faster compared with SAP D. At the age of 7 days saturation of SAP A was 10% whereas saturation degree of SAP D was about 50%. It was explained by less amount of water entrained in paste SAP A 0.30+0.06, i.e. $(w/c)_e$ probably was 0.04 due to water absorption of SAP A of 17 g/g instead of 24 g/g.

However, in the following chapters the absorption capacity of SAP A still refers to the value of 24 g/g predicted by mortar spread tests in chapter 4. The assumption that water absorption capacity of SAP A depends on w/c ratio requires validation. To this end, absorption and release of water should be examined in pastes of various w/c ratios through imaging technique like neutron tomography.

6 Autogenous phenomena studied on cement paste

6.1 Introduction

Experimental series were performed in order to demonstrate the effects of SAP addition on autogenous phenomena in hardening Portland cement paste. Measurements of autogenous deformation, internal relative humidity, elastic material properties and pore solution analysis are presented and discussed within this chapter. The examinations attempt to attain two goals:

- 1) The demonstration of the potential of SAP as admixture for internal curing.
- 2) The provision of data for modelling of the self-desiccation shrinkage of Portland cement paste as a function of the internal relative humidity.

The calculation of the self-desiccation shrinkage follows an approach presented by Lura [Lura 2003]. It was refined by the continuous determination of the dynamic elastic material properties. The study on IC of high performance mortar, following in chapter 7, banks on the findings and conclusions presented at the end of this chapter.

6.2 Materials and methods

6.2.1 Tested cement pastes

Table 6.1 lists all cement pastes investigated within the present experimental series. Three reference pastes with w/c ratios of 0.30, 0.36 and 0.42 and six SAP-modified pastes with w/c ratios of 0.30+0.06 and 0.36+0.06 were investigated. The volume of entrained water corresponds to the amount theoretically needed to prevent complete self-desiccation. Three types of SAP were used: SAP A, SAP B and SAP D. The cement used was of type CEM I 42.5 R. Batches of 5 liter were mixed by means of a 10 liter epicyclic Hobart mixer. The total mixing time was 5 min.

Table 6.1: Specifications of tested Portland cement pastes

Cement paste	w/c _{basic} [-]	w/c _e [-]	SAP size _{dry} [μm]	SAP [m.-% by c]	Air pores [% by vol.]	ρ _{CP} [kg/dm ³]
Ref 0.42	0.42	-	-	-	0.4	1.91
SAP A 0.36+0.06	0.36	0.06	63-125	0.25	0.5	1.91
SAP B 0.36+0.06	0.36	0.06	<500	0.17	0.7	1.90
SAP D 0.36+0.06	0.36	0.06	<250	0.55	1.5	1.88
Ref 0.36	0.36	-	-	-	0.3	1.99
SAP A 0.30+0.06	0.30	0.06	63-125	0.25	1.2	1.97
SAP B 0.30+0.06	0.30	0.06	<500	0.17	1.0	2.00
SAP D 0.30+0.06	0.30	0.06	<250	0.55	0.8	2.02
Ref 0.30	0.30	-	-	-	0.5	2.08

6.2.2 Measurement of autogenous deformation

Free autogenous deformation of cement paste was measured according to [ASTM C1698-09] using corrugated tubes made of polyethylene as a mould. The watertight moulds with circa 420 mm in length and an outer diameter of 29 ±0.5 mm were closed by two circular end plugs after they had been filled with fresh cement paste. During filling the moulds were supported by a

rigid plastic tube which was clamped to the vibrating table turned on. To avoid bleeding and expansion due to reabsorption of bleed water at early age, as suspected by Mohr & Hood [Mohr & Hood 2010] for paste systems with w/c above 0.30, all filled moulds were rotated in a rotational device by 10 rpm for at least three hours. At the latest one hour before setting was expected, rotation was stopped in order to prevent impacts on microstructure build up and the risk of postponed setting. Afterwards the moulds were placed horizontally in self-built dilatometers as shown in Figure 6.1. One end plug was fixed with glue in the centre point by point to the tip of a screw embedded in the steel plate. At the free end the longitudinal deformations were measured by linear variable differential transformers (LVDT) of type SRINDH50 [Rinder 2002] with a repeatability of $<0.15 \mu\text{m}$. The specimens of each cement paste were prepared in duplicate and were measured simultaneously. A third specimen was prepared in order to monitor the temperature development due to heat of hydration in the paste by means of a temperature sensor placed in the centre of the mould.



Figure 6.1: Connection detail (free end) of corrugated tube mould embedded horizontally in dilatometer for autogenous deformation measurement.

6.2.3 Measurement of relative humidity

The change in internal relative humidity of the cement pastes during sealed hydration was determined by the Rotronic HygroLab3 station shown in Figure 6.2. The station was equipped with an AW-DIO sensor for water activity and temperature measurements. About 12 g of hardened cement paste fragments were filled into a plastic tray placed in the hermetic measuring cell of the station. Initially, the fresh cement pastes had been cast into another plastic tray right after mixing and remained sealed until they were removed and crushed for testing. The measurements took place in a thermostatically controlled laboratory at $20 \pm 0.2^\circ\text{C}$. Assuming thermal equilibrium between sensor and sample, the measured relative humidity (RH) is regarded as internal relative humidity. In the first hours after water addition, the RH measurements are affected by the development of heat of hydration in the paste. Condensation may occur if the sample has a higher temperature than the sensor itself. On this account, the RH measurements every 10 minutes were started 24 to 36 hours after mixing. The sensor was calibrated and, if necessary, adjusted before each measurement. Three saturated salt solutions with known constant RH in the range 80 to 95% RH were used. In doing so, the global uncertainty of the sensor is expected to yield less than $\pm 1\%$ RH.



Figure 6.2: Rotronic station equipped with AW-DIO sensor for RH measurement.

6.2.4 Determination of elastic material properties

The elastic material parameters were determined by using the testing device FreshCon. FreshCon was developed for the continuous monitoring of the hardening of cementitious materials in the 1990s at the University of Stuttgart [Reinhardt et al. 2000] and was later patented [Reinhardt et al. 2001]. The method behind FreshCon is ultrasound (US) transmission testing [Große 2005]: short ultrasonic pulses are sent into the test material and recorded on the opposite. With known distance between transmitter and receiver and by determining the travel time of the signal, the velocities of the pulses can be calculated. The present version of the device is shown in Figure 6.3 on page 79. It allows combined measurements with pressure (P) and shear (S) waves [Krüger et al. 2011]. Due to the innovative application of shear wave sensors it is possible to determine the dynamic elastic material parameters. To this end, two containers made of perspex, one for measuring pressure waves and one for measuring shear waves, were filled with about 500 cm³ of fresh cement paste. The containers resemble the setup recommended by RILEM [Rilem 2011]. Each container was equipped with two P-sensors or with two S-sensors, respectively. The sensors were assembled flexible by means of pre-tensioned spins fixing them opposite to each other in circular perforations on the container walls. Coupling was arranged by thin polyimide foil (0.25 μm). The sensor distance was 50 mm. The continuous monitoring was aimed on the first 7 days of hardening. Under the assumption that cement paste is homogenous and isotropic, the dynamic elastic material parameters can be calculated on the basis of the P-wave velocity v_p [m/s], the S-wave velocity v_s [m/s] and the density of the fresh cement paste ρ_{CP} [kg/dm³] according to:

$$\mu_{dyn} = \frac{1/2 \cdot v_p^2 - v_s^2}{v_p^2 - v_s^2} \quad (6.1)$$

$$E_{dyn} = \frac{(1 + \mu_{dyn}) \cdot (1 - 2\mu_{dyn})}{(1 - \mu_{dyn})} \cdot v_p^2 \cdot \rho_{CP} \cdot 10 = (2 + 2\mu_{dyn}) \cdot v_s^2 \cdot \rho_{CP} \cdot 10 \quad (6.2)$$

$$G_{dyn} = \frac{E_{dyn}}{2 + 2\mu_{dyn}} = v_s^2 \cdot \rho_{CP} \cdot 10 \quad (6.3)$$

with μ_{dyn} = Poisson's ratio [-], E_{dyn} = dynamic modulus of elasticity (Young's modulus) [GPa] and G_{dyn} = dynamic shear modulus [GPa].

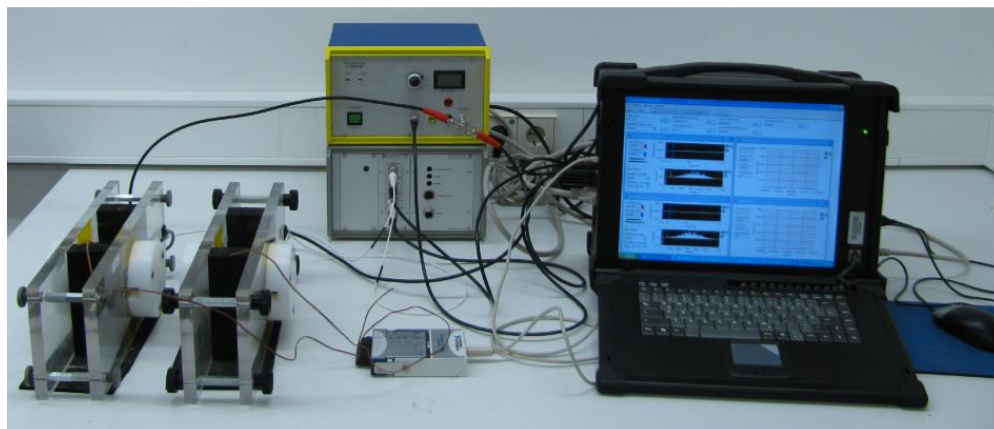


Figure 6.3: Picture of the FreshCon system.

In general, one sensor acts as US-transmitter connected to the amplifier generating the short ultrasonic pulses, while the other sensor picks the onsets of the transmitted signals. The generation of the US wave is done by a piezoelectric crystal. By applying a short voltage pulse, the crystal contracts and a sound wave is generated. The difference in the crystals for P-wave and S-wave generation is in the direction of polarization and the geometry of the crystals: P-waves show propagation in the direction of polarization, the material therefore is compressed. S-waves show oscillation perpendicular to the direction of wave propagation. As a result, shear stresses are induced into the material. The frequency of the used signals is in the lower ultrasonic range, since the sound absorption of the test material increases with higher frequencies [Herb 2003]. In case of P-waves, transmitter and receiver worked with a center frequency of 500 kHz. In case of S-waves, broadband sensors with a centre frequency of 250 kHz were used. Incident and transmitted pulses are analogous signals, digitalized by means of an A/D converter and subsequently recorded by hard disk. The entire system is triggered automatically. The recording intervals were set to 5 min at the very beginning of the test and to 10 min afterwards. The recorded signals were evaluated with respect to the speed of the primary wave transmitted by the test material. To this end, the onset times of the transmitted signals were determined by software SmartPick [Krüger & Lehmann 2010].

Besides the travel time, which was of most interest here, frequency, amplitude and wave shape are the parameters detectable. Unfortunately the shear wave transducer also induces a pressure wave into the hardening paste. This pressure wave precedes and superimposes the shear wave onset and prevents the direct S-wave onset determination. On this account the time signal has to be first transformed into a time-frequency domain by means of a continuous wavelet transformation. In doing so, a scalable mother wavelet is moved along the time axis and its correlation with the signal is calculated. The distance on the time axis between the first and the second extreme value of the obtained wavelet graph finally leads to the onset time of the S-wave [Krüger et al. 2011].

The picker for the determination of the P-wave onset is based on the Akaike Information Criterion (AIC) [Akaike 1974], adapted for ultrasonic signals [Kurz et al. 2005]. A detailed description of the S-wave and the P-wave picker and the evaluation processes involved is presented in [Krüger & Lehmann 2010].

6.2.5 Mechanical properties

In addition to the non-destructive determination of elastic material parameters, compressive and flexural strength were determined on prisms (40 x 40 x 160 mm³) at the age of up to 91 days. The static modulus of elasticity at ages of 3 and 28 days was determined on cylindrical specimens of 100 mm in diameter and 200 mm in height according to [DIN 1048-5 1991]. All specimens were sealed by adhesive vapour barrier foil until testing.

6.2.6 Pore solution analysis

Pore solutions of cement pastes Ref 0.30, Ref 0.36 and SAP 0.30+0.06 were investigated with respect to concentrations of Na⁺, K⁺ and Ca⁺⁺ ions and surface tension. Ion chromatographic analysis was carried out on eluates obtained 2 hours, 3, 7 and 28 days after mixing. About 500 g of fresh paste were filtered by means of a water-jet-pump to extract pore solution at early age. At later age, pore solution was extracted from three cylindrical specimens of about 250 ml in volume by using a special die loaded in a universal testing machine with up to 3000 KN. The extracted pore solutions of at least 10 ml each were flushed by argon and sealed in a special cup.

The surface tension of the pore solution was determined experimentally by means of contact angle measurements using the device Dataphysics STA 20. The surface tension of a liquid γ_L [mN/m] is the sum of the polar component γ_L^p and the nonpolar component γ_L^n :

$$\gamma_L = \gamma_L^p + \gamma_L^n \quad (6.4)$$

Droplets of 3 μ l in volume were placed automatically on two planar substrates. Substrate S1 was coated with gold and substrate S2 was coated with chrome. The side profiles of the droplets were photographed by CCD-camera and the contact angles β_1 and β_2 [°] were evaluated computer-based. Besides the surface tension of the liquid, the free surface energy of the substrate γ_S [mN/m], split in polar component γ_S^p and nonpolar component γ_S^n , defines the contact angle. For the determination of the surface tension of the pore solution, the following equation system has to be solved for γ_L^p and γ_L^n :

$$\left\{ \begin{array}{l} \gamma_L (1 + \cos \beta_1) = 2 \left[\sqrt{\gamma_L^p \cdot \gamma_{S1}^p} + \sqrt{\gamma_L^n \cdot \gamma_{S1}^n} \right] \\ \gamma_L (1 + \cos \beta_2) = 2 \left[\sqrt{\gamma_L^p \cdot \gamma_{S2}^p} + \sqrt{\gamma_L^n \cdot \gamma_{S2}^n} \right] \end{array} \right\} \quad (6.5)$$

with $\gamma_{S1} = \gamma_{S1}^p + \gamma_{S1}^n$ = free surface energy of substrate S1 coated with gold [mN/m] and $\gamma_{S2} = \gamma_{S2}^p + \gamma_{S2}^n$ = free surface energy of substrate S2 coated with chrome [mN/m].

Since the free energy of the substrates was unknown, the contact angle of two reference liquids was measured previously and equation (6.5) was solved for γ_{S1} and γ_{S2} . The liquids used as reference were demineralized water (polar) and diodomethane (nonpolar). The surface tension was adopted from [Randler 2001] as reported in Table 6.2.

Table 6.2: Surface tension of reference liquids [Randler 2001]

Reference liquid	γ_L [mN/m]	γ_L^p [mN/m]	γ_L^n [mN/m]
Demineralized water (H ₂ O)	72.8	51.0	21.8
Diodomethane (CH ₂ I ₂)	50.8	2.3	48.5

6.3 Results and discussion

6.3.1 Determination of time zero

The time zero t_0 is defined as the time at which the cement paste develops sufficient structure to enable tensile stress transfer [Weiss 2003]. It is expected that autogenous deformations measured before time zero do not influence stress development and early age cracking, which is why they are considered no further, i.e. the deformation curves have to be zeroed at this time. There is no question that active restraint systems appear to provide the most direct measure of the real time zero by determining the onset of the tensile stress development as done e.g. in [Pirskawetz et al. 2011]. Since the necessary test equipment was not available, some alternative options for the experimental estimation of time zero were investigated:

- time of setting (Vicat), i.e. t_{set}^{ini} and t_{set}^{fin} ,
- time of maximum deformation rate, i.e. t_{as}^0 ,
- time when the turning point in the P-wave velocity curve occurs, i.e. t_{tp}^0 ,
- time when the dynamic shear modulus exceeds 0.1 GPa, i.e. t_{Gdyn}^0 .

The most common method is the determination of the setting times. However, in this study the reference pastes were zeroed at time of maximum deformation rate according to [Fontana 2007]. This method is expected to meet the real time zero the closest, not least because it is derived from one and the same specimen. The maximum deformation rate is equal to the turning point of the deformation curve as shown exemplarily for paste Ref 0.30 in Figure 6.4 (lower diagram). The deformation rate increases at the beginning due to fast development of hydration which is accompanied by high chemical shrinkage. Afterwards the plastic cement paste starts to form a solid skeleton and gains in stiffness. As a result the deformation resistance is increasing, which is reflected in a decrease of the deformation rate. As from that point in time the rigidity of the paste is expected to be sufficient to enable the transfer of tensile stresses. The gain in stiffness is also visible in the P-wave velocity curve (upper diagram). The turning point of the curve was found to be in good agreement with the turning point in the deformation curve. It should be noted that the P-wave velocity curves at hand all exhibited turning points, but its occurrence is not mandatory. In addition, the setting times of the reference pastes found by the Vicat test correlated quite well with time zero. At last, an empirical correlation between the initial set and the time when the dynamic shear modulus exceeds the value of 0.1 GPa was found. It is due to the fact that shear stresses are transmitted in solid matter only. The value of 0.1 GPa indicates that the cement paste has already set and constitutes a rigid body.

Table 6.3: Setting in hours

Experiment	FreshCon	Vicat set needle		Dilatometer
Time criteria	$G_{dyn} > 0.1 \text{ GPa}$	Initial set	Final set	Max. def. rate
Ref 0.42	6.4	7.0	8.2	7.7
SAP A 0.36+0.06	6.5	5.8	7.4	-
SAP B 0.36+0.06	-	6.8	7.7	-
SAP D 0.36+0.06	5.6	5.5	7.1	-
Ref 0.36	5.3	5.3	5.8	6.0
SAP A 0.30+0.06	5.7	5.2	6.2	-
SAP B 0.30+0.06	-	5.7	6.3	-
SAP D 0.30+0.06	-	4.6	5.1	-
Ref 0.30	4.2	4.3	4.9	5.0

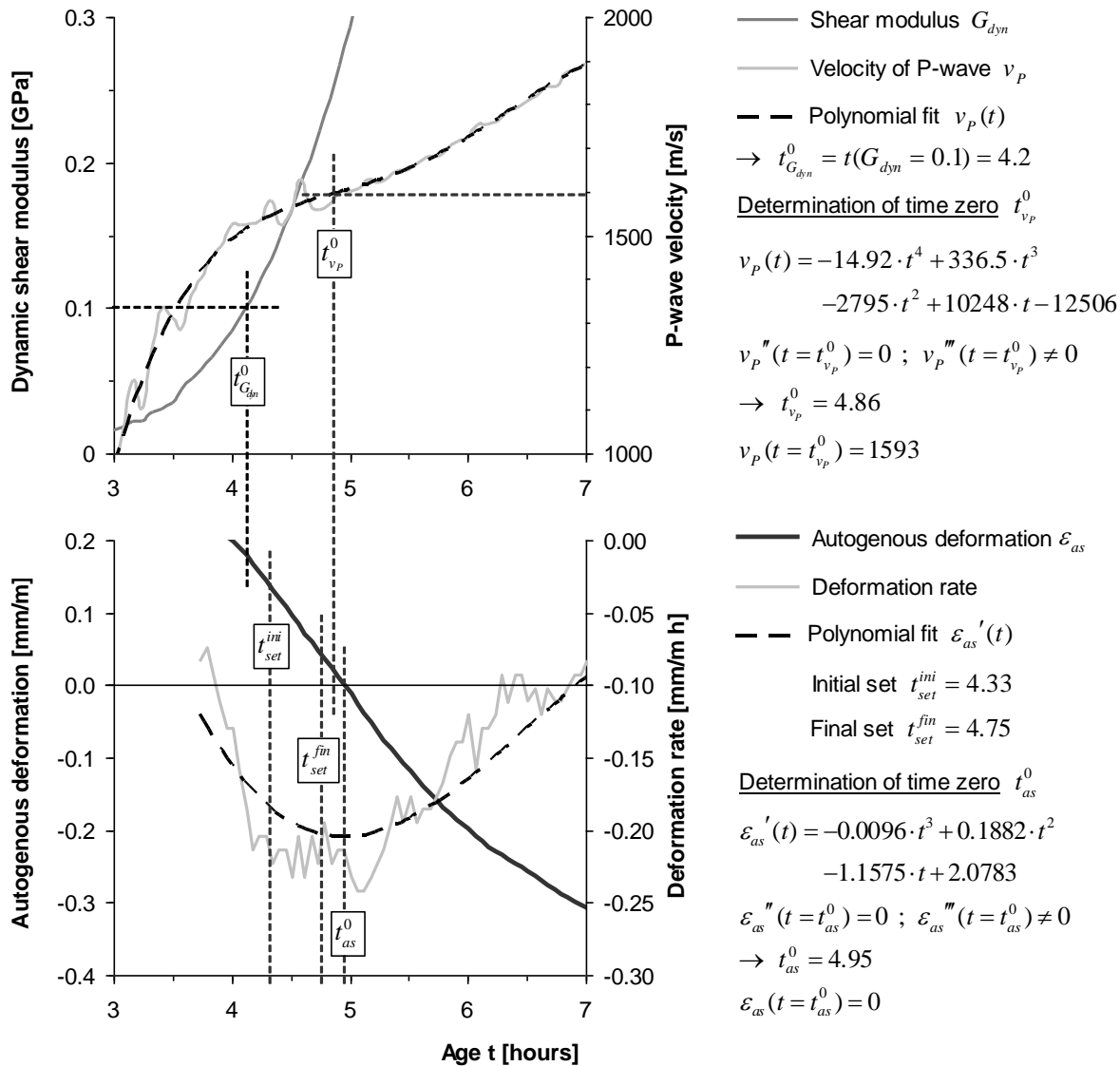


Figure 6.4: Options for the estimation of time zero demonstrated for paste Ref 0.30.

The deformations of SAP-modified pastes were zeroed at time of first expansion, which was in the first 6 to 9 hours after water addition. Since expansion takes place at the same time with chemical shrinkage, swelling can occur after setting only, i.e. when the reaction products are formed within a solid skeleton.

6.3.2 Autogenous deformation

In Figure 6.5 to Figure 6.7 the autogenous deformations of the cement pastes are shown as a function of age. Each curve is the average of two replicates. For reasons of better comparability the curves of the reference pastes recur in all diagrams. The deformations of the reference pastes were zeroed at time of maximum deformation rate. The SAP-modified pastes were zeroed at first occurrence of expansion. The initial shrinkage deformation until time zero (not shown in the diagrams), which occurred for both, plain and water-entrained cement pastes, is due to chemical shrinkage, i.e. before setting chemical shrinkage and autogenous deformation may be identical. After setting, chemical shrinkage results mainly in internal voids, i.e. chemical shrinkage may be 50 times larger than autogenous deformation on a volume basis [Jensen & Hansen 2001a].

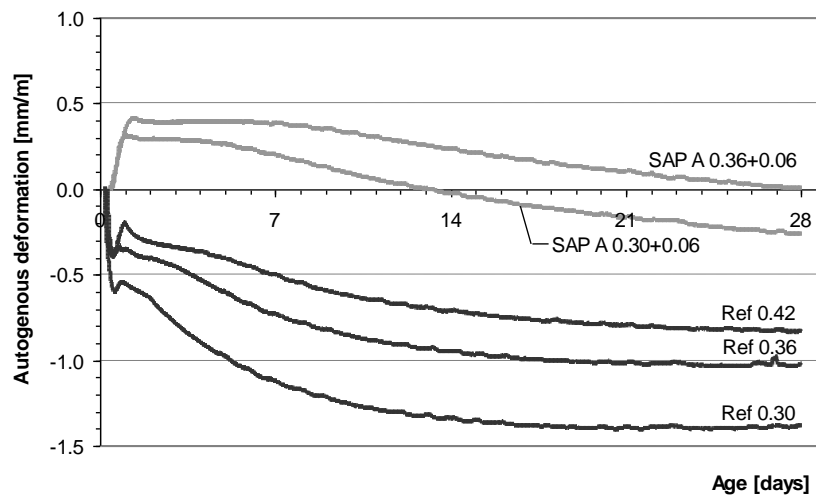


Figure 6.5: Autogenous deformation vs. age of reference and SAP A-modified pastes.

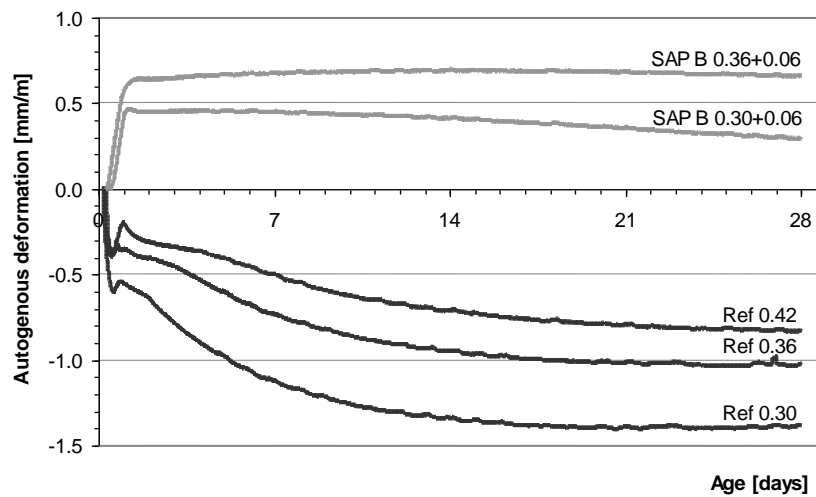


Figure 6.6: Autogenous deformation vs. age of reference and SAP B-modified pastes.

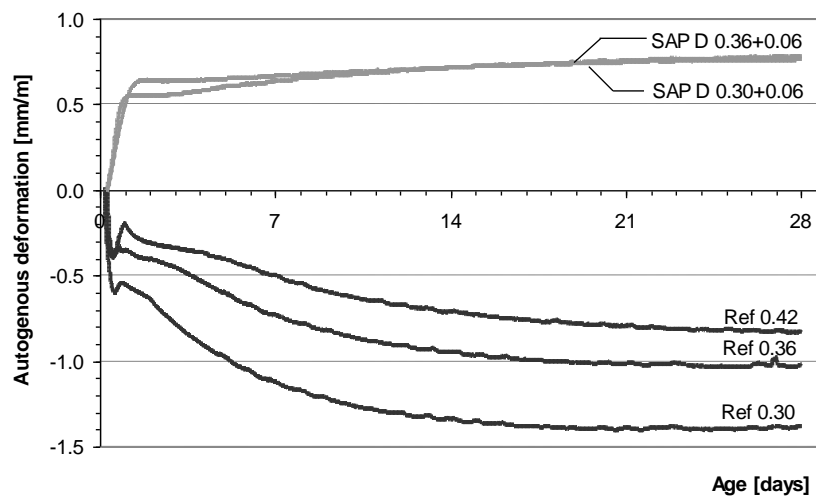


Figure 6.7: Autogenous deformation vs. age of reference and SAP D-modified pastes.

All three reference pastes show high autogenous shrinkage. Of course, shrinkage is increasing with decreasing the w/c ratio: At the age of 28 days shrinkage amounts to 820 μ strain for Ref 0.42, 1020 μ strain for Ref 0.36 and 1380 μ strain for Ref 0.30. However, approximately 15 to 16 hours after mixing, the shrinkage rates of reference pastes are temporarily decreased. For a short period of 6 to 10 hours the deformation even turns into expansion. It might be a result of thermal dilation caused by heat of hydration that counteracts autogenous shrinkage. But for paste Ref 0.30 with highest heat development, the maximum difference compared to the ambient temperature in the laboratory was found to yield approximately 4 K, as shown in Figure 6.8. The ingress of 4 K can not be solely responsible for the hump in the graphs, especially because the maximum of expansion occurred delayed to the peak in temperature. It is reabsorption of bleed water that is expected to contribute to expansion of reference pastes (section 2.3.5). Bleeding was observed primary on specimens that were prepared for the Vicat test. But also the corrugated mould specimens might have been subject to bleeding, since rotation was stopped at the latest 1 hour before setting. With higher w/c ratio, bleeding was stronger. Further, modified formation of portlandite and/or ettringite might have counteracted autogenous shrinkage as well [Sant et al. 2011]. However, the SAP-modified pastes did not show bleeding.

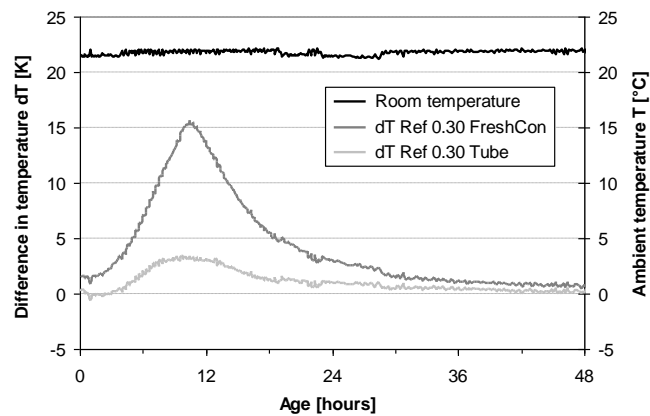


Figure 6.8: Ambient temperature measured in the laboratory and heat increase of paste Ref 0.30 in corrugated tube and FreshCon container.

Water entrainment had a substantial impact on the autogenous deformation after setting. SAP addition induced initial expansion of about 300 to 650 μ strain as a result of provision of internal curing water. This effect is comparable to expansion of neat cement paste cured in water. So the total volume of cement paste increases with increasing degree of hydration when external water may enter the paste [Brouwers 2004]. It is interesting that the initial expansion is even increasing by at least 120 μ strain within the following 4 weeks in case of SAP D whereas it turns into shrinkage after a short period of constant deformation in case of SAP A and SAP B, respectively. Once the SAP-modified paste starts to shrink, the deformation curve tends to run parallel to the curve of the reference paste with same total water content. Obviously, SAP D prevented autogenous shrinkage the most effective. Already Jensen [Jensen & Hansen 2002] found stable expansion for at least 4.5 months. In contrast, SAP A and SAP B are not able to prevent self-desiccation shrinkage permanently. In doing so, SAP A performs even worse than SAP B. Possible reasons for insufficient longterm curing are:

- 1) The amount of entrained curing water is less than expected.
- 2) The curing zone of IC water is too small.
- 3) The IC water is retained in the polymer too long.

The last two reasons seem somewhat incongruous since the SAP A modified paste with the worst outcome possesses the smallest spacing of SAP inclusions. Last but not least, the fact that water retention by SAP may withstand self-desiccation of the surrounding matrix is improbable. Indeed, the most plausible cause for insufficient longterm curing is an insufficient amount of IC water. Already in [Jensen & Hansen 2002] it is reported that reduced amounts of entrained water are not effective for longterm prevention of autogenous shrinkage. Even though initial expansion is also induced by small amounts of SAP, shrinkage follows the earlier the smaller the volume of entrained water is. The NMR measurements on paste SAP A 0.30+0.06 indicated that SAP A obviously entrains less water than expected, see chapter 5. This seems to hold true for chemically related type SAP B, too. The comparison to results with NMR shows that the onset of shrinkage is linked to the point in time when the water in SAP is depleted. This gives rise to self-desiccation resulting in self-desiccation shrinkage. As stated in chapter 5.3.4, SAP A probably absorbed 17 g/g corresponding to $(w/c)_e$ of 0.045 (SAP A 0.30+0.06) instead of the accepted $(w/c)_e$ of 0.06. Further it was presumed that increasing $(w/c)_{\text{basic}}$ leads to an increase of the absorption capacity of SAP A. So the expected water absorption capacity of 24 g/g was estimated by mortar spread tests at w/c of 0.50. This would explain why the paste SAP A 0.36+0.06 shows later onset of shrinkage compared with SAP A 0.30+0.06, although the IC water was expected to be exhausted earlier, see chapter 5.3.3.

6.3.3 Literature review on efficiency of IC

Schröfl [Schroefl et al. 2012] found that different types of SAP with same amount of initially entrained water do not necessarily mitigate autogenous shrinkage with the same success. They explained this phenomenon with different abilities of SAP to retain water. Their strain measurements performed on mortars were accompanied by tea bag tests which were used to observe the absorption and desorption behaviour of various SAP in synthesized pore solution. Schröfl claims that less effectiveness of IC is linked to a pronounced liquid release of the respective SAP after initial absorption in the tea bag test, i.e. before setting. This liquid release was not observed for SAP that completely prevented autogenous shrinkage. Still, the question remains what happens to water that is released back into the fresh paste? The underlying assumption should be that in the proximity of the macropore inclusion, the w/c ratio of the bordering paste is partially increased.

However, the measurements reported by Schröfl were aimed on the first 7 days of sealed hardening, i.e. the period when most of the SAP-modified pastes investigated here were reliably spared from autogenous shrinkage as well. Information on the long-term behaviour is not available. If SAP A did suffer from water release prior to setting, NMR measurements would have revealed it. Hence, early release of curing water can be excluded for the pastes under examination.

6.3.4 Change of internal relative humidity

The development of internal relative humidity with age of cement paste is shown in Figure 6.9. The curves represent the RH measured after an equilibrium between sensor and sample was reached. To avoid condensation of the sensor, measurements were started 24 hours after casting, i.e. when the impact of heat release from hydration is negligible, see Figure 6.8. For reference pastes Ref 0.36 and Ref 0.30 the RH decreased with hydration time. Each curve is the average of two tests. After 28 days Ref 0.36 and Ref 0.30, asymptotically approach the values of 88% RH and 84% RH, respectively. In [Paillère et al. 1989] it is shown that self-desiccation slows down as age increases but does not fall below 75% RH. At the latest at this minimum RH, hydration stops

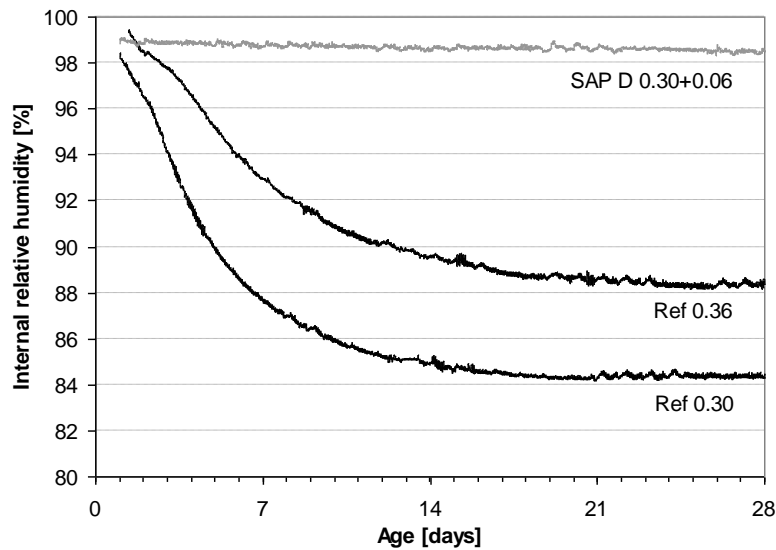


Figure 6.9: Internal relative humidity of cement paste as a function of age.

independently of w/c ratio or silica fume addition. A similar trend was already found by Powers [Powers 1947]. On the other hand, the maximum values found for cement paste are below RH of 100%. The initial drop in RH can be attributed to dissolved salts in the pore solution, mainly alkali ions that reduce the initial RH down to about 98% as reported e.g. in [Bentz et al. 2001]. The relative humidity RH_s due to dissolved salts can be estimated by Raoult's law that states RH_s to be equal to the molar mass fraction of water in the pore fluid X_l [Jensen 1993]:

$$RH_s = X_l \quad (6.6)$$

The curve of SAP D 0.30+0.06 represents the result of one single test. The measured RH levelled off at 99% after 24 hours and decreased to 98.5% within the following 4 weeks. This decrease in RH is expected to be caused by sensor drift or by change in the composition of the pore fluid with hydration. The second test constantly showed 100% RH during the whole test period and thus was dismissed. Probably insufficient thermostatic control during calibration caused the failure. It is known that near saturation at 20°C a temperature difference of 1 K may cause an error of about 6% RH [Jensen & Hansen 1999] as cited in [Lura 2003].

Pastes modified with SAP A and SAP B, respectively, were not measured. It is expected that they would have shown a decrease in RH as soon as the initial expansion starts to turn into shrinkage, i.e. when the IC water is depleted or the degree of saturation has reached a critical limit.

6.3.5 Autogenous deformation vs. internal RH

In Figure 6.10 the autogenous deformations of both reference pastes are plotted as a function of the internal RH. The corresponding linear regression lines are reported in the Figure 6.11. The curves start from 24 hours after mixing in case of Ref 0.30 and from 36 hours after mixing in case of Ref 0.36. At this time, autogenous shrinkage was already found to yield 550 μ strain and 285 μ strain, respectively. Potentially, it is a result of capillary pressure acting on the very early age paste system which has still large deformation capability. In [Chang-wen et al. 2007] a tensiometer setup was embedded into fresh cement paste which allows to directly measure the capillary pressure development. They found that water consumed only in large pores of several microns causes

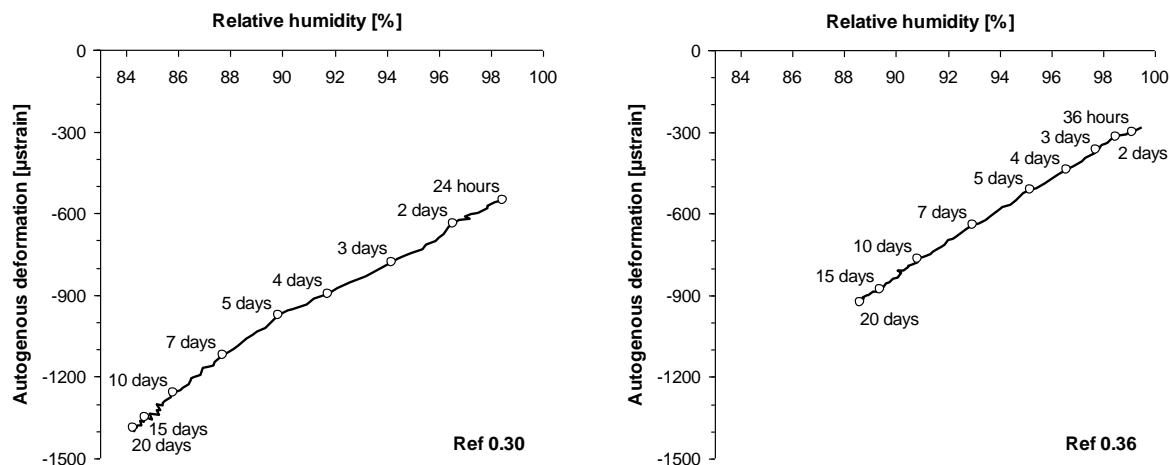


Figure 6.10: Autogenous deformation of paste Ref 0.30 (left) and Ref 0.36 (right) as a function of internal relative humidity.

about 100 kPa capillary depression. Obviously, this pressure is sufficient to induce rapid self-desiccation shrinkage if the paste still has low deformation resistance while the deformation is negligible if the paste has already solidified. Due to formation of larger capillaries with increasing w/c ratio, the water consumption at early age may result in a much slower rise of menisci pressure compared to low w/c ratio systems. This could be an explanation for the higher initial shrinkage of Ref 0.30 by contrast with Ref 0.36. Moreover, it is supposed that reabsorption of bleed water may arrest the capillary pressure build-up. Another reason for the high autogenous deformation immediately after time zero might be the collapse of the first self-supportive skeleton formations. Principally, reaction products of C_3S and C_2S constituting long fibres build first weak bridges between the hydrating cement particles. Only when the interconnection is strong enough, micropores can stably exist and collapse is avoided. Further, creep could also contribute to high initial autogenous shrinkage. Lura [Lura 2003] supposed that creep at early age is very fast and is measured as quasi-instantaneous deformation.

Actually, the steepness of the shrinkage-RH curves was expected to decrease within the first days of hydration as a consequence of gain in stiffness, which is evident from the increase in elastic material properties, see section 6.3.5. However, creep superposes self-desiccation shrinkage mainly at low RH resulting in a slight increase in deformation per RH% at later age.

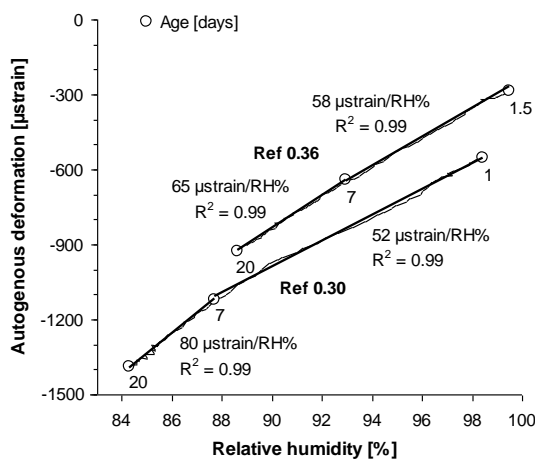


Figure 6.11: Linear regression of shrinkage-RH curves up to 7 days and between 7 and 20 days.

6.3.6 US-wave velocity

Figure 6.12 reports on the P-wave velocity in hydrating cement paste as a function of age. Figure 6.13 shows the S-wave velocity correspondingly. At the very beginning of the tests, the sensitivity of the receiver is not sufficient to resolve the recorded signals, which is why the curves start not until the onsets of the waves could be differentiated from noise. According to Biot's theory [Biot 1956a], [Biot 1956b] two pressure waves propagate in a fluid saturated porous solid: the slow P-wave and the so-called fast P-wave. Both cement pastes with w/c_{basic} of 0.30 show the fast P-wave at early stage of detection. It is a phenomenon of mainly high viscous mixes with low air content [Sayers & Dahlin 1993]. The fast P-wave mainly propagates through the fluid phase, which is why its velocity is close to the velocity in water (1500 m/s). Usually, as in the case here, the fast P-wave disappears in the process of hydration. The slow P-wave is detectable in the higher frequency range only. It is referred to as P-wave in the following. Due to attenuation, it propagates much slower in fresh cement paste compared to its velocity in water. At approximately 1600 to 1700 m/s the P-wave velocity curve shows a turning point. In section 6.3.1. this turning point was already discussed as a rough indication for setting, i.e. the point in time when the plastic cement paste starts to form an interconnected rigid structure.

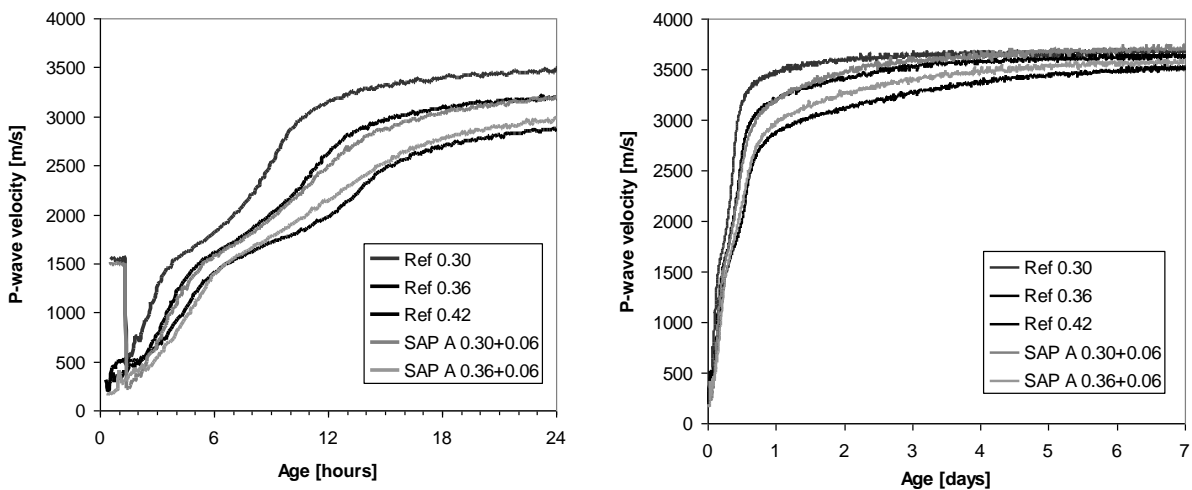


Figure 6.12: P-wave velocity as a function of age up to 24 hours (left) and 7 days (right).

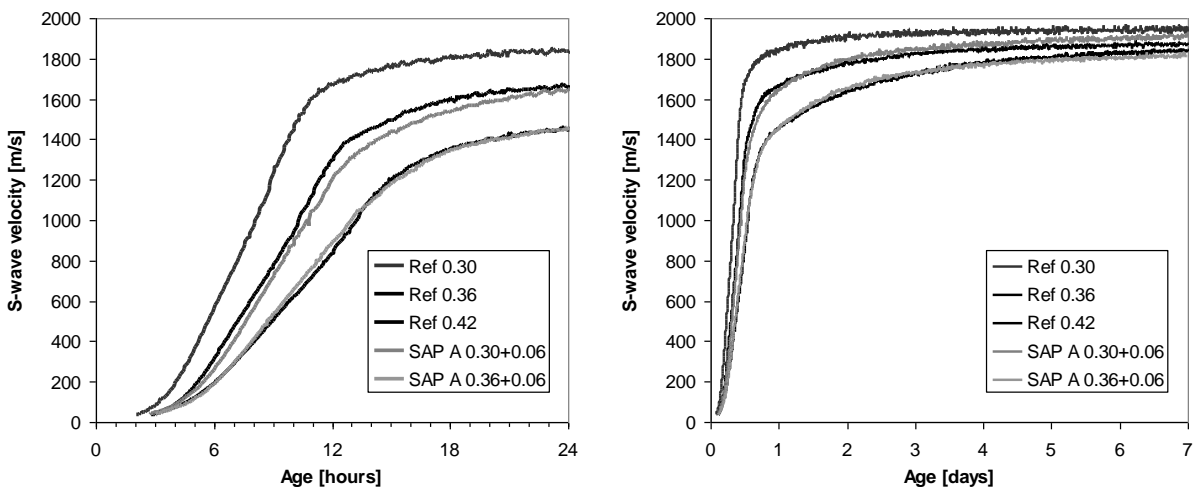


Figure 6.13: S-wave velocity as a function of age up to 24 hours (left) and 7 days (right).

Because of lower velocity and higher attenuation the first S-waves were picked later than the first P-waves. As can be seen clearly, both wave velocities develop slower with increasing the water content, or vice versa: The lower the w/c ratio, the higher the density and consequently the faster the wave propagation. Further, it seems to be irrelevant whether the water was added ordinarily or was absorbed by SAP: Both, water-enrained and plain cement pastes, show the same trends in the wave velocity curves provided that the total water content is the same. The same relationship was found for the development of the degree of hydration in chapter 5. Nevertheless, this result is surprising, since it is known that interfacial transition zones impair the transmission of P-waves, i.e. a small increase in the air content leads to a strong decrease in the P-wave velocity. On the other hand, the existence of air voids has only little influence on the shear wave propagation [Zhu et al. 2011]. With this in mind, it was expected that the initially water-saturated macropore inclusions affect the P-wave velocity as soon as their degree of saturation decreases as a result of hydration. However, the higher density of the pore structure (due to less capillary porosity) seems to compensate this effect. As from 24 hours after mixing, the SAP-modified pastes even show higher P-wave velocities compared to reference pastes with same total w/c.

In general, the influence of the air content makes it difficult to directly correlate the P-wave velocity to mechanical properties of the hardening cement paste. The analysis of the S-wave propagation is more promising for the correlation with mechanical properties since the transmission of S-waves is directly linked to the shear viscosity of the paste. Already in [D'Angelo et al. 1995] it was found that shear waves are more sensitive to solid structure development than P-waves. In [Bentz et al. 1994] it was found by simulation that the shear wave energy is correlated with the volume fraction of connected solids in the paste. In the following the combination of P-wave and S-wave velocity leads to the dynamic elastic material parameters which provide new possibilities for the evaluation of the state of hardening.

6.3.7 Dynamic elastic material parameter

The calculated dynamic elastic material parameters are presented as a function of age in Figure 6.14 to Figure 6.16. The dynamic Poisson's ratio μ_{dyn} reported in Figure 6.14 starts at the initial value of 0.50 and drops down to values in the range of 0.33 (SAP A 0.30+0.06) to 0.30 (Ref 0.30) within the first days of hydration. As long as the Poisson's ratio is below the value of 0.50, uniaxial loading will result in volume reduction. In return, at the initial value of 0.50 the volume is kept constant and indicates that the cement paste is still fluid. It is conspicuous that pastes with lower w/c ratio not only show the lowest values for μ_{dyn} , but also the sharpest drop. Besides the w/c ratio, the Poisson's ratio is affected by various other parameters, e.g. age, moisture content, ambient temperature, cement content or the load applied during testing, as already Ghosh showed for ordinary concrete [Ghosh 1965]. Pereyra [Pereyra 2007] found that with increasing the stress-strength ratio above 50%, the Poisson's ratio increases disproportionately as a result of micro-cracking. When the load under uniaxial testing approaches the short-term strength, the static Poisson's ratio will reach again 0.50. Below 50% of the stress-strength ratio the Poisson's ratio is independent on the stress to a great extent, e.g. the Poisson's ratio of self-compacting concrete yields between 0.20 and 0.25 [Pereyra 2007]. Only at very low stress-strength ratios the statically measured Poisson's ratio is increased. This fact causes the phenomenon of higher dynamic Poisson's ratio compared with statically determined values, i.e. no load is applied when the US waves travel through the specimen. However, according to [DIN 1045-1 2008] the Poisson's ratio of concrete is assumed to be constant at 0.20.

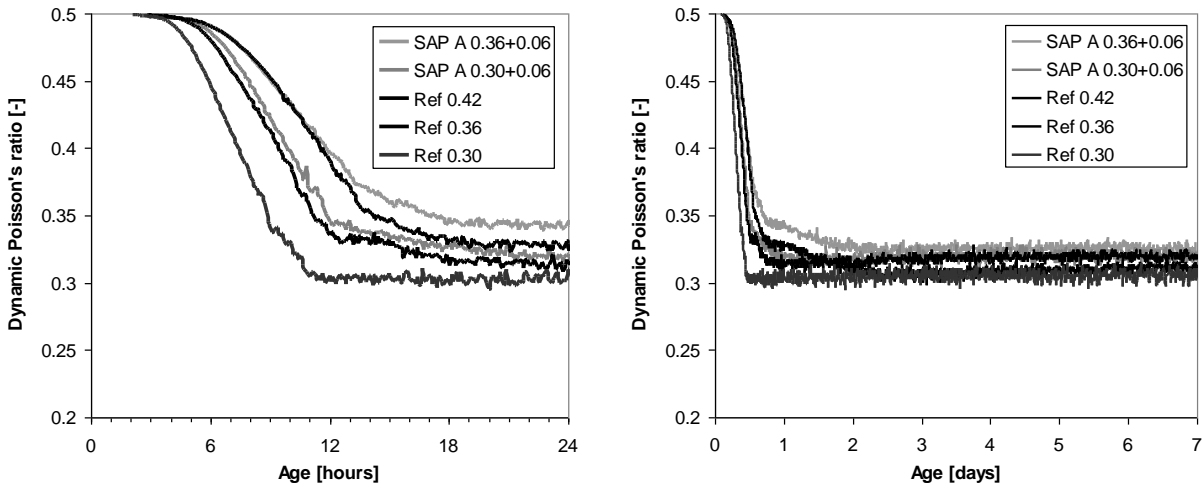


Figure 6.14: Dynamic Poisson's ratio as a function of age up to 24 hours (left) and 7 days (right).

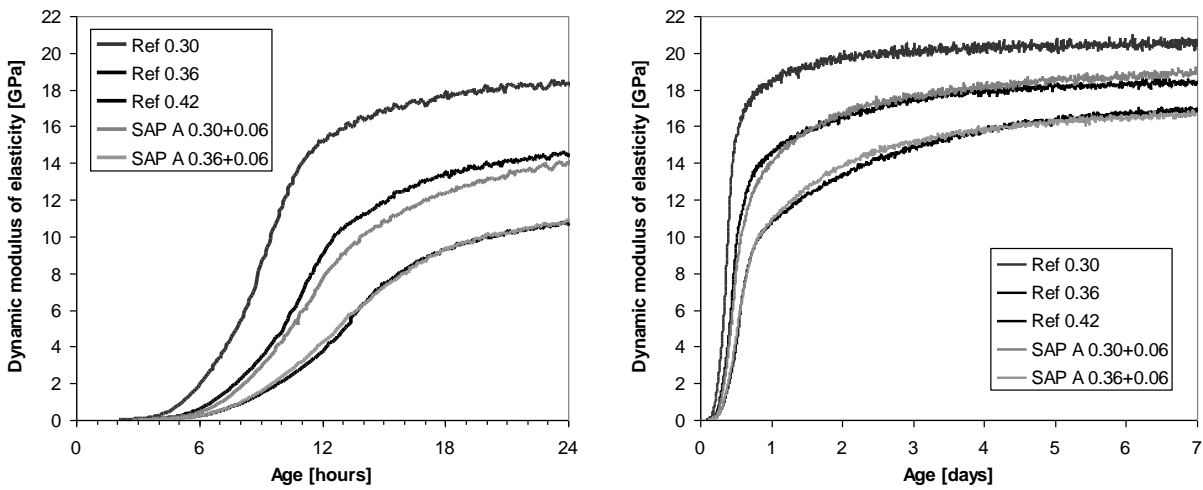


Figure 6.15: Dynamic elastic modulus as a function of age up to 24 hours (left) and 7 days (right).

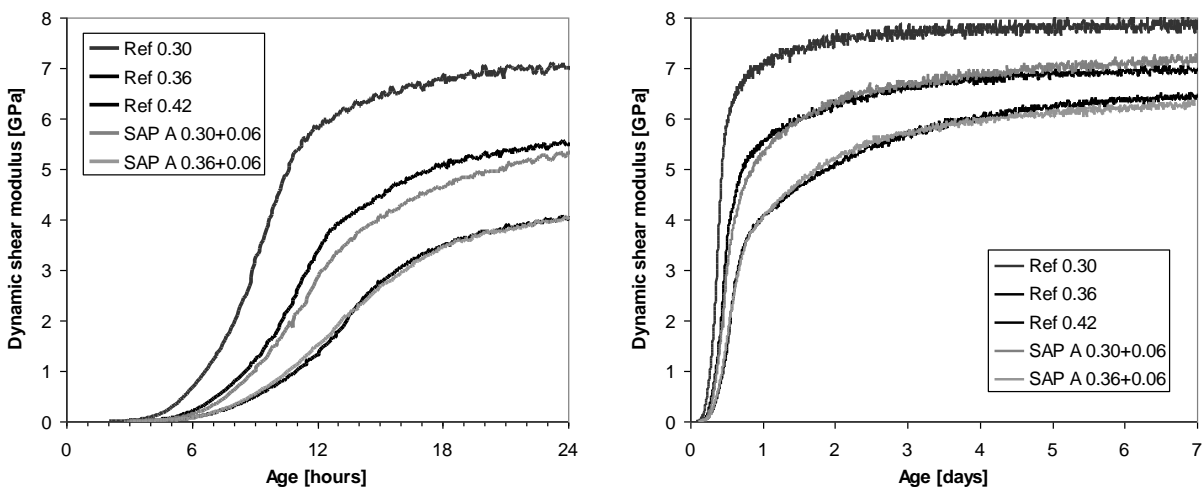


Figure 6.16: Dynamic shear modulus as a function of age up to 24 hours (left) and 7 days (right).

Figure 6.15 reports on the dynamic modulus of elasticity. Compared to the wave velocities the curves of the pastes have more distance to each other, especially at higher age. Except paste Ref 0.42, which shows slightly lower values at the beginning, the SAP-modified pastes show very similar curve shapes. Here again, it can be seen that the paste with lowest w/c ratio adopts the highest values. The same is true for the dynamic shear modulus, which is converted from the dynamic modulus of elasticity. Values for the dynamic bulk modulus are reported in appendix 6.

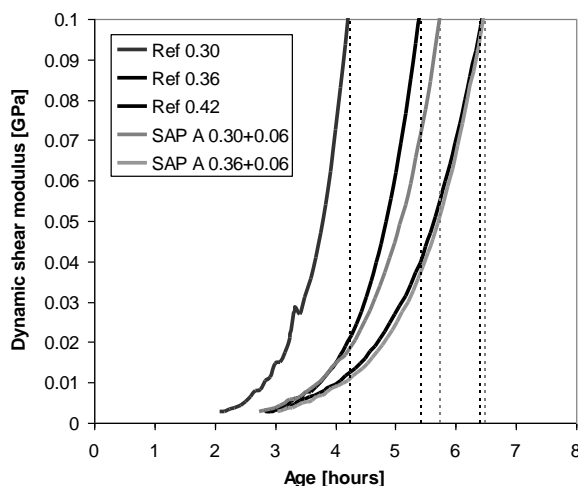


Figure 6.17: Dynamic shear modulus as a function of age.

In [Robeyst 2009] methods for the determination of setting by using US-through transmission testing on the basis of P-waves are discussed. According to [Robeyst 2009] and [Reinhardt & Grosse 2004] the velocity of 1500 m/s is seen as a rough guide for the estimation of the final setting time. However, the monitoring of the dynamic elastic material properties provides new instruments for the estimation of the setting times. As mentioned above, the time when the dynamic shear modulus passes the value of 0.1 GPa, cf. Figure 6.17, was found to correlate well with the initial set found by the Vicat method, see Table 6.3 on page 81. The velocity of the shear wave at this time was found to yield in the range 225 to 235 m/s.

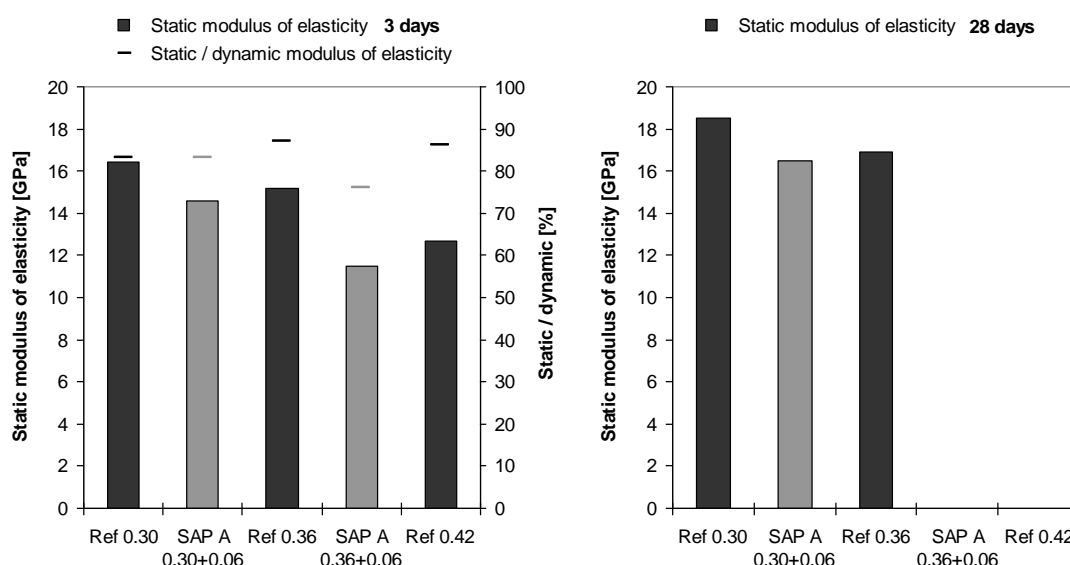


Figure 6.18: Static Young’s modulus at the age of 3 days (left) and 28 days (right). Bars mark absolute values; short lines give the values relative to the dynamic Young’s modulus.

Figure 6.18 reports on the dynamic modulus of elasticity measured at 3 days and at the age of 28 days compared to statically determined values. The latter are 10% (Ref 0.36) to 25% (SAP A 0.36+0.06) lower compared to the dynamic values. Further, the static modulus of elasticity of SAP-modified pastes is not the same compared to reference pastes with same total water content, but is up to 10% less. This reduction was not found for the dynamic modulus of elasticity. It appears as if the influence of SAP on the microstructure as well as the degree of saturation affects the static elastic material parameter but not so the dynamic material parameter. On this account, the preference will be to analyse attenuation and energy content of the transmitted waves in future.

6.3.8 Compressive and flexural strength

The results of the compressive strength tests are reported in Figure 6.19. Each diagram compares one SAP A-modified paste with values of the two corresponding reference pastes. It is striking that the water-entrained pastes show entirely the lowest strength values. Compared to reference pastes with same basic w/c ratio, the strength-increasing effect due to increased degree of hydration could apparently not counterbalance the strength reducing effect of SAP A voids, see Figure 6.21. The difference to the reference paste with same total water content might be partly explained by the reduced effective w/c ratio resulting from bleeding of reference pastes. In general, bleeding occurred stronger the higher the w/c ratio was. For Ref 0.30 only little bleeding and for pastes with SAP addition no bleeding was observed. This effect might have also caused the somewhat small discrepancy in strength values among the reference pastes. Another reason contributing to less strength of water-entrained pastes at early age could be the higher degree of saturation of the pore system. It is an effect comparable to the influence of water-storage on the compressive strength, i.e. water regarded as incompressible weakens the strength in case of complete water-saturation of the pore system. The lead in strength of the reference paste with low w/c ratio melts away at higher age due to proceeding hydration of the pastes with higher w/c ratio and SAP addition, respectively. At last, self-desiccation may play a role since micro-cracking, whether internal or external, weakens strength.

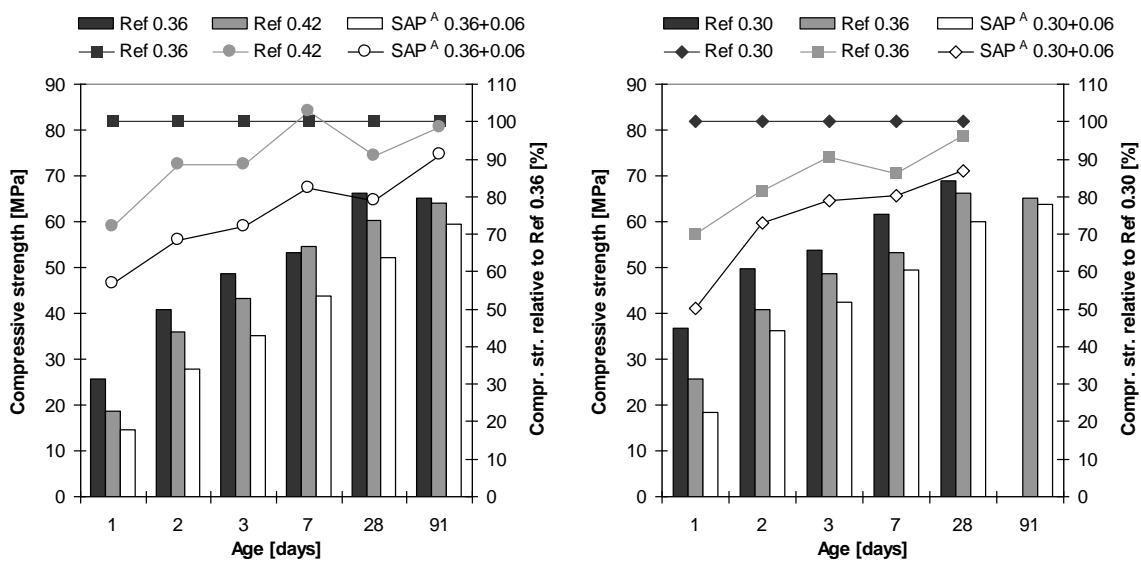


Figure 6.19: Compressive strength measured on cement paste prisms cured in foil at 20°C. Absolute values are given as columns; relative strength values are shown as curves.

Especially flexural strength suffers from micro-cracking. The diagrams in Figure 6.20 report on the flexural strength measured on paste prisms that had been wrapped in adhesive vapour barrier foil until testing. It is very likely that surface cracks occurred at the age of 7 to 28 days. All cement pastes have in common a decrease in absolute strength values at this age. As anticipated, the water-entrained pastes were affected the least. An increase in flexural strength of up to 30% compared to the value of Ref 0.36 was noticed for SAP A 0.36+0.06 at the age of 91 days.

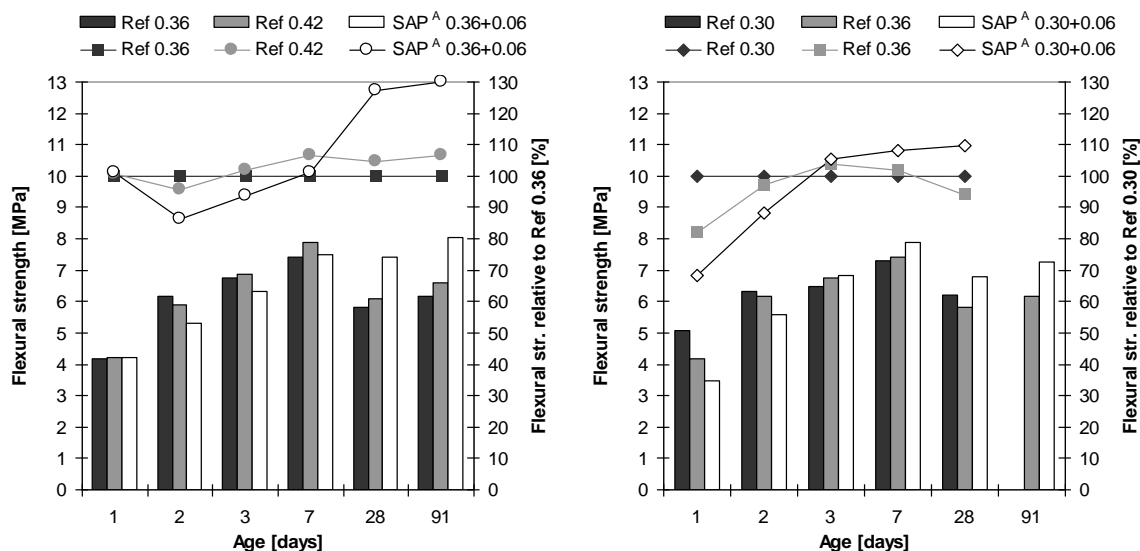


Figure 6.20: Flexural strength measured on cement paste prisms cured in foil at 20°C. Absolute values are given as columns; relative values are shown as curves.

In the left diagram of Figure 6.21 the compressive strength is shown as a function of the degree of hydration. It illustrates that for a given degree of hydration, see chapter 5, the SAP-modified paste possesses the lowest strength. The right diagram shows the correlation between dynamic modulus of elasticity and compressive strength. For a given dynamic modulus of elasticity the SAP-modified pastes possess less compressive strength compared to reference pastes with same w/c ratio. The diagram illustrates the finding that the dynamic elastic material parameters are less sensitive to partially water-filled macropore inclusions than the statically determined parameters.

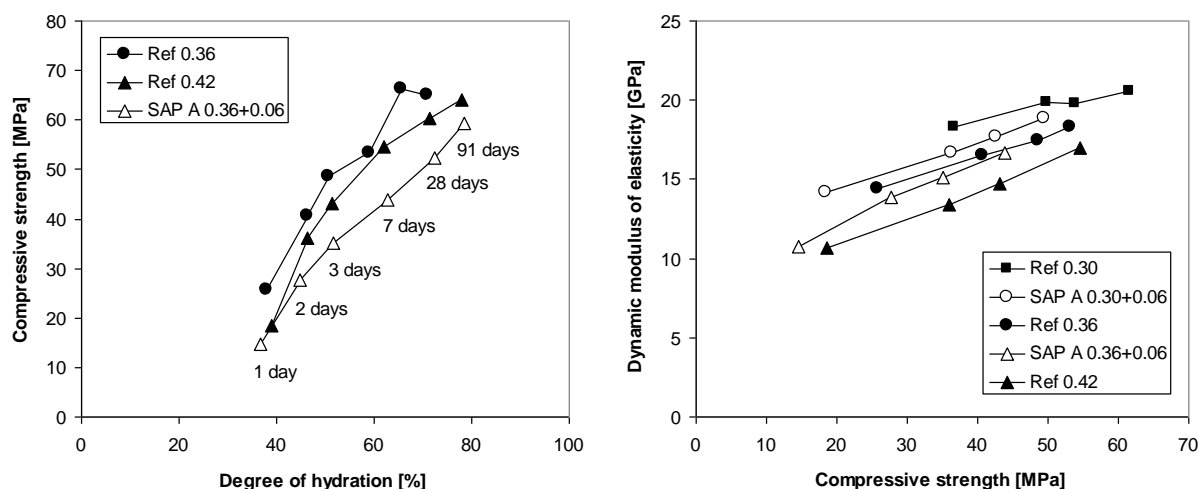


Figure 6.21: Compressive strength vs. degree of hydration (left) and dynamic Young’s modulus vs. compressive strength at the age of 1, 2, 3 and 7 days (right).

6.3.9 Pore water analysis

The surface tension of pore water was found to yield 0.074 ± 0.002 N/m. There was no distinct influence of age or paste composition on the surface tension. Similar results were found by Schaeffel [Schaeffel 2009] who extracted pore solution between the age of 1 and 91 days. He determined the surface tension by following the Wilhelmy plate method. The average value found was 0.072 ± 0.001 N/m for Portland cement pastes at w/c ratios in the range 0.25 to 0.42. Lura [Lura 2003] measured the surface tension of synthesized pore solution with a DuNouy tensiometer and found a value of 0.078 N/m. The results of ion chromatographic analysis are reported in appendix 6. Only small differences in the ion concentrations were found.

6.3.10 Cracking due to restraint

Crack formation due to restraint autogenous shrinkage was not observed in the scope of this thesis. Cracking occurs when the tensile stresses caused by restraint shrinkage reach the tensile strength of the material. A theoretical approach for the calculation of the stresses σ_{ind} that would develop in the hardening cement paste if autogenous shrinkage was restraint, is provided by equation (6.7) on the basis of Hooke's law:

$$\sigma_{ind} = E_{dyn} \cdot \varepsilon_{CP} \quad (6.7)$$

where ε_{CP} is the measured free autogenous shrinkage of cement paste and E_{dyn} is the dynamic modulus of elasticity determined by FreshCon.

Figure 6.22 presents the theoretical stress development calculated for paste Ref 0.30 in comparison to the measured bending tensile strength. Naturally, this approach is a strong simplification since the time-dependent behaviour, i.e. relaxation is not considered. In practice, relaxation of the paste would reduce the actual stress. But, it is very likely that the reference paste would show cracking in the first 3 days of sealed hardening, cf. [Jensen & Hansen 2002]. In contrast, restraint expansion of the water-entrained cement pastes would induce compressive stresses. Only a little number of papers exists so far that deal with the measure of induced tensile stresses, see chapter 3.2.2. Future research has to clarify the minimum amount of entrained water necessary to reliably prevent sealed concrete from early age cracking at restraint condition.

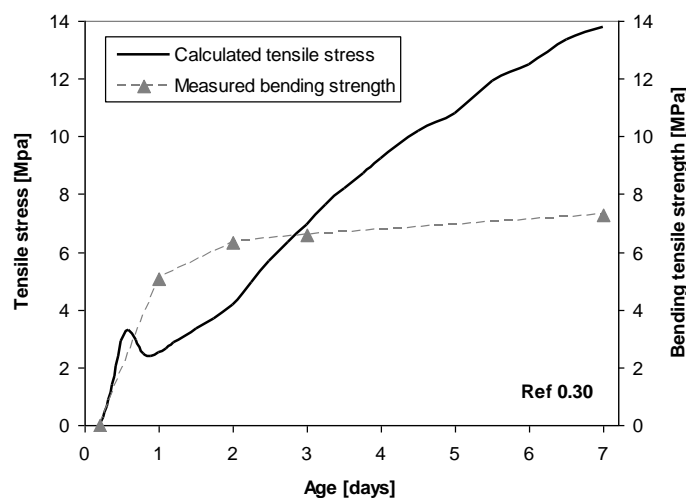


Figure 6.22: Cracking potential of paste Ref 0.30 due to restraint autogenous shrinkage - a theoretical approach.

6.4 Modelling of self-desiccation shrinkage

6.4.1 Introduction

The measured RH change reported in 6.3.4 occurred after setting of the reference pastes and is attributed to self-desiccation. On the basis of the RH change due to both formation of water-air menisci and dissolution of salts in the pore fluid, a calculation procedure adopted from Lura [Lura 2003] is presented that was used to model the self-desiccation shrinkage of Ref 0.30 and Ref 0.36 in the first 7 days of hardening. The model bases on an equation introduced by Bentz [Bentz et al. 1998]. The advantage of this approach is that no knowledge about the pore size distribution is required. The only input parameters are the measured RH, the determined elastic material parameters and the saturation degree of the pores.

6.4.2 Autogenous RH change

The change in internal relative humidity RH_K [-] due to water-air menisci formation in a circular cylindrical pore is given by Kelvin's equation with Kelvin radius r [m] as follows:

$$RH_K = \exp\left(-\frac{2\gamma \cdot V_w \cdot \cos\theta}{r \cdot RT}\right) \quad (6.8)$$

where γ [N/m] is the surface tension of the pore fluid, V_w [m³/mol] the molar volume of water, 18.02×10^{-6} [m³/mol], R [J/molK] the ideal gas constant, i.e. 8.314 J/molK, T [K] the absolute temperature, i.e. 293 K and θ [-] the contact angle between water and solids, with $\theta \approx 0$ and $\cos\theta \approx 1$, respectively, by assuming perfect wetting.

The measured relative humidity RH [%] reflects the RH drop from water-air menisci formation RH_K [-] and dissolution of salts RH_s [-] and is therefore written as:

$$RH = RH_s \cdot RH_K = X_l \cdot \exp\left(-\frac{2\gamma \cdot V_w}{r \cdot RT}\right) \quad (6.9)$$

6.4.3 Kelvin radius and tensile stress in the pore fluid

The radius of the largest capillary pore filled with water can be calculated directly from the RH measurements by equation (6.10). In doing so, γ was assigned to 0.074 N/m and the RH drop due to dissolved salts was assumed to remain constant during hydration. In particular, RH_s refers to the highest RH measured. Figure 6.23 (left) shows the calculated Kelvin radius for Ref 0.36.

$$r = -\frac{2\gamma \cdot V_w}{\ln\left(\frac{RH}{RH_s}\right) \cdot RT} \quad (6.10)$$

The tensile stress in the pore fluid σ_{cap} [MPa] can be calculated with the Laplace law applicable for circular cylindrical pores by assuming perfect wetting:

$$\sigma_{cap} = -\frac{2\gamma}{r} \quad (6.11)$$

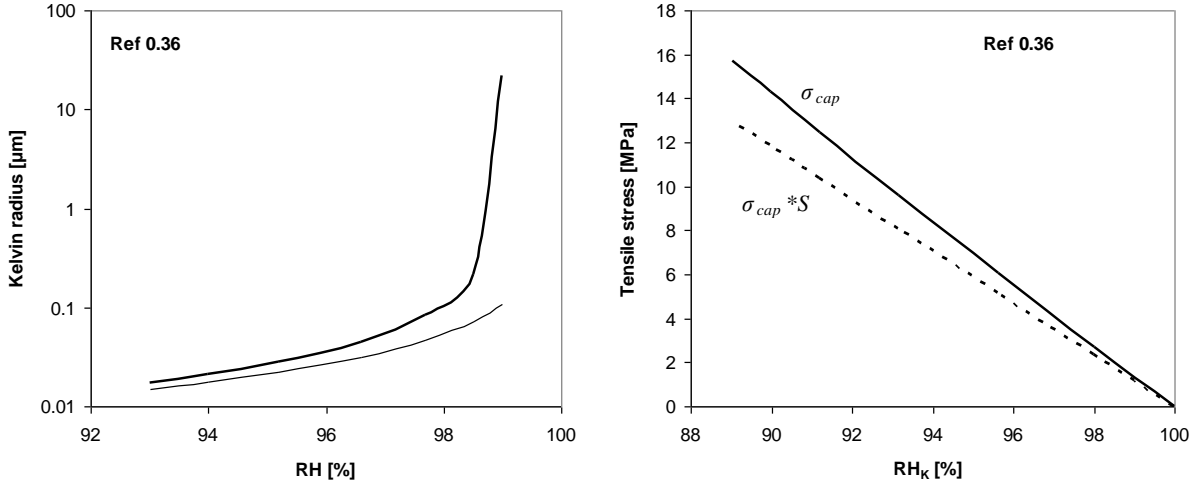


Figure 6.23: Radius of largest capillary pore filled with water calculated with (bold line) and without (thin line) correction for the influence of dissolved salts, i.e. constantly 1.5% RH (left) and stress in the pore fluid as a function of RH_K (right).

The Laplace law states that two paste systems of same pore volume but different pore size distribution have different capillary stresses acting on the pore walls. But insertion of Kelvin's law into equation (6.11) leads to equation (6.12) where the capillary pressure depends on RH_K only, i.e. neither knowledge of the pore system nor the surface tension of the pore water is required.

$$\sigma_{cap} = \frac{\ln(RH_K) \cdot RT}{V_W} \quad (6.12)$$

The tensile stress in the pore fluid calculated for paste Ref 0.36 is shown in Figure 6.23 (right). The dashed line reports on the tensile stress multiplied with the saturation degree of the pores.

6.4.4 Saturation of capillary pores

The degree of saturation S [m^3 water / m^3 pore] can be calculated by using Powers' model for the volumetric phase distribution of hardening Portland cement paste [Powers & Brownyard 1948], see chapter 2.2.3 and appendix 2. S can be expressed as a function of the degree of hydration a [-], which was determined in chapter 5 by thermogravimetric analysis:

$$S = \frac{V_{CW}(\alpha)}{V_P(\alpha)} = \frac{V_{CW}(\alpha) + V_{GW}(\alpha)}{V_{CW}(\alpha) + V_{GW}(\alpha) + V_{CS}(\alpha)} \quad (6.13)$$

where V_{CW} [-] is the volume of capillary water, V_{GW} [-] the volume of gel water, V_{CS} [-] the volume of chemical shrinkage and V_P [-] is the pore volume.

Figure 6.24 reports on the decline in saturation of pores calculated for the reference pastes. The curves provided by the left diagram are extended by dashed lines up to the maximum degree of hydration, i.e. $a_{max} = 0.71$ for w/c of 0.30 and $a_{max} = 1$ for $w/c \geq 0.42$. For $w/c \leq 0.42$ the saturation of pores is about 75% at a_{max} , independent of w/c . In case of $w/c \geq 0.42$ the degree of saturation at a_{max} increases with increasing the w/c ratio. The right diagram shows the saturation of pores in dependency of the age of cement paste and applies to sealed hardening at 20 °C.

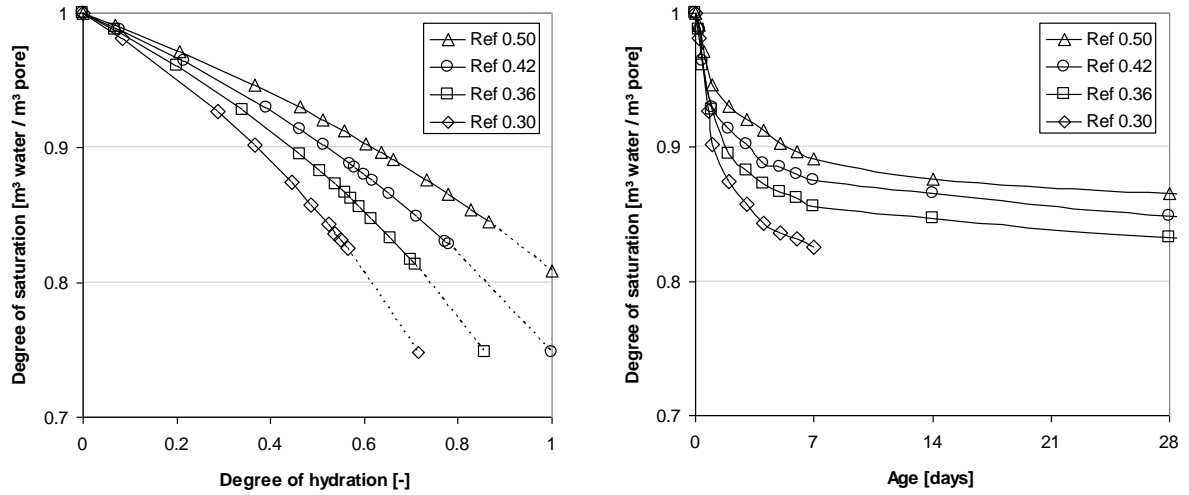


Figure 6.24: Calculated pore saturation of plain cement paste as a function of hydration degree (left) and age of cement paste (right).

The degree of saturation of water-entrained cement paste is expected to permanently reach full water-saturation. Only when the SAP pores are empty or the saturation of SAP pores is very low, drainage of the smaller capillary pores will start. For pastes SAP D 0.30+0.06 and SAP D 0.36+0.06, full water-saturation of the capillary pores is expected until the maximum degree of hydration is reached.

6.4.5 Elastic material properties

The dynamic bulk modulus K_{dyn} [MPa] of cement paste can be derived from the dynamic modulus of elasticity E_{dyn} [MPa] and the dynamic Poisson's ratio μ_{dyn} [-] according to:

$$K_{dyn} = \frac{E_{dyn}}{3 \cdot (1 - 2\mu_{dyn})} \quad (6.14)$$

The development of the dynamic bulk modulus is reported in appendix 6.

6.4.6 Deformation of cement paste

Finally, the deformation of the cement paste ε_{CP} is calculated according to the following equation which was adopted from [Bentz et al. 1998]:

$$\varepsilon_{CP} = \frac{S \cdot \sigma_{cap}}{3} \cdot \left(\frac{1}{K} - \frac{1}{K_{solid}} \right) \quad (6.15)$$

where K [MPa] is the bulk modulus of cement paste and K_{solid} [MPa] is the bulk modulus of the solid material, i.e. 50 GPa [Nielsen 1991].

In a first approach, the cement paste strain was calculated by using K_{dyn} as bulk modulus. The calculation results are shown in Figure 6.25 (left). To account for the fact that the FreshCon results overvalue the static elastic modulus of elasticity by 15%, see section 6.3.7, the bulk modulus of the paste was reduced in a second step (right diagram), where $\mu = 0.20$ was assumed:

$$K = \frac{0.85 \cdot E_{dyn}}{3(1 - 2 \cdot 0.2)} \approx 0.472 \cdot E_{dyn} \quad (6.16)$$

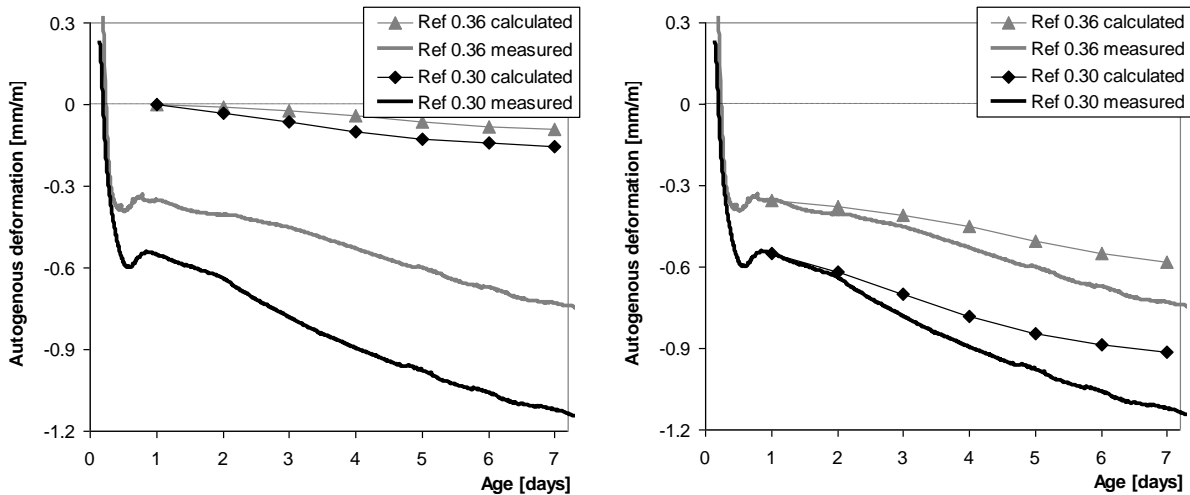


Figure 6.25: Comparison of measured and calculated self-desiccation shrinkage without (left) and with (right) modification of the dynamic elastic material properties. At the age of 24 hours, calculated and measured values were put at the same level (right).

6.4.7 Discussion

The initial shrinkage of cement paste occurring before the start of the RH drop, i.e. between setting and the age of 24 hours, is not captured by the model. Further, the model will lead to significant smaller shrinkage compared with strain measurements if the dynamic bulk modulus is used. Reduction of the bulk modulus according to equation (6.16) results in a better forecast of self-desiccation shrinkage. But the calculated values are still small, which may have three reasons:

- First, the used capillary tension model supposes elastic material behaviour, i.e. creep is not taken into account. Obviously, the elastic deformation is only a part of the total deformation. Lura suspected that the effect of creep becomes more evident at the lower RH range [Lura 2003]. To compensate this effect, the Young's modulus at early age might be reduced. Hua et al. used a capillary tension model to predict autogenous deformations as well [Hua et al. 1995]. They found greater consistency between measured and calculated values if creep of cement paste was considered by an extra term in their calculation function. This means that the restraint stresses are overestimated if they are derived from the free autogenous deformation only. However, the weak point of Hua's model is in the mercury intrusion porosimetry method that was used to experimentally determine the capillary tension in the pore water.
- Second, the conversion of ettringite - which was assumed to contribute to early age swelling - into monosulphate, may have caused additional shrinkage.
- Third, the RH drop may result in a decrease of the disjoining pressure causing further contraction of the paste system.

6.5 Conclusion and outlook

6.5.1 Conclusions

- 1) The dynamic shear modulus of 0.1 GPa correlated well with initial setting (Vicat). For plain paste the time of maximum deformation rate was assumed to meet time zero the closest.

- 2) Autogenous shrinkage of reference pastes was increasing with decreasing the w/c ratio. So was the drop in internal RH. A large part of the autogenous deformation occurred around setting and was not related to the RH drop. It is supposed that capillary pressure induced autogenous shrinkage at very early age, i.e. when the paste had large deformation capability. In contrast, water-entrained cement pastes showed expansion right after setting.
- 3) SAP D was able to permanently maintain stable expansion of the paste. So was the internal relative humidity kept constant at about 98% RH. Deformation of SAP A and SAP B-modified pastes turned into shrinkage after 3 weeks at the latest. It was assumed that with decreasing the w/c ratio, SAP A and SAP B entrained less water than expected, i.e. $(w/c)_e < 0.06$. Once the internal water sources were consumed, self-desiccation and self-desiccation shrinkage started. In doing so, the autogenous deformation curve was parallel to the one of the reference paste with same total w/c ratio.
- 4) The dynamic modulus of elasticity was higher for pastes with low w/c ratio, i.e. 0.30, and developed faster than pastes with high w/c ratio, i.e. 0.42. Further, the development was almost the same for both, reference pastes and SAP-modified pastes, provided that the total water content was the same. Not so was the static modulus of elasticity which was reduced by up to 10% due to SAP addition. Further, the 3 days static modulus of elasticity was reduced by 10 to 25% compared with corresponding dynamic values.
- 5) Compared to reference pastes with same $(w/c)_{\text{basic}}$ the strength-increasing effect due to proceeded hydration could not counterbalance the strength-reducing effect of SAP voids even at later age. Actually, when compared with reference pastes of same water content, the compressive strength was still reduced, which might be traced back to bleeding of the reference samples. However, the flexural strength of SAP-modified paste exceeded the values of reference paste at later ages possibly due to prevention of micro-cracking.
- 6) The surface tension of the pore solution yielded 0.074 ± 0.002 N/m independent of age and w/c ratio. Only small differences in the concentration of ions were found.
- 7) Modelling of self-desiccation shrinkage of reference pastes by the capillary tension approach did not capture the high initial autogenous deformation. The model led to significantly smaller shrinkage compared with strain measurements. It was expected that the discrepancy was mainly caused by creep, which was not considered in the calculation.

6.5.2 Outlook

To avoid dispute about the real time zero in future, it is recommended to directly measure the onset of the tensile stress development in active restraint systems. Moreover, the recording of the induced tensile stress would allow to state on the development of the cracking potential. Hence, for practical issues the SAP dosage should be generally reduced to small fractions in order to only mitigate autogenous shrinkage at very early age, i.e. when the cracking potential is high due to little tensile strength. In doing so, the insertion of dispensable macropores would be omitted.

Concerning measurements with FreshCon, the future evaluation method should consider the analysis of attenuation and energy content of the transmitted waves instead of wave velocity only.

In addition, the mechanisms causing expansion are still to be investigated in more detail.

And, last but not least, the prediction of the self-desiccation shrinkage model should be improved by taking into account the effect of creep and the initial autogenous shrinkage, i.e. the deformation that occurs before the RH depression due to menisci formation. The latter could be considered by measuring the capillary tension with a tensiometer embedded in the fresh paste.

7 Internal curing of high performance mortar

7.1 Introduction

This chapter deals with the application of SAP for the purpose of internal curing of high performance mortar (HPM). The investigation comprises measurements on free autogenous shrinkage using corrugated tubes as a mould, strength tests performed on prisms and the computer based evaluation of microsections. To this end, five mortars were produced, varying in total water content (w/c ratios of 0.30 to 0.37), SAP type (SAP C or SAP D) and dosage of SAP. The investigation tries to provide answers on the following questions:

- What is the effect of SAP type and dosage on internal curing and mechanical properties?
- Do the results comply with findings of the paste measurements presented in chapter 6?

To give reasons for ineffective curing of SAP C that occurred despite sufficiently high amounts of entrained water, the spatial distribution of SAP pores was calculated on the basis of imaging analysis results and the travel distance of water in the hardening cement paste was estimated.

7.2 Materials and methods

7.2.1 High performance mortar

Five high performance mortar mixtures containing 1/10 silica fume by weight of cement were produced. The composition of the reference mix with w/c of 0.30 is provided by Table 7.1. It is similar to the one used in the context of the round robin test (RRT) on autogenous shrinkage managed by the RILEM TC 225 - SAP [Mechtcherine et al. 2013]. A second reference mix with w/c of 0.34 and three mixes with $(w/c)_{\text{basic}}$ of 0.30 plus water entrainment due to SAP C or SAP D, respectively, corresponding to $(w/c)_e$ of 0.04 and 0.07, were produced for comparison. The value of $(w/c)_e$ of 0.07 corresponds to the amount of entrained water theoretically needed to prevent complete self-desiccation of the HPM mix, see appendix 3. The basic composition provided by Table 7.1 was kept constant in all mixes. That means the increase in w/c ratio of the second reference mix and the water entrainment of mixes containing SAP was done by adding extra water and SAP “on top”. Due to this kind of pragmatic approach, the total volumes are somewhat increased. However, the fractions of dry SAP were 2.8 kg/m³ for SAP C 0.30+0.04, 4.9 kg/m³ for SAP C 0.30+0.07 and 4.45 kg/m³ were added in case of SAP D 0.30+0.07.

Table 7.1: Design of reference HPM with w/c = 0.30

Component	kg/m ³	dm ³ /m ³
Cement CEM I 42.5 R	700	224.4
Silica fume	70	30.0
Water	210	210.0
Quartz sand 2-4 mm	427.1	161.2
Quartz sand 0-2 mm	911.4	343.8
Superplasticizer PCE	11.5	10.5
Air content	-	20

The silica fume was a dry powder available on the market as Sika Elkem grade 971-U. Mixing was done by means of an epicyclic 10 l Hobart mixer. All dry ingredients were pre-mixed for 30 s. Then the superplasticizer was added pre-solved with the water during the following 90 s of mixing. The total mixing time was 5 min, whereof for 2 min the speed was increased from 170 rpm to 198 rpm. The superplasticizer used was Glenium 51 from BASF. The added amount was reduced for mixes with total w/c of 0.34 and 0.37 to 9.6 kg/m³ and 6.3 kg/m³, respectively. The spread of fresh mortar was found to yield 21 to 23 cm and the air content was 1.1 to 2.3%.

7.2.2 Strength tests

Compressive and flexural strength were tested on prisms (40 x 40 x 160 mm³) that were sealed by adhesive aluminium vapour barrier foil directly after demoulding at the age of 1 day. The strength tests were performed 4, 7, 14, 28 and 91 days after casting.

7.2.3 Strain measurements

Free autogenous deformation was measured by using corrugated tubes as a mould according to [ASTM C1698-09]. A detailed description of the testing method and the sample preparation is given in chapter 6.2.

7.2.4 Imaging analysis

Microsections of sealed cement paste prisms containing SAP A and SAP D were prepared according to [DIN EN 12407 2007] at the age of 7 days. The mix design of the pastes was analogous to the composition of the HPM mixtures with w/c = 0.30+0.07, but contained neither aggregates nor superplasticizer. For each mix a total surface of 4800 mm² was evaluated by computer-based imaging analysis with respect to volume and size distribution of SAP pores (see chapter 4.4.3).

7.3 Results

7.3.1 Mechanical properties

Results of compressive strength and flexural strength tests are listed in Table 7.2. The reference HPM with w/c of 0.30 reaches the strength class C80/95. Further, an increase of strength between 28 and 91 days is reported that is potentially dominated by the reaction of silica fume. Due to addition of extra water and SAP, the strength is generally decreased. The strength reduction is at the same extent for both addition of extra water with and without SAP, provided that the total amount of added water is the same. The type of SAP does not seem to have an influence on strength development.

Table 7.2: Compressive and flexural strength of HPMs tested on prisms (40 x 40 x 160 mm³)

HPM mixture	Compressive strength of prisms [MPa]					Bending tensile strength of prisms [MPa]				
	4 d	7 d	14 d	28 d	91 d	4 d	7 d	14 d	28 d	91 d
Ref 0.30	71.1	82.6	98.9	107.8	117.2	10.3	11.0	12.3	12.8	13.0
SAP C 0.30+0.04	-	77.1	87.4	100.4	109.8	-	9.7	10.8	11.0	13.1
Ref 0.34	-	77.3	92.3	101.3	109.7	-	10.7	11.3	11.8	12.7
SAP C 0.30+0.07	50.9	-	69.3	87.6	96.8	8.6	-	9.3	10.8	12.4
SAP D 0.30+0.07	51.3	62.9	68.7	88.3	97.4	8.5	9.6	10.2	10.7	12.6

7.3.2 Free autogenous shrinkage

In Figure 7.1 the autogenous deformations of the HPMs are reported as a function of age. Each curve represents the average of two tests. For both reference mixes the deformations were zeroed at the time of maximum deformation rate as shown in appendix 7. Deformations of the SAP-modified HPMs were zeroed at the time of first expansion, which occurred earlier than setting of reference mixes. Probably due to higher content of PCE, setting of Ref 0.30 was comparable to Ref 0.34 although the total water content was lower.

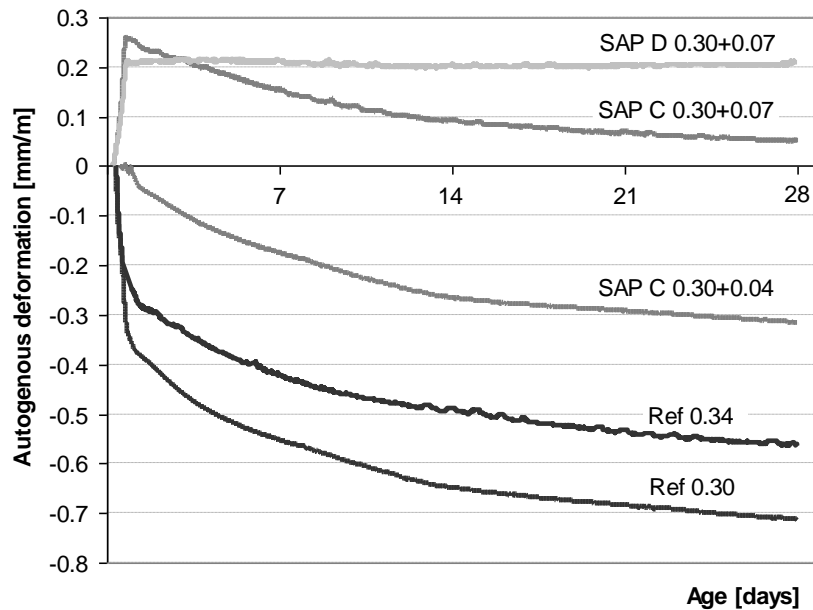


Figure 7.1: Autogenous deformations of HPMs in the first 28 days.

Both reference HPMs show high autogenous shrinkage. With decreasing the w/c ratio, the shrinkage is increasing. After 4 weeks the shrinkage amounts to 720 and 570 μ strain, respectively. It is about half of the shrinkage value found for plain Portland cement paste with same w/c ratio. This is not surprising since about half the volume of HPM is accounted for aggregates. The expansion measured for SAP D 0.30+0.07 is about 200 μ strain. This expansion remained constant at least for the first 4 weeks, i.e. autogenous shrinkage was completely prevented. Mixture SAP C 0.30+0.07 showed comparable expansion of about 250 μ strain. But already one day after casting expansion was followed by shrinkage. The shrinkage amounted to 200 μ strain within the next 4 weeks. As a result the actual deformation zeroed at the time of first expansion was found to yield about +50 μ strain after 28 days. For SAP C 0.30+0.04 only little expansion of 10 μ strain was measured around setting. This expansion turned into shrinkage one day after casting as well. Till the end of measurement the shrinkage increased by more than 300 μ strain. This value is comparable to the shrinkage of Ref 0.34 and amounts to 1.5 times the shrinkage of SAP C 0.30+0.07 in the same period of time.

7.4 Discussion

7.4.1 Mechanical properties

Figure 7.2 reports on the strength values of Ref 0.34 and SAP C 0.30+0.04 relative to the values of Ref 0.30. The increase in w/c ratio of 0.04 led to decrease in compressive strength of approxi-

mately 6% for both, plain and water-entrained HPM, independent of age. This finding is in conflict with results in [Lura et al. 2006b] where no influence of SAP on compressive strength of mortar was noticed. The flexural strength is also decreased due to addition of extra water and water entrainment, respectively. The reduction amounts up to 15% for SAP C 0.30+0.04. At the age of 91 days an increase in strength compared to Ref 0.30 was measured for both, Ref 0.34 and SAP C 0.30+0.04. As found for cement paste in section 6.3.5, the strength increasing effect of proceeding hydration does not counterbalance the strength reducing effect of SAP voids.

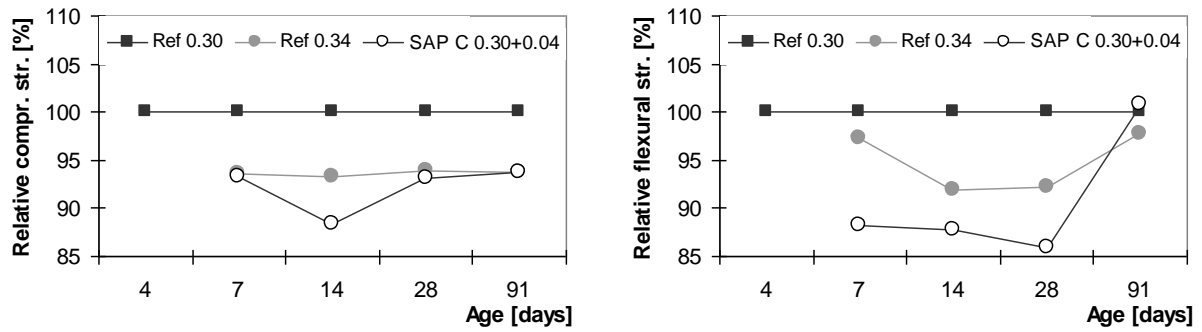


Figure 7.2: Compressive (left) and flexural strength (right) of mix Ref 0.34 and SAP C 0.30+0.04 relative to the value of Ref 0.30.

7.4.2 Effectiveness of internal curing

Figure 7.3 reports on the absolute autogenous shrinkage values measured at the age of 1, 2, 3, 7, 14 and 28 days and the reduction of shrinkage related to Ref 0.30. In the first day of hydration, autogenous shrinkage of SAP C 0.30+0.04 is completely prevented, i.e. the reduction rate is almost 100%, see left diagram. Afterwards, the reduction rate becomes less with increasing age. Direct comparison of absolute shrinkage between the age of 1 day and 28 days manifests the same increase of shrinkage for both Ref 0.34 and SAP C 0.30+0.04. However, it is expected that the initial reduction in autogenous shrinkage would be easily sufficient to prevent early age crack-ing if restraint conditions were considered.

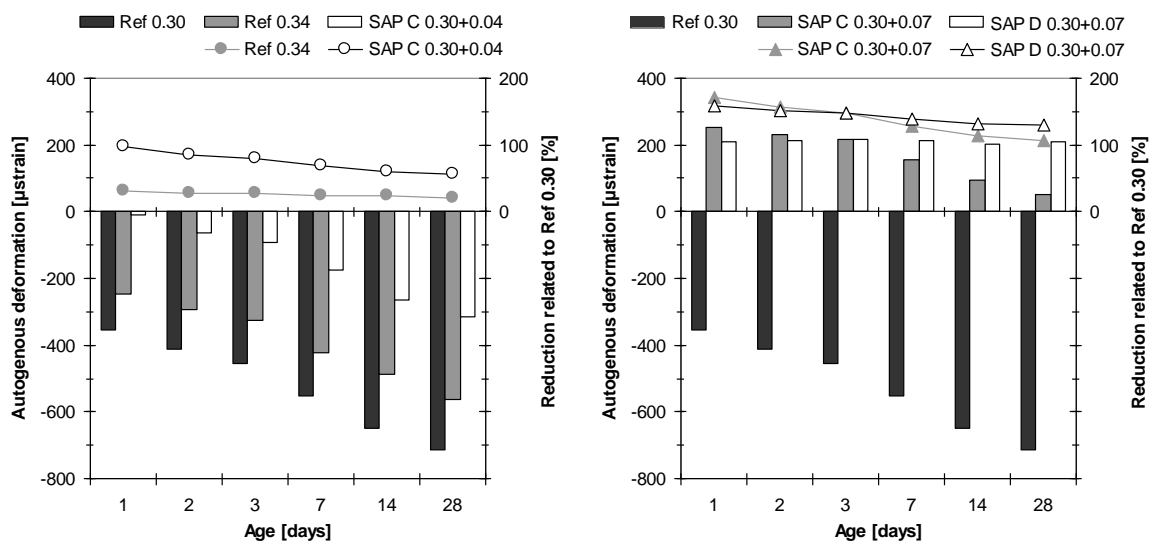


Figure 7.3: Reduction of autogenous shrinkage of HPMs at the age of 1, 2, 3, 7, 14 and 28 days related to Ref 0.30 (curve) and absolute shrinkage value related to setting (column).

Compared to SAP C 0.30+0.07, the smaller dosage of SAP C reduced autogenous shrinkage less effectively. It is a phenomenon related to inadequate amount of entrained curing water, i.e. insufficient availability of curing water. As a result, self-desiccation is not prevented but mitigated compared to Ref 0.30 and retarded compared to Ref 0.34. This hypothesis was already substantiated by measurements on RH change of cement paste with SAP D, referred to SAP A in Jensens paper [Jensen & Hansen 2002]. On the other hand, the expected amount of IC water of $(w/c)_e = 0.07$ agrees with the theoretical amount necessary for complete prevention of self-desiccation of the mortar. For SAP D 0.30+0.07 this holds true since the initial expansion was maintained during the whole test. In contrast, initial expansion of mortar SAP C 0.30+0.07 was directly followed by shrinkage. That means that even at early age of hydration, some points in the matrix were not protected from self-desiccation. Possible reasons might be:

- A considerable amount of IC water is not released but rather retained in SAP C.
- The speed of water supply is too slow, i.e. it does not meet the demand of hydration.
- The spacing of SAP C cavities is larger than the influence zone of the curing water.

Consequently, two aspects that affect the dimension of cured paste volume have to be considered in general, viz the spatial distribution of macropore inclusions and the mobility of IC water in the hardening cement paste. Inefficient curing as a result of less water absorption of SAP at low w/c ratio, as revealed in case of SAP A and SAP B in chapter 6, can be excluded here, as evident from results of imaging analysis (IA).

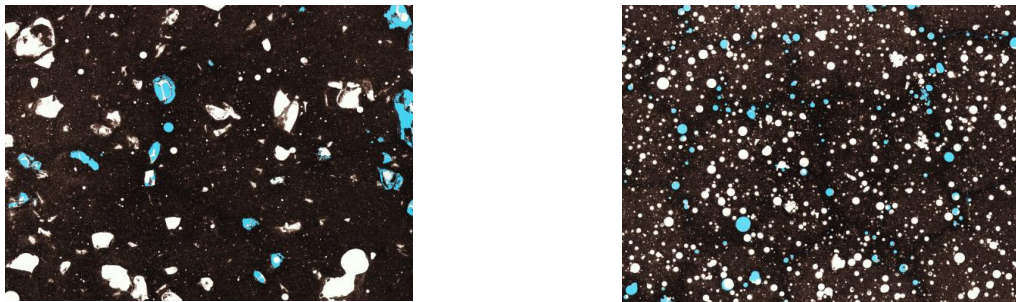


Figure 7.4: Microsections ($27 \times 20 \text{ mm}^2$) of hardened cement paste SAP C 0.30+0.07 (left) and SAP D 0.30+0.07 (right).

IA, as described in section 4.4.3, was executed on microsections of hardened cement pastes, corresponding to the w/c of the mortars, viz 0.30+0.07. The target of IA was the collection of information on volume, spacing and size distribution of SAP C and SAP D pores, respectively. Details of the microsections are presented in Figure 7.4. The colouring of some pores is the result of epoxy resin applied to the surface during sample preparation. The comparison of both pictures clearly visualizes differences in size and spacing of SAP C and SAP D pores. Table 7.3 reports on the analysis results, e.g. the volumes of matrix, V_{Matrix} , air, V_{Air} and SAP pores, V_{SAP} . The found surface fraction of SAP C pores agrees well with the expected pore volume, i.e. the actual water absorption capacity χ_{actual} calculated according to equation (4.10) on page 56, coincides with the expected value χ_{nominal} of 10 g/g.

Table 7.3: Result of imaging analysis on hardened cement paste

Parameter	Unit	SAP C 0.30+0.07	SAP D 0.30+0.07
$V_{\text{Matrix}} / V_{\text{Air}} / V_{\text{SAP}}$	[%]	88.05 / 1.15 / 10.80	86.43 / - / -
$\chi_{\text{nominal}} / \chi_{\text{actual}}$	[g/g]	10 / 10.14	11 / -

As mentioned in chapter 4.3.4, IA does not allow distinction between air pores and spherical SAP D pores. On this account, the pore size distribution of both pastes presented in Figure 7.5 includes air voids. But the falsification from air voids is expected to be only minor. The diagram shows that in case of SAP D 0.30+0.07 50% of the pore volume is provided by pores of less than 600 μm in diameter. The corresponding value of SAP C 0.30+0.07 is more than double that.

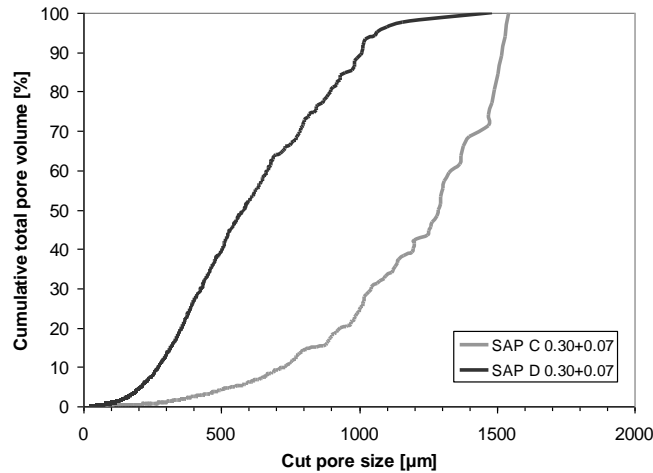


Figure 7.5: Size distribution of total pores found by IA of cement paste micro-sections.

The key figure in explaining insufficient curing of SAP C 0.30+0.07 is expected to be in the distance curing water can travel in the hydrating matrix. Mönning [Mönning 2009] assessed the theoretical influence zone of a single SAP particle in hydrating cement paste at $w/c < 0.42$ with:

$$\Delta r = r_{SAP}^s \cdot \left[\sqrt[3]{\left(\frac{100}{V_{CS}} + 1 \right)} - 1 \right] \quad (7.1)$$

where Δr [μm] is the radius of the influence shell, r_{SAP}^s [μm] is the radius of the saturated particle and V_{CS} [%] is the volume of chemical shrinkage in analogy with appendix 3.

The calculation assumes that all of the water stored in SAP can travel into the hydrating cement paste, i.e. the volume created from chemical shrinkage gets completely occupied by IC water. Figure 7.6 reports on the calculated values in dependence on the volume of chemical shrinkage (CS) and the radius of an individual spherical macropore inclusion.

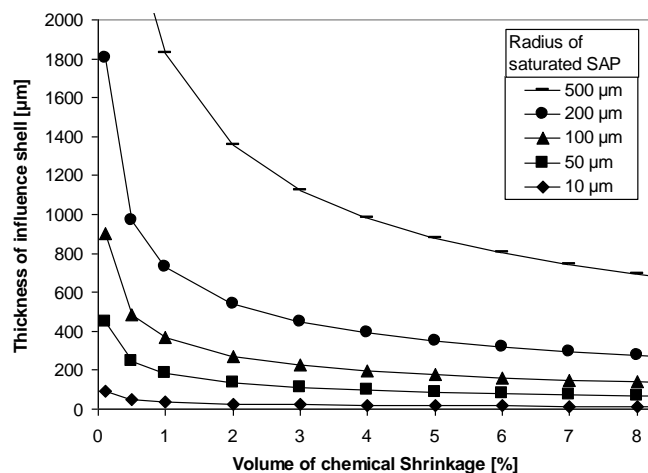


Figure 7.6: Theoretical thickness of influence shell as a function of CS and SAP pore radius.

For an infinitesimally small CS volume the cured volume tends towards infinity, which is an impossible result, whereas for high porosities the curing zone inclines towards approximately 20 μm . Of course, this approach is a strong simplification since, for example, the permeability of the matrix decreases with hydration time and strongly affects the travel distance. The question to consider is what is a reasonable estimate of the distance IC water can travel from the internal reservoir into the hydrating cement paste in order to protect the matrix from self-desiccation.

7.4.3 Estimate of water travel distance and protected paste fraction

On the basis of a first analysis presented by Weber and Reinhardt [Weber & Reinhardt 1999], the water flow distance can be calculated by assuming input parameters for the permeability and pore size distribution of the paste, the chemical shrinkage of the binder and the surface tension, density and viscosity of the pore solution [Bentz et al. 2007]. Table 7.4 provides simulation results performed on low w/b cement paste in concrete, as cited in [Bentz & Weiss 2011]. The underlying mixture composition exhibits a cement content of 700 kg/m^3 and assumes chemical shrinkage of 0.07 ml per 100 g cement reacted. Both values are suitable for the HPM mixes at hand. The early and middle age estimates are in good agreement with X-ray absorption profiles obtained from mortar measurements at w/c of 0.40 [Bentz 2002]. Further, penetration depths of several millimeters during the first days of sealed curing, i.e. middle age, were also reported in [Zhutovsky et al. 2004]. But, due to both silica fume addition and lower $(w/c)_{\text{basic}}$ in case of HPM at hand, Table 7.4 is expected to overestimate the actual water travel distance in the HPM matrix.

Table 7.4: Distance of water travel from surfaces of internal reservoirs [Bentz et al. 2007]

Hydration Age	Estimated travel distance of water
Early (i.e. < 1 day)	20 mm
Middle (i.e. 1 day to 3 days)	5 mm
Late (i.e. 3 days to 7 days)	1 mm
Worst case (i.e. > 28 days)	0.25 mm

In an earlier work of Bentz and Garboczi [Bentz & Garboczi 1991b] the limit for the water travel distance after depercolation of the capillary porosity (worst case) was estimated as 100 to 200 μm . On the basis of microhardness testing on hydrating cement paste samples at w/c of 0.25+0.045, Igarashi [Igarashi et al. 2010] suggested the self-desiccation protection shell at most 200 μm from the SAP surface. According to second-order functions of spatial statistics, the nearest neighbour point was found in the distance of 2 mm from the SAP surface and the mean distance from an arbitrary point in the matrix to the nearest surface of SAP was 400 μm . Consequently, it was not possible to cover the whole cement paste matrix with protected regions even for higher amounts of entrained water. This holds true for both, SAP C 0.30+0.07 and SAP D 0.30+0.07, too, but does not necessarily imply that curing is inefficient, as will be shown in the following.

The remaining question concerns the fraction of cement paste that is located in the influence zone of the SAP inclusions. In a first step the cement pastes were simulated with the hard-core-soft-shell (HCSS) model [Bentz et al. 1999] in order to state on the fraction of paste that is located within a certain distance of the SAP voids. The idea behind the model is very similar to the concept of “protected paste volume” developed for characterizing air void systems in concrete [Bentz & Snyder 1999]. Figure 7.7 illustrates the simulation results of modified pastes SAP C 0.30+0.07 and SAP D 0.30+0.07 and Table 7.5 reports on the related data set. In all HCSS simulations the size distribution of SAP C and SAP D pores was adopted from Figure 7.5.

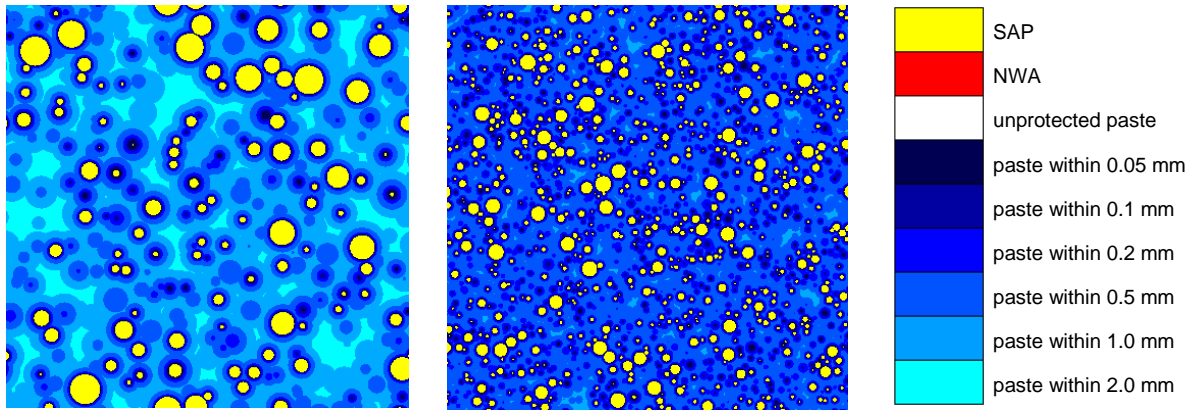


Figure 7.7: Two-dimensional plot ($30 \times 30 \text{ mm}^2$) of the HCSS model for paste SAP C 0.30+0.07 (left) and SAP D 0.30+0.07 (middle) and curing range of cement paste (right).

As can be seen clearly, the paste fraction in the far away distance of the SAP pore surface is higher in case of paste SAP C 0.30+0.07, i.e. about 55% of the paste is located in a distance of $> 500 \mu\text{m}$ from the nearest pore surface. In contrast, nearly all the paste, i.e. 98%, is located within a distance of $< 500 \mu\text{m}$ from the next pore surface in case of SAP D 0.30+0.07. It is a result of smaller pore sizes of SAP D compared with SAP C, see Figure 7.5 on page 105.

Table 7.5: Protected paste volume as a function of distance from SAP surface

Distance from SAP surface [mm]	Protected paste fraction [-]	
	SAP C 0.30+0.07	SAP D 0.30+0.07
0.050	0.026	0.074
0.100	0.058	0.179
0.200	0.134	0.456
0.500	0.456	0.981
1.000	0.910	1.000
2.000	1.000	1.000

The HCSS approach allows the consideration of normal weight aggregates (NWA), which is a benefit compared with other models, e.g. the work of Lu and Torquato [Lu & Torquato 1992]. So the HPM mixes SAP C 0.30+0.07 and SAP D 0.30+0.07 were simulated in a second step. The results are reported in Figure 7.8 as well as Table 7.6 and confirm to a large extent the findings of the above paste simulations, even though the mean distances are somewhat increased.

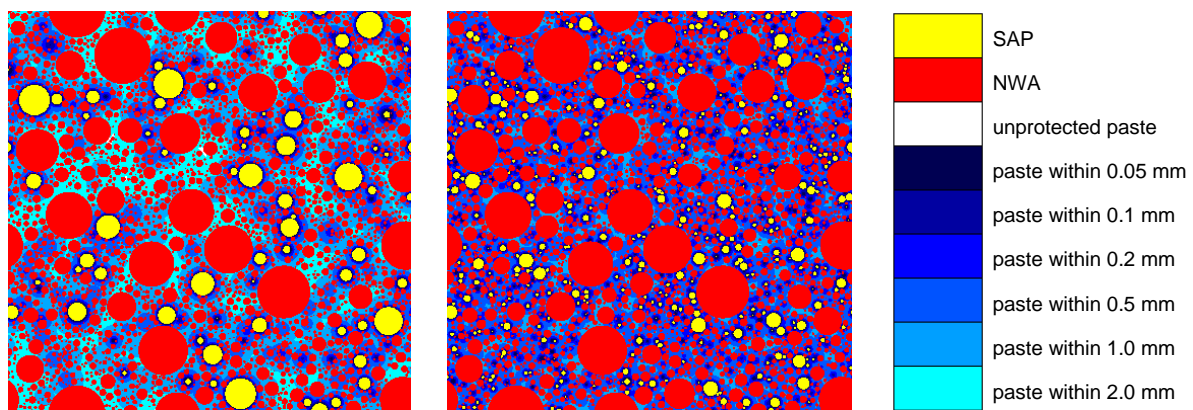


Figure 7.8: Two-dimensional plot ($30 \times 30 \text{ mm}^2$) of the HCSS model for mortar SAP C 0.30+0.07 (left) and SAP D 0.30+0.07 (middle) and curing range of cement paste matrix (right).

Table 7.6: Protected matrix volume as a function of distance from SAP surface

Distance from SAP surface [mm]	Protected matrix fraction [-]	
	SAP C 0.30+0.07	SAP D 0.30+0.07
0.050	0.029	0.073
0.100	0.061	0.164
0.200	0.124	0.362
0.500	0.343	0.871
1.000	0.750	1.000
2.000	0.998	1.000

Using Table 7.4 as a rough guide, the time can be estimated when the first points in the matrix are not covered by the curing zone anymore. This time is assumed to mark the onset of self-desiccation and consequently self-desiccation shrinkage. In case of SAP C 0.30+0.07 the nearest neighbour point can be found within the distance of about 2 mm around the surface of the SAP C inclusions. Therefore the corresponding onset of self-desiccation is expected within the 3rd or 4th day of hydration. However, SAP C 0.30+0.07 exhibited autogenous shrinkage from the first day of hydration. An explanation for this discrepancy could be a faster decrease in permeability of the matrix due to reaction of silica fume. Further, due to smaller pore size distribution of SAP D inclusions and consequently larger fractions of protected matrix at smaller distances from the SAP surface, the respective onset of self-desiccation is postponed. The earliest time when specific points in the matrix of SAP D 0.30+0.07 are not protected anymore is at least the 7th day of hydration. Actually, SAP D 0.30+0.07 prevented self-desiccation for at least 28 days and probably even longer, cf. [Jensen & Hansen 2002].

A general weak point of the estimate is that the surface to volume ratio of the SAP inclusion is not taken into account. The travel distance of water is assessed by the distance of the nearest neighbour point from the surface of SAP only, i.e. independent of the volume of the water reservoir. But with smaller SAP size the IC water is exhausted faster and the protection zone especially at early stage of hydration might be smaller than the proposed travel distance of several mm, see Figure 7.6. Further, as mentioned above, with the maximum travel distance of 200 μm assumed at the late stage of hydration, none of the SAP types used in practice will be able to provide long-term protection of the whole matrix. Thus, efficient curing as observed e.g. for SAP D 0.30+0.07 is expected to be a matter of high mobility of water in the paste at early hydration.

Wyrzykowski [Wyrzykowski et al. 2012] modelled the water-migration process during internal curing with SAP. He used a recently developed mechanistic-type numerical model of Gawin [Gawin et al. 2006]. His analysis showed that water is distributed not only from the macropore inclusion to the cement paste in its vicinity, but is also redistributed from regions of higher water saturation to those neighbouring regions of lower saturation, even after the permeability has become very low. Blocking of capillary pores with hydration products was accompanied with a drop in permeability down to approximately $1 \times 10^{-19} \text{ m}^2$. As a result, the water will be distributed nonuniformly as water transport is inhibited or at least is very slow. If IC water is still present in SAP at this time, further drop in permeability will lead to poor accessibility. This observation is in good agreement with results obtained by neutron tomography [Trtik et al. 2010]. The permeability threshold in [Wyrzykowski et al. 2012] was deduced in analogy with [Cui & Cahyadi 2001] as 0.18. From experimental observations on Portland cement paste at w/c of 0.30 reported in [Lura et al. 2006c], it was suggested that the depercolation of the capillary porosity occurs at a hydration degree of about 50%, i.e. at the age of about 2 days in case of the HPM mixes.

It can be noted that insufficient curing of SAP C 0.30+0.07 may be the result of poor accessibility of water present in large SAP C pores at the time when the permeability of the matrix is very low, as of approximately 2 days of sealed curing. Since the largest distance IC water must travel to protect all points in the matrix is about 2 mm (HCSS model), the speed of water redistribution from regions of higher degree of saturation into regions of lower degree of saturation, as proposed by Wyrzykowski, is expected to not meet the demand of hydration. In consequence, the internal RH is expected to drop causing autogenous shrinkage although IC water is still present in SAP C. This last assumption should be clarified by combining NMR with RH measurements.

7.5 Conclusion and outlook

7.5.1 Conclusion

Five high performance mortar mixes viz two without and three with internal curing due to SAP were investigated with respect to strength and free autogenous deformation. The results comply to a great extent with findings of investigations on plain and water-entrained cement pastes:

- It was established that SAP D can be used for successful long-term prevention of autogenous shrinkage in HPM as well.
- Absolute shrinkage of reference mortar amounted to circa 50% of the respective paste value, which is in good correlation with the volume of aggregates.
- The strength tests confirmed that compressive and flexural strength is reduced at the same rate for both, addition of extra water and water entrainment.
- Additionally, it could be shown that a smaller or even to put it this way, insufficient amount of entrained water significantly reduces the effectiveness of internal curing on a time basis, i.e. autogenous shrinkage was rather mitigated than prevented.

A new phenomenon was observed on mortar SAP C 0.30+0.07. Although the amount of entrained water was theoretically sufficient for complete prevention of autogenous shrinkage, the strain measurements revealed shrinkage directly after first expansion, i.e. after 1 day of sealed curing. To account for this observation, the spatial distribution of SAP C pores in the hardening mortar was calculated by the HCSS model and the distance water can travel in the hydrating matrix was estimated. The essential considerations are as follows:

- The unprotected paste fraction is increasing with hydration due to reduced permeability of the matrix and with decreasing the surface to volume ratio of SAP.
- It is expected that SAP C pores are still partially saturated when self-desiccation starts in the unprotected matrix zone as a consequence of poor accessibility and too slow redistribution of curing water from saturated regions into regions with less saturation degree.
- As a rough guide, long-term protection of self-desiccation shrinkage is assumed when the nearest neighbour point is in the distance of at most 1 mm from the SAP surface.

7.5.2 Outlook

Combined RH and NMR measurements could bring evidence on the assumption that the onset of self-desiccation of SAP C 0.30+0.07 is at the same time when the polymer still retains substantial parts of the curing water. In general, further measurements on the permeability threshold and studies on the spatial distribution of SAP are needed to give recommendations for reliable long-term prevention of self-desiccation or to predict the onset of autogenous shrinkage.

8 Shrinkage and tensile creep of concrete

8.1 Introduction

In this chapter the effects of SAP on shrinkage of concrete and tensile creep of concrete under constant load are investigated. Three normal strength concrete (NSC) mixtures with w/c ratios of 0.42, 0.36 and 0.36+0.06 (SAP A) were produced. All strain measurements were performed on dog-bone shaped specimens and started one day after casting. The specimens were either sealed by adhesive aluminium vapour barrier foil or were exposed to moderate drying. The tensile load was applied from 28 days after casting and amounted to 60% of the 28 days tensile strength. Simultaneously measured unloaded specimens served as reference to determine the share of shrinkage in total deformation. The strain measurements ended after 6 months.

8.2 Materials and methods

8.2.1 Concrete compositions

Three concretes of strength class C50/60 to C55/67 were designed as reported in Table 8.1. In contrast to HPM mixtures presented in chapter 7, the content of cement is constant for all NSC mixtures. The lower total water content of Ref 0.36 was compensated by the higher content of aggregates. As a result, the volume of the cement paste matrix was reduced compared to mixtures SAP A 0.36+0.06 and Ref 0.42. The grading curve of aggregates followed an approximated Fuller curve [Fuller & Thompson 1907] with gradation exponent of 0.50 and maximum aggregate size of 8 mm. The size range of dry SAP A was 63-125 μm . To maintain workability, superplasticizer Glenium ACE 30 from BASF was used. The concretes were mixed in batches of at least 70 l by means of a 150 l pan-type mixer. Cement powder, oven-dried aggregates and dry SAP were pre-mixed for 30 s before the first half of the mixing water was added. After 120 s of mixing the second half of the water was added together with the superplasticizer. The total mixing time was 5 min. Actual values for the air content measured on the fresh concretes according to [DIN EN 12350-7 2009] ranged between 1.8 and 2.3%. The concrete spread was found to yield consistency class F3 (420 to 480 mm).

Table 8.1: Scheduled compositions of NSC

Component	Unit	Ref 0.42	SAP A 0.36+0.06	Ref 0.36
Strength class	-	C50/60	C50/60	C55/67
CEM I 42.5 R	kg/m ³	450	450	450
Aggregate 0/8	kg/m ³	1697	1695	1768
Water total	l/m ³	189	189	162
Water in SAP	l/m ³	-	27	-
(w/c) _{basic}	-	0.42	0.36	0.36
(w/c) _e	-	-	0.06	-
SAP A dry (63-125)	kg/m ³	-	1.13	-
PCE	kg/m ³	0.5	0.8	1.0
Air content	l/m ³	20	20	20

8.2.2 Strain measurements

The aim of the testing program was to investigate the effect of SAP on shrinkage and creep of concrete under constant tensile loading. To this end, strain measurements were performed on specimens that were either loaded from 28 days after casting at 60% of the stress-strength ratio σ_t/f_{ct} or remained unloaded. In the latter case, shrinkage was measured. Superimposing both concurrent measurements led to the approximated creep strain as a function of time, see section 2.8.



Figure 8.1: Dog-bone shaped specimens: drawing in mm, unsealed test sample, test sample in PE-envelope, test sample sealed by aluminium vapour barrier foil (from left to right).

The strain measurements took place in a thermostatically controlled room at $20 \pm 2^\circ\text{C}$ and $65 \pm 2\%$ RH. They were performed on dog-bone shaped specimens that were especially designed for tensile testing of concrete by Rinder [Rinder 2002]. Shape and dimensions are shown in Figure 8.1 (left). For each concrete mix 17 dog-bone shaped specimens were produced: 2 for observing weight loss due to drying, 8 for the determination of the 28 days tensile strength and 7 for measuring strains. The latter were each equipped with two LVDTs attached to extension rods along the two lateral sides of the specimen with constant cross section. Both the LVDTs and the extension rods were mounted via aluminium supports that were stuck on the specimen by means of two-component glue X60. The measuring distance was 300 mm. Further sample preparation was made in dependence on the test mode the specimens were intended for as provided by Table 8.2. Figure 8.1 shows examples of the three different curing regimes:

- unsealed
- packed in PE-envelope
- sealed by vapour barrier foil.

Table 8.2: Testing program conducted for the investigation of shrinkage and tensile creep of NSC

Sample No.	Measurements from 1 day to 28 days		Measurements between 28 days and 6 months		
	Curing regime	Strain _{meas.}	Loaded	Regime during test	Strain _{meas.}
1 (I)	Unsealed	$\varepsilon_{as} + \varepsilon_{ds}$	No	Unsealed	$\varepsilon_{as} + \varepsilon_{ds}$
2 (I)	PE-envelope	$\varepsilon_{as} + \varepsilon_{ds}$	No	PE-envelope	$\varepsilon_{as} + \varepsilon_{ds}$
3 (I)		$\varepsilon_{as} + \varepsilon_{ds}$	Yes		$\varepsilon_{as} + \varepsilon_{ds} + \varepsilon_{el} + \varepsilon_{bc} + \varepsilon_{dc}$
4 (II)	Vapour barrier foil	ε_{as}	No	Vapour barrier foil	ε_{as}
5 (II)		ε_{as}	Yes		$\varepsilon_{as} + \varepsilon_{el} + \varepsilon_{bc}$
6 (II)		ε_{as}	No	Unsealed	$\varepsilon_{as} + \varepsilon_{ds}$
7 (II)	ε_{as}	Yes	$\varepsilon_{as} + \varepsilon_{ds} + \varepsilon_{el} + \varepsilon_{bc} + \varepsilon_{dc}$		

Sealing by adhesive aluminium vapour barrier foil was expected to provide an appropriate environment for measuring autogenous deformation. In contrast, wrapping in PE-foil was not a real sealing condition. The objective was rather to slowly approach the ambient air humidity inside the PE-envelope and thus provide decelerated drying. Unsealed means the specimens were exposed to drying at room climate either from the first day or from 28 days after casting. In the latter case, the sealing was removed in time.

Due to insufficient number of LVDTs the testing program was split in a sequence of two series. The first series (I) contained measurements on all no.1 to no.3 specimens. After the first series had been finished the second series started. In the second series (II) all no.4 to no.7 specimens were tested. All measurements within a series were performed simultaneously in order to maintain comparability among the concrete mixes. In all cases the strain measurements started 24 hours after casting and ended 6 months later.

Unloaded specimens were stored upright on two steel rods with a centre distance of 550 mm. In case of loaded specimens, steel anchors known from the pre-cast industry had been encased centrally at the top and bottom in order to apply the tensile load into the specimen. Socket bolts were inserted in the anchors connected to the loading frame via hinges. The loading frame consisted of a steel lever with a load ratio of 20:1 using steel plates as loading weights. The steel plates were initially stacked on a rotary stool which was wind down in order to approach monotonical loading of the specimen. The creep stress was reached once the steel plates were free of contact. This took about 120 s. A drawing of the loading frame is provided in appendix 8.

The total deformation ε_{tot} of a loaded specimen exposed to drying is the sum of several contributions including crack formation and crack propagation. At constant temperature ε_{tot} is:

$$\varepsilon_{tot}(t, t_d, t_0) = \varepsilon_{as}(t) + \varepsilon_{ds}(t, t_d) + \varepsilon_{el}(t_0) + \varepsilon_{bc}(t, t_0) + \varepsilon_{dc}(t, t_d) \quad (8.1)$$

with ε_{as} = autogenous shrinkage, ε_{ds} = drying shrinkage, ε_{el} = instantaneous strain at loading, ε_{bc} = basic creep, ε_{dc} = drying creep, t = age of concrete, t_d = age at begin of drying and t_0 = age at loading.

The differences in ε_{ds} and ε_{dc} between specimens in PE-envelope and unsealed specimens base on the fact that the latter specimens are exposed to severe drying conditions. No.8 and no.9 specimens used for measuring weight loss due to drying were stored by analogy with specimen no.1 and no.6, respectively. Weight loss of the specimens in PE-envelope could not be observed.

8.2.3 Mechanical properties

The loading rate applied for creep measurements was 60% of the measured average 28 days tensile load capacity. On this account, the 28 days tensile strength was determined both on four samples packed in PE-envelope as part of the first series, and on four samples sealed by adhesive aluminium vapour barrier foil as part of the second series. As the strain measurements had been finished, the bone-shaped specimens were stored unloaded for 6 and 18 months, respectively, before their residual tensile strengths were determined.

The compressive strengths after 28 days, 1 year (series II) and 2 years (series I) were determined on cubes with 150 mm edge length that were all stored in PE-envelope until testing. Further, cylinders with diameter of 150 mm and height of 300 mm were also stored in PE-envelope and were used for the determination of the Young's modulus at the age of 28 days according to [DIN 1048-5 1991]. The Young's modulus in tension was derived from the stress-strain curve at loading and thus is the secant modulus of elasticity.

8.3 Results and discussion

8.3.1 Mechanical properties

Table 8.3 provides the data on mechanical properties of series I specimens which were all wrapped in PE-envelope until testing. Table 8.4 reports on the data of series II specimens which were sealed by adhesive aluminium vapour barrier foil, unless stated otherwise. The residual tensile strengths measured after one year and two years, respectively, provide the data of one single specimen only. It is either the value of the unloaded autogenous shrinkage specimen or the value of the loaded creep specimen which was, after unloading at the age of 6 months, stored load-free until testing. During loading of the creep specimen, the elastic modulus in tension was determined as secant modulus. The cylinder strength provides test results obtained within the scope of the Young's modulus measurements in compression.

Table 8.3: Mechanical properties of series I specimens (PE-envelope) in MPa

NSC mixture	Tensile strength			Cube strength		Elastic modulus		Cyl. str.
	28 d	2 a ¹⁾	2 a ²⁾	28 d	2 a	28 d	28 d ³⁾	28 d
Ref 0.42	4.38	4.90	5.66	62.8	85.8	38800	41700	58.8
SAP A 0.36+0.06	4.42	5.88	5.86	63.4	91.1	38400	41400	62.2
Ref 0.36	4.99	6.07	6.60	75.3	98.8	44500	46700	71.0

¹⁾: autogenous shrinkage specimen no.2 (I) or no.4 (II), respectively.

²⁾: creep specimen no.3 (I) or no.5 (II) stored load-free after unloading at the age of 6 months.

³⁾: secant modulus of elasticity in tension measured on specimen no.3 at loading.

Table 8.4: Mechanical properties of series II specimens (vapour barrier foil) in MPa

NSC mixture	Tensile strength			Cube strength		
	28 d	1 a ¹⁾	1 a ²⁾	28 d ⁴⁾	1 a ⁴⁾	1 a ⁵⁾
Ref 0.42	4.50	6.1	5.8	66.6	80.6	78.8
SAP A 0.36+0.06	4.74	6.3	6.7	65.7	87.0	77.8
Ref 0.36	5.48	7.1	7.4	74.0	98.7	94.2

⁴⁾: stored in PE-envelope

⁵⁾: stored unsealed at 20°C and 65% RH.

Mixture Ref 0.36 consistently shows the highest strength values. In general, values measured in series II are somewhat higher compared with values of series I. In case of tensile strength, it may be the result of different storing conditions, i.e. PE-envelope (moderate drying) vs. aluminium vapour barrier foil (real sealing condition). The latter storage is expected to mitigate micro-cracking of concrete skin more powerful. However, the cubes were stored in PE-envelope until testing in case of both test series. It seems as if the second series produced higher quality of concrete probably due to different batches of cement used. At the age of 28 days, tensile strength, compressive strength and Young's modulus of the SAP-modified concrete is similar to Ref 0.42. At later age of one or two years, the strength of SAP A 0.36+0.06 is on the higher increase compared to Ref 0.42. The cube strength of Ref 0.36 does not differ much between 1 year (series II) and two years (series I), which may be explained by the fact that hydration has dramatically slowed down. The Young's modulus in tension was generally higher compared to the compression case since no cyclic loading was applied. The compressive strength measured on cylinder is decreased by up to 7% compared with the cube strength. So the cubes exposed to room climate for one year possessed up to 10% less strength compared with cubes stored in PE-envelope.

The 28 days tensile strength value is the average value of 4 specimens tested. The standard deviation was rather high, i.e. up to 0.6 N/mm². The loading factor of 60% is related to the mean strength value and is not a ratio of the individual specimen strength. Details on load application are reported in appendix 8. The residual tensile strength measured after 1 and 2 years, respectively, represents the data of one single specimen and is therefore less meaningful. However, with exception of mixture Ref 0.42, the unloaded companion specimens exhibited less tensile strength than the formerly loaded creep specimens. Such observation was also reported in [Cornelissen & Reinhardt 1986] and in [Reinhardt & Rinder 2006]. Reinhardt and Rinder concluded that hydration of high-strength concrete is accelerated when under tensile load in accordance with [Blaschke 1993]. Due to loading, pores are widened and water transport is facilitated. Also in this regard, they found that loaded specimens dry faster than unloaded specimens. This tendency was also found in case of Ref 0.36, as evident from Table 8.5. But again, the test result is of little significance since the data is obtained from single specimens only.

Table 8.5: RH inside PE-envelope of creep and companion specimen

Concrete Mix	RH after 1 day		RH after 28 days		RH after 100 days		RH after 150 days	
	-	-	loaded	unloaded	loaded	unloaded	loaded	unloaded
Ref 0.42	100%	100%	96.3%	95.6%	91.1%	90.4%	85.6%	85.2%
SAP A 0.36+0.06	100%	100%	96.5%	96.1%	93.0%	93.3%	86.7%	87.5%
Ref 0.36	100%	100%	93.7%	93.0%	87.5%	89.7%	82.3%	85.1%

The humidity around loaded and unloaded specimens at $(w/c)_{tot}$ of 0.42 developed more or less the same. Of course the RH decreases faster, the lower the w/c ratio is. Nevertheless, condensation occurred within the first days of sealing independent on w/c ratio. The humidity around the series I cubes at the age of 2 years was 80.4% RH in case of Ref 0.42, 82.9% RH in case of SAP A 0.36+0.06 and 78.7% RH in case of Ref 0.36. This means that no equilibrium between ambient air humidity inside and outside the foil was reached even after 2 years. From measurements on internal RH of cement paste (see chapter 6.3.4) it can be assumed that the decrease of internal RH of concrete due to self-desiccation is steeper.

Another aspect contributing to higher residual tensile strength of formerly loaded specimens is that the elastic delayed creep strain as from unloading has been subsided at the age of testing.

8.3.2 Deformations due to shrinkage, loading and tensile creep

Figure 8.2 to Figure 8.4 provide the total deformations measured from 1 day after casting. The no.2 and no.4 specimens represent the unloaded specimens used to measure free concrete shrinkage. In the first 28 days after casting, i.e. before loading, no.3 and no.5 specimens serve for the determination of shrinkage as well. All concretes have in common the higher shrinkage of series I specimens as a result of moderate drying in PE-envelope, compared with sealed series II specimens. In case of NSC Ref 0.36 the difference, viz the extra drying shrinkage strain, is very small due to low w/c ratio and small weight loss potential. Shrinkage of no.3 and no.5 specimens is almost the same with the companion specimens no.2 and no.4, respectively. Exception is made for shrinkage strains of NSC SAP A 0.36+0.06 which scatter much. On the one hand, specimen no.2 shows initial expansion of 10 μ strain and later on, at 28 days, shrinkage of 30 μ strain. On the other hand, the 28 days shrinkage of specimen no.3, which belongs to series I, too, is about 65 μ strain. As revealed in chapter 6, SAP A is not able to prevent complete autogenous shrinkage due to less water absorption than expected, i.e. $(w/c)_e < 0.06$, but rather retards shrinkage.

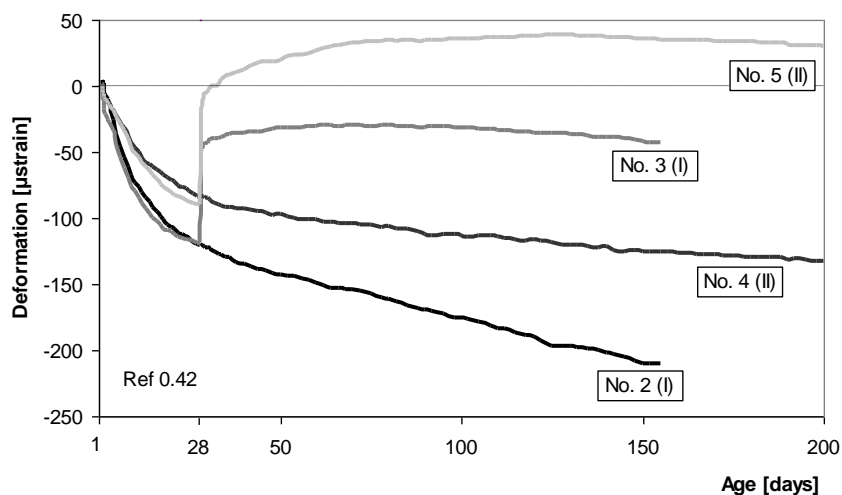


Figure 8.2: Total deformation of specimens no.2 to no.5 of NSC Ref 0.42.

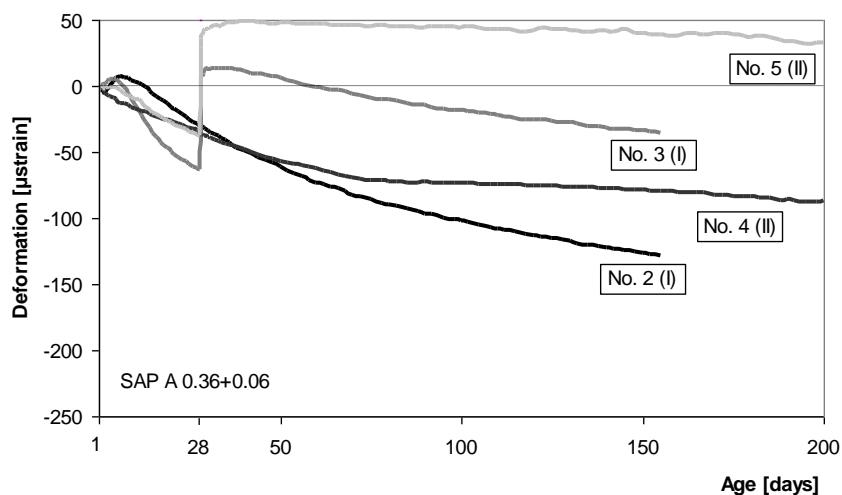


Figure 8.3: Total deformation of specimens no.2 to no.5 of NSC SAP A 0.36+0.06.

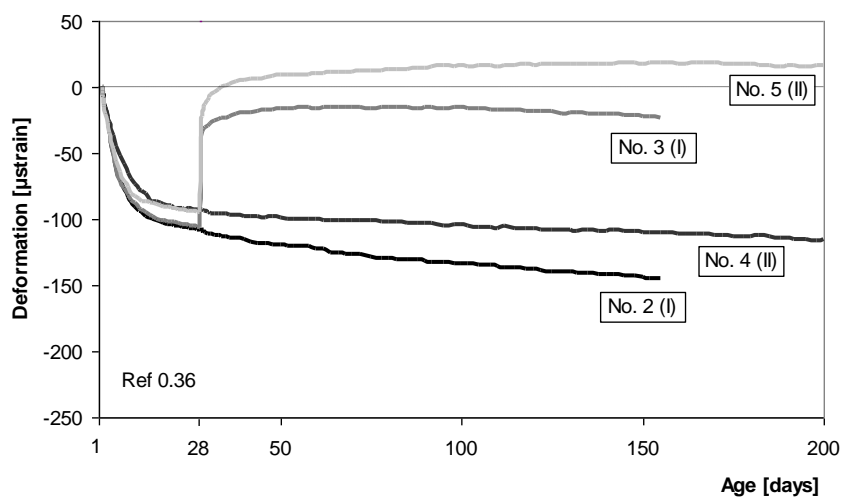


Figure 8.4: Total deformation of specimens no.2 to no.5 of NSC Ref 0.36.

As known from autogenous shrinkage measurements on sealed cement paste, see section 6.3.2, concrete Ref 0.36 is expected to show high autogenous shrinkage within the first 24 hours. After this early age period the strain-time curve flattens. Unfortunately, it was not possible to measure concrete strain at the first day. This fact might explain the small difference in autogenous shrinkage between Ref 0.42 and Ref 0.36. In section 8.3.6 an approach is presented that approximates the real concrete shrinkage as from setting. Most total deformation curves of loaded specimens are plotted as negative, i.e. opposite to the direction of loading. It indicates that the total shrinkage deformation is higher than the sum of elastic strain at loading and creep. Shortly after loading, tensile creep is much higher than shrinkage, but at least 4 months later the total deformation curve turns into the direction of shrinkage.

The elastic strain at loading of no.3 specimen is plotted in Figure 8.5. The diagrams show the strains of both LVDTs. From the average strain, the Young's modulus in tension reported in Table 8.3 on p.113 was calculated. Further details on load application are reported in appendix 8.

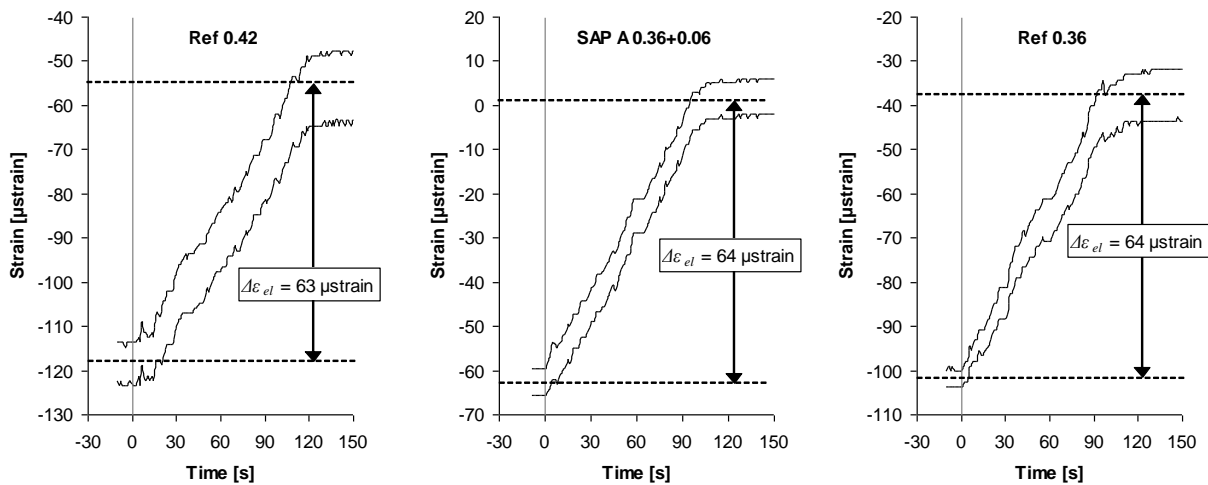


Figure 8.5: Instantaneous strain at loading of no.3 (I) specimen.

The total minus shrinkage strain of all no.3 and no.5 specimens as a function of age is presented in Figure 8.6. The plotted strain curves include the instantaneous elastic strain at loading ϵ_{el} , and the creep strain ϵ_c . The relation between these two strain components is referred to as creep coefficient and is shown as a function of age in appendix 8. The creep strain consists of irreversible plastic set, time-dependent delayed elastic strain and viscous strain component, see chapter 2.5.1. The results at hand do not allow separation of the individual creep components by quantity. But, since no.3 specimens (series I) were exposed to moderate drying whereas the no.5 specimens (series II) were measured in sealed condition, the intention was to subdivide creep strain into basic creep ϵ_{cb} and drying creep ϵ_{dc} . Here, it is rather to speak of sealed creep instead of basic creep since sealed creep means basic creep plus extra creep resulting from self-desiccation. The no.3 specimens were expected to indicate higher total creep due to extra drying creep strain. But, the direct comparison with no.5 specimens exhibits hardly any differences as evident from Figure 8.7. Consequently, it can be noted that moderate drying in PE-envelope did not lead to drying creep. To explain this finding, the origin of drying creep needs to be discussed in connection with the present test conditions. Concerning micro-cracking of concrete skin as cause of drying creep, it can be assumed from the RH measurements in PE-foil that drying of no.3 specimen is very slow and might have been exceeded by the drop of internal RH. Self-desiccation generates no eigenstresses as known from external drying since progress is always uniform over the cross-section. It

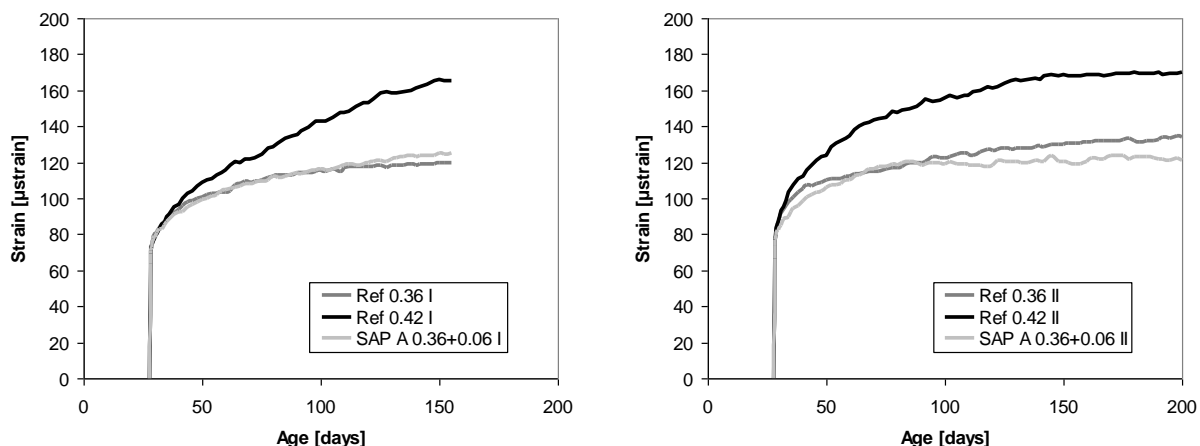


Figure 8.6: Total minus autogenous shrinkage strain as a function of age zeroed before loading. Left: no.3 minus no.2 specimen (series I). Right: no.5 minus no.4 specimen (series II).

means that micro-cracking plays only a minor role in this case since the cracking susceptibility seems to be almost unaffected by the two storage conditions and self-desiccation should amount the same for both no.3 and no.5 specimens. Additional experiments on the electrolytic resistance of concrete measured continuously by multi-ring-sensor electrodes in analogy with [Schießl & Raupach 1992] confirmed this assumption. The measurements revealed that the time-dependent change in internal resistivity is almost the same for both storage conditions, see appendix 8. The second possible cause of drying creep, viz stress induced shrinkage, may also be driven by self-desiccation instead of external drying. In consequence, no drying creep was measured, but rather sealed creep which, obviously, amounted the same for both no.3 and no.5 specimens.

It is quite possible that the moderate drying regime was too conservative and the load ratio of 60% was too low to emphasize the effect of drying creep in tension. It is well known that drying creep increases with increasing weight loss and load ratio. In [Kordina 1999] tensile creep tests of NSCs with w/c of 0.55 were performed under drying and sealed condition as of 28 days, but the difference in creep strain was only small. High concrete strength may also impede drying creep. For the compression case it was found that increasing the strength class reduces the drying creep strain almost to zero [De Larrard & Acker 1992]. The corresponding limit strength was proposed with 100 MPa [Schrage & Springenschmid 1996] and probably is lower in case of tension loading.

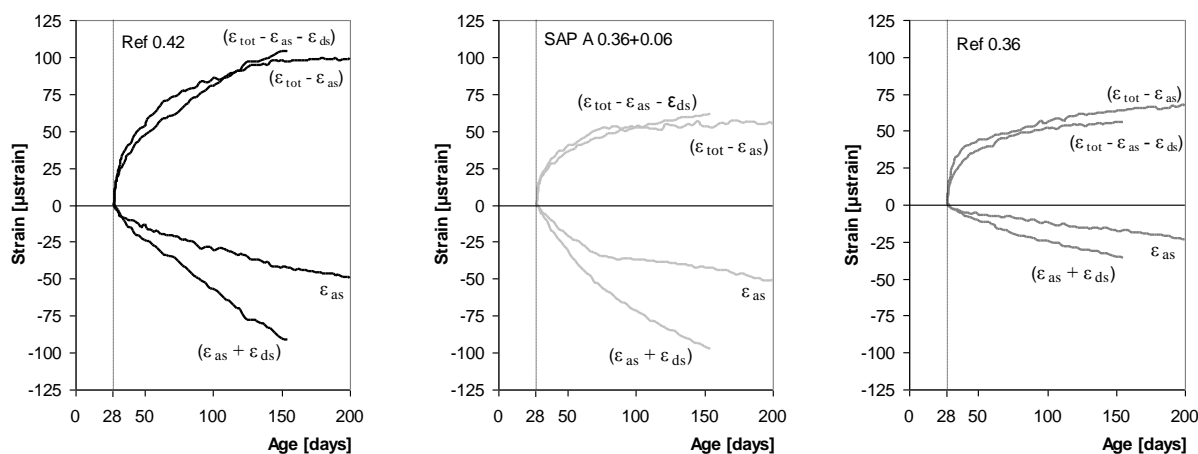


Figure 8.7: Shrinkage and total minus shrinkage strain as a function of age zeroed after loading.

8.3.3 Effect of SAP on tensile creep

The remaining question is why the creep strain of concrete SAP A 0.36+0.06 is almost the same with concrete Ref 0.36 and, at the same time, shrinkage is similar to concrete Ref 0.42.

Figure 8.7 presents the shrinkage strain measured on no.2 (I) and no.4 (II) specimens zeroed at the end of loading and the respective total strain of no.3 (I) and no.5 (II) specimens minus shrinkage strain as a function of age. Autogenous strain ε_{as} measured on no.3 specimen is of course lower compared with the first 28 days, but still existent for all concrete mixes even at higher age. It is an indication for ongoing hydration. As found in chapter 6, the pastes of Ref 0.42 and SAP A 0.36+0.06 show the same hydration development and therefore it is obvious that autogenous shrinkage is also similar, apart from different behaviour at early age. As from 28 days, autogenous shrinkage of Ref 0.36 is the smallest. The shrinkage strain ε_s measured on no.2 (I) specimen is generally higher than ε_{as} of no.4 (II) specimen since it includes moderate drying shrinkage. It can be concluded that shrinkage is more sensitive to moderate drying than creep, since extra strain from drying creep was not measured as highlighted by the total minus shrinkage strain curves in Figure 8.7.

As indicated by Figure 8.6, the creep strain of SAP-modified concrete is comparable to the reference concrete with same $(w/c)_{basic}$. This finding is of course to be understood as rough guide since it is the result of individual specimens. For example the residual tensile strength of concrete SAP A 0.36+0.06 was on the higher increase with respect to the 28 days mean tensile strength compared to concrete Ref 0.42. So it is possible that the individual tensile strength of the loaded creep specimen was higher than expected and the load ratio was less than 60%. However, validation is required, especially in regard of modified test conditions, i.e. variation of age at loading, stress-strength ratio and air humidity. Up to now, water content of concrete and possible water loss from concrete were expected to be the main factors influencing creep. This generalized view is in conflict with the results found for SAP-modified concrete which obviously shrinks the same with reference concrete of same total w/c ratio, but its creep strain is comparable to the reference concrete with less total water content. For this reason it is suggested that the micro-pore structure is the key factor influencing creep of concrete under constant tensile load. On the basis of accepted creep mechanisms introduced in chapter 2.5.3, the creep-reducing effect of SAP addition may be explained as follows:

- The seepage theory [Powers 1968] states creep to be a time-dependent removal of a swollen state of gel solid due to diffusion of gel water from regions of hindered absorption into absorptive pore space when under load. The distance of gel particles is specified by the basic w/c ratio and hence the disjoining pressure may decrease in a similar manner for both SAP A 0.36+0.06 and Ref 0.36, resulting in similar creep deformation.
- The viscous flow hypothesis [Ruetz 1968] postulates shearing or sliding of CSH particles under load to be the main source of creep. In doing so, the lubricating effect of absorbed water should depend on the water layer thickness and therefore is also defined by the basic w/c ratio.

8.3.4 Literature review on creep of internally cured concrete

Only few studies concerning creep of internally cured concrete exist. Among creep in tension of high performance concretes, Rinder [Rinder 2002] investigated one hybrid concrete mixture of strength class C70/85 in analogy with [Weber & Reinhardt 1997] by replacing the gravel at sieve size 4 to 8 mm with expanded clay. The boundary conditions were similar to the one used here,

e.g. the curing regime corresponded with “PE-envelope” and loading was done at concrete age of 28 days. However, the stress-strength ratio applied was rather high, i.e. $> 80\%$. Creep in tension was found to be higher compared to concrete produced with normal weight aggregates, but was probably caused by lower modulus of elasticity of concrete because of weak LWA.

Another investigation on tensile creep of internally-cured high-performance concrete was performed by Cusson and Hoogeveen [Cusson & Hoogeveen 2005]. They examined HPC mixes produced at w/c of 0.34 and provided internal curing by replacement of up to 20% sand by volume with pre-soaked structural lightweight aggregate made of porous expanded shale. However, the measurements were aimed on the first 7 days of sealed hydration only. Within this time the tensile creep coefficient was moderately increased for the internally cured mixes while no influence on strength or modulus of elasticity could be observed. The results are in conflict with observations presented here, which may come from different boundary conditions taken as basis.

In [Lopez et al. 2010] creep in compression was examined on high performance concretes at w/c of 0.23 with internal curing due to either pre-wetted or dryly added LWA plus extra water to account for water absorption in the latter case. The creep behaviour of both mixes was set in contrast to the reference concrete without IC. Both internally cured concretes exhibited a reduction in strength compared with the control mixture. The mixture with pre-wetted LWA showed about 10% less creep than the reference concrete while the mixture with dry LWA and extra water showed the greatest creep.

8.3.5 Shrinkage and tensile creep of concrete under severe drying conditions

The left diagram of Figure 8.8 reports on the total deformation of no.1 (I) and no.6 (II) specimens. The no.1 specimens were exposed to severe drying at 20°C and 65% RH immediately after demoulding. In case of no.6 specimens, the concrete was sealed for the first 28 days and then was unpacked in order to equilibrate to the surroundings. In the right diagram the autogenous deformation measured on companion specimen no.2 (I) and no.4 (II), respectively, was subtracted to eliminate the share of autogenous shrinkage in total strain. In doing so it becomes clear that the discrepancy in total strain of concrete Ref 0.42 and SAP A 0.36+0.06 exposed to early drying is a result of reduced autogenous shrinkage strain due to IC by SAP. In case of delayed drying the

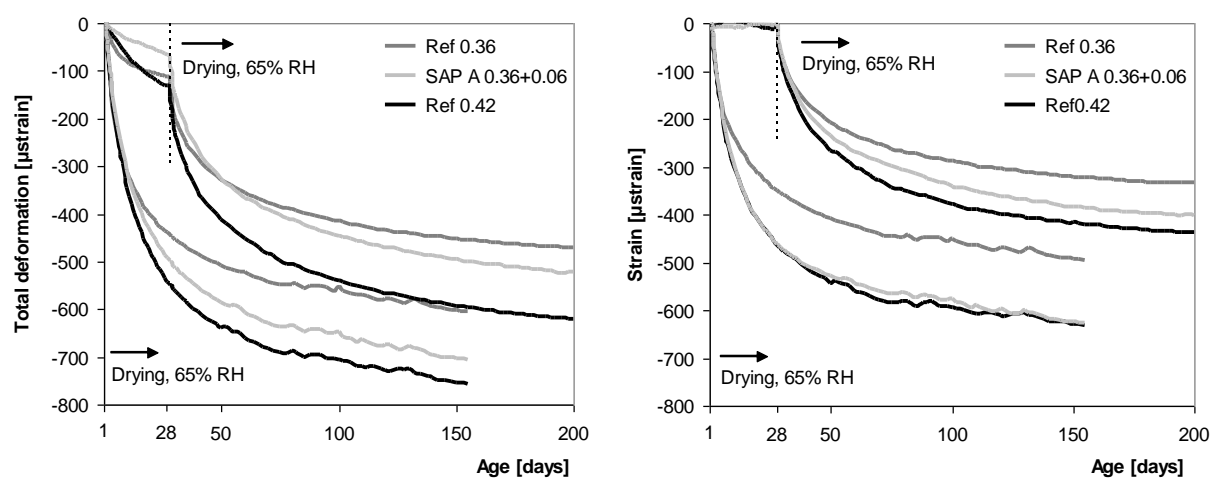


Figure 8.8: Total shrinkage of no. 1 (I) specimen exposed to early drying and no.6 (II) specimen exposed to delayed drying (left) and the respective strain curves where autogenous strain measured on companion specimen no.2 (I) and no.4 (II) was eliminated (right).

SAP-modified concrete shrinks less compared with Ref 0.42 although weight loss is higher as reported by Figure 8.9. Maybe the difference in microstructure formation caused this effect. So SAP A 0.36+0.06 possessed the finer pore structure, i.e. comparable to Ref 0.36, and also at the same time, possessed the higher saturation degree and the higher internal RH due to water reservoirs. In consequence, more water is drained via the large capillaries which is prior to loss of physically bound water and causes less shrinkage. If early drying is considered, drainage will start at complete saturation in both cases and the effect will vanish. The right diagram of Figure 8.9 shows that the deformation vs. weight loss curves of Ref 0.42 and SAP A 0.36+0.06 match well. Of course, concrete Ref 0.36 exhibits the smallest drying shrinkage and weight loss. But the total deformation would exceed the other strain curves if early age autogenous shrinkage was included.

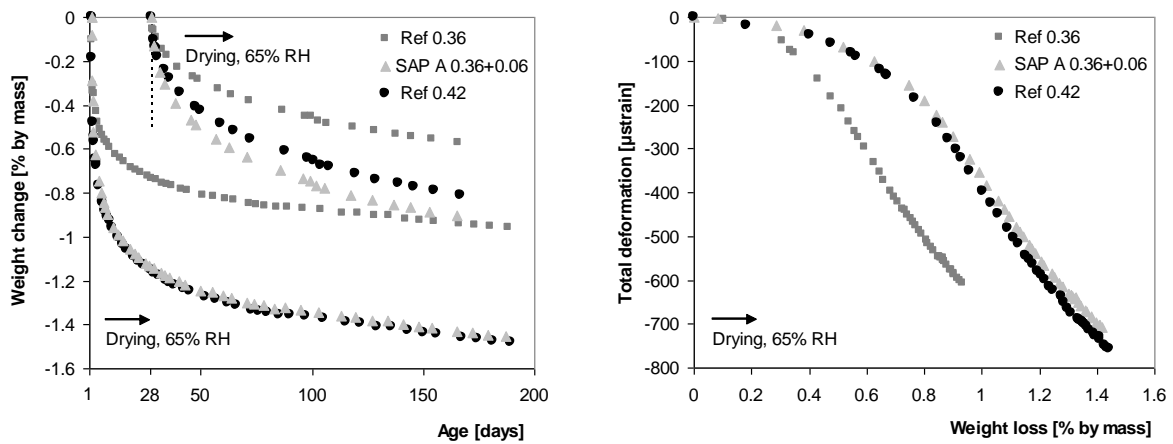


Figure 8.9: Change in weight due to drying at 65% RH as a function of age (left) and total deformation of no.1 (I) specimen as a function of weight loss (right).

In [Jensen & Hansen 2002] it is reported that the total shrinkage strain of cement paste at basic w/c of 0.30 exposed to 50% RH after sealed curing of 4.5 months was increasing with increasing the entrained water content. The strain measurements were conducted as of setting and revealed that the effect of water entrainment on autogenous deformation completely overrides the effect of residual shrinkage. However, comparative tests on weight loss and total shrinkage were not performed on plain pastes with same total water content.

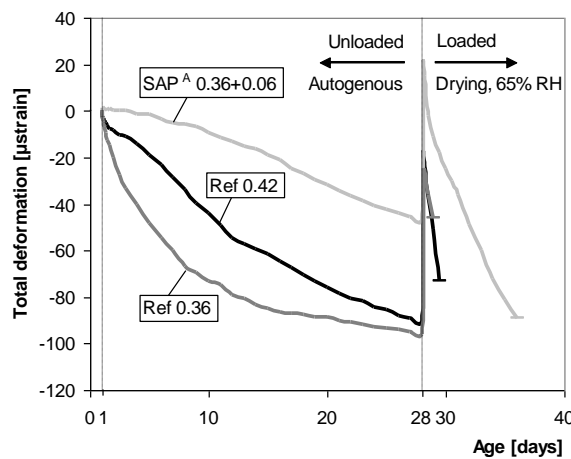


Figure 8.10: Deformation at sealed condition followed by drying under tensile load of no.7 (II) specimen until failure.

Figure 8.10 presents the total deformation of no.7 specimens until failure. The autogenous deformations up to an age of 28 days comply with results of measurements on sealed no.4 to no.6 specimens. After the load was applied, the vapour barrier foil was removed. As a consequence, tensile creep is superimposed by drying shrinkage. Micro-cracks appear on concrete skin, are extended under load and degrade the cross-section until failure. First, concrete Ref 0.36 failed 23 hours after loading, followed by Ref 0.42 with a delay of 14 hours. At last failure of SAP A 0.36+0.06 was observed 8 days after loading. It is conspicuous that the drop in total strain is flatter for SAP A 0.36+0.06. It is assumed that less micro-cracking occurred during sealed storage and/or after loading as a result of IC. Consequently, the ingress in total shrinkage strain under load developed slower. If a smaller load rate due to higher strength of the individual specimen caused longer time to failure, total shrinkage would even be increased compared with control mixes since shrinkage is in the opposite direction of tensile load.

8.3.6 Modelling of autogenous shrinkage of NSC

A large part of autogenous shrinkage occurs immediately after setting and could not be observed here, since the strain measurements on NSC specimens started 24 hours after casting. To predict the real autogenous shrinkage strains as of setting, an estimate on the basis of the cement paste measurements (chapter 6) is presented. Following Hobbs' model [Hobbs 1971], also referred to as C&CA model [Hobbs 1974], the linear shrinkage of concrete ε_C can be calculated according to:

$$\varepsilon_C = \frac{\varepsilon_{CP} \cdot (1 - \theta_A) \cdot (G_{CP} - G_A) + 2 \cdot \varepsilon_A \cdot \theta_A \cdot G_A}{G_{CP} + G_A + \theta_A \cdot (G_A - G_{CP})} \quad (8.2)$$

where ε_{CP} [m/m] is the shrinkage of cement paste, θ_A [m³/m³] the volume fraction of aggregates, ε_A [m/m] the shrinkage of aggregates and G_{CP} and G_A [GPa] are the shear moduli of the cement paste and the aggregates, respectively.

In this model concrete is treated as a two-phase material that consists of aggregates on the one hand and cement paste matrix on the other hand. The following inputs were used:

- ε_{CP} [m/m], equal to the autogenous deformation of the cement paste as a function of age obtained from dilatometer measurements presented in chapter 6.
- $\varepsilon_A = 0$, that means the shrinkage of aggregates was neglected.
- $\theta_A = 0.67$ for Ref 0.36 and $\theta_A = 0.64$ for Ref 0.42 and SAP A 0.36+0.06 mix, respectively.
- G_A was expected to be 25 GPa corresponding to average values for the elastic modulus of quartz aggregates $E_A = 60$ GPa, assuming the Poisson's ratio as $\mu_A = 0.2$.
- G_{CP} [GPa], equal to the shear modulus of the cement paste as a function of age as reported in appendix 8. The data was derived by linear regression of corresponding values for the elastic modulus E_{CP} , determined statically at the age of 1, 3 and 28 days, cf. Figure 6.18 on page 91. The Poisson's ratio of the cement paste was assumed as $\mu_{CP} = 0.2$.

The calculated autogenous shrinkage strains are presented in Figure 8.11 in comparison to the strains measured on sealed no.4 (II) specimens. At the age of 24 hours the measured strain curves are put on the same level with the calculated strain. The model overestimates autogenous shrink-age and with increasing age the prediction is even getting worse. Probably the creep capability of the matrix reduced the stresses from internal restraints of aggregates and reduced the actual concrete shrinkage. The use of superplasticizer in the concrete mixes may have also falsified the prediction of Hobb's model. According to measurements of Fontana [Fontana 2007] the use of PCE leads to reduction of autogenous deformation.

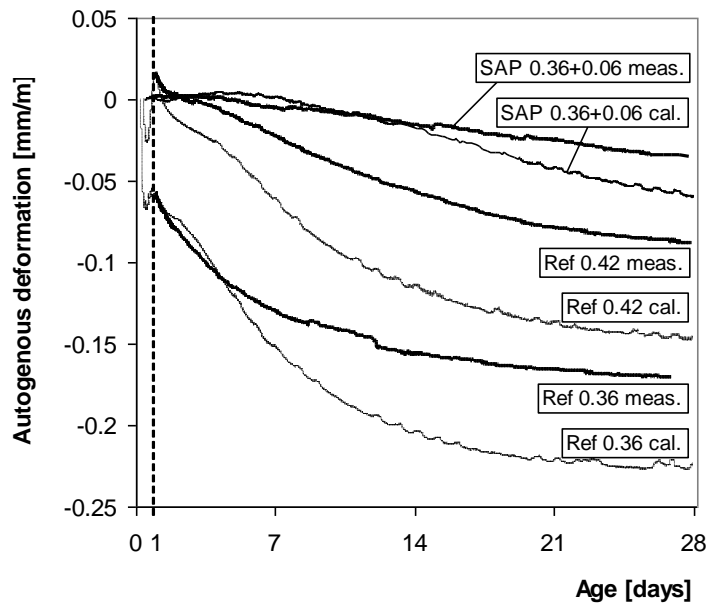


Figure 8.11: Measured autogenous shrinkage of NSCs compared to shrinkage calculated with Hobb's model on the basis of cement paste measurements presented in chapter 6. Measured values are put on the same level with calculated values at the age of 1 day.

Anyway, in case of concretes Ref 0.36 and SAP A 0.36+0.06 the calculated shrinkage matches with the measurements for at least the first 5 and 15 days, respectively. In particular the period of early expansion of SAP A 0.36+0.06 is in good agreement with paste measurements.

Another model for the prediction of concrete shrinkage is for example Pickett's model [Pickett 1956]. Compared with Hobb's model it has some disadvantages, i.e. it requires data on the modulus of elasticity of the concrete as input. On this account Pickett's model has not been pursued here. An empirical model for the prediction of concrete shrinkage was presented in chapter 2.3.7. This model underestimates concrete shrinkage as can be seen from appendix 8.

8.4 Conclusion

Shrinkage and tensile creep of one concrete modified with SAP A produced at w/c of 0.36+0.06 and two control mixes with w/c of 0.36 and 0.42 were investigated. To this end strain measurements were conducted on dog-bone shaped specimens that were either loaded at 28 days after casting at 60% of the mean tensile strength or were stored unloaded. Further, three storage conditions were applied, viz drying at 20°C and 65% RH, curing in PE-envelope in order to provide moderate drying and sealing by adhesive aluminium vapour barrier foil. The comparison of creep strain between the different curing regimes was intended to highlight possible drying creep. From superimposing strains measured on loaded and unloaded specimens, information on the effect of SAP addition on sealed and drying shrinkage, sealed creep and drying creep was anticipated. Unfortunately, concrete SAP A 0.36+0.06 was not prevented from self-desiccation permanently, which agrees with findings of paste measurements presented in chapter 6.

However, from measurements on concrete some new conclusions can be drawn:

- 1) Water entrainment by SAP reduces tensile creep compared to reference concrete with same total water content: The total minus shrinkage strain showed the same curve as the

reference concrete with same basic w/c ratio. This finding is in accordance with viscous flow hypothesis and seepage theory, which are interpreted to mean that creep is determined by the basic w/c ratio. It primarily defines the distance of gel particles and the layer thickness of absorbed water both influencing the creep mechanisms.

- 2) Shrinkage is more sensitive to drying than creep in tension: Exposed to moderate drying conditions, concrete showed higher shrinkage but the same total minus shrinkage strain compared with specimens stored sealed. That means no drying creep strain was measured. It is expected that the drying regime was too conservative and the load ratio was too low to emphasize the possible effect of drying creep.
- 3) Apart from delayed shrinkage at early age, autogenous shrinkage as of 28 days is almost the same for both water-entrained concrete and control concrete with same total water content. Exposed to delayed drying, the concrete strain was higher for the control mix although weight loss was lower. This finding may be explained by the finer pore structure of SAP-modified concrete at later age in combination with higher saturation degree.
- 4) Changing the curing regime from sealed to drying at 65% RH directly after loading the creep specimens showed fast failure. However, the SAP-modified concrete specimen failed at last. It was found that the total strain developed slower. Probably micro-cracking of concrete skin was less due to internal curing.
- 5) Modelling of autogenous shrinkage of concrete by Hobb's model on the basis of measured cement paste strain overestimates the measured concrete deformation particularly at higher age. Effects from superplasticizer used for concrete production may have caused reduction of shrinkage as well as creep capability of the matrix.
- 6) Results on mechanical properties of concrete confirmed findings of mortar and paste measurements: The compressive strength of the SAP-modified mix is similar to the control mix with same total water content at 28 days but is on the higher increase at later age. Concerning tensile strength the tendency was found that formerly loaded specimens possess higher strength compared to continuously unloaded companion specimens.

The observed reduction of tensile creep strain due to addition of SAP is advantageous in case of partially pre-stressed concrete structures where creep results in desirable reduction of deflection. In contrast, high creep capability has positive effects on eigenstresses and longterm stresses induced from restraints. For example, restraint autogenous deformation is considered to be one of the most prominent causes for cracking of high-strength concrete at early age. Here, creep reduces detrimental stresses. However, water entrainment results in mitigation of autogenous shrinkage, which is assumed to be much more effective than high creep capability.

8.5 Outlook

More investigations are needed for confirmation of the presented results. Besides creep under constant tension loading at different stress-strength ratios, the effect of SAP addition on creep in compression should be investigated. Further, the general question could be explored whether creep is higher in tension or in compression. Investigations available in literature produced inconsistent results, e.g. in [Kordina et al. 2000] tensile creep was found to be much less compared with creep in compression whereas in [Brooks & Neville 1977] it was found the opposite.

Severe drying is recommended to highlight possible effects of SAP on drying creep. So far no drying creep was measured since the applied curing regime (PE-envelope) was too conservative

compared to sealed storage (vapour barrier foil). Investigations on drying creep should include fracture mechanical examinations to clarify the share of micro-cracking induced creep in drying creep strain and the possible effect of SAP on micro-cracking.

Further, the influence of age of loading has not been considered yet. For example creep behaviour at early age is very important since thermal stress and high stress from restraint autogenous deformation superimpose creep. It is known that the capability for tensile basic creep is reduced with age, especially in the first days of hydration [Østergaard et al. 2001].

The use of SAP that is able to permanently prevent complete autogenous shrinkage may be used for investigation of real basic creep of high-strength concrete instead of sealed creep. This approach may contribute to solve the question about the mechanisms causing basic and drying creep of concrete that are still under discussion. It is expected that self-drying shrinkage of concrete under stress, which was recently proposed to be the main cause of basic creep strain by Rossi [Rossi et al. 2012], may be prevented by appropriate water entrainment and may bring evidence on several outstanding assumptions on the occurrence of creep.

At last, the possible effect of SAP on delayed elastic creep strain should be investigated. Unfortunately, the strain measurements had been stopped at unloading and were not continued till the total minus shrinkage strain approached an end value.

9 Permeability and transport coefficients

9.1 Introduction

This chapter presents and discusses experimental data on the effect of SAP addition on transport of gas and water in concrete. The idea was to redistribute water by SAP causing loss of capillary porosity in favour of pre-designed macropore inclusions, see section 3.3.1. In detail, tests on oxygen and water permeability, water penetration depth, capillary absorption, chloride migration, carbonation and weight loss due to drying were performed. The series was supplemented by the characterization of the pore structure using mercury intrusion porosimetry (MIP), strain measurements on specimen exposed to drying and the determination of the 28 days compressive strength in dependence on curing condition.

Eight concrete mixtures were tested: three reference concretes with w/c ratios of 0.36, 0.42 and 0.50 and five concretes modified with SAP A having w/c ratios of 0.36+0.06, 0.36+0.14 and 0.42+0.08. The latter w/c ratio was used for production of three concretes which differed in the particle size of SAP A. The size range was denoted as follows: small (< 63 μm), medium (63-125 μm) and large (125-250 μm). Among other things, the investigation was conducted to produce findings on the effect of SAP particle size on transport coefficients and the comparison of internal curing by SAP to prolonged external curing.

9.2 Materials and methods

9.2.1 Tested concrete compositions

The mix design of all concretes investigated is reported in Table 9.1. The cement content was constant for all mixes. In return, the volume of matrix was compensated by volume of aggregate (Rhine gravel and sand) to account for changes in w/c ratio. The grading curve followed an approximated Fuller curve with gradation exponent of 0.50 [Fuller & Thompson 1907]. To account for loss of workability caused by water-absorption of SAP, superplasticizer Glenium ACE 30 from BASF was used. The mixing regime was adopted from chapter 8, see section 8.2.1.

Table 9.1: Composition of tested concretes

Component	Unit	Ref	Ref	Ref	SAP A	SAP A	SAP A	SAP A	SAP A
		0.50	0.42	0.36	0.42 +0.08	0.42 +0.08	0.42 +0.08	0.36 +0.06	0.36 +0.14
CEM I 42.5 R	kg/m ³	450	450	450	450	450	450	450	450
Aggregate 0/8	kg/m ³	1603	1697	1768	1600	1600	1600	1695	1598
Water total	l/m ³	225	189	162	225	225	225	189	225
Water in SAP	l/m ³	-	-	-	36	36	36	27	63
(w/c) _{tot}	-	0.50	0.42	0.36	0.50	0.50	0.50	0.42	0.50
(w/c) _e	-	-	-	-	0.08	0.08	0.08	0.06	0.14
SAP dry	kg/m ³	-	-	-	1.5	1.5	1.5	1.13	2.63
SAP size dry	μm	-	-	-	<63 small	63-125 medium	125-250 large	63-125 medium	63-125 medium
PCE	kg/m ³	0.7	1.8	5.6	1.80	2.0	2.0	3.6	4.0

9.2.2 Specimen preparation

Most experiments presented so far were performed on samples that had been cured in sealed condition. In practice, hydration has to face changing environmental conditions. Hence, in the present test series samples were exposed to different climates and curing periods, see Figure 9.1.

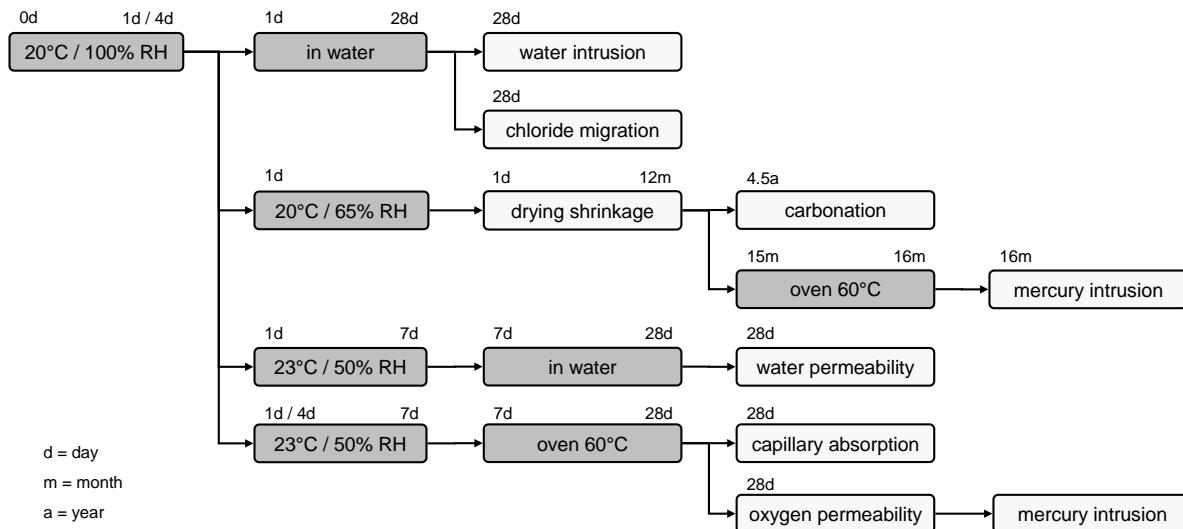


Figure 9.1: Curing regime for various test samples examined.

Cylindrical specimens were used for permeability and capillary absorption measurements. They were stored one day and/or four days at 100% RH before they were exposed to 23°C and 50% RH. At the age of six days the cylinders were cut and sealed with epoxy resin on their perimeter. One day later the samples were polished and put in the oven at 60°C to prepare for oxygen permeability and capillary suction testing, respectively, or they were saturated in water bath to prepare for water permeability testing. At the age of 28 days, weight loss of the oxygen permeability samples had been less than 0.1% during the previous 24 hours. After testing the samples were crushed by a jaw crusher and were used for mercury intrusion porosimetry. Likewise, the drying shrinkage specimens were crushed at the age of 15 months. The crushed pieces were oven-dried for one month and mercury intrusion porosimetry tests were performed subsequently.

Cubes of 150 mm edge length, produced for testing the 28 days compressive strength, were stored in four ways: at 20°C and 100% RH in the first week followed by drying at 20°C and 65% RH (standard curing), drying at 20°C and 65% RH, sealed by PE-foil or saturated in water bath.

9.2.3 Oxygen and water permeability

Basics on the determination of gas permeability of porous construction materials were first examined by Žagar [Žagar 1955]. Here, a device originally designed by Graef and Grube [Graef & Grube 1986a] was used, also known as CUMBUREAU method [Rilem 1999]. It consists of a test cell and a control unit including a precision regulator to adjust the oxygen pressure applied on the test cell and a bubble counter that is assembled behind, as illustrated by Figure 9.2 (left). The bubble counter is a gauged glass tube of constant cross-section where the rate at which a soap bubble rises due to oxygen flow through the sample can be measured by using a stopwatch. The cylindrical test sample of 100 mm in diameter and 50 mm in height was fixed in the test cell by a backup ring in analogy with Figure 9.3. Sealing on the perimeter was done by a seal pressure sleeve made of polyurethane combined with a rubber tube pressurized at 11 bar. The oxygen flow rate Q_g [m³/s] was determined for three inlet pressures p_i (absolute) of 3.0, 3.5 and 4.0 bar.

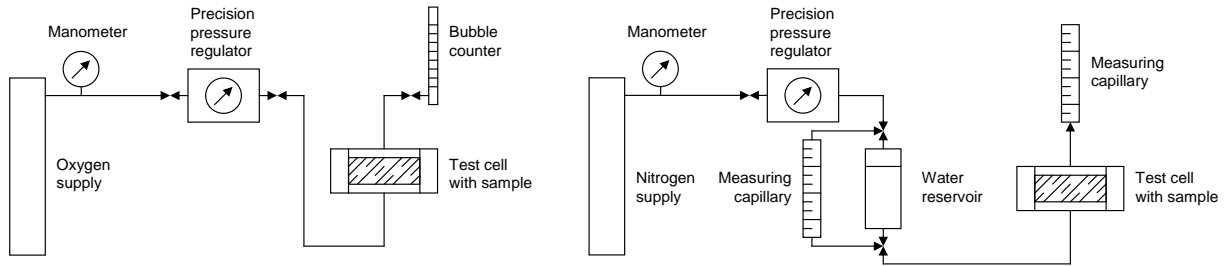


Figure 9.2: Functional diagram of oxygen permeability (left) and water permeability (right) test.

In order to reach constant flow, measurements were not started until 5 min up to 30 min after the sample had been put under the adjusted inlet pressure. According to Hagen-Poiseuille's law valid for laminar flow, cf. equation (2.14) on page 25, the specific oxygen permeability coefficient K_g [m²] can be estimated as follows:

$$K_g = 2.02 \cdot 10^{-10} \cdot \frac{Q_g \cdot L}{A} \cdot \frac{2}{(p_i^2 - 1)} \quad (9.1)$$

where the viscosity of oxygen is assumed as 2.02×10^{-10} Ns/m², the outlet pressure p_o equals the atmospheric pressure p of ca. 1 bar, L [m] is the sample height and A [m²] the test surface.

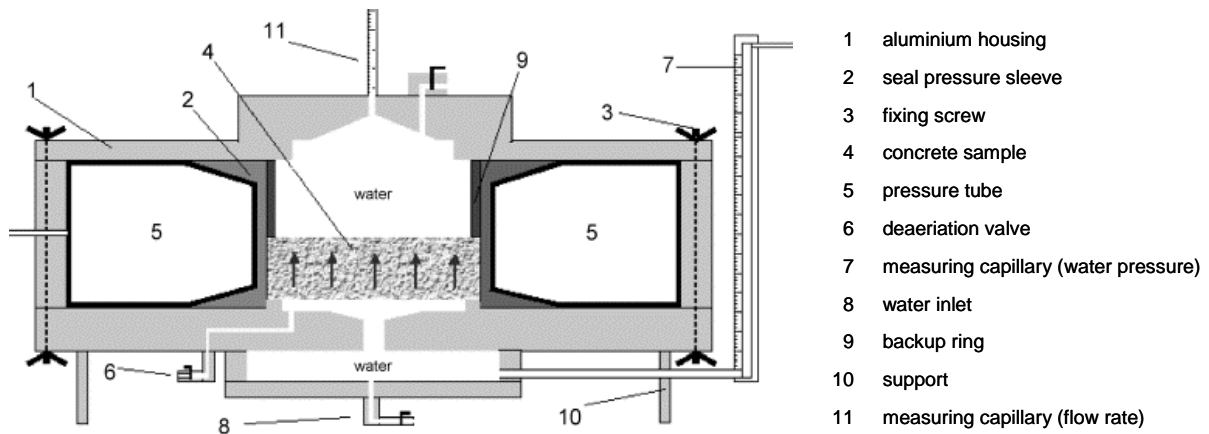


Figure 9.3: Schematic illustration of the test cell for the determination of the water permeability coefficient of concrete [Jooss & Reinhardt 2002].

The test cell used for measuring water permeability is illustrated in Figure 9.3. It was filled with water free from air bubbles. The sample had a height of 30 mm and a diameter of 150 mm. The water pressure applied was 7 bar. In doing so, nitrogen was used as a buffer, see Figure 9.2 (right). Reading the water level in the measuring capillary was started with delay of 24 hours. During this delay time (pre-test phase) the applied water pressure was intended to increase the degree of saturation prior to testing. Indeed, during the pre-test phase air bubbles rose up in the capillary as a result of air squeezed out from large pores. At the end of the pre-test phase the reading was zeroed. The water permeability coefficient k_w [m/s] was determined 1 hour and 24 hours after time zero. According to d'Arcy's law for incompressible liquids, cf. equation (2.16) on p. 25, it is:

$$k_w = \frac{Q_w \cdot L}{A \cdot \Delta h} \quad (9.2)$$

where Q_w [m³/s] is the flow rate of water derived from reading the measuring capillary and Δh [m] is the applied water pressure in meter water column.

9.2.4 Water intrusion depth

The determination of water intrusion depth is an alternative to water permeability measurements. The test was performed in compliance with [DIN EN 12390-8 2009]. Until testing the samples with dimensions of 200 x 200 x 120 mm³ were stored non-stop in water. The water pressure of 5 bar was applied for 3 days and the circular test surface had a diameter of 100 mm. The test surface was roughened with a wire scratch brush at time of demoulding. At the end of testing the samples were cut in halves and the apparent water intrusion depth x_w [mm] was measured.

9.2.5 Capillary absorption

Capillary absorption was measured on cylindrical test samples with 150 mm in diameter that were immersed in water after they had been dried for 21 days at 60°C. Due to epoxy sealing on the perimeter and large sample height of about 120 mm, only the zone close to the free test surface has been expected to reach constant mass at begin of testing. To avoid falsification from internal moisture gradient, weight ingress due to water absorption was observed for the first 4 hours only.

9.2.6 Rapid chloride migration test

Chloride migration was characterized by the rapid chloride migration (RCM) test developed by Tang [Tang 1996]. A picture of the setup is presented in appendix 9. The cylindrical samples of 100 mm in diameter and 50 mm in height were cleaned in an ultrasonic bath, fixed in a rubber hose and placed on a metal plate (cathode) in an aqueous test solution composed of 0.2 mol KOH and 0.51 mol NaCl (3.0% sodium chloride). The hose section above the sample was filled with test solution free of chlorides and the anode metal plate was placed inside. The principal of the test is to accelerate migration of chloride ions into the test sample by a voltage gradient of 30 V. Transportation of ions due to diffusion is of subordinate importance since the test duration is only a few hours. It depends on the initial current [Tang 1996] and was set to 96 hours here. At the end of testing, the samples were removed, split in two halves and sprayed with silver nitrate. Colour transformation into pink or violet indicates the presence of chlorides. The chloride migration coefficient D_{RCM} [m²/s] was determined according to:

$$D_{RCM} = \frac{R \cdot T \cdot h}{z \cdot F \cdot U} \cdot \frac{x_d - \alpha \sqrt{x_d}}{t} \quad \text{with} \quad \alpha = 2 \cdot \sqrt{\frac{R \cdot T \cdot h}{z \cdot F \cdot U}} \cdot \text{erf}^{-1} \left(1 - \frac{2 \cdot c_d}{c_0} \right) \quad (9.3)$$

Here, R [J/Kmol] is the gas constant, i.e. 8.315, T [K] the temperature, h [m] the sample height, z [-] the charge of ions, i.e. $z = 1$ for chloride, F [J/Vmol] the Faraday constant, U [V] the potential difference, i.e. 30, x_d [m] the average intrusion depth of chlorides, t [s] the test duration and c_d [mol/l] the critical chloride concentration causing colour change, i.e. 0.07, and c_0 [mol/l] the chloride concentration in the test solution, i.e. corresponding to 3% by mass.

9.2.7 Mercury intrusion porosimetry

Mercury is a non-wetting fluid to most porous solids that intrudes only due to an externally applied pressure. Mercury intrusion porosimetry (MIP) is making use of this effect: degassed samples are subjected to mercury intrusion by means of a continuously or gradually raising operating pressure. The amount of mercury intruded is measured in dependence on the pressure applied. By assuming circular cylindrical pores, the relation of both measured values leads to a hypothetical pore size distribution according to the Washburn equation:

$$r_p = -2\gamma_M \cdot \cos \theta_M / \Delta p \quad (9.4)$$

with r_p = pore radius, γ_M = surface tension of mercury, θ_M = contact angle between mercury and the pore wall and Δp = differential pressure across the mercury meniscus.

In this study the values for γ_M and θ_M were set to 0.480 N/m and 141.3°, respectively. If non-cylindrical pore geometries are considered, equation (9.4) can be modified by form factors [Cook & Hover 1993]. In general, MIP measurements base on the following assumptions:

- Surface tension γ_M and contact angle θ_M remain constant while testing.
- The system is in equilibrium at any time.
- The externally applied pressure does not lead to deformation of the solids.

Further, the significance of MIP is restricted to some substantial limitations:

- 1) The measurable pore size range typically yields 3 nm to 75 μm , e.g. in the present study. Pores of larger size underlie the effect of mercury intrusion by means of gravity. The lower limit of measurable pore size depends on the maximum pressure applied.
- 2) MIP cannot provide the true pore size distribution as the intruded mercury must pass the narrowest necks of the pore network. Large pores that are connected to the outside only through preceded cylindrical pores of smaller size cannot fill until the pressure is reached needed to fill the small pores. As a result, the volume of the large pore is accounted for the small pore radius. This problem is known as “ink-bottle” effect [Willis et al. 1998].
- 3) MIP will provide smaller than actual total porosity values since some pores are too small or too isolated to be intruded by mercury. On the other hand, total porosities measured by MIP may exceed values indicated by other techniques when the mercury pressure causes collapse of pore walls of isolated pores [Feldman 1984], [Feldman & Cheng-Yi 1985].

According to [Diamond 2000] MIP does not even approximately provide realistic information on the pore size distribution of cement-based materials. With this in mind, the evaluation of MIP measurements is focussed on three parameters regarded as comparative indexes of the pore structure: the intrudable total pore volume p_{intr} , the mode radius r_{mod} and the threshold radius r_t . The mode radius r_{mod} is the most frequently appearing radius or the radius related to the maximum of the relative pore size distribution curve. The threshold radius r_t according to [Winslow & Diamond 1970] is related to the pressure of first intrusion of large amounts of mercury when exceeded and highly depends on the w/c ratio [Cook & Hover 1999]. It can be determined graphically, since it is the intersection point of the tangents of the flat part and the first steep part of the cumulative pore size distribution curve. Hårdtl [Hårdtl 1995] defined r_t as the radius related to the point where the relative pore size distribution exceeds the value of 0.1 $\text{m}^3/(\text{g}\mu\text{m})$ for the first time. r_t can be regarded as the maximum size of pore channels that create a continuous path.

In the present series, MIP was performed on pieces of concrete of less than 5 mm in diameter. About 4 to 5 g of the test material were filled in the measuring chamber of an automated porosimeter (Porotec PASCAL 140/240) with a maximum operating pressure of 2400 bar. The pressure increase was no more than 0.45 MPa/s. The volume measurements were corrected by a blank run for differential mercury compression. Further the impact of ambient temperature on compression of mercury was considered. Evaluation was done by software PASCAL 1.04.

9.2.8 Drying shrinkage and weight loss

Weight loss and shrinkage strain of concrete prisms exposed to 20°C and 65% RH with dimensions of 100 x 100 x 5400 mm^3 were observed. Strains were measured periodically by hand using an analogous displacement gauge. The glued reference marks had a center distance of 200 mm.

9.3 Results and discussion

9.3.1 Fresh concrete properties

Table 9.2 reports on the fresh concrete properties. The spread was found to range between 38 cm (Ref 0.42) and 53 cm (SAP A 0.36+0.14). Of course, with increasing spread of fresh concrete, the air content is reduced. The latter was found to range between 0.7% and 3.4% at the time when the spread was measured, i.e. 10 minutes after first water addition. However, 20 minutes later the air content was no more than 2.5% as revealed by additional measurements (not shown in the table).

Table 9.2: Results of fresh concrete measurements

Property	Unit	Ref 0.50	Ref 0.42	Ref 0.36	SAP A 0.42 +0.08	SAP A 0.42 +0.08	SAP A 0.42 +0.08	SAP A 0.36 +0.06	SAP A 0.36 +0.14
SAP size	-	-	-	-	small	medium	large	medium	medium
Spread	cm	44	38	50	36	40	39	52	53
Temperature	°C	26.9	26.8	22.4	25.2	24.5	25.6	23.5	22.9
Bulk density	kg/m ³	2.28	2.29	-	2.27	2.27	2.28	-	2.29
Air content	%	2.0	3.4	0.7	3.0	2.4	2.5	0.8	1.3

External bleeding was not observed, but the occurrence of internal bleeding can not be excluded with certainty. As a result of internal bleeding, see also section 2.3.6, water-filled pores below the aggregates are formed which can increase the permeability as already reported in [Ruetters et al. 1935]. In Brodersen [Brodersen 1982] the same effect was found to facilitate ingress of chlorides. However, this aspect was not considered any further.

9.3.2 Compressive strength

The results of the compressive strength tests are presented Table 9.3. The standard deviation was found to range between 0.5 N/mm² (SAP A 0.36+0.14) and 2.7 N/mm² (Ref 0.50). In general, curing in water bath led to the highest strength and storage in lab climate of 20°C and 65% RH led to the lowest strength. The advantageous effect of water curing was higher the lower the w/c ratio was. Compared to strength of control concrete with same total water content, SAP-modified concrete possessed slightly increased values. Compared to control concrete with same basic (w/c) ratio, strength was reduced. For concrete SAP A 0.42+0.08 this reduction was the highest in case of water storage, i.e. 28%, and the lowest in case of storage in lab climate, i.e. 15%. For the lower w/c ratio, i.e. SAP A 0.36+0.06, internal curing seems to compensate the strength-reducing effect to some extent. The reduction in strength was found to range between 15% in case of water storage and 12% in case of standard curing.

Table 9.3: 28 days compressive strength for various curing methods

Curing method	Ref 0.50	Ref 0.42	Ref 0.36	SAP A (s) 0.42+0.08	SAP A (m) 0.42+0.08	SAP A (l) 0.42+0.08	SAP A (m) 0.36+0.06	SAP A (m) 0.36+0.14
standard	46.6	67.2	84.1	50.7	53.1	51.2	73.9	53.6
in foil	48.1	62.8	75.3	-	50.5	-	66.7	-
in water	49.1	69.3	86.5	-	49.7	-	74.3	-
20°C 65%	44.7	57.7	74.4	-	48.6	-	64.9	-

9.3.3 Oxygen permeability

Oxygen was chosen as test gas since it is inert to hydration but is important with respect to corrosion of reinforcement. The specific gas permeability coefficient K_g is reported in Figure 9.4. Each bar is the average of two test samples. The standard deviation was 6 to 13%, see Table 9.4. The determination of K_g bases on the assumption of laminar flow, which means the oxygen flow Q_g is proportional to (p_i^2-1) . In fact, the prerequisite was fulfilled well as evident from appendix 9.

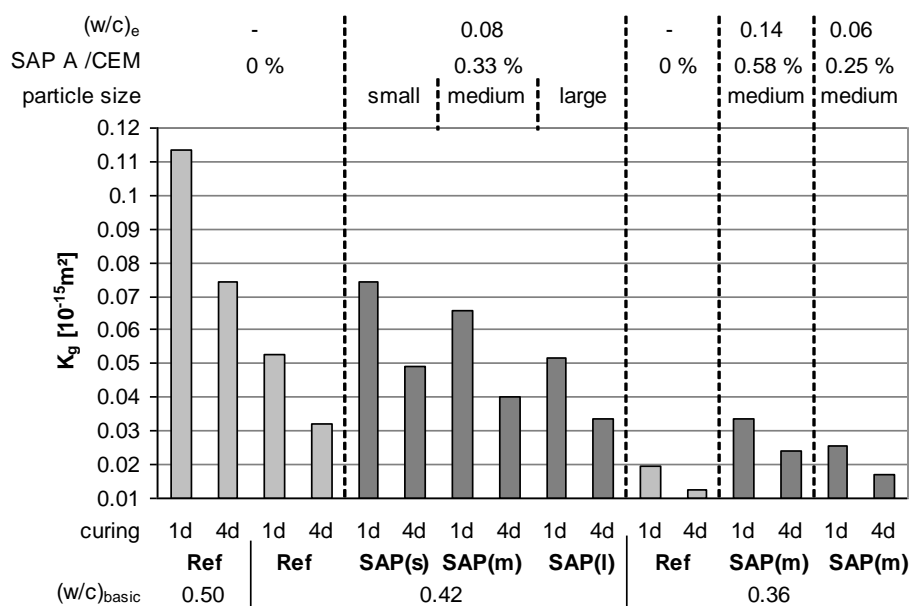


Figure 9.4: Specific oxygen permeability coefficient.

For all concretes it was found that an extension of curing at 100% RH from one day to four days reduces the oxygen permeability. Especially hydration of the surface close cross-section benefits from longer curing time and, hence, the pore structure is expected to possess higher density. K_g of samples cured for four days ranges between 60% to 70% of the corresponding value of one day cured samples. Compared to reference concrete with same total water content, addition of SAP reduces permeability as well. Obviously, redistribution of capillary pores in favour of macropore inclusions decreases oxygen permeability. This effect becomes clearer when increasing the particle size of SAP. In case of the large size fraction, permeability is even reduced to values of reference concrete with same $(w/c)_{\text{basic}}$. Large SAP seems to generate higher density of the matrix compared with small SAP. In this context it should be noted that the volume of a spherical pore depends on the third power of the diameter whereas the surface of a sphere grows only with the second power. Therefore, the larger the SAP pores with constant total porosity, the lesser accessible they are to oxygen and other fluids intruding the concrete via interconnected capillaries.

Generally, the permeability coefficients found in the range 10^{-16} to 10^{-17} m^2 agree with values from literature, e.g. [Graef & Grube 1986b], [Jacobs 1994]. However, it is known that moisture in the sample would cause drop of K_g of one or two orders of magnitude. For better comparability of results, it is recommended to keep pre-conditioning of the samples according to [Rilem 1999].

9.3.4 Water permeability and water intrusion depth

Figure 9.5 reports on the specific water permeability coefficient k_w , determined after 1 hour and after 24 hours. The latter is one order of magnitude smaller. Obviously, water permeability is decreasing over time. Some reasons might be swelling of the concrete and reactivity of water with

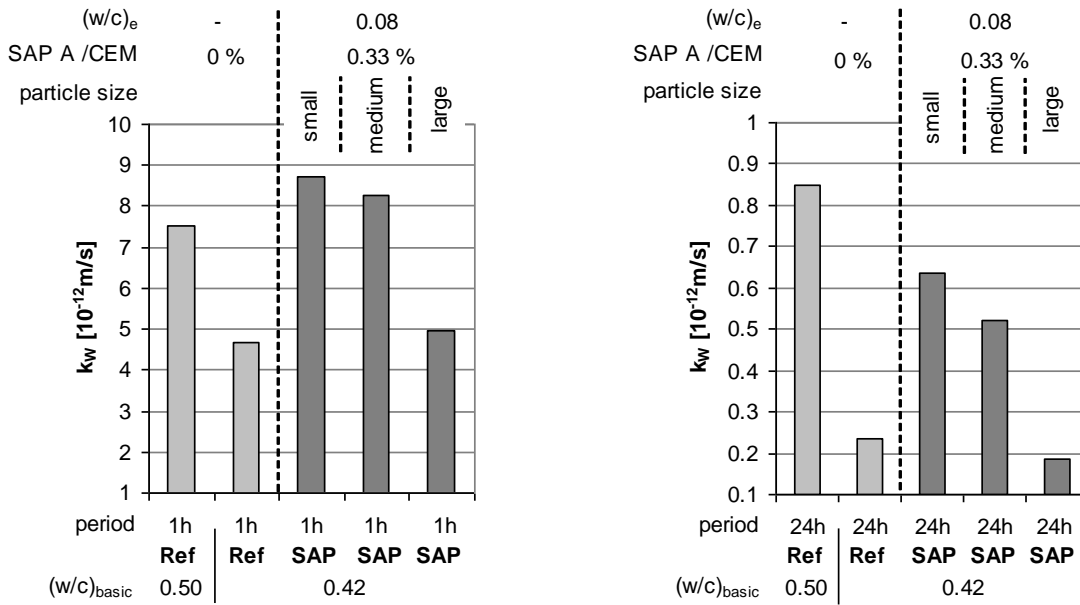


Figure 9.5: Specific water permeability coefficient after 1 hour (left) and after 24 hours (right).

unhydrated cement particles. The bars represent the average value of two samples tested. The results presented in the right diagram reflect the tendency from oxygen permeability testing: increasing the particle size leads to reduction of permeability. The large size fraction of SAP A reduces the water permeability down to the level of the reference concrete with same $(w/c)_{basic}$.

During testing it was observed that small air bubbles emerged in the measuring capillary which have falsified the test results. On the one hand, air bubbles may have been arisen from dissolved pressure gas. On the other hand, the pre-test phase of 24 hours may have been too short for complete water-saturation of the samples with height of 30 mm. The last assumption gets confirmed by the water intrusion depth x_w presented in Figure 9.6. The maximum depth after the water pressure of 5 bar had been applied for 72 hours was found to yield only 17 mm (Ref 0.50). Nevertheless, both, results from water permeability and water intrusion test, show good agreement, i.e. water permeation is reduced effectively by SAP addition, especially when large particles are used. In future, pre-conditioning of test samples should make use of a method developed in [Graef & Grube 1986a]. For saturation of samples prior to testing water pressure is applied on the test cell and at the same time the water outlet valve is connected to a vacuum pump.

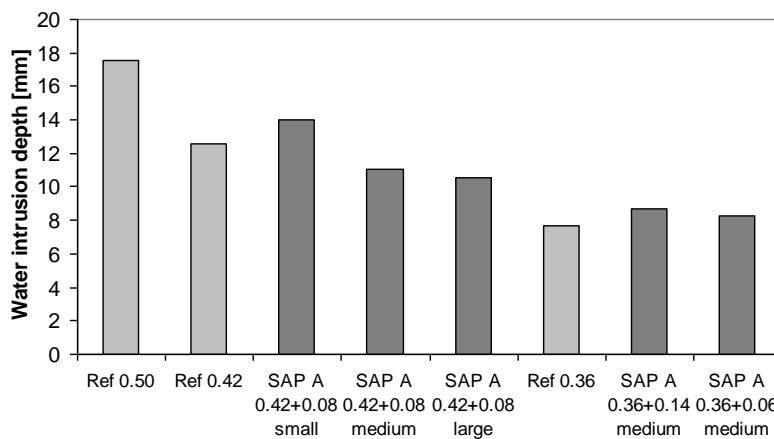


Figure 9.6: Water intrusion depth measured after 72 hours under water pressure of 5 bar.

9.3.5 Capillary suction

Figure 9.7 reports on the water absorption of samples with one day of curing at 100% RH (left) as well as four days of curing (right). Water absorption followed a square root of time law. The results were obtained from individual samples. The water absorption coefficient W [$\text{kg}/\text{m}^2\text{h}^{1/2}$] can be seen as gradient of the linear fitting regression curve and is presented in Table 9.4 on p.137.

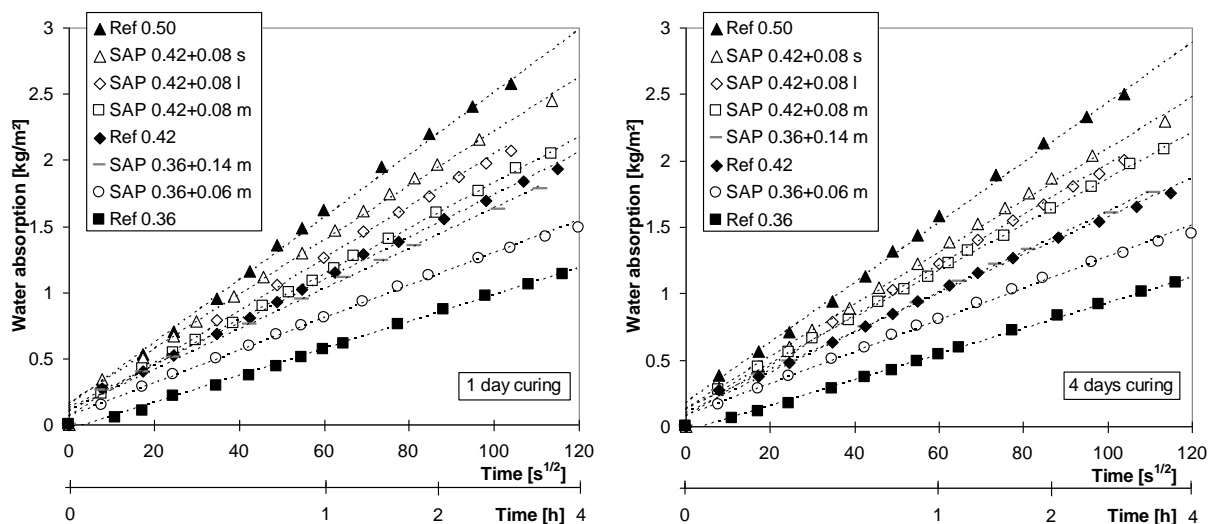


Figure 9.7: Water absorption as a function of the square root of time measured on cylinders with one day curing time (left) and four days curing time (right).

Here again, SAP addition causes reduction of water transport, even though the particle size is of lesser importance. Both medium and large size fractions reduce water absorption almost the same. In principle, capillary absorption is inversely proportional to the pore diameter. But in case of large SAP pores, which are scaled much above capillaries, this principle is reaching its limit.

9.3.6 Carbonation

Carbonation depth t_{carb} was measured on the drying shrinkage specimen after storage of 4.5 years at 20°C / 65% RH. The results are presented in Figure 9.8 and reflect the progress of CO₂ ingress due to diffusion. As expected, progress of carbonation was the highest for Ref 0.50. Due to SAP addition carbonation is reduced but is still higher compared to control mix of same $(w/c)_{basic}$.

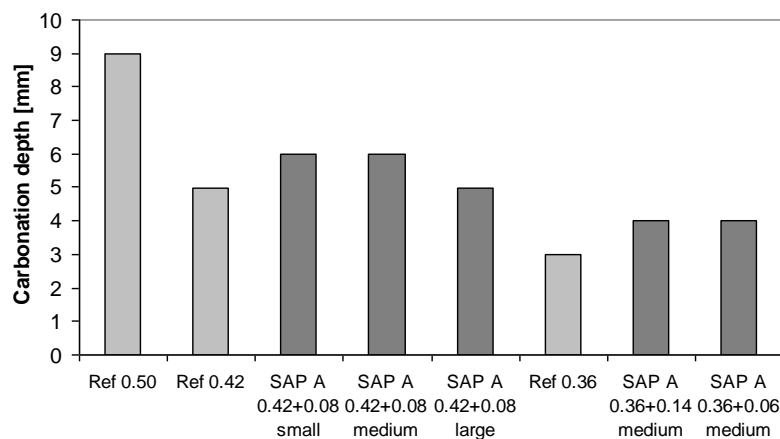


Figure 9.8: Carbonation depth measured after 4.5 years of storage at 20°C and 65% RH.

9.3.7 Chloride migration

The chloride migration coefficients obtained from RCM testing are reported in Figure 9.9 and Table 9.4, respectively. Measured values for the reference concretes are within the values given by literature [Gehlen 2000]. Migration of chlorides was slower when decreasing the w/c ratio. However, it is not possible to deduce a final result in case of SAP-modified concretes. As found in a previous study, see [Reinhardt et al. 2008], SAP addition caused either increase or decrease of D_{RCM} . It seems unlikely that SAP can affect chloride migration due to chemical binding of ions, but this issue should be examined closer.

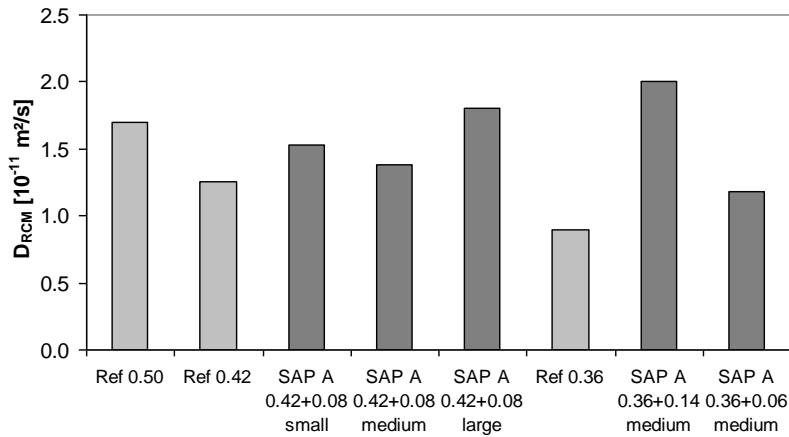


Figure 9.9: Chloride migration coefficient.

9.3.8 Mercury intrusion porosimetry

MIP and oxygen permeability tests were performed on the identical material, see Figure 9.1 on page 126. Further, drying shrinkage specimens were used for MIP after they had been crushed and dried in the oven as of the age of 15 months. In doing so, special attention was put on the location where the material was taken from. Distinction was made between crushed pieces taken from the zone close to the perimeter (outer zone), and core material (inner zone).

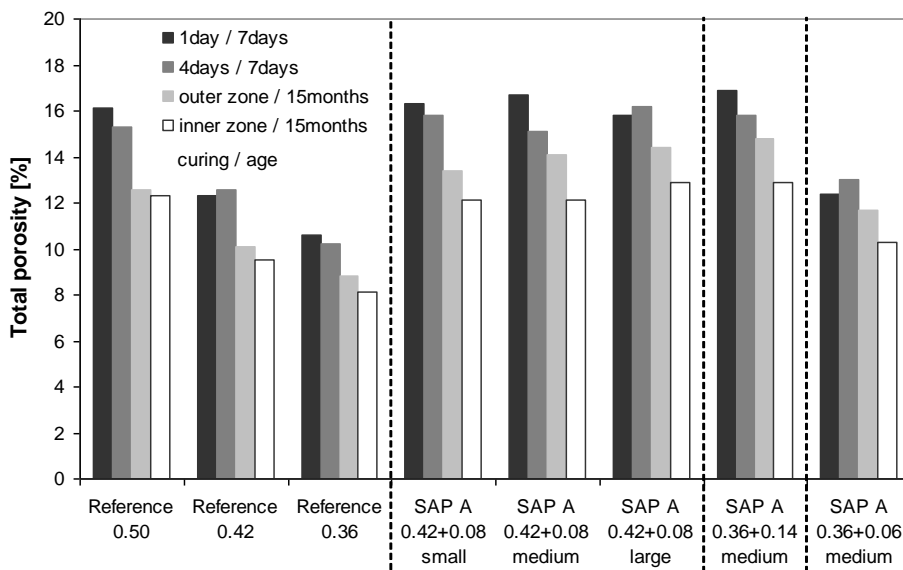


Figure 9.10: Total porosity of concrete measured by MIP.

Figure 9.10 reports on the intrudable mercury volume p_{intr} i.e. the total porosity, and Figure 9.11 reports on the mode radius r_{mod} . The total porosity depends on the water content and decreases over time due to hydration. But, MIP undoubtedly provides smaller than actual porosity values as the volume of very small and isolated pores is not included.

With few exceptions, total pore volume of samples cured for one day at 100% RH is higher compared to samples cured four days. A similar trend can be seen at the 15-month-old samples where the material taken from the outer zone shows higher porosity compared to core material. Densification of the matrix is higher for w/c of 0.42 and 0.50. For w/c of 0.36 the decrease in porosity over time is less pronounced since hydration slowed down earlier.

The total porosity can be split in air pores, SAP pores and capillary pores. The latter remains when subtracting air pores measured in fresh concrete and expected SAP pore volume from total porosity. Of course, this is a strong simplification since it is assumed that oven-drying at 60°C does not affect physically bound water present on the surface of the gel solid. Further, MIP does not capture the real volume of air voids due to high open porosity and small sample size. Nonetheless, the relevant data on fractional pore volume is presented in appendix 9. One can find that the capillary pore volume is nearly the same for all concretes provided that $(w/c)_{basic}$ is the same.

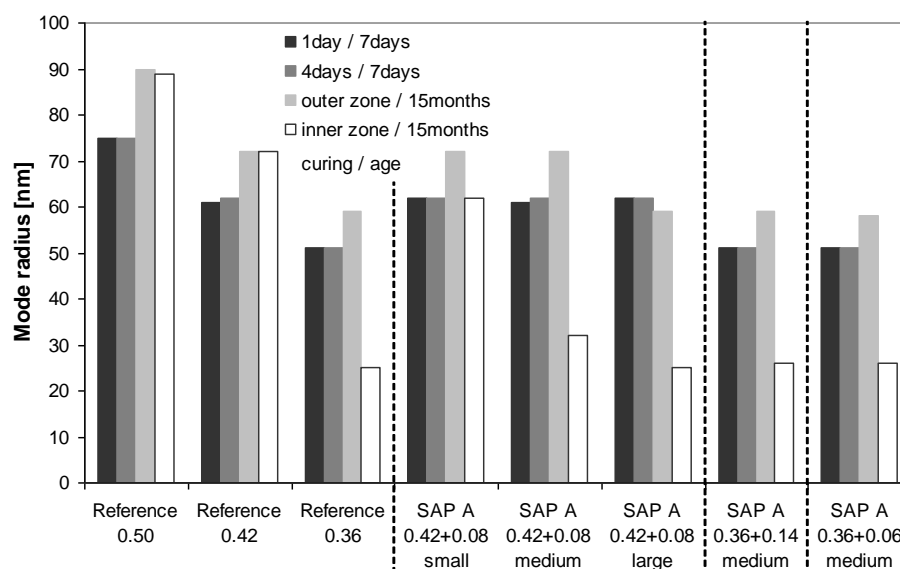


Figure 9.11: Mode radius of pore size distribution determined by MIP.

The mode radius r_{mod} indicates success of redistribution of capillary pores by macropore inclusions as well. In general, r_{mod} decreases when decreasing the w/c ratio. It is a result of less water layers surrounding the cement grains in fresh state causing the diameter of capillary pores formed during hydration to drop. Here, SAP-modified concretes show the same values for r_{mod} as reference concretes with same $(w/c)_{basic}$. However, for some concretes, e.g. Ref 0.50 and Ref 0.42, the mode radius is higher for 15-month-old samples compared to 7-day-old samples. This could be the result of isolation of small pores due to blockage of pore channels with hydration products or is rather owed to fast drying of the outer zone causing early stop of hydration.

9.3.9 Combination of MIP and pore counting

For concretes Ref 0.50, Ref 0.42 and SAP A 0.42+0.08 (m) pore counting according to [DIN EN 480-11 2005] was performed in analogy with section 10.2.4. Figure 9.12 shows the results that were combined with the pore size distribution obtained from MIP. The corresponding relative

pore size distribution is presented in appendix 9. It was assumed that the size distribution of capillary pores of SAP A 0.42+0.08 (m) equals to Ref 0.42, that means both curves are identical up to the pore size of 100 μm . It should be noted here, that MIP and pore counting are generally based on different definitions of pore size distributions, which are not compatible with each other [Münch & Holzer 2008]. Hence, the diagram has to be regarded with skepticism, but, it provides a good impression of the proportions of capillary pores in contrast to SAP pores.

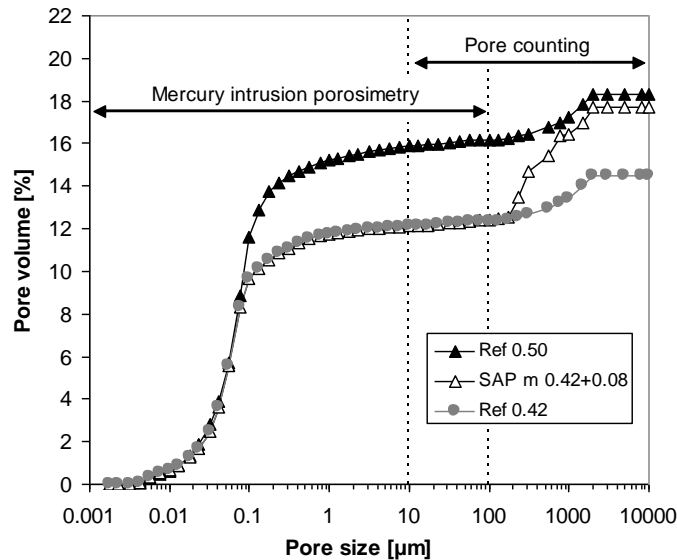


Figure 9.12: Pore size distribution obtained by combining results of MIP and pore counting.

9.3.10 Drying shrinkage and weight loss

The results of the strain measurements are presented in Figure 9.13. Figure 9.14 reports on the shrinkage strain as a function of weight loss.

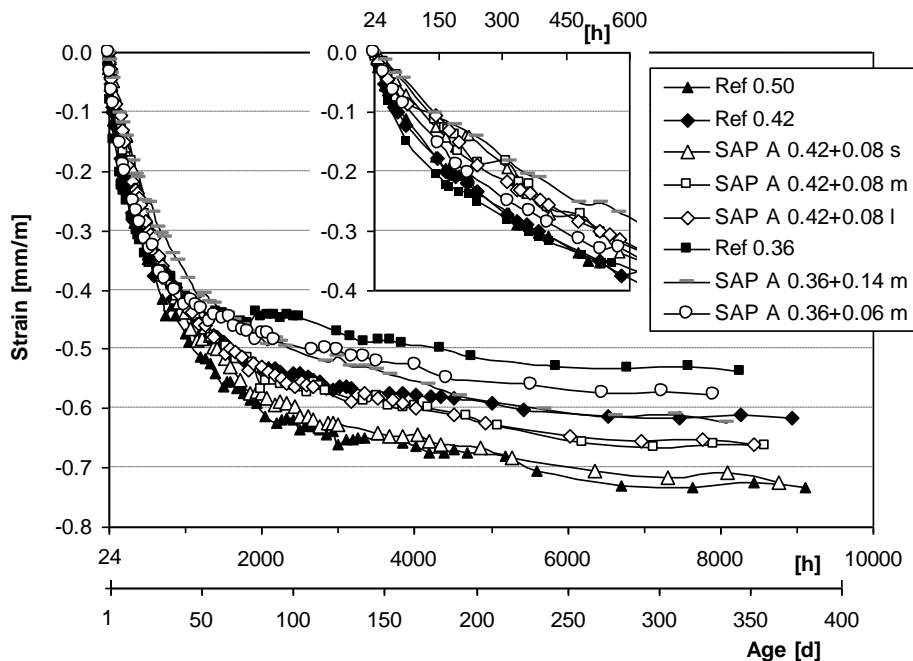


Figure 9.13: Drying shrinkage of specimen exposed to 20°C and 65% RH.

The strains were zeroed at the age of 24 hours. So was the weight loss of the specimen. It can be noticed that drying shrinkage is retarded due to addition of SAP although weight loss is higher. The results comply to a great extent with findings presented in chapter 8, see section 8.3.5. Of course, both weight loss and drying shrinkage are higher when the w/c ratio is increased. If medium and large size fractions of SAP A are considered, drying shrinkage is not only retarded but is even reduced by up to 15% after one year compared to reference concrete with same w/c. Concrete SAP A 0.36+0.14 exhibits nearly three times higher weight loss compared to Ref 0.36, but, still retarded shrinkage in the first half year and almost same shrinkage later on.

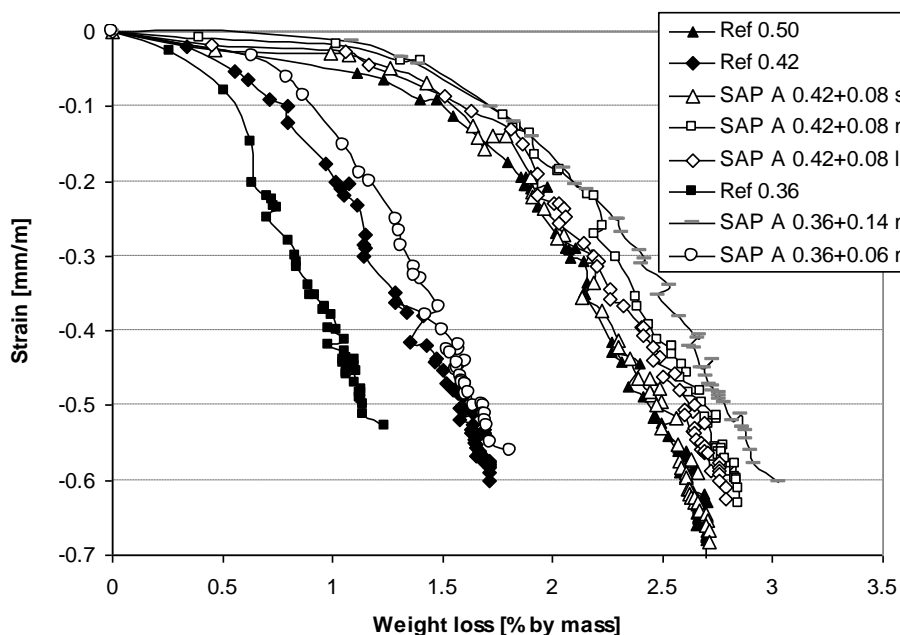


Figure 9.14: Drying shrinkage as a function of weight loss.

9.3.11 Summary

The main test results obtained in this experimental series are summarized in Table 9.4.

Table 9.4: Main test results

Property (curing)	Unit	Ref 0.50	Ref 0.42	Ref 0.36	SAP A s 0.42 +0.08	SAP A m 0.42 +0.08	SAP A l 0.42 +0.08	SAP A m 0.36 +0.06	SAP A m 0.36 +0.14
K_g (1d)	$[10^{-17}\text{m}^2]$	11.4	5.25	1.96	7.44	6.56	5.17	2.58	3.38
K_g (4d)	$[10^{-17}\text{m}^2]$	7.42	3.21	1.24	4.93	4.02	3.38	1.17	2.40
k_w^{24h} (1d)	$[10^{-12}\text{m}/\text{s}]$	0.85	0.23	-	0.64	0.52	0.19	-	-
x_w	[mm]	18	13	8	14	11	11	8	9
W (1d)	$[\text{kg}/\text{m}^2\text{h}^{1/2}]$	1.42	0.97	0.61	1.23	1.04	1.18	0.92	0.74
W (4d)	$[\text{kg}/\text{m}^2\text{h}^{1/2}]$	1.35	0.87	0.58	1.17	1.04	1.14	0.91	0.71
t_{carb}	[mm]	9	5	6	6	5	3	4	4
D_{RCM}	$[10^{-11}\text{m}^2/\text{s}]$	1.70	1.26	1.53	1.38	1.80	0.90	2.00	1.18
p_{intr} (1d)	[% by vol.]	16.1	12.3	10.6	16.3	16.7	15.8	12.4	16.9
p_{intr} (4d)	[% by vol.]	15.3	12.6	10.2	15.8	15.1	16.2	13.0	15.8
r_{mod} (1d)	[nm]	75	61	51	62	61	62	51	51
r_{mod} (4d)	[nm]	75	62	51	62	62	62	51	51

9.4 Conclusion

In this chapter the idea of redistribution of capillary water by pre-designed macropore inclusions due to SAP addition was followed. Three reference concretes with w/c ratios of 0.36, 0.42 and 0.50 and five SAP-modified concretes, varying in content and size of SAP A, i.e. small ($< 63\mu\text{m}$), medium ($63\text{-}125\ \mu\text{m}$) and large ($125\text{-}250\ \mu\text{m}$), were investigated. The series was conducted with respect to compressive strength, permeation of gas and water, capillary absorption, carbonation, chloride migration, drying shrinkage and pore structure formation. It can be concluded that:

- Redistribution of capillary pores worked well. Concretes with same total water content showed the same total pore volume - but the mode pore radius, which characterizes the capillary porosity, was the same for concretes with same $(w/c)_{\text{basic}}$.
- Gas and water permeability, capillary absorption and carbonation were reduced due to SAP addition. At constant SAP pore volume the permeability coefficients were reduced in dependence on the SAP particle size down to the level of the reference concrete with same $(w/c)_{\text{basic}}$. In doing so, the large size fraction of SAP A performed the best. It was proposed that with increasing SAP size the surface to volume ratio of the pores decreases resulting in poor accessibility.
- Drying shrinkage was not only retarded due to SAP addition but was also reduced. At the end of testing (after one year) reduction was up to 15%, although weight loss of water-entrained concrete was much higher, i.e. weight loss of SAP A 0.36+0.14 was up to three times higher compared to Ref 0.36. Water in SAP seems to have higher mobility, evaporates easier and causes less shrinkage strain.
- 28 days compressive strength was reduced due to SAP addition. Reduction was less when the test cubes were allowed to dry prior to testing. Curing in water caused the highest reduction in strength. Compared to reference concrete with same total water content, water-entrained concrete possessed slightly increased compressive strength. This effect was more pronounced in case of concrete produced at low w/c.

9.5 Outlook

The presented test results provide first data on the effect of SAP addition on transport properties of concrete. More research is needed in order to reliably state on the effects proposed by this investigation. For example the water permeability tests had to get by with only few test samples, testing of chloride migration did not lead to a final conclusion and possible effects of SAP addition on diffusion are completely unknown. Further, oxygen permeability and capillary suction tests were performed on oven-dried samples. In future, pre-conditioning of the test samples should correspond with [Rilem 1999] to allow for better comparison with data given by literature. Further, it is recommended to use drilled samples instead of cast cylinders to avoid boundary effects. Sample preparation for MIP should abstain from high temperature treatment. A more careful preparation method was already developed by [Copeland & Hayes 1953]. They used a desiccator evacuated by vacuum pump in order to dry out the evaporable water. This method is proposed to cause less micro-structural damage of the sample and allows MIP to incorporate volume of gel pores. At last, it should be noted that only one SAP type was investigated so far and the experiments were performed on concretes of strength class between C30/37 and C55/67 where concrete does not benefit from internal curing.

10 Enhanced freeze-thaw resistance

10.1 Introduction

This chapter deals with the new technology of air entrainment in concrete by the application of SAP. Ten concrete mixtures were investigated and compared to each other with respect to freeze-thaw resistance, pore system and mechanical properties. The concretes either contained ordinary AEA or SAP or neither of the two. The freeze-thaw resistance tests with de-icing salts were performed according to the Rilem recommendation for CDF-testing [Rilem 1996]. Besides the quantification of scaling, the change in ultrasonic velocity in analogy with [Rilem 2004] and the change in weight of the specimen were observed. The characterization of the pore system was managed by pore counting. The series was completed by compressive strength tests and the determination of the abrasion resistance using the wear test according to [DIN 52108 2010].

The investigation attempts to attain answers on the following main questions:

- Is the effect of initially water-filled SAP pores on scaling and internal damage of concrete comparable to the same volume of air voids generated by ordinary air-entraining agent?
- Do particle size or void spacing have an influence on the performance of concrete, provided that the total pore volume is the same?
- Does the particle shape have an influence on the performance of concrete?
- What are the advantages of air entrainment by SAP in comparison to the use of AEA?

10.2 Materials and methods

10.2.1 Tested concrete compositions

Guidelines for the mix design depend on the exposure class as laid down in [DIN 1045-2 2008]. The CDF-test applied in this series simulates conditions that correspond to class XF4. To this end, the concrete compositions have to meet the requirements reported in Table 10.1. The exception to these guidelines is earth-moist concrete with w/c ratio ≤ 0.40 .

Table 10.1: Limits for the design of concrete to meet class XF4

Requirement	XF4	Unit	Constraint
Min. f_c	C30/37 LP	N/mm ²	-
Max. w/c	0.50	-	-
Min c	320	kg/m ³	-
Max. fines content	450	kg/m ³	Max. aggregate size: ≥ 16 mm; ≤ 32 mm
Air content	≥ 4.5	Vol.-%	Max. aggregate size: 16 mm

Ten concretes were designed and tested:

- two reference concretes without additives, except superplasticizer to maintain workability,
- two concretes with air-entraining agent LP 74 (BASF),
- four concretes with SAP A of varying particle size,
- one concrete with SAP D,
- one concrete with SAF.

The mixing regime was analogous to chapter 8, see section 8.2.1.

Table 10.2: Tested concrete compositions

	Unit	Ref 0.50	Ref 0.40	AEA 0.50	AEA 0.40	SAP ^A 45-63	SAP ^A 63-90	SAP ^A 100- 125	SAP ^A 125- 200	SAP ^D 100- 125	SAF
Cement	kg/m ³	403.2	397.9	392.8	388.8	399.3	399.3	398.5	397.6	398.5	403.4
Aggregate	kg/m ³	1726	1821	1604	1690	1720	1720	1720	1712	1674	1723
Water total	l/m ³	201.6	159.2	196.4	155.5	199.6	199.6	199.3	199.3	199.3	201.7
SAP water	l/m ³	-	-	-	-	31.9	31.9	31.9	31.8	31.9	32.3
w/c _{basic}	-	0.50	0.40	0.50	0.40	0.50	0.50	0.50	0.50	0.50	0.50
w/c _e	-	-	-	-	-	0.08	0.08	0.08	0.08	0.08	0.08
SAP dry	kg/m ³	-	-	-	-	1.33	1.33	1.33	1.33	2.90	1.70
SAP size dry	µm	-	-	-	-	45-63	63-90	100- 125	125- 200	100- 125	-
AEA	kg/m ³	-	-	2.0	1.9	-	-	-	-	-	-
PCE	kg/m ³	0.6	2.6	-	1.6	2.3	2.3	2.4	2.3	2.0	6.0
Air pores	%	1.2	2.0	6.7	7.6	1.7	1.7	1.9	2.1	3.4	1.2

Data in Table 10.2 was obtained by recalculating the nominal mass fractions of concrete components on the basis of the specimen's weight. The reference concretes had w/c ratios of 0.40 and 0.50. Due to expected air content of 2%, they were intended to fail the requirements of class XF4. The design of the two concretes containing AEA was conform to the reference concretes, except for the air contents which were attempt to yield 5% due to addition of LP 74. All SAP-modified concretes had a total w/c ratio of 0.42+0.08. The entrained water of (w/c)_e = 0.08 corresponded to 3.2% by volume. The grading curve of Rhine gravel aggregates followed an approximated Fuller curve with gradation exponent of 0.50 and maximum grain size of 16 mm.

The superplasticizer used was Glenium ACE 30 (PCE) from BASF. The target value for the fresh concrete spread was the range 420 to 480 mm. Due to the liquefying effect of LP 74, the amount of PCE was reduced in the AEA mixtures. In contrast, the amount of PCE had to be highly increased in mix SAF. The concrete batches had a volume of 55 litres and were designed for casting a total of 12 cubes of 150 mm edge length: 6 for the compressive strength tests, one for the determination of the abrasion resistance and 5 for pore counting and CDF-testing, respectively. The latter were cast into moulds with a 5 mm teflon plate arranged at one side.

10.2.2 Specimen preparation

Subsequent to demoulding, 24 hours after casting, the cubes were stored at 20°C and 100% RH up to an age of 7 days. Afterwards, the 6 cubes for testing compressive strength were put in the climate chamber at 20°C and 65% RH until the age of 28 and 91 days, respectively. The other 6 cubes were sawed into two halves by wet sawing. Subsequently, the five cube halves intended for CDF-testing (surface at the teflon plate is the test surface) were stored for 21 days at 20°C and 65% RH. Within the last week the lateral sides of the CDF specimens were sealed by two layers of epoxy resin and were stored for another period of 7 days at 20°C and 65% RH with the test surface dipped in a water bath containing 3% by mass NaCl. At the beginning of CDF-testing, the specimens had an age of 35 days. The counterparts of the CDF specimens were polished on their sawn surface in order to prepare them for pore counting. From the remaining two cube halves, two samples with dimensions of 70 x 70 x 45 mm³ were sawn for testing the wear using the grinding method according to Böhme [DIN 52108 2010]. Before testing, they were dried in the oven at 105°C for 7 days.

10.2.3 Measuring scaling and internal damage

Concrete damage due to freeze-thaw attack with de-icing salts can be classified in two categories:

- 1) Surface scaling
- 2) Internal damage.

Both surface scaling and internal damage occur simultaneously. The first is an apparent defect that can be quantified by CDF-testing [Rilem 1996]. The second can dramatically reduce the lifetime of the concrete as well. Internal damage can be detected by an increase in the ultrasonic transit time as the presence of internal cracks reduces the velocity of the US-wave travelling through the specimen. To quantify both events of damage, the present experimental series included the CDF performance test extended by the measurement of the ultrasonic transit time according to the CIF-test method [Rilem 2004].

Scaling and US-wave velocity were determined at the same samples, i.e. after 4, 6, 14, 20, 28 and 56/64 freeze-thaw cycles. One freeze-thaw cycle lasted 12 hours, see appendix 10. Within the first four hours the temperature dropped from 20°C to -20°C. Then the temperature in the freezing chest stayed constant for three hours and increased to 20°C afterwards. In the following one hour the temperature was kept constant again and the cycle ends. Within this last hour the determination of the scaled material and the US-wave velocity was carried out (see appendix 10).

Figure 10.1 illustrates the experimental setup for one single CDF/CIF-specimen, as it is placed in the freezing chest during testing. The configuration allows a close simulation of real conditions, in particular the uniaxial transportation of moisture and heat perpendicular to the test surface. The temperature control is managed by the temperature controlled bath. The surface of the stainless steel container prevents infrared (IR) radiation, the narrow gap between container and sample minimizes convection and the epoxy resin on the lateral sides of the sample acts as steam break. As a result, the uniaxial transport of heat is operated by thermal conduction. If the tests were performed e.g. in a conventional climatic chamber, about 50% of the heat transfer would be managed by convection and 50% by radiation. Consequently, the micro-ice-lens pump causing damage would act less effective. In this regard the CDF/CIF-test method reproduces the most severe conditions among the established test methods.

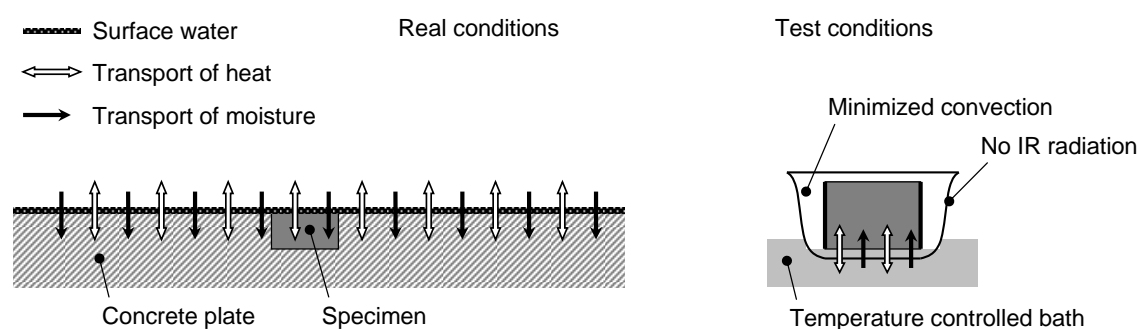


Figure 10.1: Uniaxial transportation of heat and moisture during CDF/CIF-testing (right) compared to real conditions a flat concrete member is exposed to (left).

10.2.4 Pore counting and void spacing

The parameters of the air void system in the hardened concrete were determined microscopically. Polished cross-sections with dimensions of 150 x 100 mm² were examined at 100 x magnification according to [DIN EN 480-11 2005]. The samples were obtained by wet-sawing from the counterparts of the cube halves used for CDF/CIF-testing. The measuring line investigated had a

total length T_{tot} of at least 1200 mm. It was split in pore chords T_{Pores} and solid line segments T_{Solid} . The total pore content V_{Pores} [% by vol.] is derived from the quotient of T_{Pores} to T_{tot} :

$$V_{Pores} = T_{Pores} / T_{tot} \cdot 100 \quad (10.1)$$

In case of concretes modified with SAP A forming irregular shaped pores, it was possible to split T_{Pores} further in air pore chords T_{Air} and SAP pore chords T_{SAP} . However, in the following calculations SAP pores are assumed to be of spherical shape as well.

The void spacing (VS) is an important characteristic of the air void system with respect to freeze-thaw resistance, see section 2.8.7. VS is a specific length with the unit mm. Under the assumption of equally sized pores that are placed centrally in a system of cement paste cubes, VS is the distance between the edge of the cube to the pore wall of the void imbedded. In this approach the pore volume is divided in n [-] spherical pores with average pore radius r_{Pore} [mm] and specific pore surface S [mm⁻¹]:

$$n = \frac{V_{Pores}}{4/3 \cdot \pi \cdot r_{Pore}^3} = \frac{V_{Pores} \cdot S^3}{36 \cdot \pi} \quad \text{with} \quad S = \frac{4 \cdot \pi \cdot r_{Pore}^2}{4/3 \cdot \pi \cdot r_{Pore}^3} = \frac{3}{r_{Pore}} \quad (10.2)$$

Volume V_{Cube} [mm], edge length a_{Cube} [mm] and space diagonal d_{Cube} [mm] of the n cement paste cubes are given by the following equations, where V_{Matrix} [%] is the volume of cement paste:

$$V_{Cube} = \frac{V_{Matrix} + V_{Pores}}{n} = \frac{36 \cdot \pi \cdot (V_{Matrix} + V_{Pores})}{V_{Pores} \cdot S^3} \quad (10.3)$$

$$a_{Cube} = \sqrt[3]{V_{Cube}} \quad (10.4)$$

$$d_{Cube} = \sqrt{3} \cdot a_{Cube} \quad (10.5)$$

VS [mm] is the half of the space diagonal d_{Cube} reduced by the radius r_{Pore} :

$$VS = \frac{\sqrt{3}}{2} \cdot \sqrt[3]{\frac{36 \cdot \pi \cdot (V_{Matrix} + V_{Pores})}{V_{Pores} \cdot S^3}} - \frac{3}{S} \quad (10.6)$$

This approach is used in [DIN EN 480-11 2005] as well:

$$VS = \frac{3 \cdot [1.4 \cdot (1 + R)^{1/3} - 1]}{S} \quad \text{for} \quad R = \frac{V_{Matrix}}{V_{Pores}} > 4.342 \quad (10.7)$$

10.2.5 Mechanical abrasion

The abrasion resistance of the concrete was determined by the wear test using the grinding wheel according to Böhme [DIN 52108 2010], also called grinding wheel method. Two samples of each concrete were tested. During testing, the samples with polished test surfaces of 50 cm² each, were fixed on the grinding wheel using a contact pressure of 294 N, see also appendix 10. On the grinding wheel in front of the sample, 20 g of abrasive powder were evenly distributed. After each period, with one period lasting 68 revolutions, the sample was turned clockwise by 90° and the abrasive powder was replaced with new material. Testing was finished after 16 periods, i.e. 388 revolutions. Wear was determined by the thickness loss Δt [mm³/mm²] of the sample measured at 9 specific points of the test surface before and after testing.

10.3 Results

10.3.1 Fresh concrete properties

The fresh concrete measurement results are reported in Table 10.3. The concretes were produced with a spread of 41 to 47 cm. Mixture SAF required 1.5% by mass of cement to maintain workability, see Table 10.2. Although it is well known that fibres reduce workability, this high amount could be an indication that the swelling capacity of the superabsorbent fibres was higher than expected. Another finding is that SAP D obviously entrained air bubbles in the fresh concrete.

Table 10.3: Fresh concrete properties measured just before the moulds were filled

Attribute	Unit	Ref 0.50	Ref 0.40	AEA 0.50	AEA 0.40	SAP ^A 45-63	SAP ^A 63-90	SAP ^A 100- 125	SAP ^A 125- 200	SAP ^D 100- 125	SAF
Spread	cm	43	41	47	44	41	42	42	41	46	42
Temperature	°C	20.5	21.0	19.2	20.3	20.9	21.4	20.6	22.6	20.1	19.4
Bulk density	kg/l	2.30	2.38	2.19	2.24	2.32	2.32	2.32	2.32	2.23	2.33
Air content	%	2.0	1.1	6.0	5.5	1.3	1.2	1.2	0.8	4.5	0.8

10.3.2 Pore counting

The air contents calculated on the basis of the mix proportion and the weights of the specimens measured after demoulding (Table 10.2) show slight differences compared with values measured in the fresh concrete (Table 10.3). Figure 10.2 provides a comparison of both results extended by the air pore content obtained from the pore counting method. In case of concretes with SAP D and SAF, pore counting could not be applied in order to determine the air content as it was not possible to reliably separate air pores from pores formed by the superabsorber. In general, the results of all three methods are in acceptable agreement. The total pore content referred to in the following is the one adopted from pore counting, unless stated otherwise. For concretes SAF and SAP D, the air content referred to in the following was recalculated on the basis of the weight of the specimens measured after demoulding.

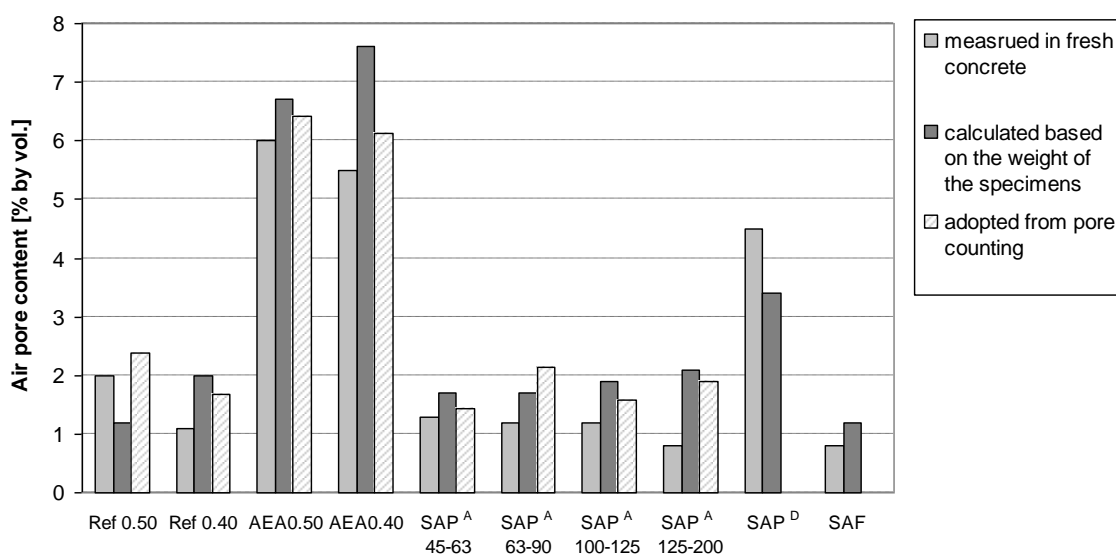


Figure 10.2: Content of air pores obtained from fresh concrete measurements, pore counting and recalculation based on the weighing of specimens after demoulding.

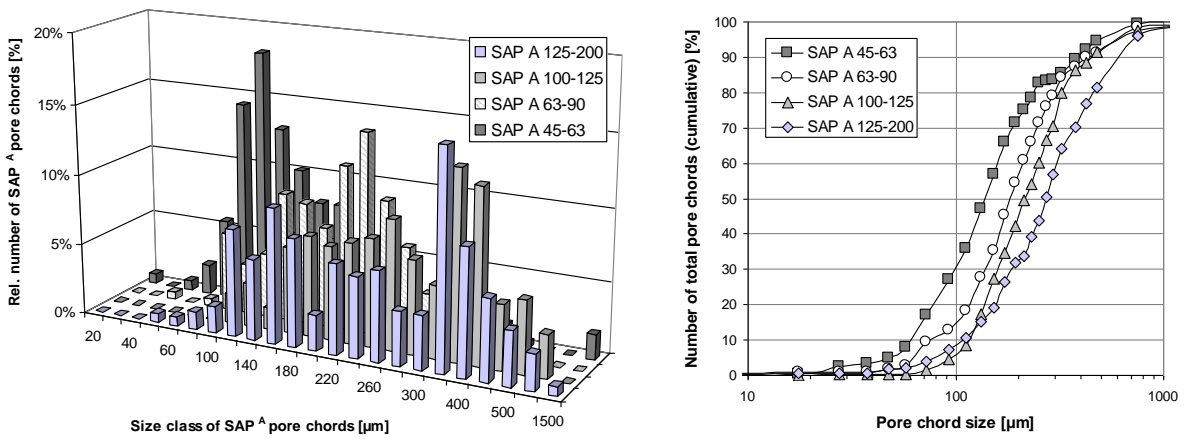


Figure 10.3: Relative size distribution of SAP A pore chords (left) and cumulative size distribution of all pore chords counted (right).

In Figure 10.3 (left) the size distribution of SAP A pore chords found by pore counting while neglecting air voids is presented. With increasing the particle size of SAP A, the distribution of the relative number of SAP pore chords is shifted towards larger sizes. This tendency is also found when SAP pores and air pores are regarded together. The right diagram shows the cumulative pore chord size distribution of all counted pores. The median pore chord sizes are as follows: 135 μm (SAP A 45-63), 180 μm (SAP A 63-90), 215 μm (SAP A 100-125) and 270 μm (SAP A 125-200). Both diagrams verify that changes in the size distribution of dry SAP particles are directly reflected in the developing pore structure. Further, the diagrams give an indication that large SAP particles may break during mixing and therefore increase the number of small pores formed.

Figure 10.4 (left) presents the SAP A pore content as a function of the pore chord size. The calculation was done by assuming the pore chord size to be the diameter of a spherical pore. The pore content of SAP A pores counted is about 3.4% which corresponds to an absorption capacity of 25 g/g. It is in good agreement with the expected volume of 3.2%. Only concrete SAP A 100-125 shows a higher value of 4.4%. The evaluated surface area was probably not representative. Figure 10.4 (right) reports on the total pore volume split in SAP and air pores.

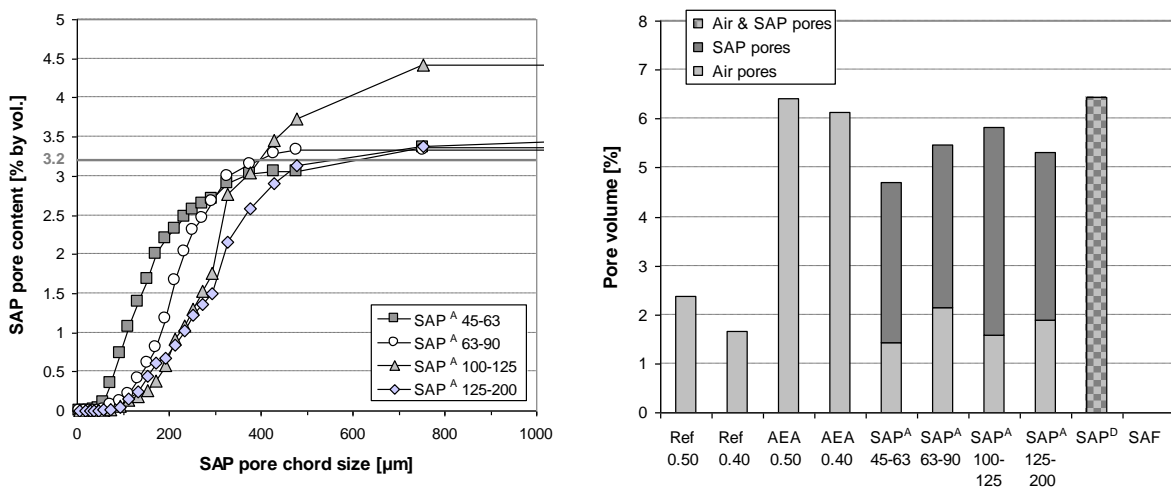


Figure 10.4: Content of SAP A pores as a function of pore chord size (left) and total pore content split in air pores and SAP pores (right).

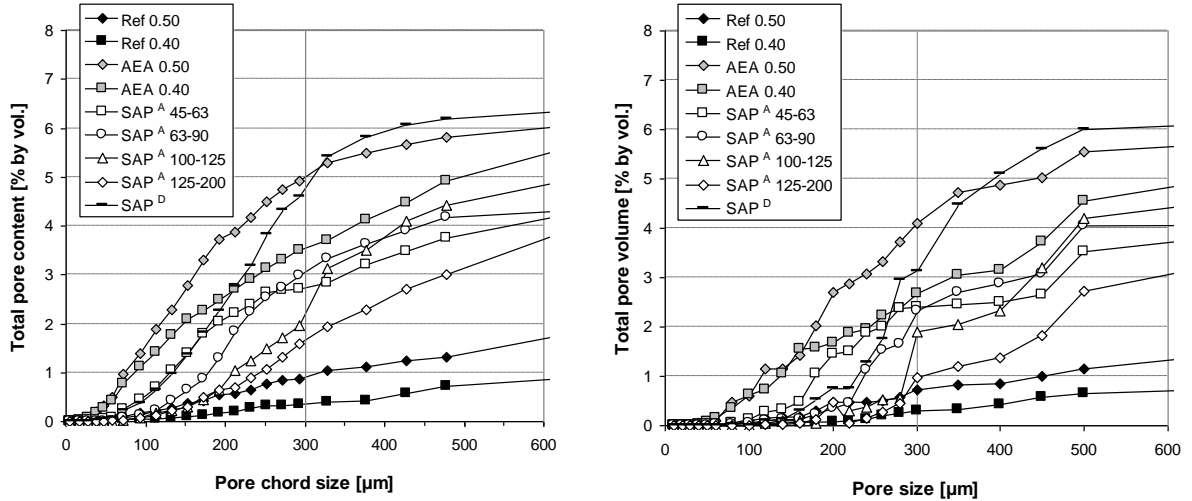


Figure 10.5: Total pore content as a function of the pore chord size assumed to be the pore diameter (left) and pore size distribution according to [DIN EN 480-11 2005] (right).

Figure 10.5 presents the total pore content as a function of the pore chord size (left) and the pore diameter calculated according to [DIN EN 480-11 2005] (right). Both AEA concretes show high pore volumes generated by small pores. The volume of pores $< 300 \mu\text{m}$ is called A_{300} . The standard requires $A_{300} > 1.5\%$ for frost-resistant concretes. The right diagram shows that all mixtures fulfil this demand except the reference concretes and concrete SAP A 125-200. The curves in the left diagram were obtained by assuming the pore chord size to be the diameter of a spherical pore. Indeed, this is a simplification because the pore chords measured are smaller than the actual pore diameters. This effect is statistically given consideration in the standard.

10.3.3 Void spacing

The average pore radius r_{pore} [mm] can be predicted on the basis of a probability calculation according to equation (10.8), see also Figure 10.6:

$$t = \frac{1}{\pi} \cdot \int_0^\pi 2 \cdot r_{\text{pore}} \cdot \sin\left(\frac{\alpha}{2}\right) \cdot d\alpha = 2 \cdot r_{\text{pore}} \cdot \frac{2}{\pi} \quad \text{with} \quad t = \frac{T_{\text{Pores}}}{n} \quad (10.8)$$

where t [mm] is the average pore chord length measured, T_{Pores} [mm] is the sum of all pore chords and n [-] is the number of counted pores. As a result, r_{pore} is obtained by the relation:

$$r_{\text{pore}} = \frac{\pi}{4} \cdot t \quad (10.9)$$

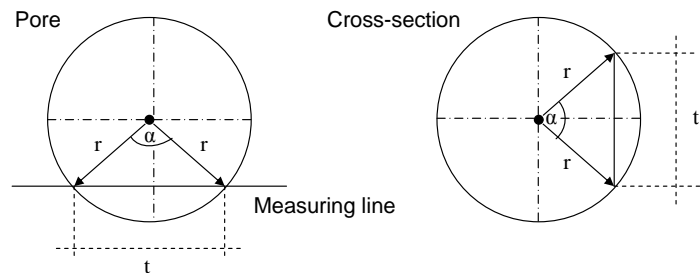


Figure 10.6: Schematic view on a pore cut by the measuring line and its cross-section.

Table 10.4: Characterization of the void system

Characteristic of pore system	Ref 0.50	Ref 0.40	AEA 0.50	AEA 0.40	SAP A 45-63	SAP A 63-90	SAP A 100-125	SAP A 125-200	SAP D
Total pore vol. [%]	2.4	1.7	6.4	6.1	4.7	5.5	5.8	5.3	6.5
SAP pore vol. [%]	-	-	-	-	3.26	3.26	4.37	3.43	(3.1)
Median chord [μm]	175	230	100	100	135	180	215	270	190
Average chord [μm]	260	410	140	160	200	255	290	365	200
Average radius [μm]	205	320	110	125	155	200	225	285	160
A_{300} [% by vol.]	0.7	0.3	4.1	2.7	2.4	2.3	1.9	1.0	3.1
V/S factor [mm]	0.475	0.860	0.165	0.200	0.265	0.320	0.345	0.460	0.220

The average pore radius r_{pore} is used as input for the V/S calculation according to equation (10.9). The results are reported in Table 10.4. In all cases the average pore chord size exceeds the median pore chord size by up to 60%. On this account, one can expect that V/S is overestimated. Further, the results confirm that increasing the particle size of dry SAP leads to increased values for V/S . The smallest values were found for concretes with AEA, which fulfil the demand for frost-resistant concretes of $V/S \leq 0.200$ mm, followed by concrete SAP D with comparable total pore content and A_{300} . The values for A_{300} are adopted from Figure 10.5 (right). Concrete SAF could not be characterized by pore counting. Anyway, the length of the pore channels created by SAF is smaller than the length of the dry fibres (5.8 mm) as they break during mixing.

10.3.4 Compressive strength

The results of the compressive strength tests are plotted in Figure 10.7. Concrete Ref 0.40 shows the highest compressive strength f_c due to lowest w/c ratio and the smallest air pore content. Compared to mixtures with AEA, which have the lowest compressive strength, mixtures with SAP show significantly improved performance. Even concrete SAP D with similar total pore content as AEA 0.40 shows higher values for f_c . The dotted lines in the right diagram indicate the influence of air entrainment by AEA on the compressive strength after 28 days at constant w/c ratios of 0.50 and 0.40. With increasing the air pore content by 1%, f_c is decreased by 3.5 MPa. Similar values can be found in literature [Neville 1995]. Concrete SAF is not plotted in the diagrams. Its 28 days compressive strength was found to yield 58.1 MPa.

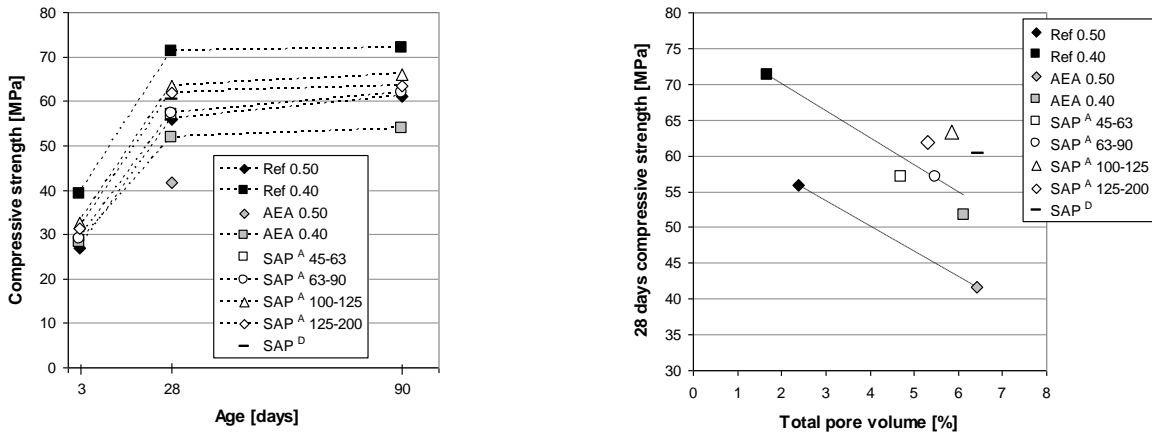


Figure 10.7: Development of compressive strength (left) and 28 days compressive strength as a function of total pore volume (right).

10.3.5 Weight change of specimen

The relative weight change was observed for specimen from the time of demoulding till the end of CDF-testing. The results are reported in Figure 10.8. The weight change zeroed at the beginning of the water bath storage is plotted in the right diagram. Within the first week the specimens increased their weight due to wet storage at 20°C and 100% RH followed by a period of weight decrease due to storage at 20°C and 65% RH. Regarding the total test period, the reference concretes show the highest weight ingress. At the end of CDF-testing it amounts to 0.6% by mass. Concretes with SAP and AEA show less weight ingress. After 28 cycles of CDF-testing, corresponding to an age of 49 days, specimens of concretes SAP A and AEA reach again their initial weight level. The specimen weight of concretes SAP D and SAF does not even exceed the initial level at the end of CDF-testing, i.e. after 64 freeze-thaw cycles.

The weight loss of SAP A mixtures during drying is comparable to the one of Ref 0.50 with same amount of total added water. On the other hand, the weight ingress due to capillary suction is comparable to the one of Ref 0.40 with less capillary porosity. The results indicate that SAP pores are partly air-filled during CDF-testing. Further it is expected that water uptake is limited closer to the surface area as compared to the other concretes.

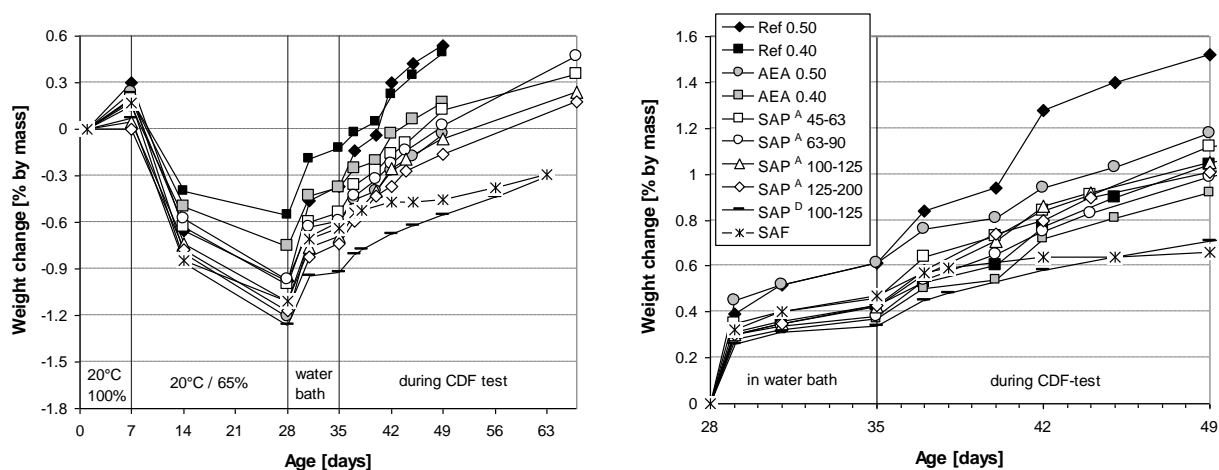


Figure 10.8: Relative weight change of specimen till the end of CDF testing, zeroed at the time of demoulding (left) and zeroed at the beginning of the water bath storage (right).

10.3.6 Change in ultrasonic velocity

The ultrasonic transit time was measured for each specimen just before scaling was determined. The results are reported in Figure 10.9 (left). In general, the US wave velocity can indicate two important changes of the material property:

- 1) An increase of the water content, which is indicated by a smaller transit time since the velocity is about 4 times larger in water than in air.
- 2) Internal damage, where a significantly increased transit time is measured, which indicates the formation of internal surfaces due to cracking.

With increasing the particle size of SAP A the initial ultrasonic transit time is decreasing. The reason for this finding is that larger particle sizes generate a higher specific pore surface. In addition, the highest initial transit time was measured for concrete AEA 0.50 which has the highest porosity. During CDF-testing the US transit time of AEA and reference concretes was increasing. The latter showed the higher increase. It is an indication for the occurrence of internal

damage. In contrast, the US transit time of SAP-modified concretes remained constant for the whole test period, although weight ingress due to water uptake proceeded similarly. It might be a first indication that SAPs limit water uptake and internal damage to surface close areas.

The change in US wave velocity can be expressed as the relative dynamic modulus of elasticity, see Figure 10.9 (right). The CIF test criterion demands a minimum of 80% after 56 freeze-thaw cycles. Unfortunately, both the reference and the AEA concretes could be observed for 28 cycles only. Nevertheless, it is most likely that the reference concretes would have failed.

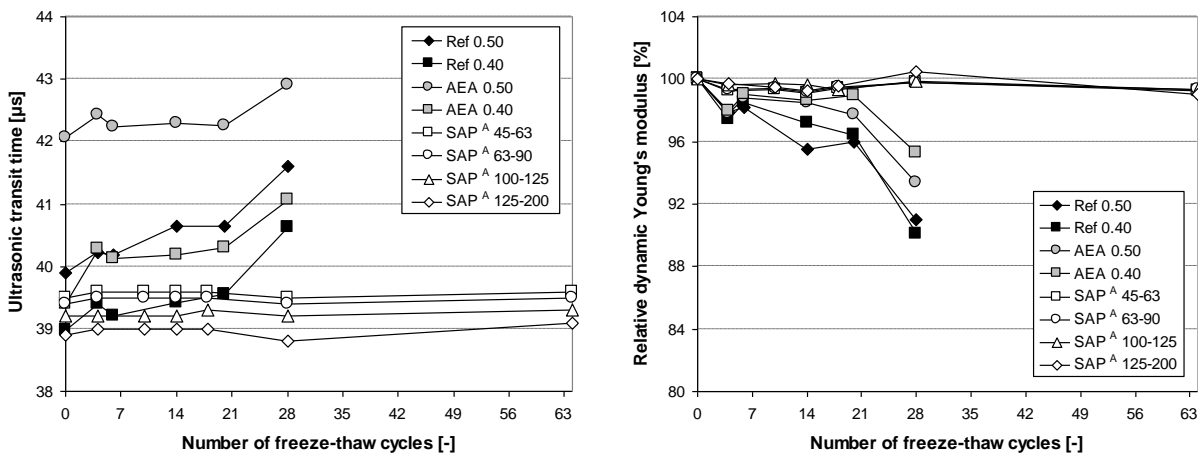


Figure 10.9: Ultrasonic transit time as a function of freeze-thaw cycles (left) and related change in relative dynamic modulus of elasticity (right).

10.3.7 Scaling of concrete

Figure 10.10 presents the measured scaling as a function of the number of freeze-thaw cycles. Except for Ref 0.40 the values reported present the average of five samples tested. Due to detached sealing of some lateral sides observed on four samples of Ref 0.40, the values refer to the sample with intact sealing. It was found that the detached sealing increased the scaling by about 9% by mass, see appendix 10. On this account the values for Ref 0.50, where defective sealing and consequently higher scaling was observed for all five samples, were reduced by 10%.

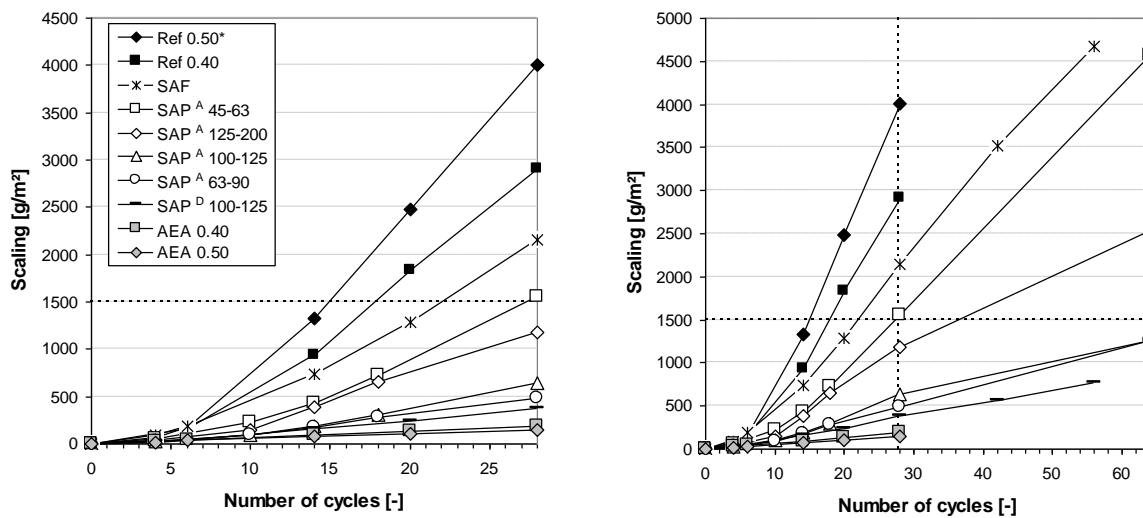


Figure 10.10: Scaling of concrete up to 28 and 64 cycles, respectively (*: values reduced by 10%).

Except for concretes Ref 0.50, Ref 0.40, SAF and SAP A 45-63 the scaling was below the limit of 1500 g/cm² recommended by Rilem [Rilem 1996]. Mixture SAP A 45-63 missed the limit narrowly whereas both reference concretes showed scaling of more than twice the limit value. Mixes with AEA showed the highest resistance against scaling, followed closely by mix SAP D. The latter did not even exceed the limit after 56 cycles. The same was found for SAP A 63-90 and SAP A 100-125. Concrete SAP A 125-200 showed higher scaling, but less than SAP A 45-63. It seems that scaling of SAP A mixtures is not directly linked to VS. Figure 10.11 presents the test surface of a SAP D sample after 56 cycles in comparison to one of Ref 0.40 after 28 cycles.

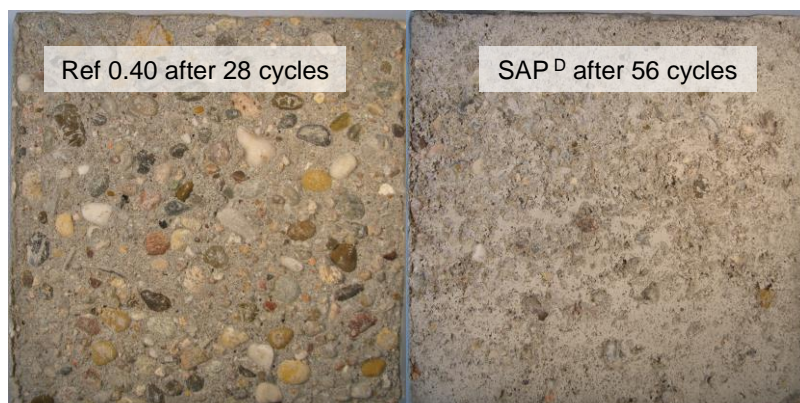


Figure 10.11: Test surface of Ref 0.40 sample after 28 cycles in comparison to SAP D sample after 56 cycles.

10.3.8 Abrasion resistance

The results of the wear test are provided by Figure 10.12. The abrasion resistance depends first and foremost on the compressive strength. With increasing compressive strength the abrasion is decreasing. Consequently, concretes with AEA show high abrasion and reference concretes show low abrasion. Concretes with SAP also share the decreasing abrasion with increased compressive strength. In addition, small particle sizes seem to enhance the abrasion resistance compared to large particles. Among all concretes investigated SAP A 100-125 has the best outcome.

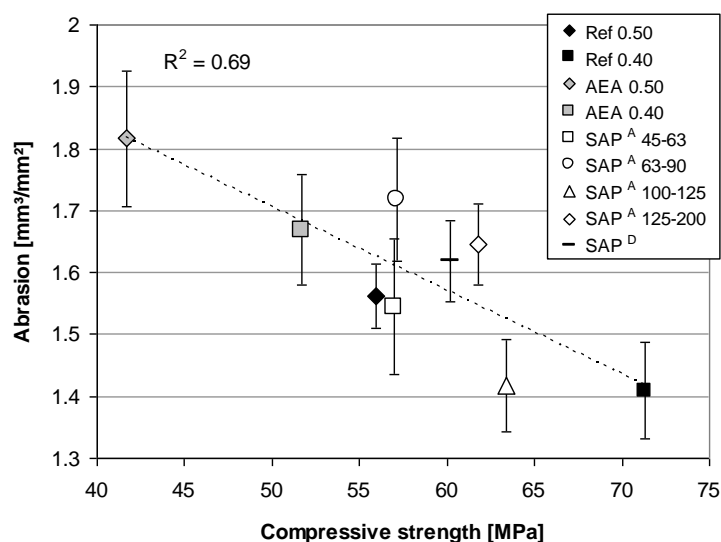


Figure 10.12: Abrasion measured after 388 rev. as a function of the 28 days compressive strength.

10.4 Discussion

10.4.1 Characterization of the pore system

Although SAP D is a deeply investigated SAP, e.g. [Jensen & Hansen 2002], no comment on its ability to entrain small air-bubbles in the fresh concrete could be found in literature. The side effect might be caused by residual tensides (see chapter 2.8.8). Tensides are used to stabilize the droplets of the monomer mix in the organic solution during inverse suspension polymerization, see chapter 2.9.3. The investigation of microsections of hardened cement paste samples indicated that small pores, supposed as air bubbles, were arranged around larger pores, supposed as the SAP D pores, see chapter 7.4. However, the total pore volume of concrete SAP D was increased unintentionally. As a consequence, the freeze-thaw resistance seemed to be further improved.

To maintain workability of concrete SAF, up to three times the amount of PCE of concrete with SAP had to be added. The high amount of PCE is an indication that SAF absorbed more pore solution than expected. Unfortunately, this could not be verified experimentally as the method of pore counting is not applicable in case of pore channels. Further investigations on the swelling capacity of SAF in pore solution are necessary, i.e. by the application of the tea-bag test method using pore solution extracted at several points in time during the dormant stage of hydration as absorbing fluid. The maximum length of the pore channels created is the length of the dry fibres, which is 5.8 mm. As the fibres break during mixing, the average length of the pore channels is a matter of guesswork. It is, however, undisputable that aggregate size, mixing time and intensity will affect the degree of fragmentation.

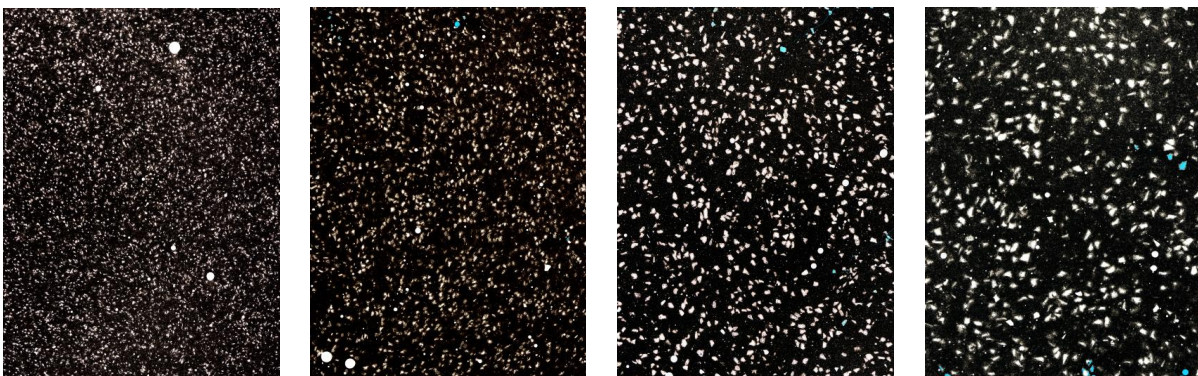


Figure 10.13: Microsections ($20 \times 27 \text{ mm}^2$) of cement paste containing 0.33% SAP A by mass of cement of different size range: 45-63, 63-90, 100-125 and 200-250 μm (from left to right).

The characteristics of pores formed by SAP A were investigated in another study, cf. Table 10.5. It was divided in two parts: The first part was imaging analysis (IA) of microsections by the method described in chapter 4.3.4. Figure 10.13 presents four microsections of hardened cement paste samples containing 0.33% SAP A by mass of cement. It is apparent that for a given pore content the V/S is reduced and the number of pores is increased with smaller particle size. The volume of SAP pores found is in good agreement with the water absorption capacity of 24 g/g, estimated by comparative mortar spread tests presented in chapter 4.4.2. The second part of the study was the characterization of the dry particles due to laser granulometry (LG) as described in section 4.2.2. From the results obtained by LG, i.e. the average particle diameter, the void spacing of SAP A pores in concrete was calculated and compared to measured values presented in Table 10.4 on page 146. The calculation approach used was derived from the hexagonal close packing (HCP) of spheres as described in chapter 4.4.5, see equation (4.14) on page 58.

Table 10.5: Properties of dry SAP A material and calculated properties of SAP A pore system

Analysis of micrographs	Unit	SAP A 45-63	SAP A 63-90	SAP A 100-125	SAP A 125-200
V_{SAP} in cement paste	%	8.23	8.01	8.28	8.37
Calc. absorption capacity	g/g	23.8	23.2	23.9	24.2
Properties of dry particles	Unit	SAP A 45-63	SAP A 63-90	SAP A 100-125	SAP A 125-200
Size range sieved	μm	45-63	63-90	100-125	125-200
Average particle size (LG)	μm	55	75	100	145
Expected average pore size	μm	180	245	330	575
Calculated VS in concrete	mm	0.110	0.150	0.205	0.295

Figure 10.14 shows the void spacing of concretes with SAP A as a function of the average pore size. The dashed line represents the calculation results obtained by assuming HCP of the pores. The solid line is a linear fitting regression of VS determined by pore counting of SAP A pores according to [DIN EN 480-11 2005]. The diagram shows that void spacing and average pore diameter are overestimated by the standard that assumes the allocation of pores in a system of cubes.

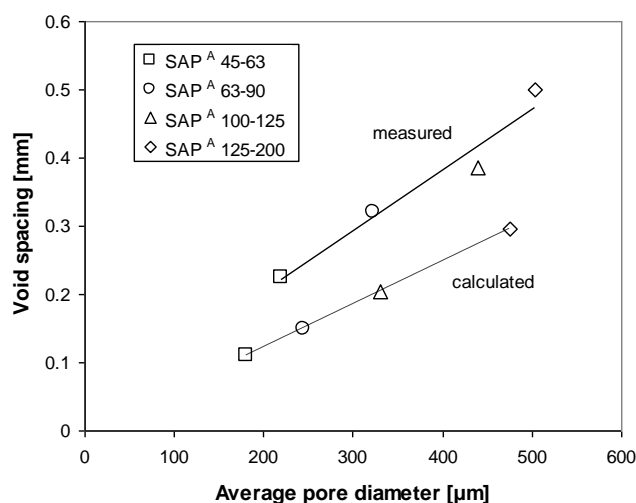


Figure 10.14: Void spacing of SAP A pores as a function of the average pore diameter at different arrangements of pores: hexagonal (calculated) vs. cubic (measured).

10.4.2 Scaling and internal damage

The freeze-thaw resistance of concrete can either be classified by measuring the scaled material or indirectly by the determination of the actual void spacing in comparison to a critical value, i.e. $VS \leq 0.200$ mm. VS is generally assumed to be the decisive parameter classifying the frost resistance of concrete. The test results obtained in the present study are in doubt about this procedure in case of SAP-modified concretes. Figure 10.15 reports on the scaling as a function of VS and A_{300} . Both diagrams show that concrete SAP A 45-63 does not fit the regression well. According to Figure 10.16 the scaling shows rather good correlation with the total pore volume. In fact, all concretes with SAP A were intended to possess the same amount of pore volume, but due to different air pore content, the total pore volume varied. Figure 10.17 presents the scaling in dependence of the 28 days compressive strength. The low compressive strength values of course belong to concretes with artificial pores and the high strength belongs to Ref 0.40.

The effect of SAP on the frost deterioration mechanisms in concrete can not be satisfactorily clarified by the study at hand. Obviously the small particles act less effectively. The reason for this

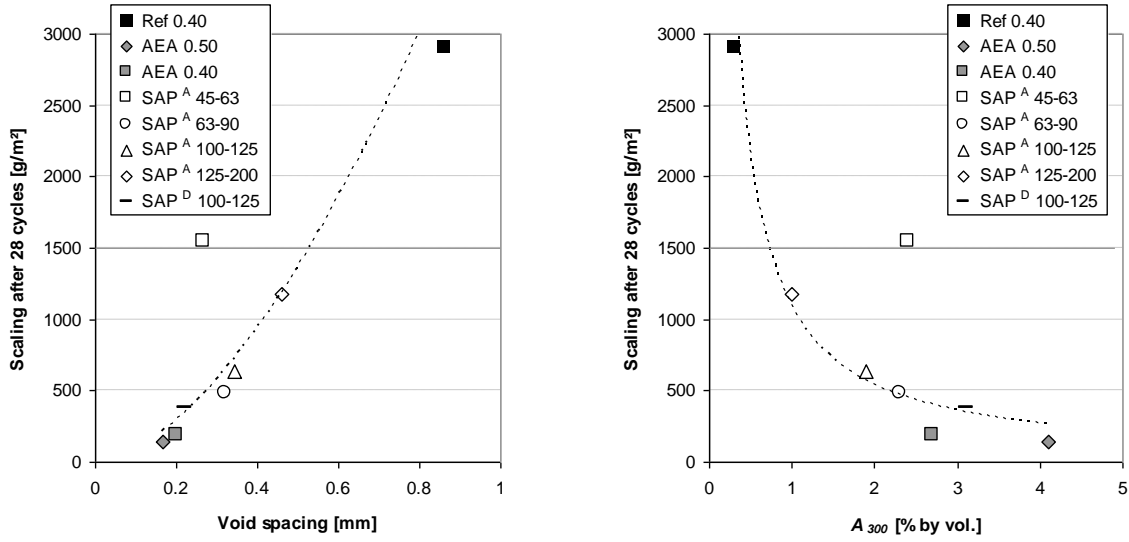


Figure 10.15: Scaling of concrete after 28 cycles as a function of VS (left) and A_{300} (right).

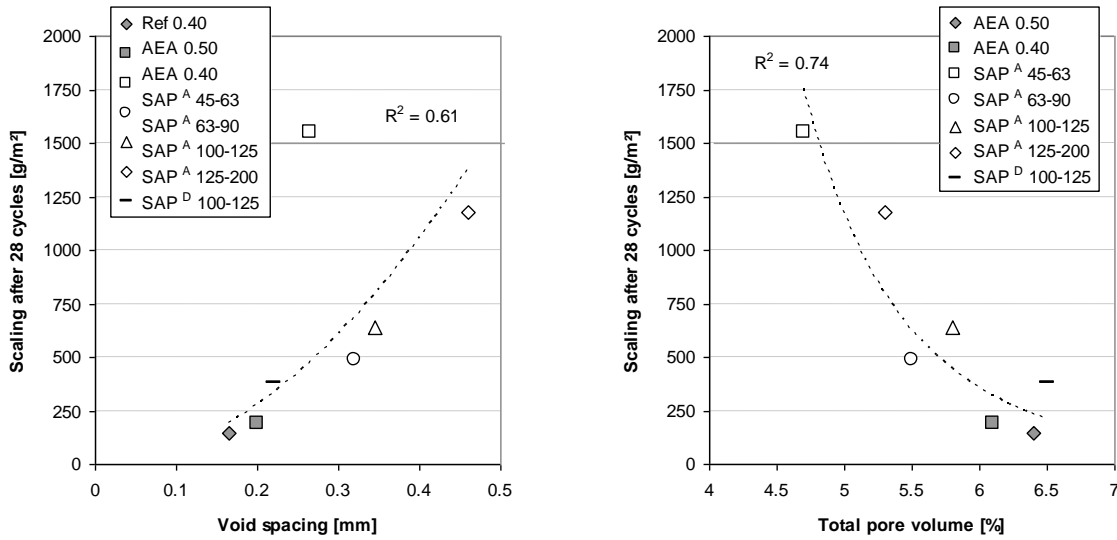


Figure 10.16: Scaling after 28 cycles as a function of VS (left) and total pore volume (right).

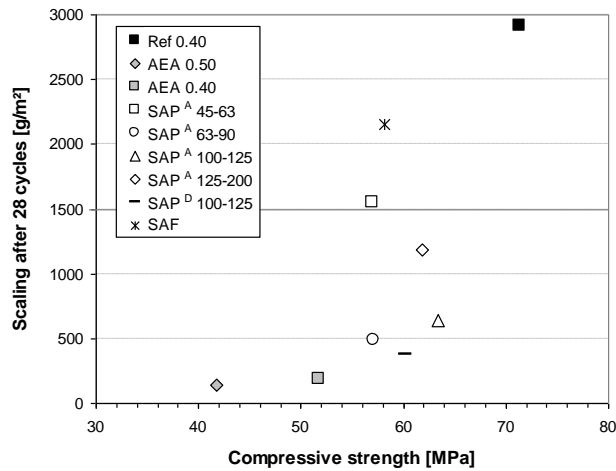


Figure 10.17: Scaling of concrete after 28 cycles as a function of 28 days compressive strength.

finding might be that a critical degree of saturation is reached earlier compared to larger-sized pores. Observations on the weight loss during the drying period previous to CDF-testing showed that among concretes with SAP A the weight loss was higher with increasing the particle size. The same behaviour was already found in chapter 9. As a consequence, concrete SAP A 45-63 might have had less air-filled SAP pore volume at the beginning of the CDF-test. In combination with lower air pore content, freeze-thaw damage might have occurred earlier and faster.

The fact that SAP-modified concretes apparently show no internal damage but surface scaling indicates that the damage is restricted to a surface close area. As it can be assumed that low temperatures do not lead to degradation of the polymers, they might reduce the penetration depth of water during testing. As a result, the saturation of pores close to the surface is increased while pores further inside show less saturation and consequently, internal damage is mitigated. Further it is known that water in SAP underlies a certain freezing point depression (see chapter 2.8.3).

10.4.3 Abrasion

Smaller SAP particle size means larger perimeter of pore cross-sections. The abrasive powder might act less effectively as it is accumulated along the high length of pore walls, leading to high abrasion resistance. In general, the absence of micro-cracks due to IC effects could mitigate abrasion of SAP-modified mixes similar to shrinkage-compensating concrete [ACI 223R 1983].

10.4.4 Literature review

In [Laustsen et al. 2008] the suspension polymerized type SAP D was investigated with respect to the effect on the freeze-thaw damage as well. The concretes had a basic w/c ratio of 0.42. Due to addition of extra water, the absorption by SAP D was accounted and the pore volume entrained by SAP D varied from 1.5 to 10%. The pore size was adjusted by sieving the dry particles in two size ranges where the average pore size was assumed to yield either 150 μm or 300 μm . Due to calculation, the void spacing was expected to be 0.15 to 0.40 mm. The freeze-thaw experiments were conducted according to [DS CEN/TS 12390-9 2006]. The results show that for a given SAP pore content the size of the pores and further their void spacing does not influence scaling much. With increasing the added amount of SAP, the scaled material was reduced of course. Further it could be shown that even concrete samples stored sealed before testing show reduced scaling. Under sealed conditions, the initially water-filled SAP pores could only be drained from water by chemical shrinkage, which was assumed to yield 1.9% by volume at maximum.

However, the paper does not report on the side effect that SAP D entraps air bubbles in the fresh concrete, as found in the experiments at hand. It can be speculated that this effect did appear as well and might have increased frost resistance besides the contribution of SAP D pores.

In [Bruedern & Mechtcherine 2010] SAP was added to prevent surface damage of strain-hardening cement-based composites (SHCC). The water to binder ratio of SHCC was 0.30, the fly ash to binder ratio was 0.55 and the amount of added fibres was 29 kg/m^3 concrete. One reference mixture and three mixtures with 2 kg SAP per cubic meter concrete were examined in CDF-tests, whereof for one concrete, the addition of SAP was accompanied by extra water of 2.5% by volume. It was found that SAP can considerably improve the freeze-thaw resistance, i.e. only the very outer matrix layer was lost. The mass loss of the mixture with extra water was only slightly increased.

Besides the experimental series at hand and the pre-tests published in [Reinhardt et al. 2008], no further investigations exist so far that compare the efficiency of SAP to ordinary AEA.

10.4.5 Summary of test results and ranking of concretes investigated

Table 10.6 lists all important test results obtained in the experimental series at hand. The weight change [% by mass] refers to the weight of the CDF samples measured after 28 freeze-thaw cycles in relation to the initial weight at demoulding. Values in brackets are estimates which could not be determined due to lack of adequate laboratory equipment.

Table 10.6: Summary of test results (*: value reduced by 10%)

Property of concrete	Ref 0.50	Ref 0.40	AEA 0.50	AEA 0.40	SAP ^A 45-63	SAP ^A 63-90	SAP ^A 100-125	SAP ^A 125-200	SAP ^D 100-125	SAF
Total pore vol. [%]	2.4	1.7	6.4	6.1	4.7	5.5	5.8	5.3	6.5	(-)
SAP pore vol. [%]	-	-	-	-	3.3	3.3	4.4	3.4	(3.1)	(3.2)
Weight change [%]	0.52	0.49	-0.03	0.17	0.13	0.06	-0.11	-0.18	-0.56	-0.45
Median chord [μm]	175	230	100	100	135	180	215	270	190	-
Av. pore size [μm]	410	640	220	250	310	400	450	570	320	-
Void spacing [mm]	0.475	0.860	0.165	0.200	0.265	0.320	0.345	0.460	0.220	-
f_c (28 days) [MPa]	55.9	71.3	41.7	51.7	57.0	57.1	63.4	61.8	60.2	58.1
Scaling 28 th c. [g/m^2]	4010*	2910	145	190	1550	485	640	1180	380	2150
Abrasion [m^3/m^2]	1.56	1.41	1.82	1.67	1.55	1.72	1.42	1.65	1.62	1.74

In Figure 10.18 the tested concretes are compared with respect to scaling after 28 cycles, total pore content and 28 days compressive strength. The three axes are standardized as follows: The best value among the concretes reached within each category is set to zero; the worst value is set to one. In case of scaling and pore content the best means the lowest value whereas in case of strength the highest value is the best. By the assumption that all properties are regarded as equivalent, the smallest surface A, described by the triangle in the diagram means the best performance. Of course, for concrete Ref 0.40 no triangle is formed as it is top rated in two categories, i.e. strength and pore volume. In the ranking among concretes with air entrainment, SAP A 100-125 ranks above SAP D. AEA mixes bring up the rear. If abrasion is included as 4th property, the relative comparison of the concretes will lead to the same ranking, see appendix 10.

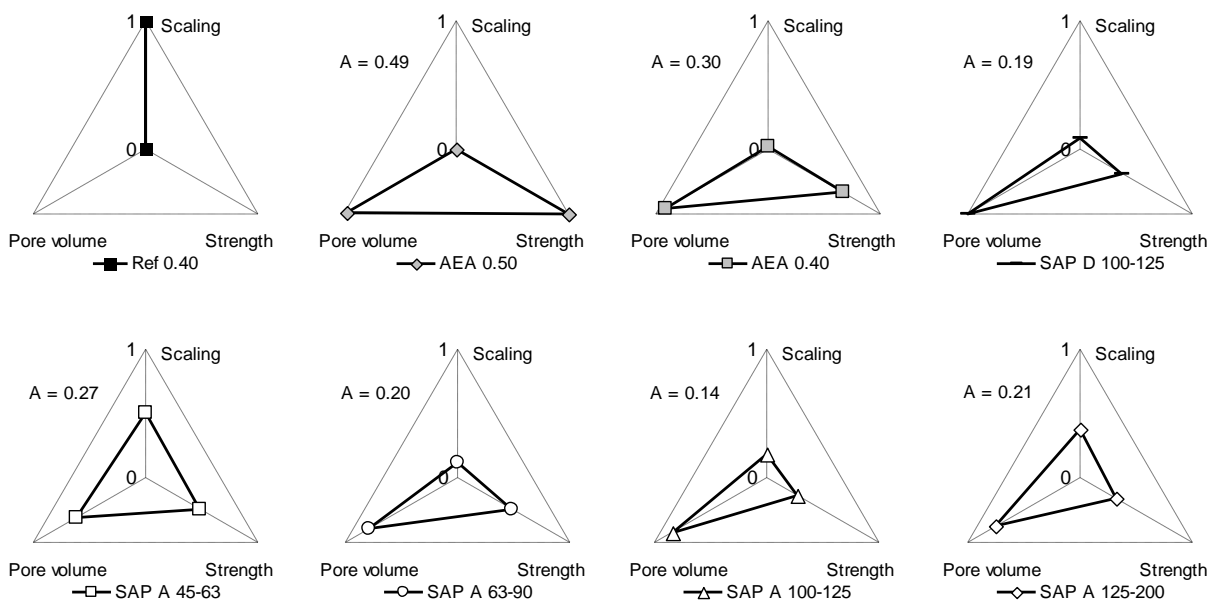


Figure 10.18: Relative performance of concretes. The worst score possible is $A=0.87$.

10.5 SAP vs. traditional AEA

Traditionally, air entrainment in concrete is achieved by the use of chemical AEA. However, this method has several disadvantages that require a high expense of initial testing and testing during construction work in order to compensate inadequate handling reliability. For example:

- The volume of air entrapped cannot be predicted based on a given dosage of AEA since the interactions of the reactive ingredients are not understood so far.
- The size distribution of the air voids created cannot be controlled satisfactorily; small air voids tend to coalesce forming larger air voids.
- The environmental conditions like temperature and compaction energy influence the air void system; the air void system is not stable in fresh concrete.
- Due to the large difference in density between air and fresh concrete, separation of individual pores and even redistribution of the air void system may occur in dependence on the rheological behaviour of the fresh concrete.

In contrast, several benefits exist that establish air entrainment by SAP as straightforward technology. Compared to traditional AEA, the following advantages are expected or even demonstrated so far, cf. also [Laustsen et al. 2008]:

- The amount of pore volume can be controlled by the dosage of SAP.
- The separation tendency is reduced due to smaller difference in the density; the pore system is stable in fresh concrete and insensitive to mixing, transportation and placing even under severe environmental conditions, e.g. shotcreting or high temperatures.
- Shape and size distribution of SAP pores are pre-designed within production related limits of the dry SAP particles.
- The compressive strength of the concretes can be increased due to internal curing effects, given that low w/c ratios are applied.

At present, no in-situ test method for fresh concrete is available that can precisely bring evidence on the volume of entrapped SAP pores as they are initially water-saturated in the fresh mix. With respect to practice, any risk of incorrect dosage of SAP has to be excluded. This suggests the addition of SAP in concrete premixed with cement as well as binder.

10.6 Conclusion

The experimental series on concrete conducted for the investigation of the influence of SAP pores on the freeze-thaw damage pointed out several interesting findings. The most prominent finding is that SAP can substantially improve the frost resistance of concrete. Both the gel-polymerized type SAP A and the suspension polymerized type SAP D can be efficiently used for air entrainment in concrete. With few exceptions regarding the size fraction of used SAP particles, the method of air entrainment by SAP can be seen as more straightforward technology compared to traditional AEA. The conclusions in detail are listed in the following:

- SAF obviously reduces the workability of fresh concrete dramatically. The absorption capacity of 18 g/g was found to be estimated too low. Further, the addition of SAF did not lead to a significant improvement of the frost-resistance, although the weight ingress due to capillary suction was effectively reduced.
- Pore counting allows distinguishing between air voids and pores formed by gel-polymerized SAP. The SAP pore content agreed with the expected water absorption capacity.

- Changes in the size distribution of dry SAP particles are directly reflected in the developing pore structure. With decreasing the particle size the pore sizes decrease, too. However, some larger SAP A particles obviously broke into smaller pieces during mixing.
- The calculated void spacing of SAP A pores based on the hexagonal arrangement of equal sized pores is smaller than the measured void spacing adopted from pore counting.

The results of compressive strength and abrasion resistance tests led to the following findings:

- The addition of AEA results in a decrease of the compressive strength of 3.5 MPa per 1% air pore volume entrapped.
- Concretes with SAP A and SAP D showed higher compressive strength than concretes with AEA. If lower w/c ratios were applied, the relative difference in strength would be further increased due to internal curing effects caused by SAP.
- The abrasion resistance primarily depends on the compressive strength. Smaller SAP particle size leads to higher abrasion resistance.

The CDF-tests produced the following conclusions:

- The weight loss of concretes with SAP A during the drying period was comparable to Ref 0.50 with same total amount of water. Further, with increasing the particle size of SAP A the weight loss was higher. However, the weight ingress due to capillary suction was comparable to Ref 0.40 with less capillary porosity.
- It is expected that SAP pores are mainly air-filled during testing; besides drying, SAP pores are emptied due to hydration, see chapter 5.
- Except concretes Ref 0.50, Ref 0.40, SAF and SAP A 45-63, all other concretes kept the limit of scaled material of 1500 g/m² measured after 28 cycles as recommended by Rilem.
- Among concretes with artificial pores due to SAP, concrete SAP D had the best outcome. One reason is that SAP D obviously entrained small air bubbles in the fresh concrete that increased the total pore volume.
- The initial US wave velocity was decreasing with increasing the particle size of SAP A.
- During testing, SAP-modified concretes did not show changes in the US wave velocity, although weight ingress was observed. This is an indication that freeze-thaw damage might be limited to areas close to the surface and internal damage is prevented due to SAP.
- For a given pore volume, smaller particle fractions of SAP lead to a higher freeze-thaw resistance. But caution is recommended in case of median SAP pore chord size < 150 μm. It could be shown that below this value, concretes show dramatically increased scaling.

10.7 Outlook

More research on the effect of SAP on the freeze-thaw damage mechanisms is needed. Strain measurements during freeze-thaw testing could bring evidence on a possible influence of SAP on frost shrinkage and frost suction.

Water movement in SAP-modified concretes caused by capillary suction could be observed by the application of neutron radiography. This method has already been applied to study the penetration depth of moisture in cracked and uncracked concrete [Wittmann et al. 2011]. Such experiments may allow to draw conclusions on the effect of SAP on the water penetration depth. It is expected that SAP limit the water penetration to areas close to the surface and therefore mitigate internal damage. Anyway, further CIF-tests should be carried out to provide more reliable data that confirm the test results obtained in the study at hand.

11 Final conclusion and future research

11.1 Final conclusion

This dissertation shows the multi-functional use of salt-insensitive superabsorbent polymers as concrete additive. Two important application methods stand out: The use of SAP for the purpose of internal curing of low w/c ratio systems and the addition of SAP in order to redistribute capillary water by artificial macropore inclusions. In both cases, the focus is put on the change of physical properties of hardened concrete. Each SAP-modified mix is compared with two SAP-free control mixes, i.e. one mix with same total water content and one mix where the total water content is reduced by the amount of water initially absorbed by SAP. The main finding on internal curing is as follows:

- SAP can be used for successful long-term prevention of self-desiccation and self-desiccation shrinkage, respectively, if two pre-requisites are fulfilled: First, the amount of entrained water equals the amount of chemical shrinkage at maximum degree of hydration and, second, the spatial distribution of SAP inclusions makes sure that the nearest pore surface is located in the distance of less than approximately 1 mm from any point of the hydrating matrix.

This finding bases on observations on autogenous phenomena of Portland cement paste and investigations on high performance mortar blended with 1/10 silica fume, produced at w/c ratios in the range 0.30 to 0.37. If the amount of entrained water is less or its kinetic availability is expected to not meet the demand of hydration, the effectiveness of IC by SAP is dramatically reduced. However, for practical applications the SAP dosage should be generally reduced to small fractions that are just enough to prevent cracking from restraint autogenous shrinkage at early age, i.e. when the matrix is especially weak and thermal stresses superimpose the shrinkage strain.

The measurements on cement paste led to some further interesting conclusions:

- Water supplied by SAP does not influence hydration much different from ordinarily added water. In the first days of sealed hardening, the degree of hydration is slightly higher for SAP-modified pastes, whereas at higher ages the degree of hydration of reference pastes shows the somewhat larger values.
- Drainage of SAP pores can be studied by high-resolution relaxometry measurements. The signal emitted from water in SAP can be filtered by applying a CPMG pulse sequence with a delay of 5 ms to the onset of data acquisition. Consumption of IC water is made visible by the loss of transverse magnetization intensity as a function of age.
- The dynamic elastic material properties studied by continuous monitoring of the hardening, using pressure and shear waves, develop the same for both reference and SAP-modified pastes, provided that the total amount of added water is the same.
- Compared to reference paste with same basic w/c ratio, the strength-increasing effect due to proceeded hydration cannot counterbalance the strength-reducing effect of SAP voids even at higher age. Only the flexural strength of SAP-modified paste exceeds the value of reference paste at higher age, possibly due to prevention of micro-cracking.

Manipulation of the pore structure due to redistribution of capillary water is intended to have positive effects on the durability of concrete. Experimental series were performed on normal

strength concretes where IC does not become operative and, hence, the results can safely be transferred to low w/c ratio systems. The following effects could be demonstrated:

- Oxygen and water permeability, capillary suction and carbonation can be reduced due to addition of SAP. This reduction is even more pronounced when the particle size of SAP is increased.
- SAP pores can be used for air-entrainment in concrete in order to enhance its freeze-thaw resistance. When dried out, SAP pores act similarly as pores generated by traditional air-entraining agents, but are stable against environmental impacts. Concerning scaling determined by the CDF-test method, the total pore volume is the decisive parameter. The void spacing has a minor role, but caution is advised when the median SAP pore chord size is less than 150 μm and saturation of pores is disproportionately high.
- Water in SAP seems to have higher mobility, evaporates easier and causes less (drying) shrinkage strain compared with capillary pore water.
- The 28 days compressive strength is reduced due to SAP addition. Reduction is less when the cubes are allowed to dry prior to testing. Curing in water causes the highest strength reduction. Compared to reference concretes with same total water content, SAP-modified concretes show slightly higher strength values. This effect is more pronounced in case of concretes produced at low w/c ratio.

Further, the effect of SAP addition on tensile creep of concrete produced at w/c ratio of 0.36 and 0.42 was studied. It was found that:

- Creep in tension is reduced by SAP addition and seems to be determined by the basic w/c ratio, which defines the distance of gel particles and the layer thickness of absorbed water, both influencing the creep mechanisms according to viscous flow hypothesis and seepage theory.
- Shrinkage is more sensitive to drying than creep in tension. Exposed to moderate drying in PE-envelope, concrete shows higher shrinkage strain but almost the same tensile creep strain compared with sealed specimens.

At last, it should be noted that the chemical and physical properties of the SAP material is expected to have a strong influence on its performance in concrete, mortar or cement paste. Consequently, the results presented in this dissertation are not unrestrictedly transferable to other SAP material, especially to commercially available, non-salt-insensitive types of SAP.

11.2 Future research

In contrast to the dry mortar market, where SAP is recently available as rheology modifier, the application of SAP as concrete additive has not been subjected to approval yet. However, it is most likely that SAP will be launched on the market someday, dryly pre-mixed with cement to prevent dosing errors and gel-blocking effects. What is certain is that the SAP technology is still in the early stage of development. In future, SAP could be coated in order to impose retarded water absorption for improved mixing, transport and placing of concrete. Further, it is conceivable that SAP is used for inward transfer of liquid additives and even for gaining control on their release.

A still persistent problem is the determination of the true water absorption capacity of SAP in cementitious environment. To this end, it is recommended to study water absorption of SAP by imaging techniques like neutron tomography.

Concerning the experimental series presented in this dissertation, some substantial improvements for ongoing research are proposed by the following considerations:

- Measurements on autogenous shrinkage should include the determination of the onset of the tensile stress development in active restraint systems to define the real time zero.
- The initial autogenous deformation that occurs before the RH depression caused by menisci formation, should be investigated by tensiometer embedded in the fresh paste.
- Freeze-thaw tests on concrete should be accompanied by strain measurements in order to state on a possible effect of SAP on frost-shrinkage and frost-suction.

Further, some open questions have remained that need to be discussed in future:

- Does SAP limit freeze-thaw damage to the surface close concrete zone?
- Does SAP reduce creep of concrete in compression?
- What is the mechanism behind autogenous expansion?
- Can self-desiccation start although IC water is still present in the SAP inclusions?

References

- [ACI 209R 1992] *Prediction of creep, shrinkage and temperature effects in concrete structures: an ACI Standard*. Farmington Hills: American Concrete Institute, 1992.
- [ACI 223R 1983] *Standard practice for the use of shrinkage-compensating concrete: ACI manual of concrete practice*. Farmington Hills: American Concrete Institute, 1983.
- [Acker & Ulm 2001] Acker, P. & Ulm, F.-J.: Creep and shrinkage of concrete: Physical origins and practical measurements. In: *Nuclear Engineering and Design* 203 (2001), No. 2-3, pp. 143-158.
- [Akaike 1974] Akaike, H.: A new look at the statistical model identification. In: *IEEE transactions on automatic control* 19 (1974), No. 6, pp. 716-723.
- [Alfes 1989] Alfes, C.: Hochfeste, verformungsarme Betone mit Silica-Staub. In: *Betonwerk + Fertigteil-Technik* 55 (1989), No. 11, pp. 62-71 (German).
- [Aligizaki 2006] Aligizaki, K.K.: *Pore structure of cement-based materials: testing, interpretation and requirements*. London: Taylor & Francis, 2006.
- [Altoubat & Lange 2002a] Altoubat, S.A. & Lange, D.A.: Tensile basic creep: Measurements and behaviour at early age. In: *ACI Materials Journal* 98 (2002), No. 5, pp. 386-393.
- [Altoubat & Lange 2002b] Altoubat, S.A. & Lange, D.A.: The Pickett effect at early age and experiment separating its mechanism in tension. In: *Materials and Structures* 35 (2002), No. 4, pp. 211-218.
- [Assmann 2008] Assmann, A.: *Bruchmechanische Untersuchung des Einflusses kleiner, mittlerer und großer Kapillarporen auf die Betonfestigkeit*. Stuttgart: University of Stuttgart, Department of Construction Materials, Diploma thesis, 2008 (German).
- [Assmann 2009] Assmann, A.: *Report about progress and results of the research conducted for the investigation of superabsorbent polymers*. Stuttgart, University of Stuttgart, Department of Construction Materials, Test report 02/09, 2009, not published.
- [ASTM C1581-09] *Standard test method for determining age at cracking and induced tensile stress characteristics of mortar and concrete under restrained shrinkage*. West Conshohocken: American Society for Testing Materials, 2009.
- [ASTM C1608-07] *Standard test method for chemical shrinkage of hydraulic cement paste*. West Conshohocken: American Society for Testing Materials, 2007.
- [ASTM C1698-09] *Standard test method for autogenous strain of cement paste and mortar*. West Conshohocken: American Society for Testing Materials, 2009.
- [ASTM C666-08] *Standard test method for resistance of concrete to rapid freezing and thawing*. West Conshohocken: American Society for Testing Materials, 2008.
- [Atrushi 2003] Atrushi, D.S.: *Tensile and compressive creep of early age concrete: Testing and modeling*. Trondheim, The Norwegian University of Science and Technology, Ph.D. thesis, 2003.
- [Auberg 1998] Auberg, R.: *Zuverlässige Prüfung des Frost- und Frost-Tausalz widerstands*. Essen, University of Essen, Dissertation, 1998 (German).

-
- [Azad et al. 2003] Azad, M.M.; Herfert, N.; Mitchel, M. & Robinson, J.: *Crosslinked polyamin coating on superabsorbent polymers*. Ludwigshafen: BASF AG, WO 2003/0436670 A1, 2003.
- [Banfill 2006] Banfill, P.F.G.: Rheology of fresh cement and concrete. In: *Rheology Reviews* (2006), pp. 61-131.
- [Bangham & Fakhoury 1931] Bangham, D.H. & Fakhoury, N.: The swelling of charcoal. In: *Proceedings of the Royal Society of London, CXXX, Series A* (1931), pp. 81-89.
- [Baroghel-Bouny & Kheirbek 2001] Baroghel-Bouny, V. & Kheirbek, A.: Effect of mix-parameters on autogenous deformation of cement pastes - microstructural interpretations. In: *Concrete Science and Engineering* 3 (2001), pp. 23-28.
- [Bažant & Chern 1985] Bažant, Z.P. & Cern, J.C.: Concrete creep at variable humidity: Constitutive law and mechanism. In: *Materials and Structures* 18 (1985), No. 1, pp. 1-20.
- [Bažant & Wittmann 1982] Bažant, Z.P. & Wittmann, F.H.: *Creep and shrinkage in concrete construction*. New York: John Wiley & Sons, 1982.
- [Bažant & Xi 1994] Bažant, Z.P. & Xi, Y.: Drying creep of concrete: constitutive model and new experiments separating its mechanisms. In: *Materials and Structures* 27 (1994), No. 1, pp. 3-14.
- [Bažant et al. 1988] Bažant, Z.P.; Dougill, J.; Huet, T.; Tsubaki, T. & Wittmann, F.: Material models for structural creep analysis. In: Bažant, Z.P. (Ed.): *Mathematical modelling of creep and shrinkage of concrete*. Chichester: John Wiley & Sons, 1988, pp. 99-215.
- [Bentz 2002] Bentz, D.: *Influence of curing conditions on water loss and hydration in cement paste with and without fly ash substitution*. Gaithersburg: U.S. Department of Commerce, NISTIR 6886, 2002.
- [Bentz et al. 1994] Bentz, D.; Coveney, P.; Garboczi, E.; Kleyn, M. & Stutzman, P.: Cellular automation simulations of cement hydration and microstructure development. In: *Modelling and Simulation in Materials Science and Engineering* 2 (1994), No. 4, pp. 783-808.
- [Bentz et al. 1998] Bentz, D.P.; Garboczi, E.J. & Quenard, D.A.: Modelling drying shrinkage in reconstructed porous materials: application to porous Vycor glass. In: *Modelling and Simulation in Materials Science and Engineering* 6 (1998), pp. 211-236.
- [Bentz et al. 1999] Bentz, D.P.; Garboczi, E.J. & Snyder, K.A.: *A hard core/soft shell microstructural model for studying percolation and transport in three-dimensional composite media*. Gaithersburg: U.S. Department of Commerce, NISTIR 6265, 1999.
- [Bentz et al. 2001] Bentz, D.P.; Geiker, M.R. & Hansen, K.K.: Shrinkage-reducing admixtures and early-age desiccation in cement pastes and mortars. In: *Cement and Concrete Research* 31 (2001), No. 7, pp. 1075-1085.
- [Bentz et al. 2007] Bentz, D.; Koenders, E.; Mönning, S.; Reinhardt, H.-W.; van Breugel, K. & Ye, G.: Materials science-based models in support of internal curing water. In: Kovler, K. & Jensen, O.M. (Eds.): *RILEM, State-of-the-Art-Report of*

- RILEM Technical Committee 196-ICC: Internal Curing of Concrete*. Bagnaux: RILEM Publications, 2007, pp. 29-43.
- [Bentz & Garboczi 1991a] Bentz, D.P. & Garboczi, E.J.: Simulation study of the effects of mineral admixtures on the cement paste-aggregate interfacial zone. In: *ACI Materials Journal* 88 (1991), No. 5, pp. 518-529.
- [Bentz & Garboczi 1991b] Bentz, D.P. & Garboczi, E.J.: Percolation of phases in a three-dimensional cement paste microstructural model. In: *Cement and Concrete Research* 21 (1991), No. 2-3, pp. 325-344.
- [Bentz & Snyder 1999] Bentz, D.P. & Snyder, K.A.: Protected paste volume in concrete - extension to internal curing using saturated lightweight fine aggregates. In: *Cement and Concrete Research* 29 (1999), No. 11, pp. 1863-1867.
- [Bentz & Weiss 2011] Bentz, D.P. & Weiss, W.J.: *Internal curing: A 2010 state-of-the-art review*. Gaithersburg, US Department of Commerce, NISTIR 7765, 2011.
- [Biot 1956a] Biot, M.A.: Theory of propagation of elastic waves in fluid-saturated porous solid. I. Low-frequency range. In: *The Journal of the Acoustical Society of America* 28 (1956), No. 2, pp. 168-178.
- [Biot 1956b] Biot, M.A.: Theory of propagation of elastic waves in fluid-saturated porous solid. II. Higher frequency range. In: *The Journal of the Acoustical Society of America* 28 (1956), No. 2, pp. 179-191.
- [Blaschke 1993] Blaschke, F.: *Zugtragverhalten von Beton*. Kassel, Gesamthochschule Kassel, Dissertation, 1993 (German).
- [Blinc et al. 1978] Blinc, R.; Burgar, M.; Lahajnar, M.; Rozmarin, M.; Rutar, V.; Kocuvan, I. & Uric, J.: NMR relaxation study of absorbed water in cement and C3S pastes. In: *Journal of American Ceramic Society* 61 (1978), No. 1-2, pp. 35-37.
- [Braam et al. 2006] Braam, C.R.; van der Ham, H.W.M. & Koenders, E.A.B.: Early-age shrinkage control and strength development of concrete. In: Jensen, O.M.; Lura, P. & Kovler, K. (Eds.): *International RILEM Conference on Volume Changes of Hardening Concrete: Testing and Mitigation*. Bagnaux: RILEM Publications, 2006 (Rilem Proceedings ; 52), pp. 185-194.
- [Bramshuber & Schießl 2000] Bramshuber W. & Schießl, P.: *Einfluss von Flugasche auf den Frost-Tausalz-Widerstand von Beton*. Aachen: RWTH Aachen, Institut für Bauforschung, Forschungsbericht F 759, 2000 (German).
- [van Breugel 1991] Breugel, K. van: *Simulation of hydration and formation of structure in hardening cement-based materials*. Delft, Technical University Delft, Ph.D. thesis, 1991.
- [Brooks & Neville 1977] Brooks, J.J. & Neville, A.M.: A comparison of creep, elasticity and strength of concrete in tension and in compression. In: *Magazine of Concrete Research* 29 (1977), No. 100, pp. 131-141.
- [Brouwers 2004] Brouwers, H.J.H.: The work of Powers and Brownnyard revisited: Part 1. In: *Cement and Concrete Research* 34 (2004), No. 9, pp. 1697-1716.
- [Bogue 1955] Bogue, R.H.: *The chemistry of Portland cement*. 2. ed. New York: Reinhold Publishing Corporation, 1955.
- [BRE 1996] Building Research Establishment: *Sulphate and acid resistance of concrete in ground*. United Kingdom, 1996 (BRE Digest ; 363).

- [Brodersen 1982] Brodersen, H.A.: *Zur Abhängigkeit der Transportvorgänge verschiedener Zonen im Beton von Struktur und Zusammensetzung des Zementsteins*. Aachen, RWTH Aachen, Dissertation, 1982 (German).
- [Bruedern & Mechtcherine 2010] Brüdern, A.-E. & Mechtcherine, V.: Multifunctional use of SAP in strain-hardening cement-based composites. In: Jensen, O.M.; Hascholt, M.T. & Laustsen, S. (Eds.): *Use of superabsorbent polymers and other new additives in concrete*. Bagnoux: RILEM Publications, 2010 (Rilem Proceedings ; 74), pp. 11-22.
- [Buchholtz & Graham 1998] Buchholtz, F.L. & Graham, A.T. (Eds.): *Modern Superabsorbent Polymer Technology*. New York: Wiley-VCH, 1998.
- [CEB 2003] *CEB-FIB Model Code 1990/* Comité Euro-International du Béton (CEB). London: Thomas Telford, 1993.
- [Chang-wen et al. 2007] Chang-wen, M.; Qian, T.; Wei, S. & Jia-ping, L.: Water consumption of early-age paste and the determination of „time-zero“ of self-desiccation shrinkage. In: *Cement and Concrete Research* 37 (2007), No. 11 pp. 1496-1501.
- [Chmelir & Pauen 1988] Chmelir, M. & Pauen, J.: *Verfahren und Vorrichtung zum kontinuierlichen Herstellen von Polymerisaten und Copolymerisaten der Acrylsäure und/oder Methacrylsäure*. Krefeld: Stockhausen GmbH, DE 3544770 C2, 1988 (German).
- [Claridge 1999] Claridge, T.D.W.: *High-resolution NMR techniques in organic chemistry*. Oxford: Elsevier Science, 1999.
- [Cnudde & Jacobs 2003] Cnudde, V. & Jacobs, P.: Preliminary results of X-ray micro-tomography applied in conservation and restoration of natural building stones. In: Otani, J. & Obara, Y. (Eds.): *Proceedings of the International Workshop on X-ray CT for Geomaterials*. Kumamoto: Balkema Publ., 2003, pp. 367-371.
- [Cusson & Hoogeveen 2005] Cusson, D. & Hoogeveen, T.: Internally-cured high-performance concrete under restraint shrinkage and creep. In: Pijaudier-Gabot, G.; Gerard, B. & Acker, P. (Eds.): *Concreep7 Workshop on Creep, Shrinkage and Durability of Concrete and Concrete Structures, Nantes, France, 12-14 September 2005*. Nantes: Ecole Centrale de Nantes, 2005, pp. 579-584.
- [Cohen et al. 1990] Cohen, M.D.; Olek, J. & Dolch, W.L.: Mechanism of plastic shrinkage cracking in Portland cement and Portland cement-silica fume paste and mortar. In: *Cement and Concrete Research* 20 (1990), No. 1, pp. 103-109.
- [Cook & Hover 1993] Cook, R.A. & Hover, K.C.: Mercury porosimetry of cement-based materials and associated correction factors. In: *Construction and Building Materials* 7 (1993), No. 4, pp. 231-240.
- [Cook & Hover 1999] Cook, R.A. & Hover, K.C.: Mercury porosimetry of hardened cement pastes. In: *Cement and Concrete Research* 29 (1999), No. 6, pp. 933-943.
- [Copeland & Hayes 1953] Copeland, L.E. & Hayes, J.C.: Determination of non-evaporable water in hardened Portland cement paste. In: *ASTM Bulletin* 194 (1953), pp. 70-74.

- [Cornelissen & Reinhardt 1986] Cornelissen, H.A. & Reinhardt, H.-W.: Effect of static and fatigue preloading and residual strength and stiffness of plain concrete. In: Elst, H.C. & van Bakker, A. (Eds.): *Fracture control of engineering structures*. Warley: EMAS Publishing, 1986, pp. 2087-2103.
- [Cui & Cahyadi 2001] Cui, L. & Cahyadi, J.H.: Permeability and pore structure of OPC paste. In: *Cement and Concrete Research* 31 (2001), No. 2, pp. 277-282.
- [Cusson et al. 2012] Cusson, D.; Mechtcherine, V. & Lura, P.: Application of superabsorbent polymers in concrete and other building materials. In: Mechtcherine, V. & Reinhardt, H.-W. (Eds.): *RILEM, State-of-the-Art-Report of RILEM Technical Committee 225-SAP: Application of Superabsorbent Polymers (SAP) in Concrete Construction*. Dordrecht: Springer, 2012, pp. 147-158.
- [DAfStB 2005] Deutscher Ausschuss für Stahlbeton (Ed.): *Sachstandsbericht Übertragbarkeit von Frost-Laborprüfungen auf Praxisverhältnisse*. Berlin: Beuth Verlag, 2005 (Schriftenreihe des DAfStB ; 560) (German).
- [D'Angelo et al. 1995] D'Angelo, R.; Plona, T.J.; Schwartz, P. & Coveney, P.: Ultrasonic measurements on hydrating cement slurries: onset of shear wave propagation. In: *Advanced Cement Based Materials* 2 (1995), No. 1, pp. 8-14.
- [Davis 1940] Davis, H.E.: Autogenous volume changes of concrete. In: *Proceedings - American Society for Testing Materials* 40 (1940), pp. 1103-1112.
- [Dela 2000] Dela, B.F.: *Eigenstresses in hardening concrete*. Lyngby, Technical University of Denmark, Ph.D. thesis, 2000.
- [De Larrard & Acker 1992] De Larrard, F. & Acker, P.: Creep in high and very high performance concrete. In: Malier, Y. (Ed.): *High Performance Concrete - From Material to Structure*. Paris: E & FN Spon, 1992, pp. 115-126.
- [De Larrard & Belloc 1997] De Larrard, F. & Belloc, A.: The influence of aggregate on compressive strength of normal and high strength concrete. In: *ACI Materials Journal* 94 (1997), No. 5, pp. 417-426.
- [Dettling 1962] Dettling, H.: *Die Wärmedehnung des Zementsteins, der Gesteine und der Betone*. Stuttgart: Otto-Graf-Institut, 1962 (Schriftenreihe des Otto-Graf-Instituts ; No. 3) (German).
- [Diamond 2000] Diamond, S.: Mercury porosimetry - an inappropriate method for the measurement of pore size distributions in cement-based materials. In: *Cement and Concrete Research* 30 (2000), No. 10, pp. 1517-1525.
- [DIN 1045-1 2008] *Tragwerke aus Beton, Stahlbeton und Spannbeton - Teil 1: Bemessung und Konstruktion*. Berlin: Deutsches Institut für Normung, 2008 (German).
- [DIN 1045-2 2008] *Tragwerke aus Beton, Stahlbeton und Spannbeton - Teil 2: Festlegung, Eigenschaften, Herstellung und Konformität - Anwendungsregeln zu DIN EN 206-1*. Berlin: Deutsches Institut für Normung, 2008 (German).
- [DIN 1048-5 1991] *Prüfverfahren für Beton - Teil 5: Festbeton, gesondert hergestellt Probekörper*. Berlin: Deutsches Institut für Normung, 1991 (German).
- [DIN 52108 2010] *Prüfung anorganischer nichtmetallischer Werkstoffe - Verschleißprüfung mit der Schleifscheibe nach Böhme - Schleifscheiben-Verfahren*. Berlin: Deutsches Institut für Normung, 2010 (German).

- [DIN EN 12350-7 2009] *Prüfung von Frischbeton – Luftgehalte; Druckverfahren*. Berlin: Deutsches Institut für Normung, 2009 (German).
- [DIN EN 12390-8 2009] *Prüfung von Festbeton - Teil 8: Wassereindringtiefe unter Druck*. Berlin: Deutsches Institut für Normung, 2009 (German).
- [DIN EN 12390-9 2009] *Prüfung von Festbeton - Teil 9: Frost- und Frost-Tausalz-Widerstand - Abwitterung*. Berlin: Deutsches Institut für Normung, 2009 (German).
- [DIN EN 12407 2007] *Prüfverfahren für Naturstein – Petrographische Prüfung*. Berlin: Deutsches Institut für Normung, 2007 (German).
- [DIN EN 13263-1 2009] *Silikastaub für Beton - Teil 1: Definitionen, Anforderungen und Konformitätskriterien*. Berlin: Deutsches Institut für Normung, 2009 (German).
- [DIN EN 196-1 2005] *Prüfverfahren für Zement - Teil 1: Bestimmung der Festigkeit*. Berlin: Deutsches Institut für Normung, 2005 (German).
- [DIN EN 1991-1-2 2010] *Eurocode 1: Einwirkung auf Tragwerke - Teil 2: Allgemeine Einwirkungen; Brandeinwirkungen auf Tragwerke*. Berlin: Deutsches Institut für Normung, 2010 (German).
- [DIN EN 206-1 2001] *Beton - Teil 1: Festlegung, Eigenschaften und Konformität*. Berlin: Deutsches Institut für Normung, 2001 (German).
- [DIN EN 459-2 2010] *Baukalk - Teil 2: Prüfverfahren*. Berlin: Deutsches Institut für Normung, 2010 (German).
- [DIN EN 480-11 2005] *Zusatzmittel für Beton, Mörtel und Einpressmörtel – Prüfverfahren Teil 11: Bestimmung von Luftporenkennwerten in Festbeton*. Berlin: Deutsches Institut für Normung, 2005 (German).
- [DS CEN/TS 12390-9 2006] *Testing hardened concrete - Part 9: Freeze-thaw resistance - Scaling*. Copenhagen: Danish Standards, 2006.
- [Dudziak & Mechtcherine 2008] Dudziak, L. & Mechtcherine, V.: Mitigation of volume changes of ultra-high-performance concrete (UHPC) by using superabsorbent polymers. In: Fehling, E.; Schmidt, M. & Stürwald, S. (Eds.): *Ultra High Performance Concrete (UHPC)*. Kassel: Kassel University Press GmbH, 2008, pp. 425-432.
- [Dudziak & Mechtcherine 2009] Dudziak, L. & Mechtcherine, V.: Reducing the cracking potential of ultra-high-performance concrete by using super absorbent polymers. In: van Zijl, G.P.A.G. & Boshoff, W.P. (Eds.): *Advances in Cement-Based Materials*. London: Taylor & Francis, 2009, pp. 11-18.
- [Dudziak & Mechtcherine 2010] Dudziak, L. & Mechtcherine, V.: Enhancing early-age resistance of cracking in high-strength cement-based materials by means of internal curing using superabsorbent polymers. In: Brameshuber, W. (Ed.): *International RILEM Conference on Material Science*. Bagneux: RILEM Publications, 2010 (Rilem Proceedings ; 77), pp. 129-139.
- [EDANA 2002a] EDANA - European Disposals and Nonwovens Association: *Recommended test method: Determination of content of respirable particles*, ERT 420.2-02, 2002.
- [EDANA 2002b] EDANA – European Disposals and Nonwovens Association: *Recommended test method: free swell capacity*, ERT 440.2-02, 2002.

- [Esteves 2009] Esteves, L.P.: *Internal curing in cement-based materials*. Aveiro, Universidade de Aveiro, Ph.D. thesis, 2009.
- [Esteves 2010a] Esteves, L.P.: On the absorption kinetics of superabsorbent polymers. In: Jensen, O.M.; Hasholt, M.T.; Laustsen, S. (Eds.): *Use of superabsorbent polymers and other new additives in concrete*. Bagnoux: RILEM Publications, 2010 (Rilem Proceeding ; 74), pp. 77-84.
- [Fagerlund 1973] Fagerlund, G.: *Significance of critical degrees of saturation at freezing of porous and brittle materials*. Lund: Lund Institute of Technology, Division of Building Materials, Technical Report 40, 1973.
- [Feldman 1984] Feldman, R.F.: Pore structure damage in blended cements caused by mercury intrusion. In: *Journal of the American Ceramic Society* 67 (1984), No. 1, pp. 30-33.
- [Feldman & Cheng-Yi 1985] Feldman, R.F. & Cheng-Yi, H.: Properties of Portland cement-silica fume pastes. I. Porosity and surface properties. In: *Cement and Concrete Research* 15 (1985), No. 5, pp. 765-774.
- [Feldman & Sereda 1968] Feldman, R.F. & Sereda, P.J.: A model for hydrated Portland cement paste as deduced from sorption length change and mechanical properties. In: *Materials and Structures* 1 (1968), No. 6, pp. 509-520.
- [Feldrappe & Müller 2004] Feldrappe V. & Müller, C.: Auswirkungen einer Frostbeanspruchung auf dichte hochfeste Betone. In: *Beton* 54 (2004) No. 10/11, pp. 513-515/575-579 (German).
- [Ferrari & Brocchi 2012] Ferrari, G. & Brocchi, A.: Zero impact recycling of returned concrete. In: *XVI ERMCO Congress, Verona, Italy, 21-22 June 2012*. Verona: ERMCO, 2012, pp. 4/35-4/43.
- [Ferraris & Wittmann 1987] Ferraris, C.F. & Wittmann, F.H.: Shrinkage mechanisms of hardened cement paste. In: *Cement and Concrete Research* 17 (1987), No. 3, pp. 453-464.
- [Fischer 2008] Fischer, C.: *Dokumentation Rapide Chloride Migration Test*. Stuttgart: University of Stuttgart, Department of Construction Materials, Documentation, 2008 (German).
- [Fontana 2007] Fontana, P.: *Einfluss der Mischungszusammensetzung auf die frühen autogenen Verformungen der Bindemittelmatrix von Hochleistungsbetonen*. Berlin: Beuth Verlag, 2007 (Schriftenreihe des DAfStB ; 570) (German).
- [Friedemann et al. 2006] Friedemann, K.; Stallmach, F. & Kärger, J.: NMR diffusion and relaxation studies during cement hydration - A non-destructive approach for clarification of the mechanism of internal post curing of cementitious materials. In: *Cement and Concrete Research* 36 (2006), No. 5, pp. 817-826.
- [Friedemann et al. 2008] Friedemann, K.; Schönefelder, W.; Stallmach, F. & Kärger, J.: NMR relaxometry during internal curing of Portland cements by lightweight aggregates. In: *Materials and Structures* 41 (2008), No. 10, pp. 1647-1655.
- [Friedemann et al. 2009] Friedemann, K.; Stallmach, F. & Kärger, J.: Carboxylates and sulfates of polysaccharides for controlled internal water release during

- cement hydration. In: *Cement and Concrete Composites* 31 (2009), No. 4, pp. 244-249.
- [Friedrich 2012] Friedrich, S.: Superabsorbent polymers (SAPs). In: Mechtcherine, V. & Reinhardt, H.-W. (Eds.): *RILEM, State-of-the-Art-Report of RILEM Technical Committee 225-SAP: Application of Superabsorbent Polymers (SAP) in Concrete Construction*. Dordrecht: Springer, 2012, pp. 15-21.
- [Fujii et al. 1970] Fujii, K.; Kondo, W. & Watanabe, T.: Über die Hydratation von Portlandzement sofort nach dem Anmachen. In: *Zement - Kalk - Gips* 29 (1970), No. 2, pp. 72-79 (German).
- [Fuller & Thompson 1907] Fuller, W.B. & Thompson E.: The laws of proportioning concrete. In: *Transactions of the American Society of Civil Engineers* 57 (1907), No. 2, pp. 67-143.
- [Gawin et al. 2006] Gawin, D.; Pesavento, F. & Schrefler, B.A.: Hygro-thermo-chemo-mechanical modelling of concrete at early ages and beyond. Part I: Hydration and hygro-thermal phenomena. In: *International Journal for Numerical Methods in Engineering* 67 (2006), No. 3, pp. 299-331.
- [Gehlen 2000] Gehlen, C.: *Probabilistische Lebensdauerbemessung von Stahlbetonbauwerken – Zuverlässigkeitsbetrachtungen zur wirksamen Vermeidung von Bewehrungskorrosion*. Berlin: Beuth Verlag, 2000 (Schriftenreihe des DafStB ; 510) (German).
- [Geiker 1983] Geiker, M.: *Studies of Portland cement hydration: Measurements of chemical shrinkage and a systematic evaluation of hydration curves by means of the dispersion model*. Lyngby, Technical University of Denmark, Ph.D. thesis, 1983.
- [Geiker et al. 2004] Geiker, M.; Bentz, D. & Jensen, O.M.: Mitigating autogenous shrinkage by internal curing. In: Ries, J.P. & Holm, T.A. (Eds.): *High Performance Structural Lightweight Concrete*. Farmington Hills: American Concrete Institute, 2004 (ACI Special Publication ; 218), pp. 143-148.
- [Ghosh 1965] Ghosh, R.K.: Querdehnung von Beton. Versuche zur Bestimmung der Poisson'schen Zahl. In: *Beton* 15 (1965), No. 10, pp. 422-426 (German).
- [Graef & Grube 1986a] Graef, H. & Grube, H.: Verfahren zur Prüfung der Durchlässigkeit von Mörtel und Beton gegenüber Gasen und Wasser. In: *Beton* 36 (1986), No. 5, pp. 184-187, and *Beton* 36 (1986), No. 6, pp. 222-226 (German).
- [Graef & Grube 1986b] Graef, H. & Grube, H.: Einfluss der Zusammensetzung und der Nachbehandlung des Betons auf seine Gasdurchlässigkeit. In: *Beton* 36 (1986), No. 11, pp. 426-429 and *Beton* 36 (1986), No. 12, pp. 473-476 (German).
- [Große 2005] Große, C.U.: Qualitätssicherung von Betonwaren - Frischbetonanalyse mit Ultraschall. In: *Betonwerk+Fertigteil-Technik* 71 (2005), No. 6, pp. 26-32 (German).
- [Grube 1991] Grube, H.: *Ursachen des Schwindens von Beton und Auswirkungen auf Betonbauteile*. Düsseldorf: Beton-Verlag, 1995 (Schriftenreihe der Zementindustrie ; 52) (German).

- [Härdtl 1995] Härdtl, R.: *Veränderungen des Betongefüges durch die Wirkung von Steinkohlenflugasche und ihr Einfluß auf die Betoneigenschaften*. Berlin: Beuth Verlag, Schriftenreihe des DAFStB, No. 448, 1995 (German).
- [Hahn 1950] Hahn, E.: Spin echos. In: *Physical Review* 80 (1950), No. 4, pp. 580-594.
- [Haist et al. 2009] Haist, M.; Djuric, Z. & Müller, S.: Betontechnologische Grundlagen zur Herstellung frostbeständiger Betone. In: Müller, S.; Nolting, U. & Haist, M. (Eds.): *Dauerhafter Beton - Grundlagen, Planung und Ausführung bei Frost- und Frost-Taumittel-Beanspruchung, 6. Symposium Baustoffe und Bauwerkserhaltung Universität Karlsruhe*. Karlsruhe: Universitätsverlag Karlsruhe, 2009, p. 20 (German).
- [Hammer 1992] Hammer, T.A.: High strength LWA concrete with silica fume-effect of water content in the LWA on mechanical properties. In: *Supplementary papers in the 4th CANMET/ACI International Conference on Fly Ash, Silica Fume, Slag and Natural Pozzolans in Concrete, Turkey*. Istanbul: CANMET, 1992, pp. 314-330.
- [Han et al. 2000] Han, J.; Zhang, X. & Li, Y.: Study on shrinkage of concrete with slag composite admixture. In: Baroghel-Bouny, V. & Aïtcin, P.-C. (Eds.): *International RILEM Workshop on Shrinkage of Concrete "Shrinkage 2000"*. Bagnaux: RILEM Publications, 2000 (Rilem Proceedings ; 17), pp. 155-160.
- [Hansen 1986] Hansen, T.C.: Physical structure of hardened cement paste. A classical approach. In: *Materials and Structures* 19 (1986), No. 6, pp. 423-436.
- [Halperin et al. 1994] Halperin, W.P.; Jehng, J.-Y. & Song, Y.-Q.: Application of spin-spin relaxation to measurement of surface area and pore size distributions in hydrating cement paste. In: *Magnetic Resonance Imaging* 12 (1994), No. 2, pp. 169-173.
- [Harrison 1991] Harrison, T.: Introducing controlled permeability formwork. Increase concrete durability in the cover zone. In: *Publication # C910198 Aberdeen's Concrete Construction* 36 (1991), No. 2, pp. 198-200.
- [Hasholt et al. 2010a] Hasholt, M.T.; Jespersen, M.H.S. & Jensen, O.M.: Mechanical properties of concrete with SAP part I: Development of compressive strength. In: Jensen, O.M.; Hasholt, M.T.; Laustsen, S. (Eds.): *Use of superabsorbent polymers and other new additives in concrete*. Bagnaux: RILEM Publications, 2010 (Rilem Proceedings ; 74), pp. 117-126.
- [Hasholt et al. 2010b] Hasholt, M.T.; Jespersen, M.H.S. & Jensen, O.M.: Mechanical properties of concrete with SAP part II: Modulus of elasticity. In: Jensen, O.M.; Hasholt, M.T.; Laustsen, S. (Eds.): *Use of superabsorbent polymers and other new additives in concrete*. Bagnaux: RILEM Publications, 2010 (Rilem Proceedings ; 74), pp. 127-136.
- [Herb 2003] Herb, A.T.: *Indirekte Beobachtung des Erstarrens und Erhärtens von Zementleim, Mörtel und Beton mittels Schallwellenausbreitung*. Stuttgart, University of Stuttgart, Department of Construction Materials, Dissertation, 2003 (German).
- [Hertz 2003] Hertz, K.D.: Limits of spalling of fire-exposed concrete. In: *Fire Safety Journal* 38 (2003), No. 2, pp. 103-116.

- [Hobbs 1971] Hobbs, D.W.: The dependence of the bulk modulus, Young's modulus, creep, shrinkage and thermal expansion of concrete upon aggregate volume concentration. In: *Materials and Structures* 4 (1971), No. 2, pp. 107-114.
- [Houst 1993] Houst, Y.F.: Influence of shrinkage on carbonation shrinkage kinetics of hydrated cement paste. In: Bažant, Z.P. & Carol, I. (Eds.): *Creep and Shrinkage of Concrete, Proceedings of the 5th International RILEM Symposium, Barcelona*. London: E & FN Spon, 1993, pp. 121-126.
- [Hua et al. 1995] Hua, C.; Acker, P. & Ehrlacher, A.: Analysis and models of the autogenous shrinkage of hardening cement paste I. Modelling at macroscopic scale. In: *Cement and Concrete Research* 25 (1995), No. 7, pp. 1457-1468.
- [Igarashi & Watanabe 2006] Igarashi, S. & Watanabe, A.: Experimental study on prevention of autogenous deformation by internal curing using super-absorbent polymer particles. In: Jensen, O.M.; Lura, P. & Kovler, K. (Eds.): *International RILEM Conference on Volume Changes of Hardening Concrete: Testing and Mitigation*,. Bagneux: RILEM Publications, 2006 (Rilem Proceedings ; 52), pp. 77-86.
- [Igarashi et al. 2010] Igarashi, S.; Aragane, N. & Koike, Y.: Effects of spatial structure of superabsorbent polymer particles on autogenous shrinkage behaviour of cement paste. In: Jensen, O.M.; Hasholt, M.T.; Laustsen, S. (Eds.): *Use of superabsorbent polymers and other new additives in concrete*. Bagneux: RILEM Publications, 2010 (Rilem Proceedings ; 74), pp. 137-147.
- [Irie et al. 1996] Irie, Y.; Hatsuda, T.; Yonemura, K. & Kimura, K.: *Method of production of particulate hydrogel polymer and absorbent resin*. Osaka: Nippon Shokubai Co. Ltd., EP 508810 B1, 1996.
- [Jacobs 1994] Jacobs, F.P.: *Permeabilität und Porengefüge zementgebundener Werkstoffe*. Zürich, ETH Zürich, Dissertation, 1994 (German).
- [Jennings et al. 1981] Jennings, H.M.; Dalglish, B.J. & Pratt, P.L.: Morphological development of hydrating tricalcium silicate as examined by electron microscopy techniques. In: *Journal of the American Ceramic Society* 64 (1981), No. 10, pp. 567-572.
- [Jensen 1993] Jensen, O.M.: *Autogenous deformation and RH-change – self-desiccation and self-desiccation shrinkage*. Lyngby, Technical University of Denmark, Building Materials Laboratory, Ph.D. thesis, 1993.
- [Jensen 1995] Jensen, O.M.: Thermodynamic limitation of self-desiccation. In: *Cement and Concrete Research* 25 (1995), No. 1, pp. 157-164.
- [Jensen 2008] Jensen, O.M.: Use of superabsorbent polymers in construction materials. In: Sun, W.; van Breugel, K.; Miao, C.; Ye, G. & Chen, H. (Eds.): *Microstructure related durability of cementitious composites*. Bagneux: RILEM Publications, 2008 (Rilem Proceedings ; 61), pp. 757-764.
- [Jensen & Hansen 1995] Jensen, O.M. & Hansen, P.F.: Dilatometer for measuring autogenous deformation in hardening Portland cement paste. In: *Materials and Structures* 28 (1995), No. 7, pp. 406-409.

- [Jensen & Hansen 1996] Jensen, O.M. & Hansen, P.F.: Autogenous deformation and change of the relative humidity in silica fume-modified cement paste. In: *ACI Materials Journal* 93 (1996), No. 6, pp. 539-543.
- [Jensen & Hansen 1999] Jensen, O.M. & Hansen, P.F.: Influence of temperature on autogenous deformation and relative humidity change in hardening cement paste. In: *Cement and Concrete Research* 29 (1999), No. 4, pp. 567-575.
- [Jensen & Hansen 2001a] Jensen, O.M. & Hansen, P.F.: Autogenous deformation and RH-change in perspective. In: *Cement and Concrete Research* 31 (2001), No. 12, pp. 1859-1865.
- [Jensen & Hansen 2001b] Jensen, O.M. & Hansen, P.F.: Water-entrained cement-based materials I. Principles and theoretical background. In: *Cement and Concrete Research* 31 (2001), No. 6, pp. 647-654.
- [Jensen & Hansen 2002] Jensen, O.M. & Hansen, P.F.: Water-entrained cement-based materials II. Experimental observations. In: *Cement and Concrete Research* 32 (2002), pp. 973-978.
- [Jensen & Lura 2006] Jensen, O.M. & Lura, P.: Techniques and materials for internal water curing of concrete. In: *Materials and Structures* 39 (2006), No. 9, pp. 817-825.
- [Jensen et al. 2010] Jensen, O.M.; Hasholt, M.T. & Laustsen, S. (Eds.): *International RILEM Conference on use of superabsorbent polymers and other new additives in concrete*. Bagnoux: RILEM Publications, 2010 (Rilem Proceeding ; 74).
- [Johansen et al. 2009] Johansen, N.A.; Millard, M.J.; Mezencevova, A.; Garas, V.Y. & Kurtis, K.E.: New method for determination of absorption capacity of internal curing agents. In: *Cement and Concrete Research* 39 (2009), No. 1, pp. 65-68.
- [Jolin & Beaupré 2003] Jolin, M. & Beaupré, D.: Understanding wet-mix shotcrete: mix design, specifications, and placement. In: *Shotcrete* (2003), Summer, pp. 6-12.
- [Jooss & Reinhardt 2002] Jooss, M. & Reinhardt, H.-W.: Permeability and diffusivity of concrete as function of temperature. In: *Cement and Concrete Research* 32 (2002), No. 9, pp. 1497-1504.
- [Jungwirth et al. 1986] Jungwirth, D.; Breyer, E. & Grübl, P.: *Dauerhafte Betonbauwerke. Substanz-erhaltung und Schadensvermeidung in Forschung und Praxis*. Düsseldorf: Betonverlag, 1986 (German).
- [Kahn et al. 2000] Kahn, M.I.; Lynsdale, C.J. & Waldron, P.: Porosity and strength of PFA/SF/OPC ternary blended pastes. In: *Cement and Concrete Research* 30 (2000), No. 8, pp. 1225-1229.
- [Kellenberg 1993] Kellenberg, S.R.: *Absorbent products containing hydrogels with ability to swell against pressure*. Wisconsin: Kimberley-Clark Corporation, Nenah, USA, EP 339461 B1, 1993.
- [Khoury & Anderberg 2000] Khoury, G.A. & Anderberg, Y.: *Concrete spalling review*. Report submitted to the Swedish National Road Administration.
- [Klemm & Sikora 2012] Klemm, A. & Sikora, K.: The effect of cement type on the performance of mortars modified by superabsorbent polymers. In: Alexander, M.G.; Beushausen, H.-D.; Dehn, F. & Moyo, P. (Eds.): *Concrete Repair*,

- Rehabilitation and Retrofitting III*. London: Taylor Francis Group, 2012, pp. 210-216.
- [Kordina 1999] Kordina, K.: Beton unter Langzeit-Zugbeanspruchung. In: *Bautechnik* 76 (1999), No. 6, pp. 479-488 (German).
- [Kordina et al. 2000] Kordina, K.; Schubert, L. & Troitzsch, U.: *Kriechen von Beton unter Zugbeanspruchung*. Berlin: Beuth Verlag, 2000 (Schriftenreihe des DafStB ; 498) (German).
- [Kovler 1994] Kovler, K.: Testing system for determining the mechanical behaviour of early-age concrete under restrained and free uniaxial shrinkage. In: *Materials and Structures* 27 (1994), No. 6, pp. 324-330.
- [Kovler 1995] Kovler, K.: Interdependence of creep and shrinkage for concrete under tension. In: *Journal of Materials in Civil Engineering* 7 (1995), No. 2, pp. 96-101.
- [Kovler 1996] Kovler, K.: Why sealed concrete swells. In: *ACI Materials Journal* 93 (1996), No. 4, pp. 334-340.
- [Kovler 1999] Kovler, K.: A new look at the problem of drying creep of concrete under tension. In: *Journal of Materials in Civil Engineering* 11 (1999), No. 1, pp. 84-87.
- [Kovler 2001] Kovler, K.: Drying creep of stress-induced shrinkage. In: Ulm, F.-J.; Bažant, Z.P. & Wittmann, F.H. (Eds.): *Creep, Shrinkage and Durability Mechanics of Concrete and other Quasi-Brittle Materials*. Amsterdam: Elsevier, 2001, pp. 67-72.
- [Kovler et al. 1999] Kovler, K.; Igarashi, S. & Bentur, A.: Tensile creep behaviour of high strength concretes at early ages. In *Materials and Structures* 32 (1999), No. 5, pp. 383-387.
- [Krischer & Kast 1974] Krischer, O. & Kast, W.: *Die wissenschaftlichen Grundlagen der Trocknungstechnik*. Essen: Th. Goldschmidt AG, 3rd edition, 1974 (German).
- [Kropp & Hilsdorf 1995] Kropp, S. & Hilsdorf, H.K. (Eds.): *Performance criteria for concrete durability, RILEM, State-of-the-art report of the RILEM Technical Committee 116-PCD: Permeability of Concrete as a Criterion of its Durability*. London: E & FN SPON, 1995.
- [Krüger & Lehmann 2010] Krüger, M. & Lehmann, F.: *SmartPick - User Manual, Rev. 1.50*. Stuttgart: Smartmote, 2010.
- [Krüger et al. 2011] Krüger, M.; Große, C.U.; Lehmann, F. & Reinhardt, H.-W.: Zuverlässige Qualitätssicherung von Frischbeton mit Ultraschall - das FreshCon-System. In: *Messtechnik im Bauwesen Ernst + Sohn Spezial* (2011), pp. 88-92 (German).
- [Kurz et al. 2005] Kurz, J.H.; Große, C.U. & Reinhardt, H.-W.: Strategies for reliable automatic onset time picking of acoustic emissions and of ultrasound signals in concrete. In: *Ultrasonics* 43 (2005), No. 7, pp. 538-546.
- [Lange & Altoubat 2003] Lange, D.A. & Altoubat, S.A.: Early creep. In: Bentur, A. (Ed.): *RILEM, State-of-the-Art-Report of RILEM Technical Committee 181-EAS: Early Age Cracking of Cementitious Materials*. Bagnoux: RILEM Publications, 2003, pp. 57-62.

- [Laustsen et al. 2008] Laustsen, S.; Hasholt, M.T. & Jensen, O.M.: A new technology for air-entrainment of concrete. In: Sun, W.; van Breugel, K.; Miao, C.; Ye, G. & Chen, H. (Eds.): *Microstructure related durability of cementitious composites*. Bagnaux: RILEM Publications, 2008 (Rilem Proceedings ; 61), pp. 1223-1230.
- [Lea 1970] Lea, F.M.: *The chemistry of cement and concrete*. 3. ed. London: Arnold, 1970.
- [Le Chatelier 1900] Le Chatelier, H.: Sur les changements de volume qui accompagnent le durcissement des ciments. In: *Bulletin de la Société pour l'Encouragement de l'Industrie Nationale* 5 (1900), No. 5, pp. 54-57 (French).
- [L'Hermite 1960] L'Hermite, R.: Volume changes of concrete. In: *Proceedings of the 4th International Symposium on the Chemistry of Cement, Washington DC*. Washington D.C.: US Department of Commerce, 1960, pp. 659-694.
- [Locher et al. 1976] Locher, F.W.; Richartz, W. & Sprung, S.: Erstarren von Zement, Teil I: Reaktion und Gefügeentwicklung. In: *Zement - Kalk - Gips* 29 (1976), No. 10, pp. 435-442 (German).
- [Lopez et al. 2010] Lopez, M.; Kahn, L.F. & Kurtis, K.E.: High-strength self-curing low-shrinkage concrete for pavement applications. In: *International Journal of Pavement Engineering* 11 (2010), No. 5, pp. 333-342.
- [Lu & Torquato 1992] Lu, S. & Torquato, B.L.: Nearest-surface distribution-functions for poly-dispersed particle-systems. In: *Physical Review A* 45 (1992), No. 8, pp. 5530-5544.
- [Ludwig & Pence 1956] Ludwig, N.C. & Pence, S.A.: Properties of Portland cement pastes cured at elevated temperatures and pressures. In: *Journal of the American Concrete Institute* 27 (1956), No. 6, pp. 673-687.
- [Lura 2003] Lura, P.: *Autogenous deformation and internal curing of concrete*. Delft, Technical University Delft, Ph.D. thesis, 2003.
- [Lura & Jensen 2007] Lura, P. & Jensen, O.M.: Measuring techniques for autogenous strain of cement paste. In: *Materials and Structures* 40 (2007), No. 4, pp. 431-440.
- [Lura et al. 2003] Lura, P.; Jensen, O.M. & van Breugel, K.: Autogenous shrinkage in high-performance cement paste: An evaluation of basic mechanism. In: *Cement and Concrete Research* 33 (2003), No. 2, pp. 223-232.
- [Lura et al. 2006a] Lura, P.; Durand, F. & Jensen, O.M.: Autogenous strain of cement paste with superabsorbent polymers. In: Jensen, O.M.; Lura, P. & Kovler, K. (Eds.): *International RILEM Conference on Volume Changes of Hardening Concrete: Testing and Mitigation*. Bagnaux: RILEM Publications, 2006 (Rilem Proceedings ; 52), pp. 57-65.
- [Lura et al. 2006b] Lura, P.; Durand, F.; Loukili, A.; Kovler, K. & Jensen, O.M.: Strength of cement pastes and mortars with superabsorbent polymers. In: Jensen, O.M.; Lura, P. & Kovler, K. (Eds.): *International RILEM Conference on Volume Changes of Hardening Concrete: Testing and Mitigation*. Bagnaux: RILEM Publications, 2006 (Rilem Proceedings ; 52), pp. 117-125.
- [Lura et al. 2006c] Lura, P.; Bentz, D.P.; Lange, D.A.; Kovler, K.; Bentur, A. & van Breugel, K.: Measurement of water transport from saturated pumice aggregates to

- hardening cement paste. In: *Materials and Structures* 39 (2006), No. 9, pp. 861-868.
- [Lutz et al. 2002] Lutz, P. ; Jenisch, R.; Klopfer, H.; Freymuth, H.; Petzold, K.; Stohrer, M.; Fischer, H. & Richter, E.: *Lehrbuch der Bauphysik - Schall - Wärme - Feuchte - Licht - Brand - Klima*. 5.ed. Wiesbaden: Teubner, 2002 (German).
- [Malier 1992] Malier, Y.: *High performance concrete - from material to structure*. London: E & FN SPON, 1992.
- [McDonald et al. 2005] McDonald, P.J.; Korb, J.P.; Mitchell, J. & Montheilhet, L.: Surface relaxation and chemical exchange in hydrating cement pastes: a two-dimensional NMR relaxation study. In: *Physical Review E* 72 (2005), No. 1.
- [Mechtcherine 2012] Mechtcherine, V. (2012): Superabsorbierende Polymere als neues Beton-zusatzmittel. In: *Betonwerke International* (2012), No. 2, pp. 42-48 (German).
- [Mechtcherine et al. 2006] Mechtcherine, V.; Dudziak, L.; Schulze, J. & Staehr, H.: Internal curing by super absorbent polymers (SAP) – effects on material properties of self-compacting fibre-reinforced high performance concrete. In: Jensen, O.M.; Lura, P. & Kovler, K. (Eds.): *International RILEM Conference on Volume Changes of Hardening Concrete: Testing and Mitigation*. Bagnoux: RILEM Publications, 2006 (Rilem Proceedings ; 52), pp. 87-96.
- [Mechtcherine et al. 2009] Mechtcherine, V.; Dudziak, L. & Hempel, S.: Mitigating early-age shrinkage of ultra-high-performance concrete by using superabsorbent polymers (SAP). In: Sato, R.; Maekawa, K.; Tanabe, T.; Sakata, K.; Nakamura, H. & Mihashi, H. (Eds.): *Creep, Shrinkage and Durability Mechanics of Concrete & Concrete Structures*. London: Taylor & Francis, 2009, pp. 847-853.
- [Mechtcherine et al. 2013] Mechtcherine, V. et al.: Effect of internal curing by using superabsorbent polymers (SAP) on autogenous shrinkage and other properties of a high-performance fine-grained concrete: Results of a RILEM Round-Robin test, TC 225-SAP. In: *Materials and Structures* (2013), accepted.
- [Mohr & Hood 2010] Mohr, B.J. & Hood, K.L.: Influence of bleed water absorption on cement paste deformation. In: *Cement and Concrete Research* 40 (2010), No. 2, pp. 220-225.
- [Mönnig 2005] Mönnig, S.: Water saturated super-absorbent polymers used in high strength concrete. In: *Otto-Graf-Journal* 16 (2005), pp. 193-202.
- [Mönnig 2009] Mönnig, S.: *Superabsorbing additions in concrete - applications, modelling and comparison of different internal water sources*. Stuttgart, University of Stuttgart, Department of Construction Materials, Dissertation, 2009.
- [Monteny et al. 2000] Monteny, J.; Vincke, E.; Beeldens, A.; De Belie, N.; Taerwe, L.; Van Gamert, D. & Verstraate, W.: Chemical, microbiological, and in situ test methods for biogenic sulfuric acid corrosion of concrete. In: *Cement and Concrete Research* 30 (2000), No. 4, pp. 623-634.
- [Müller & Kvitsel 2002] Müller, H.S. & Kvitsel, V.: Kriechen und Schwinden von Beton. In: *Beton- und Stahlbetonbau* 97 (2002), No. 1, pp. 8-19 (German).

- [Müller et al. 1999] Müller, H.S.; Küttner, C.H. & Kvitsel, V.: Creep and shrinkage models of normal and high performance concrete - concept for a unified code-type approach. In: *Revue Francaise du Genie Civil* 3 (1999), No. 7, pp. 113-132.
- [Müller et al. 2012] Müller, H.S.; Reinhardt, H.-W. & Wiens, U.: Beton. In: Bergmeister, K.; Fingerloos, F.; Wörner, J.-D. (Eds.): *Beton-Kalender 2012, Teil 1*. Berlin: Ernst & Sohn, 2012, pp. 303-458 (German).
- [Münch & Holzer 2008] Münch, B. & Holzer, L.: Contradicting geometrical concepts in pore size analysis attained with electron microscopy and mercury intrusion. In: *Journal of the American Ceramic Society* 91 (2008), No. 12, pp. 4059-4067.
- [Nestle et al. 2002] Nestle, N.; Zimmermann, C.; Dakkouri, M. & Kärger, J.: Transient high concentrations of chain anions in hydrating cement - indications from proton spin relaxation measurements. In: *Journal of Physics D: Applied Physics* 35 (2002), No. 2, pp. 166-171.
- [Nestle et al. 2007] Nestle, N.; Galvosas, P. & Kärger, J.: Liquid-phase self-diffusion in hydrating cement pastes - results from NMR studies and perspectives for further research. In: *Cement and Concrete Research* 37 (2007), No. 3, pp. 398-413.
- [Nestle et al. 2009] Nestle, N.; Kühn, A.; Friedemann, K.; Horch, C.; Stallmach, F. & Herth, G.: Water balance & pore structure development in cementitious materials in internal curing with modified superabsorbent polymer studied by NMR. In: *Microporous and Mesoporous Materials* 125 (2009), No. 1-2, pp. 51-57.
- [Neville 1995] Neville, A.M.: *Properties of concrete*. 4. ed. London: Longman Group, 1995.
- [Neville & Jones 1928] Neville, H.A. & Jones, H.C.: The study of hydration changes by a volume-change method. In: *Colloid Symposium Monograph* 6 (1928), pp. 309-318.
- [Nielsen 1991] Nielsen, L.F.: *A research note on sorption, pore size distribution and shrinkage of porous materials*. Lyngby: Technical University of Denmark, Building Materials Laboratory, Technical report, 1991.
- [Østergaard et al. 2001] Østergaard, L.; Lange, D.A.; Altoubat, S.A. & Stang, H.: Tensile basic creep of early-age concrete under constant load. In: *Cement and Concrete Research* 31 (2001), No. 12, pp. 1895-1899.
- [Paillère et al. 1989] Paillère, A.M.; Buil, M & Sarrano, J.J.: Effect of fibre addition on autogenous shrinkage of silica fume concrete. In: *ACI Materials Journal* 87 (1989), No. 2, pp. 139-144.
- [Pereyra 2007] Pereyra, M.N.: *Querdehnung von Selbstverdichtendem Beton*. München, Technische Universität München, Dissertation, 2007 (German).
- [Pickett 1942] Pickett, G.: The effect of change in moisture content on the creep of concrete under a sustained load. In *ACI Journal* 38 (1942), pp. 333-355.
- [Pickett 1956] Pickett, G.: Effect of aggregate on shrinkage of concrete and a hypothesis concerning shrinkage. In: *ACI Journal* 52 (1956), No. 5, pp. 581-590.
- [Piérard et al. 2006] Piérard, J.; Pollet, V. & Cauberg, N.: Mitigating autogenous shrinkage in HPC by internal curing using superabsorbent polymers. In: Jensen, O.M.; Lura, P. & Kovler, K. (Eds.): *International RILEM Conference on Volume Changes of Hardening Concrete: Testing and Mitigation*. Bagneux: RILEM Publications, 2006 (Rilem Proceedings ; 52), pp. 97-106.

-
- [Pirskawetz et al. 2011] Pirskawetz, S.; Weise, F. & Fontana, P.: Zwangsinduzierte Rissbildung bei erhärtendem Hochleistungsbeton. In: Rogge, A. & Meng, B. (Eds.): *Tagungsband 52. DAfStb-Forschungskolloquium, BAM Bundesanstalt für Materialforsch-ung und -prüfung, Berlin*. Berlin: DAfStB, 2011 (German).
- [Powers 1935] Powers, T.C.: Absorption of water by Portland cement paste during the hardening process. In: *Industrial and Engineering Chemistry* 27 (1935), No. 7, pp. 790-794.
- [Powers 1945] Powers, T.C.: A working hypothesis for further studies of frost resistance of concrete. In: *Journal of the American Concrete Institute* 41 (1945), No. 1, pp.245-272.
- [Powers 1947] Powers, T.C.: A discussion of cement hydration in relation to the curing of concrete. In: *Proceedings of the Highway Research Board* 27 (1947), pp. 178-188.
- [Powers 1949] Powers, T.C.: The air-requirement of frost-resistant concrete. In: *Research Laboratories of the Portland Cement Association, Bulletin* 33 (1949), pp.1-28.
- [Powers 1959] Powers, T.C.: Causes and control of volume change. In: *Journal of the Portland Cement Association Research and Development Laboratories* 1 (1959) No. 1, pp. 29-39.
- [Powers 1960] Powers, T.C.: Physical properties of cement paste. In: *Proceedings of the 4th International Symposium on the Chemistry of Cement, Washington DC*. Washington D.C.: US Department of Commerce, 1960, pp. 577-613.
- [Powers 1968] Powers, T.C.: The thermodynamics of volume changes and creep. In: *Materiaux et constructions* 1 (1968), No. 6, pp. 487-507.
- [Powers & Brownyard 1948] Powers, T.C. & Brownyard, T.L.: Studies of the physical properties of hardened Portland cement paste. In: *Research Laboratories of the Portland Cement Association, Bulletin* 22 (1948), pp. 101-132.
- [Rajabipour et al. 2008] Rajabipour, F.; Sant, G. & Weiss, J.: Interactions between shrinkage reducing admixtures (SRA) and cement paste's pore solution. In: *Cement and Concrete Research* 38 (2008), No. 5, pp. 606-615.
- [Randler 2001] Randler, M.: *Herstellung von gedruckten Flüssigkristall-Anzeigen auf Folien-substraten mit vakuumfreiem Zellenbau*. Stuttgart, University of Stuttgart, IGM, Dissertation, 2008 (German).
- [Ravina & Shalon 1968] Ravina, D. & Shalon, R.: Plastic shrinkage cracking. In: *Journal of the American Concrete Institute* 65 (1968), No. 4, pp. 282-292.
- [Radocea 1992] Radocea, A.: *Study on the mechanism of plastic shrinkage of cement-based materials*, Chalmer, Chalmers University of Technology, Ph.D. thesis, 1992.
- [Reinhardt & Assmann 2010a] Reinhardt, H.-W. & Assmann, A.: Application of SAP in lightweight concrete with porous matrix. In: Jensen, O.M.; Hasholt, M.T.; Laustsen, S. (Eds.): *Use of superabsorbent polymers and other new additives in concrete*. Bagnex: RILEM Publications, 2010 (Rilem Proceedings ; 74), pp. 299-304.
- [Reinhardt & Grosse 2004] Reinhardt, H.-W. & Grosse, C.U.: Continuous monitoring of setting and hardening of mortar and concrete. In: *Construction and Building Materials* 18 (2004), No. 3, pp. 145-154.

- [Reinhardt & Mönning 2006] Reinhardt, H.-W. & Mönning, S.: Results of a comparative study of the shrinkage behaviour of concretes with different internal water sources. In: Jensen, O.M.; Lura, P. & Kovler, K. (Eds.): *International RILEM Conference on Volume Changes of Hardening Concrete: Testing and Mitigation*. Bagnaux: RILEM Publications, 2006 (Proceedings ; 52), pp. 67-76.
- [Reinhardt & Rinder 2006] Reinhardt, H.-W. & Rinder, T.: Tensile creep of high-strength concrete. In: *Journal of Advanced Concrete Technology* 4 (2006), No. 2, pp. 277-283.
- [Reinhardt et al. 2000] Reinhardt, H.-W.; Grosse, C.U. & Herb, A.: Ultrasonic monitoring of setting and hardening of cement mortar - a new device. In: *Materials and Structures* 33 (2000), No. 9, pp. 580-583.
- [Reinhardt et al. 2001] Reinhardt, H.-W.; Grosse, C.U.; Herb, A.; Weiler, B. & Schmidt, G.: *Method for examining a solidifying and/or hardening material using ultrasound, receptacle and ultrasound sensor for carrying out the method*. US Patent no. 09/857, 536; Patent Nr. 198 56 259.4, Germany and Europe, 2001.
- [Reinhardt et al. 2008] Reinhardt, H.-W.; Assmann, A. & Mönning, S.: Superabsorbent polymers (SAPs) - an admixture to increase the durability of concrete. In: Sun, W.; van Breugel, K.; Miao, C.; Ye, G. & Chen, H. (Eds.): *Microstructure related durability of cementitious composites*. Bagnaux: RILEM Publications, 2008 (Rilem Proceedings ; 61), pp. 313-322.
- [Richartz 1969] Richartz, W.: Die Bindung von Chlorid bei der Zementerhärtung. In: *Zement - Kalk - Gips* 22 (1969), No. 10, pp. 447-456 (German).
- [Rilem 1996] RILEM recommendation, RILEM TC 117-FDC: CDF-test - Test method for the freeze thaw resistance of concrete with sodium chloride solutions. In: *Materials and Structures* 29 (1996), No. 9, pp. 523-528.
- [Rilem 1999] RILEM recommendation, RILEM TC 116-PDC: Permeability of concrete as a criterion of its durability. In: *Materials and Structures* 32 (1999), No. 3 pp. 174-179.
- [Rilem 2004] RILEM recommendation, RILEM TC 176-IDC: Test methods of frost resistance of concrete: CIF-Test: Capillary suction, internal damage and freeze thaw test - Reference method and alternative methods A and B. In: *Materials and Structures* 37 (2004), No. 10, pp. 743-753.
- [Rilem 2007] RILEM, State-of-the-art report of the Rilem Technical Committee 196-ICC: *Internal curing of concrete*. Kovler, K. & Jensen, O.M. (Eds.), Bagnaux: RILEM Publications, 2007.
- [Rilem 2011] RILEM recommendation, RILEM TC 218-SFC: Sonic methods for quality control of fresh cementitious materials. Testing of fresh concrete by ultrasound transmission. In: *Materials and Structures* 44 (2011), No. 6, pp. 1047-1062.
- [Rilem 2012] RILEM, State-of-the-art report of the Rilem Technical Committee 225-SAP: *Application of superabsorbent polymers (SAP) in concrete construction*. Mechtcherine, V. & Reinhardt, H.-W. (Eds.). Dordrecht: Springer, 2012.
- [Rinder 2002] Rinder, T.: *Hochfester Beton unter Dauerzuglast*. Stuttgart, University of Stuttgart, Department of Construction Materials, Dissertation, 2002 (German).

- [Robeyst 2009] Robeyst, N.: *Monitoring setting and microstructure development in fresh concrete with the ultrasonic through-transmission method*. Ghent, Ghent University, Ph.D. thesis, 2009.
- [Rose 1965] Rose, D.A.: Water movement in unsaturated porous materials. In: *RILEM Bulletin* 29 (1965), pp. 119-123.
- [Rossi et al. 2012] Rossi, P.; Tailhan, J.-L.; Le Maou, F.; Gaillet, L. & Martin, E.: Basic creep behaviour of concretes investigation of the physical mechanisms by using acoustic emission. In: *Cement and Concrete Research* 42 (2012), No. 1, pp. 61-73.
- [Ruettgers et al. 1935] Ruettgers, A.; Vidal, E.N. & Wing, S.P.: An investigation of the permeability of mass concrete with particular reference to boulder dam. In: *Proceedings ACI* 31 (1935), No. 3, pp. 378-389.
- [Ruetz 1968] Ruetz, W.: A hypothesis for the creep of hardened cement paste and the influence of simultaneous shrinkage. In: *Proceedings of the International Conference of the Structure of Concrete, London*. London: Cement and Concrete Association, 1968, pp. 365-387.
- [Sant et al. 2011] Sant, G.; Lothenbach, B.; Juilland, P.; Le Saout, G.; Weiss, J. & Scrivener, K.: The origin of early age expansions induced in cementitious materials containing shrinkage reducing admixtures. In: *Cement and Concrete Research* 41 (2011), No. 3, pp. 218-229.
- [Sayers & Dahlin 1993] Sayers, C. & Dahlin, A.: Propagation of ultrasound through hydrating cement pastes at early age. In: *Advanced Cement Based Materials* 1 (1993), No. 1, pp. 12-21.
- [Sárosi 2007] Sárosi, M.: *Analyse der Materialeigenschaften der Betonmischungen einer großvolumigen Bodenplatte, insbesondere ihrer Rissneigung*. Stuttgart, University of Stuttgart, Department of Constr. Materials, Diploma thesis, 2007 (German).
- [Schaeffel 2009] Schäffel, P.: *Zum Einfluss schwindreduzierender Zusatzmittel und Wirkstoffe auf das autogene Schwinden und weitere Eigenschaften von Zementstein*. Weimar, Bauhaus-Universität Weimar, Dissertation, 2009 (German).
- [Schießl & Raupach 1992] Schießl, P. & Raupach, M.: Monitoring system for the corrosion risk of steel in concrete. In: *Concrete International* 14 (1992), No. 7, pp. 52-55.
- [Schrage 1994] Schrage, I.: *Hochfester Beton. Sachstandsbericht. Teil 1: Betontechnologie und Beton-eigenschaften*, Berlin: Beuth, 1994 (Schriftenreihe d. DAfStB ; 438) (German).
- [Schrage & Springenschmid 1996] Schrage, I. & Springenschmid, R.: Creep and shrinkage data of high strength concrete. In: *Proceedings of the 4th International Symposium on Utilization of High-Strength/High-Performance Concrete*. Paris: Presses de l'Ecole nationale des ponts et chaussees, 1996, pp. 331-338.
- [Schroefl et al. 2012] Schröfl, C.; Mechtcherine, V. & Gorges, M.: Relation between the molecular structure and the efficiency of superabsorbent polymers (SAP) as concrete admixture to mitigate autogenous shrinkage. In: *Cement and Concrete Research* 42 (2012), No. 6, pp. 865-873.
- [Schwarz 2005] Schwarz, V.: *Superabsorber in concrete*. Trostberg: BASF Construction Chemicals GmbH, Presentation, 2005.

- [Setzer 1977] Setzer, M.J.: *Einfluss des Wassergehalts auf die Eigenschaften des erhärteten Betons*. Berlin: Beuth, 1977 (Schriftenreihe des DafStB ; 280) (German).
- [Setzer 2001] Setzer, M.J.: Mechanical stability criterion, triple-phase condition and pressure differences of matter condensed in a porous matrix. In: *Journal of Colloid and Interface Science* 235 (2001), No. 1, pp. 170-182.
- [Setzer 2002] Setzer, M.J.: Development of the micro-ice-lens model. In: Setzer, M.J.; Auberg, R. & Heck, H.J. (Eds.): *2nd International RILEM Workshop on Frost-Resistance of Concrete*. Bagnaux: RILEM Publications, 2002 (Rilem Proceedings ; 24), pp. 133-145.
- [Setzer 2009] Setzer, M.J.: Physikalische Grundlagen der Frostschädigung. In: Müller, S.; Nolting, U. & Haist, M. (Eds.): *Dauerhafter Beton - Grundlagen, Planung und Ausführung bei Frost- und Frost-Taumittel-Bbeanspruchung, 6. Symposium Baustoffe und Bauwerkserhaltung Universität Karlsruhe (TH)*. Karlsruhe: Universitätsverlag Karlsruhe, 2009, pp. 5-11 (German).
- [Slater 1983] Slater, E.: *Corrosion of metals in association with concrete*. Ann Arbor: American Society for Testing and Materials, 1983.
- [Smolczyk 1984] Smolczyk, H.G.: Stand der Kenntnis über Chloriddiffusion in Beton. In: *Beton + Fertigteil-Technik* 50 (1984), No. 12, pp. 837-843 (German).
- [Sommer 1978] Sommer, H.: Ein neues Verfahren zur Erzielung der Frost-Tausalz-Beständigkeit des Betons. In: *Beton + Fertigteil-Technik* 44 (1978), No. 9, pp. 476-484 (German).
- [Spanka et al. 1998] Spanka, G.; Grube, H. & Thielen, G.: Wirkungsmechanismen verflüssigender Zusatzmittel. In: *Betontechnische Berichte 1995-1997*, Band 27. Düsseldorf: Verein Deutscher Zementwerke, 1998, pp. 45-60 (German).
- [Stanton 1941] Stanton, T.E.: Expansion of concrete through reaction between cement and aggregate. In: *Proceedings of the American Society of Civil Engineers* 66 (1941), pp. 1781-1811.
- [Stark & Wicht 2000] Stark, J. & Wicht, B.: *Zement und Kalk: der Baustoff als Werkstoff*. Basel: Birkhäuser Verlag, 2000 (German).
- [Stark & Wicht 2001] Stark, J. & Wicht, B.: *Dauerhaftigkeit von Beton: Der Baustoff als Werkstoff*. Basel: Birkhäuser Verlag, 2001 (German).
- [Stockhausen 1981] Stockhausen, N.: *Die Dilatation hochporöser Festkörper bei Wasseraufnahme und Eisbildung*. Munich, Technical University of Munich, Dissertation, 1981 (German).
- [Tang 1996] Tang, L.: *Chloride transport in concrete - measurement and prediction*. Gothenburg, Chalmers University Gothenburg, Ph.D. thesis, 1996.
- [Tang & Zhu 2007] Tang, L. & Zhu, W.: Chloride penetration. In: De Schutter, G. & Audenaert, K. (Eds.): *RILEM, State-of-the-Art-Report of RILEM Technical Committee 205-DSC: Durability of Self-Compacting Concrete*. Bagnaux: RILEM Publications, 2007, pp. 77-88.
- [Taylor 1997] Taylor, H.F.W.: *Cement chemistry*. 2.ed. London: Thomas Telford, 1997.
- [Toledo Filho et al. 2012] Toledo Filho, R.D.; Silva, E.F.; Lopes, A.N.M.; Mechtcherine, V. & Duziak, L.: Effect of superabsorbent polymers on workability of fresh

- concrete and mortar. In: Mechtcherine, V. & Reinhardt, H.-W. (Eds.): *RILEM, State-of-the-Art-Report of RILEM Technical Committee 225-SAP: Application of Superabsorbent Polymers (SAP) in Concrete Construction*. Springer, Dordrecht, 2012, pp. 39-50.
- [Trtik et al. 2010] Trtik, P.; Muench, B.; Weiss, W.J.; Herth, G.; Kaestner, A.; Lehmann, E. & Lura, P.: Neutron tomography measurements of water release from superabsorbent polymers in cement paste. In: Brameshuber, W. (Ed.): *Additions Improving Properties of Concrete*. Bagnaux: RILEM Publications, 2010 (Rilem Proceedings ; 77), pp. 175-185.
- [Tsuji et al. 1998] Tsuji, M.; Okuyama, A. ; Enoki, K. & Suksawang, S.: Development of new concrete admixture preventing from leakage of water through cracks. In: *JCI Proceedings of Cement and Concrete* 52 (1998), pp. 418-423.
- [Tsuji et al. 1999] Tsuji, M.; Koyano, H. & Isobe, D.: Study on method of test for leakage through cracks of hardened concrete. In: *JCI Proceedings of Cement and Concrete* 53 (1999), pp. 462-468.
- [Tzschichholz et al. 1996] Tzschichholz, F.; Herrmann, H.J. & Zanni, H.: Reaction-diffusion model for the hydration and setting of cement. In: *Physical Review E*. 53 (1996), No. 3, pp. 2629-2637.
- [Valenta 1969] Valenta, D.: Kinetics of water penetration into concrete as an important factor of its deterioration and of reinforcement corrosion. In: *International Symposium on Durability of Concrete, Prag, Preliminary Report, Part I*. Prag: Technical University of Prag, 1969, pp. 177-193.
- [Vogel 2011] Vogel, M.: *Schädigungsmodell für die Hydroabrasionsbeanspruchung zur probabilistischen Lebensdauerprognose von Betonoberflächen im Wasserbau*. Karlsruhe, Karlsruhe Institute of Technology, Dissertation, 2011 (German).
- [Wang et al. 2009] Wang, F.; Zhou, Y.; Peng, B.; Liu, Z. & Hu, S.: Autogenous shrinkage of concrete with super-absorbent polymer. In: *ACI Materials Journal* 106 (2009), No. 2, pp. 123-127.
- [WBCSD 2009] World Business Council for Sustainable Development - WBCSD: *The Cement Sustainability Initiative - recycling concrete*. Report available online, URL: <http://www.wbcscement.org/pdf/CSI-RecyclingConcrete-fullreport.pdf>
- [Weber & Reinhardt 1997] Weber, S. & Reinhardt, H.-W.: A new generation of high performance concrete: concrete with autogenous curing. In: *Advanced Cement Based Materials* 6 (1997), No. 2, pp. 59-68.
- [Weber & Reinhardt 1999] Weber, S. & Reinhardt, H.-W.: Manipulating the water content and microstructure of high performance concrete using autogenous curing. In: Dhir, R. & Dyer, T. (Eds.): *Modern Concrete Materials: Binders, Additions and Admixtures*. London: Thomas Telford, 1999, pp. 567-577.
- [Weiss 2003] Weiss, J.: Experimental determination of the “time zero” t_0 (majority-zero, M_0). In: Bentur, A. (Ed.): *RILEM Report 25 of Technical Committee 181-EAS: Early-age Cracking in Cementitious Systems*. Bagnaux: RILEM Publications, 2003, pp. 195-206.

- [Weigler & Grübl 2001] Weigler, H. & Grübl, K.: *Beton - Arten, Herstellung und Eigenschaften*. Berlin: Ernst & Sohn, 2001 (German).
- [Willis et al. 1998] Willis, K.L.; Abell, A.B. & Lange, D.A.: Image-based characterization of cement pore structure using Wood's metal intrusion. In: *Cement and Concrete Research* 28 (1998), No. 12, pp. 1695-1705.
- [Winslow & Diamond 1970] Winslow, D.N. & Diamond, S.: A mercury porosimetry study of the evolution of porosity in Portland cement. In: *ASTM Journal of Materials* 5 (1970), pp. 564-585.
- [Wittmann 1976] Wittmann, F.H.: On the action of capillary pressure in fresh concrete. In: *Cement and Concrete Research* 6 (1976), No. 1, pp. 49-56.
- [Wittmann 1977] Wittmann, F.H.: *Grundlagen eines Modells zur Beschreibung charakteristischer Eigenschaften des Betons*. Berlin: Ernst & Sohn, 1977 (Schriftenreihe des DAfStB ; 290), pp. 43-101 (German).
- [Wittmann 1982] Wittmann, F.H.: *Creep and shrinkage mechanisms. Creep and shrinkage in concrete structures*. Chichester: Wiley & Sons, 1982, pp. 129-161.
- [Wittmann et al. 2011] Wittmann, F.H.; Zhang, P. & Zhao, T.J.: Application of Neutron Radiography to study moisture movement in cracked and uncracked concrete. In: Leung, C. & Wan, K.T. (Eds.): *Advances in Construction Materials through Science and Engineering. Abstract book*. Bagneux: RILEM Publications, 2011 (Rilem Proceedings ; 79), p. 117.
- [Wyrzykowski et al. 2011] Wyrzykowski, M.; Lura, P.; Pesavento, F. & Gawin, D.: Modeling of internal curing in maturing mortar. In: *Cement and Concrete Research* 41 (2011), No. 12, pp. 1349-1356.
- [Wyrzykowski et al. 2012] Wyrzykowski, M.; Lura, P.; Pesavento, F. & Gawin, D.: Modeling of water migration during internal curing with superabsorbent polymers. In: *Journal of Materials in Civil Engineering* 24 (2012), No. 8, pp. 1006-1016.
- [Žagar 1955] Žagar, L.: Die Grundlagen zur Ermittlung der Gasdurchlässigkeit von feuerfesten Baustoffen. In: *Archiv für das Eisenhüttenwesen* 26 (1955), No. 5, pp. 777-782 (German).
- [Zeiml et al. 2008] Zeiml, M.; Lackner, R.; Leithner, D. & Eberhardsteiner, J.: Identification of residual gas-transport of concrete subjected to high temperatures. In: *Cement and Concrete Research* 38 (2008), No. 5, pp. 699-716.
- [Zhu et al. 2011] Zhu, J.; Kee, S.-H.; Han, D. & Tsai, Y.-T.: Effects of air voids on ultrasonic wave propagation in early age cement pastes. In: *Cement and Concrete Research* 41 (2011), No. 8, pp. 872-881.
- [Zhutovsky et al. 2004] Zhutovsky, S.; Kovler, K. & Bentur, A.: Assessment of water migration distance in internal curing of high-strength concrete. In: Jensen, O.M.; Bentz, D.P. & Lura, P. (Eds.): *Autogenous deformation of concrete*. Farmington Hill: American Concrete Institute, 2004 (ACI Special Publication ; 220), pp. 181-197.

Appendix

Appendix to chapter 2

Powers' volumetric model for plain and silica fume modified Portland cement paste

The equations presented in the following base on [Jensen & Hansen 2001b] and refer to a citation in [Lura 2003]. The phase composition of a hardening Portland cement paste is:

- Chemical shrinkage: $V_{CS} = 0.20 \cdot (1-p) \cdot \alpha$
- Capillary water: $V_{CW} = p - 1.32 \cdot (1-p) \cdot \alpha$
- Gel water: $V_{GW} = 0.60 \cdot (1-p) \cdot \alpha$
- Gel solid: $V_{GS} = 1.52 \cdot (1-p) \cdot \alpha$
- Unhydrated cement: $V_{UC} = (1-p) \cdot (1-\alpha)$

where it is:
$$\sum_i V_i = 1 \quad \text{and} \quad p = \frac{w/c}{(w/c) + (\rho_w / \rho_c)}$$

w and c refer to masses of water and cement, respectively, and it is ρ_c the density of cement, i.e. 3150 kg/m³, and ρ_w the density of water, i.e. 1000 kg/m³.

The constants in Powers' model are derived from the following assumptions:

- The maximum amount of chemically bound water is 0.23 g per 1 g fully hydrated cement
- The maximum amount of physically bound water is 0.19 g per 1 g fully hydrated cement
- The chemical shrinkage amounts to 6.4 ml per 100 g fully hydrated cement.

The phase composition of Portland cement paste blended with silica fume is given in the following. It is assumed that silica fume reacts proportionally to cement.

- Chemical shrinkage: $V_{CS} = k \cdot (0.20 + 0.69 \cdot (s/c)) \cdot (1-p) \cdot \alpha$
- Capillary water: $V_{CW} = p - k \cdot (1.32 + 1.57 \cdot (s/c)) \cdot (1-p) \cdot \alpha$
- Gel water: $V_{GW} = k \cdot (0.60 + 1.57 \cdot (s/c)) \cdot (1-p) \cdot \alpha$
- Gel solid: $V_{GS} = k \cdot (1.52 + 0.74 \cdot (s/c)) \cdot (1-p) \cdot \alpha$
- Unhydrated cement: $V_{UC} = k \cdot (1-p) \cdot (1-\alpha)$
- Silica fume: $V_S = k \cdot (1.43 \cdot (s/c)) \cdot (1-p) \cdot (1-\alpha)$

where it is:
$$\sum_i V_i = 1$$

and
$$p = \frac{w/c}{(w/c) + (\rho_w / \rho_c) + (\rho_w / \rho_s) \cdot (s/c)} \quad \text{and} \quad k = \frac{1}{1 + \frac{\rho_c}{\rho_s} \cdot (s/c)}$$

s refer to masses of silica fume and it is ρ_s the density of silica fume, i.e. 2200 kg/m³.

The constants in the model base on the assumptions presented below:

- The maximum amount of chemically bound water is 0 g per 1 g fully reacted silica fume
- The maximum amount of physically bound water is 0.5 g per 1 g fully reacted silica fume
- The chemical shrinkage amounts to 22 ml per 100 g fully reacted silica fume.

Classification of pores

Figure A 2.1 reports on the classification of pores in concrete as suggested by various authors.

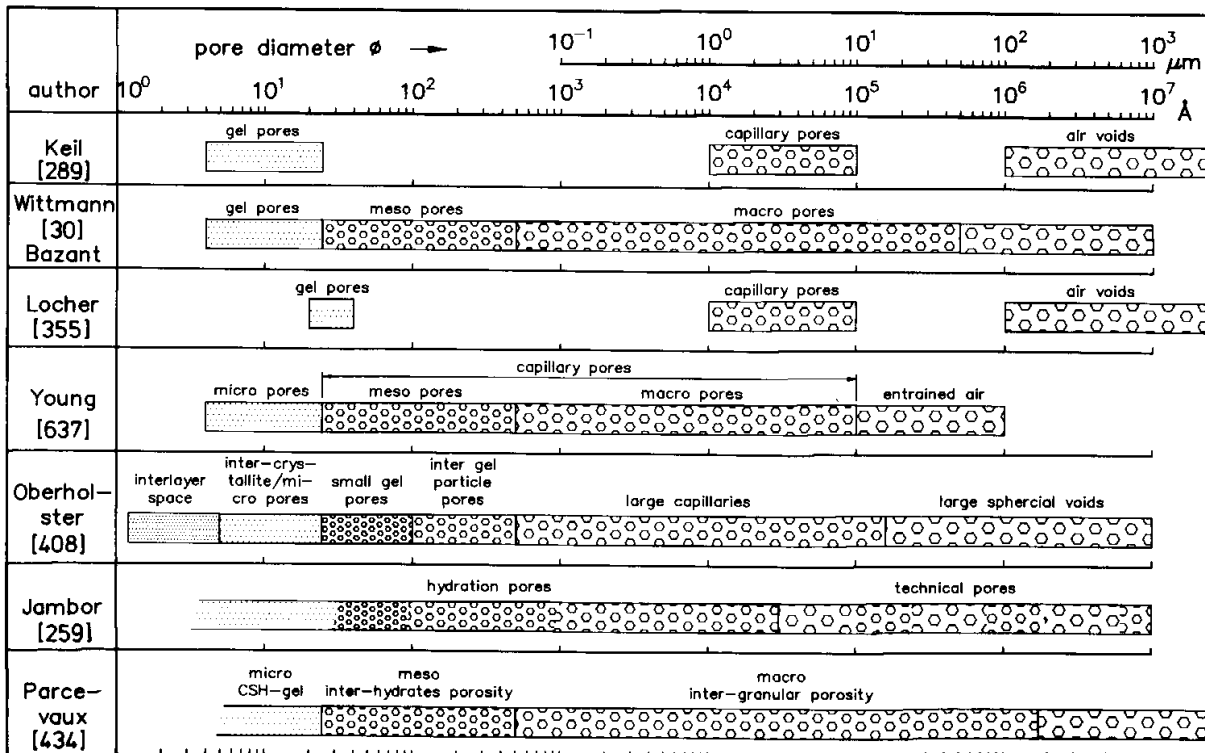


Figure A 2.1: Classification of pores in concrete [van Breugel 1991].

Exposure classes for concrete

Table A.2.1 and Table A2.2 provide non-exhaustive lists of examples for concrete structural elements categorized in exposure classes according to [DIN 1045-2 2008].

Table A.2.1: Exposure classes for corrosion of reinforcement

Class	Description	Informative example
No risk of corrosion or attack		
X0	Concrete without reinforcement not exposed to freeze-thaw, abrasion or chemical attack Concrete with reinforcement or embedded metal in very dry conditions	Unreinforced concrete surfaces inside structures Reinforced concretes inside buildings with very low air humidity
Corrosion induced by carbonation		
XC1	Dry or permanently wet	Concrete inside buildings with low humidity and concrete permanently immersed in water
XC2	Wet, rarely dry	Concrete subjected to long-term water contact
XC3	Moderate humidity	Concrete inside buildings with moderate or high air humidity and concrete exposed to rain
XC4	Cyclic wet and dry	Concrete surfaces subject to water contact, not within class XC2

Corrosion induced by chlorides other than from sea water		
XD1	Moderate humidity	Concrete surfaces exposed to airborne chlorides
XD2	Wet, rarely dry	Swimming pools and concrete exposed to industrial waters containing chlorides
XD3	Cyclic wet and dry	Bridge elements exposed to spray containing chlorides, pavements and car park slabs
Corrosion induced by chlorides from sea water		
XS1	Exposed to airborne salt but not in direct contact with sea water	Structures near to the coast
XS2	Permanently submerged	Elements of marine structures
XS3	Tidal, splash and spray zones	Elements of marine structures

Table A.2.2: Exposure classes for concrete attack

Class	Description	Informative example
Freeze-thaw attack		
XF1	Moderate water saturation, without de-icing agents	Vertical concrete surfaces exposed to rain and freezing
XF2	Moderate water saturation, with de-icing agents	Vertical concrete surfaces of road structures exposed to freezing and airborne de-icing agents
XF3	High water saturation, without de-icing agents	Horizontal concrete surfaces exposed to rain and freezing
XF4	High water saturation, with de-icing agent or sea water	Road and bridge decks exposed to de-icing agents, direct spray containing de-icing agents and freezing; Splash zones of marine structures exposed to freezing
Chemical attack		
XA1	Slightly aggressive chemical environment	Sewage plant tanks and liquide manure tanks
XA2	Moderately aggressive chemical environment	Concrete surface exposed to sea water and structures in aggressive soils
XA3	Highly aggressive chemical environment	Concrete for wastewater systems with aggressive industrial waters, feed platforms and cooling towers of exhaust systems
Mechanical abrasion		
XM1	Moderate wear	Stiffening industrial floors impacted by pneumatic wheels
XM2	Severe wear	Stiffening industrial floors impacted by solid rubber tyres
XM3	Very severe wear	Stiffening industrial floors impacted by steel rollers or track vehicles; bed-loaded hydraulic engineering structures
Moisture classes / alkali silica reaction		
W0	Dry	Concrete surfaces in structures and surfaces not exposed to direct weathering
WF	Wet	Concrete surfaces exposed to high air humidity and direct weathering
WA	Wet and external alkali supply	Concrete structures exposed to sea water; elements exposed to agricultural alkali salts
WS	Wet, external alkali supply and dynamic loading	Concrete roads exposed to de-icing salts

Appendix to chapter 3

Necessary amount of entrained water to prevent complete self-desiccation of plain cement paste

The amount of entrained water V_{EW} needed to prevent complete self-desiccation equals the chemical shrinkage V_{CS} of cement paste at maximum degree of hydration α_{max} in saturated conditions. Further, it is assumed that hydration at low w/c ratio stops when all capillary water is consumed and the space is taken up by gel water V_{GW} , gel solid V_{GS} , and unhydrated cement V_{UC} . According to Powers' model (see appendix 2) it is [Jensen & Hansen 2001b]:

$$V_{GS} + V_{GW} + V_{UC} = 1 \quad \text{for} \quad \alpha = \alpha_{max}$$

$$0.60 \cdot (1-p) \cdot \alpha_{max} + 1.52 \cdot (1-p) \cdot \alpha_{max} + (1-p) \cdot (1-\alpha_{max}) = 1$$

In an open system with low w/c ratio the maximum degree of hydration is:

$$\alpha_{max} = \frac{p}{1.12 \cdot (1-p)}$$

The amount of initially entrained water $V_{EW,0}$ equals the chemical shrinkage V_{CS} at maximum degree of hydration given by the above equation. Further, the initial porosity p equals to the volume of initial capillary water $V_{CW,0}$:

$$V_{EW,0} = 0.20 \cdot (1-p) \cdot \alpha_{max} = 0.18 \cdot p = 0.18 \cdot V_{CW,0}$$

The initial capillary water can be expressed on a w/c ratio basis (kg water / kg cement):

$$(w/c) = \frac{V_{CW,0} \cdot \rho_W}{V_{UC,0} \cdot \rho_C}$$

For the amount of entrained water corresponding to $(w/c)_e$ follows:

$$(w/c)_e = \frac{V_{EW,0} \cdot \rho_W}{V_{UC,0} \cdot \rho_C}$$

As a result, the quantity of entrained water necessary to obtain α_{max} is:

$$(w/c)_e = 0.18 \cdot (w/c) \quad \text{for} \quad (w/c) < 0.36$$

For w/c in the range 0.36 to 0.42, where complete hydration in an open system is possible, the necessary amount of entrained water is less:

$$(w/c)_e = 0.42 - (w/c) \quad \text{for} \quad 0.36 \leq (w/c) \leq 0.42$$

Necessary amount of entrained water to prevent complete self-desiccation of cement paste containing silica fume

According to appendix 2, Powers' model states that α_{max} of cement paste blended with silica fume is:

$$V_{GS} + V_{GW} + V_{UC} + V_S = 1 \quad \text{for} \quad \alpha = \alpha_{max}$$

$$k \cdot (0.60 + 1.57 \cdot (s/c)) \cdot (1-p) \cdot \alpha_{\max} + k \cdot (1.52 + 0.74 \cdot (s/c)) \cdot (1-p) \cdot \alpha_{\max} \\ + k \cdot (1-p) \cdot (1-\alpha_{\max}) + k \cdot (1.43 \cdot (s/c)) \cdot (1-p) \cdot (1-\alpha_{\max}) = 1$$

$$\alpha_{\max} = \frac{1 - k \cdot (1 + 1.43 \cdot (s/c)) \cdot (1-p)}{k \cdot (1.12 + 0.9 \cdot (s/c)) \cdot (1-p)} = \frac{p}{k \cdot (1.12 + 0.88 \cdot (s/c)) \cdot (1-p)}$$

The initial amount of entrained water $V_{EW,0}$ that equals the volume of chemical shrinkage at maximum degree of hydration can be written as [Lura 2003]:

$$V_{EW,0} = k \cdot (0.20 + 0.69 \cdot (s/c)) \cdot (1-p) \cdot \alpha_{\max}$$

$$V_{EW,0} = k \cdot (0.20 + 0.69 \cdot (s/c)) \cdot (1-p) \cdot \frac{p}{k \cdot (1.12 + 0.88 \cdot (s/c)) \cdot (1-p)} = \frac{(0.2 + 0.69 \cdot (s/c)) \cdot p}{(1.12 + 0.88 \cdot (s/c))}$$

Expressed on a w/c ratio basis, one obtains:

$$(w/c)_e = \frac{0.2 + 0.69 \cdot (s/c)}{1.12 + 0.88 \cdot (s/c)} \cdot (w/c)$$

provided that it is:

$$(w/c) \leq (0.36 + 0.28 \cdot (s/c))$$

Above this w/c ratio complete hydration is achievable with less entrained water viz:

$$(w/c)_e = (0.42 + 0.73 \cdot (s/c)) - (w/c)$$

provided that it is:

$$(0.36 + 0.28 \cdot (s/c)) \leq (w/c) \leq (0.42 + 0.73 \cdot (s/c))$$

Figure A.3.1 shows the amount of entrained water needed to prevent complete self-desiccation of a Portland cement paste blended with 1/10 silica fume as a function of the w/c ratio.

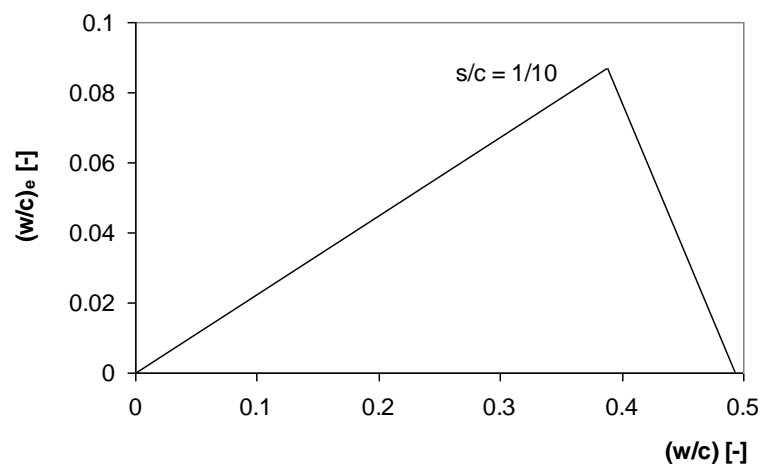


Figure A.3.1: Entrained w/c ratio necessary to prevent complete self-desiccation as a function of w/c ratio for s/c of 1/10.

Composition of lightweight concretes with porous matrix

Table A.3.1 reports on the mix composition of lightweight concrete with porous matrix [Reinhardt & Assmann 2010a]. The SAP used in this series was a type that is commercially available on the market (BASF Luquasorb).

Table A.3.1: Composition of lightweight concretes with porous matrix

Component	Unit	Ref M	MF10	MSAP10	MF20	MSAP20	MF30	MSAP30
CEM I 52.5 R	kg/m ³	340	265	265	190	190	120	120
Water	kg/m ³	150	120	120	90	90	60	60
w/c _{basic}	-	0.44	0.45	0.45	0.47	0.47	0.50	0.50
Sand ≤ 2 mm	kg/m ³	360	240	240	120	120	-	-
Liaver 2-4 mm	kg/m ³	180	180	180	180	180	180	180
PCE	kg/m ³	1.5	1.0	1.0	0.5	0.5	-	-
Protein foam	l/m ³	-	100	-	200	-	300	-
SAP _{dry}	kg/m ³	-	-	8	-	12	-	13
Extra water	l/m ³	-	-	96	-	192	-	286
Matrix porosity	l/m ³	5	105	104	200	204	300	299

Appendix to chapter 4

Results of air-jet sieving

SAP D particles were characterized by air-jet-sieving. Figure A.4.1 provides the test results.

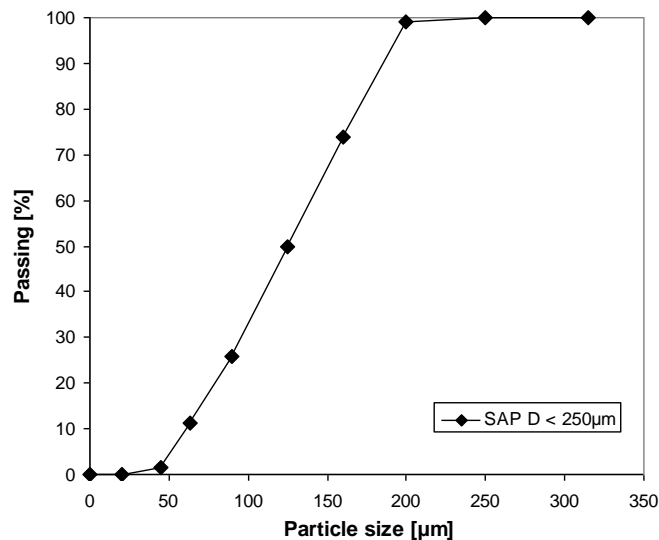


Figure A.4.1: Particle size distribution of SAP D particles obtained from air-jet-sieving.

Results of mortar spread tests

Results of mortar spread tests of SAP A of different size fractions.

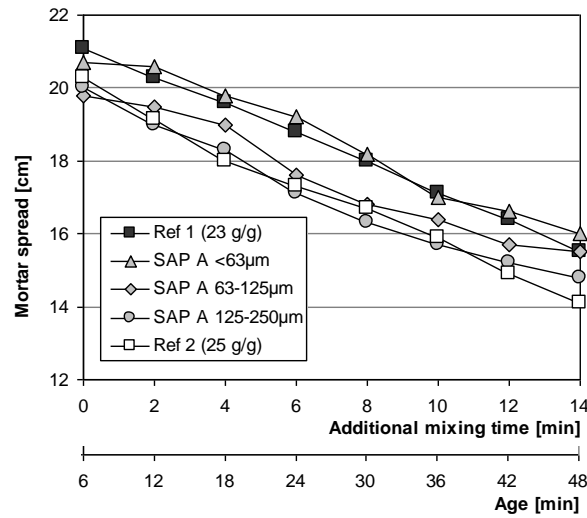


Figure A.4.2: Results of mortar spread tests for SAP A.

Derivation of saturated SAP particle diameter

The saturated polymer radius r_{SAP}^s is derived in the following, using the water absorption capacity χ of a dry SAP particle with radius r_{SAP}^d .

The mass m_s of a saturated particle is:

$$m_s = m_d \cdot (1 + \chi)$$

where m_d is the mass of the dry particle.

One can write as well:

$$\rho_s \cdot V_s = \rho_d \cdot V_d \cdot (1 + \chi)$$

where ρ and V are density and volume of dry (d) and saturated (s) particles, respectively.

Further, the volume of a sphere is given by:

$$V = 4/3 \cdot \pi \cdot r^3$$

As a result one obtains:

$$\rho_s \cdot 4/3 \cdot \pi \cdot (r_{SAP}^s)^3 = \rho_d \cdot 4/3 \cdot \pi \cdot (r_{SAP}^d)^3 \cdot (1 + \chi)$$

Solving for r_{SAP}^s leads to:

$$r_{SAP}^s = r_{SAP}^d \cdot \sqrt[3]{\frac{\rho_{SAP}^d}{\rho_{SAP}^s} \cdot (1 + \chi)}$$

Derivation of actual water absorption capacity obtained from IA

The volume of a cement paste sample V_{CP} consists of the following components:

$$V_{CP} = \frac{w}{\rho_w} + \frac{c}{\rho_c} + V_{SAP} + V_{Air} = 1$$

where it is V_{SAP} the volume of SAP pores (equal to surface fraction of SAP pores) and V_{Air} is the volume of air voids (equal to surface fraction of air voids) and ρ_w and ρ_c are the densities of water and cement, respectively.

Hence, the cement content c and the water content w are given by:

$$c = \frac{1 - V_{Air}}{1/\rho_c + (w/c)/\rho_w + f_{SAP}/\rho_{SAP}^d}$$

$$w = (w/c) \cdot c$$

where f_{SAP} is the amount of added SAP, i.e. here (paste SAP A 0.36+0.06) it is $f_{SAP} = 0.0025 c$. The volume of SAP pores can be written as:

$$V_{SAP} = \frac{(1 + \chi) \cdot m_{SAP}^d}{\rho_{SAP}^s} \quad \text{with} \quad \rho_{SAP}^s = \frac{(1 + \chi)}{\left(\frac{1}{\rho_{SAP}^d} + \frac{\chi}{\rho_w}\right)}$$

where ρ_{SAP}^s is the saturated density of SAP and m_{SAP}^d is the mass fraction of dry SAP.

Solved for χ , the actual water absorption capacity χ_{actual} can be written as:

$$\chi_{actual} = \frac{V_{SAP}}{\rho_w \cdot f_{SAP} \cdot c} - \frac{1}{\rho_w \cdot \rho_{SAP}^d}$$

Spacing of SAP pores and number of dry particles per 1 kg of dry SAP

Figure A4.3 presents a schematical illustration of the hexagonal close packing formation (HCP) in two-dimensional space.

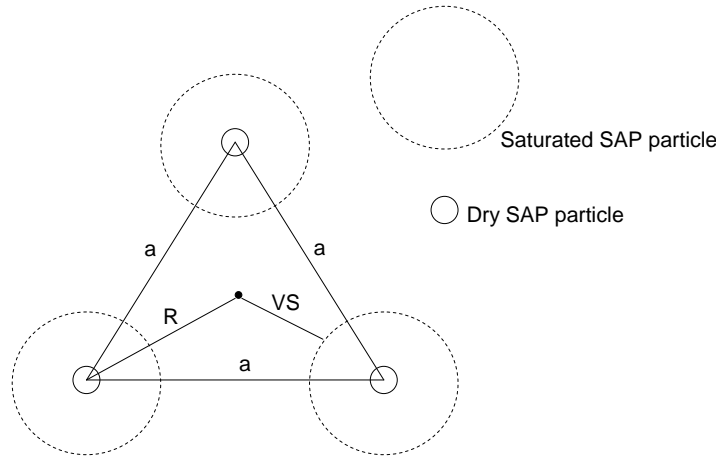


Figure A.4.3: Schematical illustration of HCP formation of pores in two-dimensional space.

The void spacing factor VS can be calculated according to the following equations, where the lengths a [μm] and R [μm] are variable according to the illustration presented by Figure A.4.3:

$$VS = R - r_{Pore} \quad \text{with} \quad a = \left(\frac{1}{n_{EZ} \cdot \sqrt{2}}\right)^{\frac{1}{3}} \quad \text{and} \quad R = \left(a^2 - \frac{a^2}{4}\right)^{\frac{1}{2}} \cdot \frac{2}{3}$$

Further, it is:

$$n_{EZ} = (f_{SAP} \cdot n_{SAP}^d) / 2 \cdot 10^{18}$$

where n_{EZ} [-] is the number of unit cells per $1 \mu\text{m}^3$ of cement paste. It is:

$$n_{SAP}^d = 1 / (\rho_{SAP}^d \cdot V_{SAP}) \cdot 10^{15}$$

where n_{SAP}^d [-] is the number of dry SAP particles per 1 kg of dry SAP, ρ_{SAP}^d [kg/dm^3] is the density of dry SAP particles and V_{SAP} [μm^3] is the volume of one single SAP particle with:

$$V_{SAP} = 4/3 \cdot \pi \cdot (r_{Pore}/\omega)^3$$

It is r_{Pore} [μm] the true average pore radius, cf. equation (4.13) on page 57, and ω [-] the swelling factor, cf. equation (4.4) on page 55:

$$r_{Pore} = \sqrt{\frac{2 \cdot A_{Pore}^\phi}{\pi}} = \sqrt{2} \cdot r_{Pore}^\phi$$

$$\omega = \sqrt{\frac{\rho_{SAP}^d}{\rho_{SAP}^s} \cdot (1 + \chi)} \quad \text{with} \quad \rho_{SAP}^s = (1 + \chi) / \left(\frac{1}{\rho_{SAP}^d} + \frac{\chi}{\rho_W} \right)$$

where A_{Pore}^ϕ [μm^2] and r_{Pore}^ϕ [μm] are the average cut pore surface and radius adopted from IA. Insertion of the respective equations for a and R leads to:

$$VS = 1 / \sqrt{3} \cdot (\sqrt{2} \cdot n_{EZ})^{-1/3} - r_{Pore}$$

Appendix to chapter 5

Analysis of dry cement

Table A.5.1 reports on the XRD results of the used Portland cement of type CEM I 42.5 R, produced by Schwenk KG in Allmendingen.

Table A.5.1: XRD results

Phase	[% by mass]
C ₃ S Alite	65.1
β-C ₂ S Belite	7.7
C ₃ A total	8.4
C ₄ AF Ferrite	7.9
CaSO ₄ Anhydrite	2.0
Dihydrate	1.3
Arcanite	1.0
Syngenite	1.0
CaO Free Lime	0.0
MgO Periglase	1.0
CaCO ₃ Calcite	2.6
CaMg(CO ₃) ₂ Dolomite	0.5
MgCO ₃ Magnesite	0.0
SiO ₂ Quartz	0.3
Ca(OH) ₂ Portlandite	0.0

Results of NMR measurements

Figure A.5.1 presents the longitudinal relaxation time constant (left) and the brutto signal intensity of longitudinal magnetization (right) of paste Ref 0.36 as a function of age. Distinction is made for NMR experiments conducted with and without spin-echo sequence.

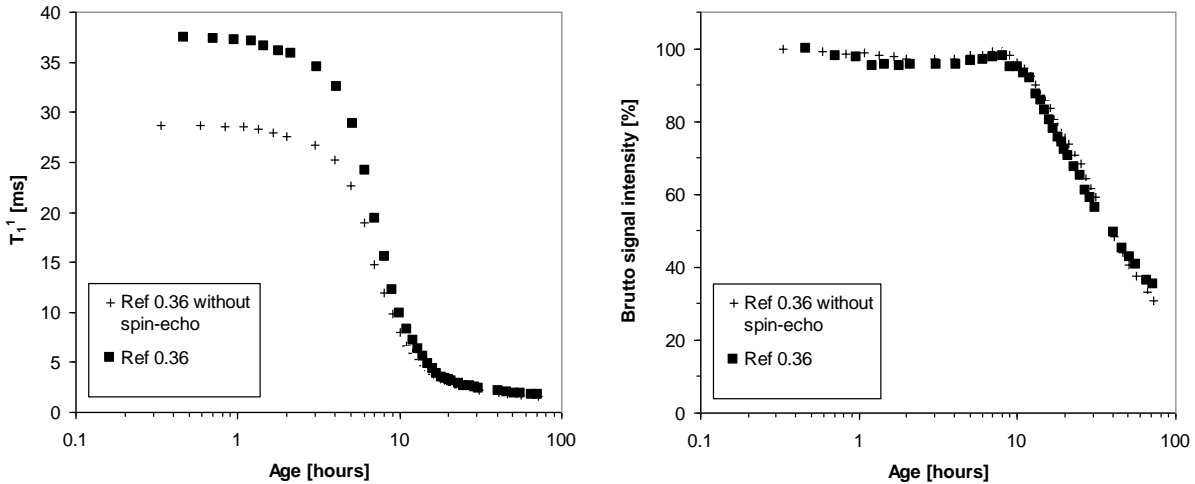


Figure A.5.1: Longitudinal relaxation time (left) and brutto signal intensity (right) measured for paste Ref 0.36 with and without application of spin-echo.

Figure A.5.2 presents the filtered signal of transverse magnetization of paste SAP D 0.30+0.06. The curves are normalized to the first measurement, i.e. the first value at onset of data acquisition. The data acquisition started after various delay. However, the curve propagation is insensitive to the delay. Only at delay of 80 ms, the faster drop of the filtered signal becomes apparent. It can be assumed that the loss of the filtered transverse magnetization during the delay of 5 ms is rather small.

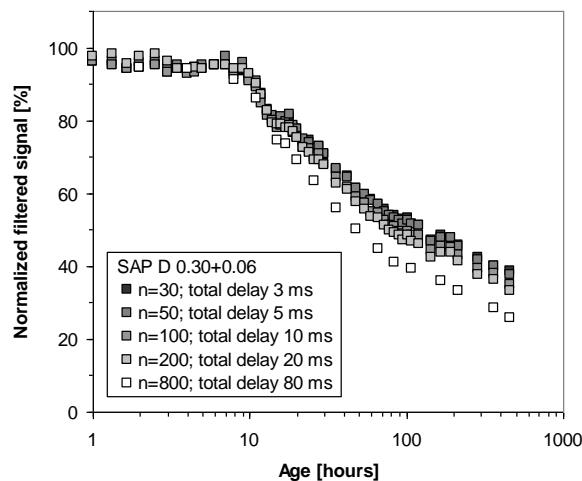


Figure A.5.2: Normalized filtered signal of transverse magnetization determined after various total delay.

Appendix to chapter 6

Ion concentration adopted from ion chromatographic analysis

Figure A.6.1 reports on the ion concentration found in the cement paste's pore solution by ion chromatographic analysis.

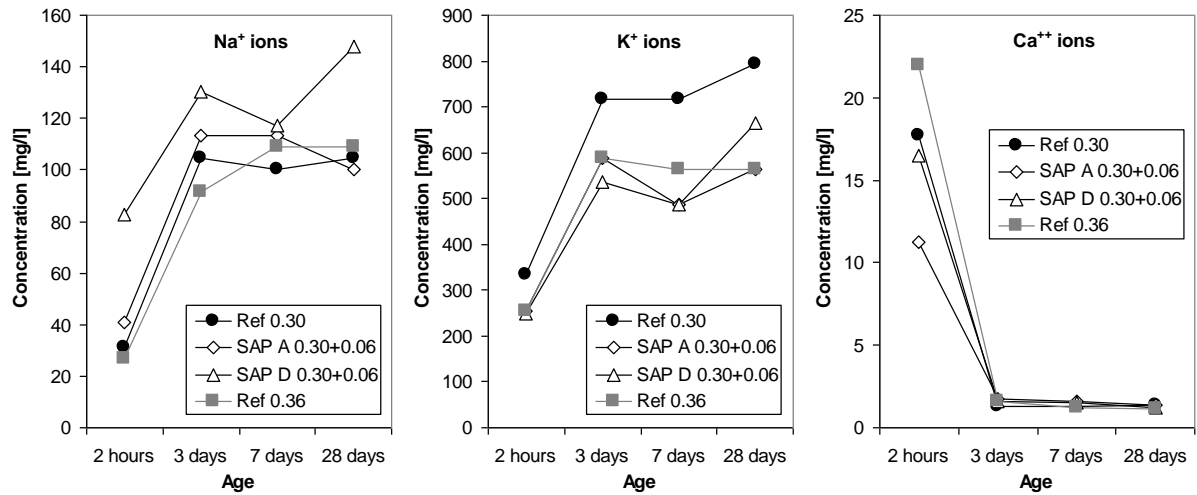


Figure A.6.1: Ion concentration in extracted cement paste pore solution.

Dynamic bulk modulus determined by FreshCon

Figure A.6.2 shows the dynamic bulk modulus as a function of age.

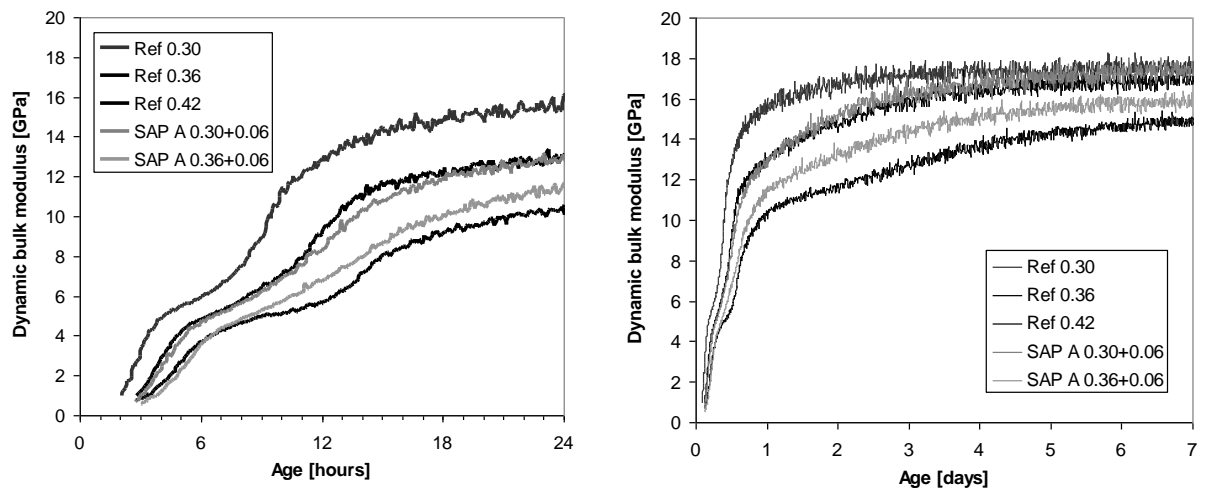


Figure A.6.2: Dynamic bulk modulus as a function of age.

Appendix to chapter 7

Determination of time zero of HPM

Figure A.7.1 illustrates the determination of time zero of reference HPM Ref 0.30 (left) and Ref 0.34 (right). The autogenous deformations were zeroed at time of maximum deformation rate.

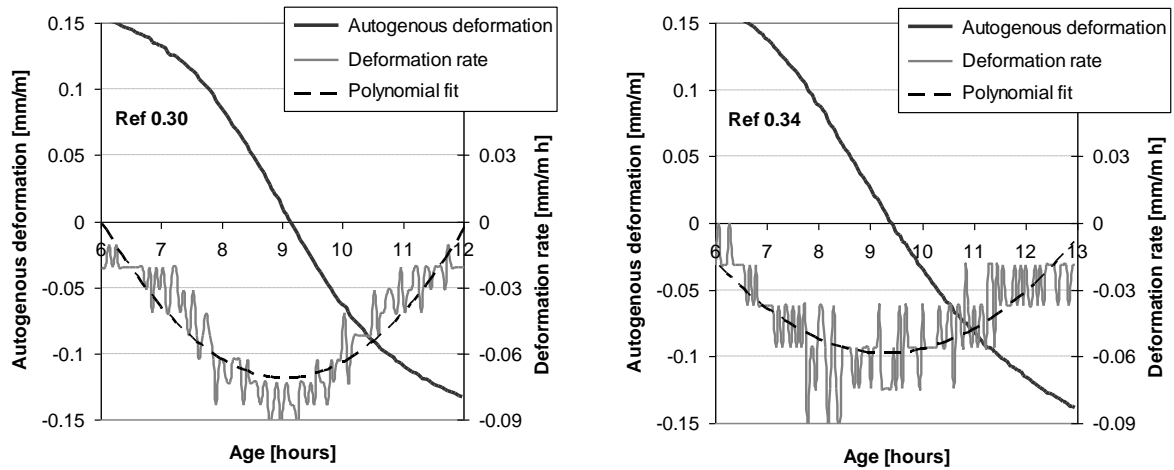


Figure A 7.1: Determination of time zero of HPM Ref 0.30 (left) and Ref 0.34 (right).

Appendix to chapter 8

Information on creep measurements

Figure A.8.1 presents the loading frame used for creep measurements which was developed by Rinder [Rinder 2002].

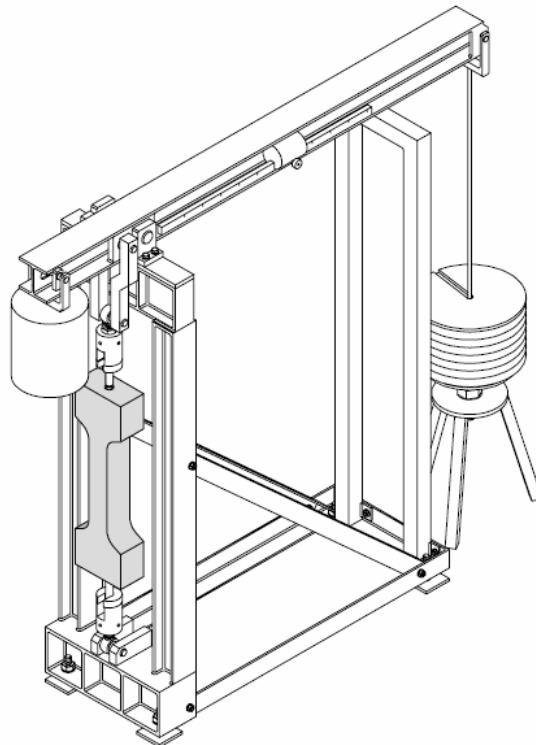


Figure A.8.1: Loading frame for creep measurements [Rinder 2002].

Details on load application of no.3 specimen

Table A.8.1 reports on details of the load application of the no.3 (series I) specimens. The load was applied within 120 seconds, i.e. the load rate was about 0.175 kN/s. The recording interval of the LVDTs was one second.

Table A.8.1: Details on load application of No. 3 specimens

NSC mixture	Sample No.	Load [kN]	Tensile stress [MPa]	Instant strain at loading [μ strain]	E in tension [MPa]	E in compression [MPa]
Ref 0.42	3 (I)	21.1	2.63	63	41700	38800
SAP A 0.36+0.06	3 (I)	35.4	2.65	64	41400	38400
Ref 0.36	3 (I)	39.9	2.99	64	46700	44500

Creep coefficient as a function of age

Figure A.8.2 presents the creep coefficients measured on no.3 (series I) and no.5 (series II) specimens. In case of sealed no.5 specimens, the creep coefficients approach an end value in the range 0.9 (SAP A 0.36+0.06) and 1.4 (Ref 0.42).

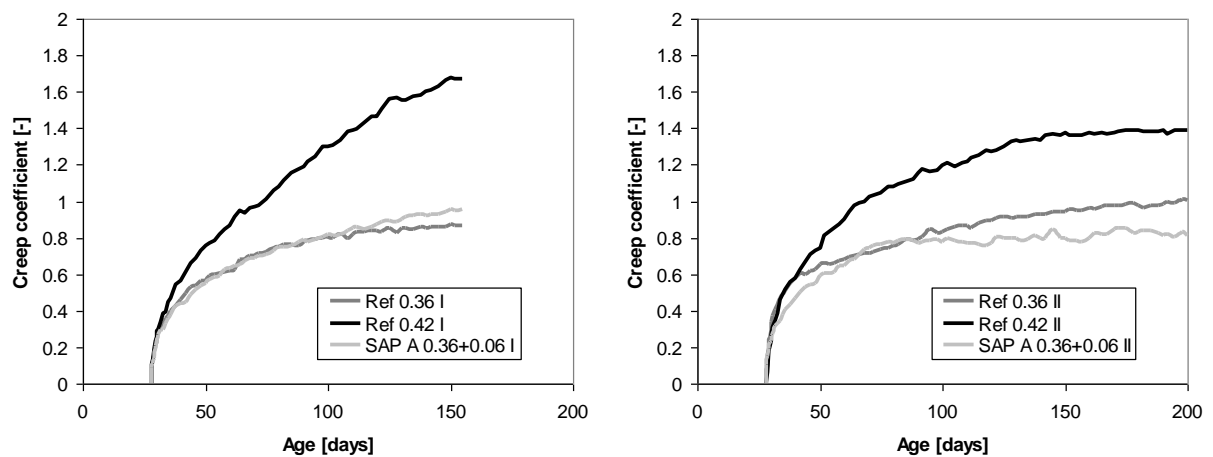


Figure A.8.2: Creep coefficients of no.3 (series I) specimens (left) and no.5 (series II) specimens (right).

Internal resistivity measured by multi-ring-sensor electrode (MRSE)

The measurements were performed with MRSE according to [Schiebl & Raupach 1992]. The MRSE had a length of 48 mm and consisted of 6 rings. The sensors were cast in cylindrical specimens of 150 mm in diameter. The results are shown in Figure A.8.3. The curves are the average of the 6 signals of a sensor, corresponding to 6 rings. Thick line means that the specimen was stored in analogy with specimen no.2 (series I), i.e. wrapped in PE-envelope. Thin line means that the specimen was stored in analogy with specimen no.4 (series II), i.e. sealed by adhesive aluminium vapour barrier foil. Both curves show hardly any difference. From this finding it was concluded that the storage condition had no significant influence on the process of self-desiccation of the concrete interior. Of course, with decreasing total w/c ratio, the resistivity is increasing faster, indicating earlier self-desiccation of the concrete with smaller total water content.

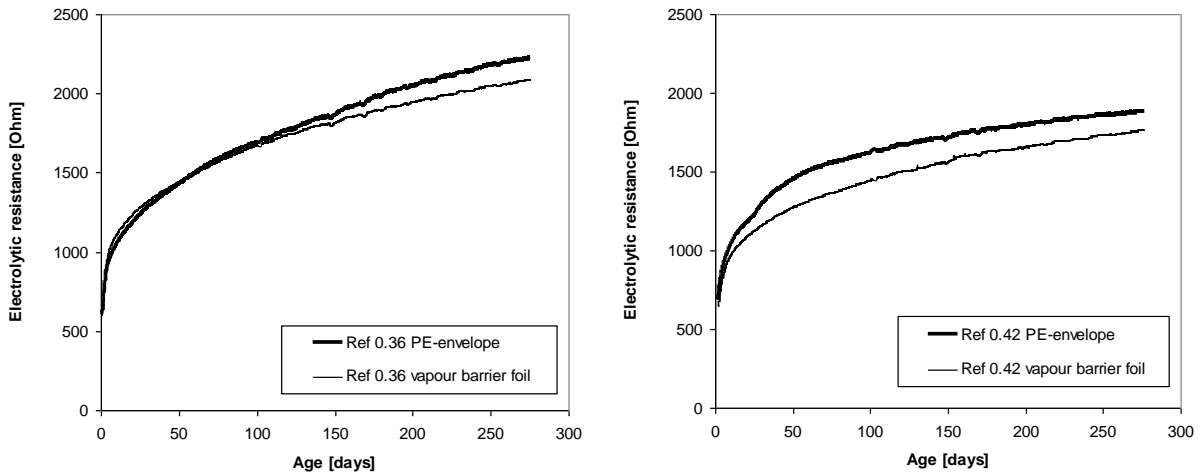


Figure A.8.3: Internal resistivity of concrete measured with MRSE as a function of age in dependence on storage conditions: thick line means wrapped in PE-envelope and thin line means sealed by vapour barrier foil. Left: Ref 0.36. Right: Ref 0.42.

Static shear modulus for modelling autogenous shrinkage of concrete

Table A.8.2 reports on the estimate of the static shear modulus in dependence of age t of cement paste, used for calculating the concrete strain according to Hobb's model.

Table A.8.2: Static shear modulus of cement paste

Cement paste	Shear modulus G_{CP} [MPa]			$G_{CP}(t)$ [MPa]	
	1 day	3 days	28 days	$1 < t \leq 3$	$3 < t \leq 28$
Ref 0.36	4420	6340	7050	$960t + 3460$	$28.3t + 6250$
Ref 0.42	3500	5300	5950	$900t + 2600$	$26.7t + 5200$
SAP A 0.36+0.06	3300	5100	5750	$900t + 2400$	$26.7t + 5000$

Modelling of autogenous shrinkage of concrete according to CEB FIB

An empirical model for calculating autogenous shrinkage of concrete is provided by [CEB 2003].

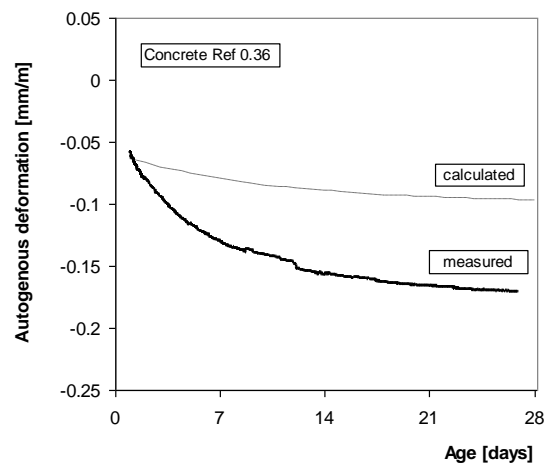


Figure A.8.4: Measured autogenous strain in comparison to strain calculated according to an empirical model presented in [CEB 2003].

However, this model underestimates the real concrete shrinkage, as exemplarily shown by Figure A.8.4 for concrete Ref 0.36. The calculated strain was put at the same level with the measured strain at the age of 24 hours.

Appendix to chapter 9

Rapid chloride migration test

Figure A.9.1 provides a photo of the test setup used for chlorid migration testing according to the RCM test developed by Tang [Tang 1996].

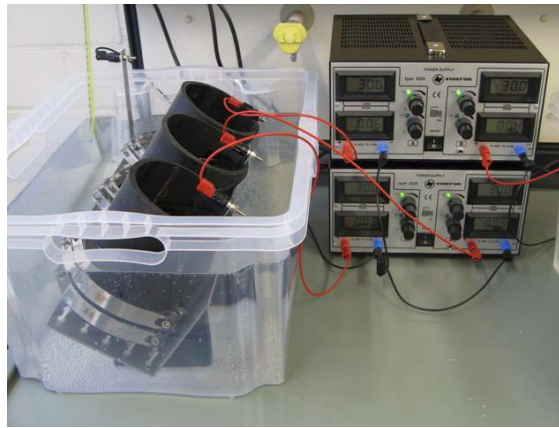


Figure A.9.1: Photo of the test setup used for rapid chloride migration testing [Fischer 2008].

Oxygen flow value in dependence on inlet pressure

Figure A.9.2 presents the oxygen flow rate Q_g as a function of (p_i^2-1) . Flow rates were measured at three inlet pressures p_i , i.e. 3.0, 3.5 and 4.0 bar. Each point is the average of two tested specimen. Since the linear regression (dotted line) fits quite well, the assumption of laminar flow, i.e. Q_g is proportional to (p_i^2-1) , is acceptable. The specific permeability coefficient K_g can be regarded as gradient of the linear regression curve.

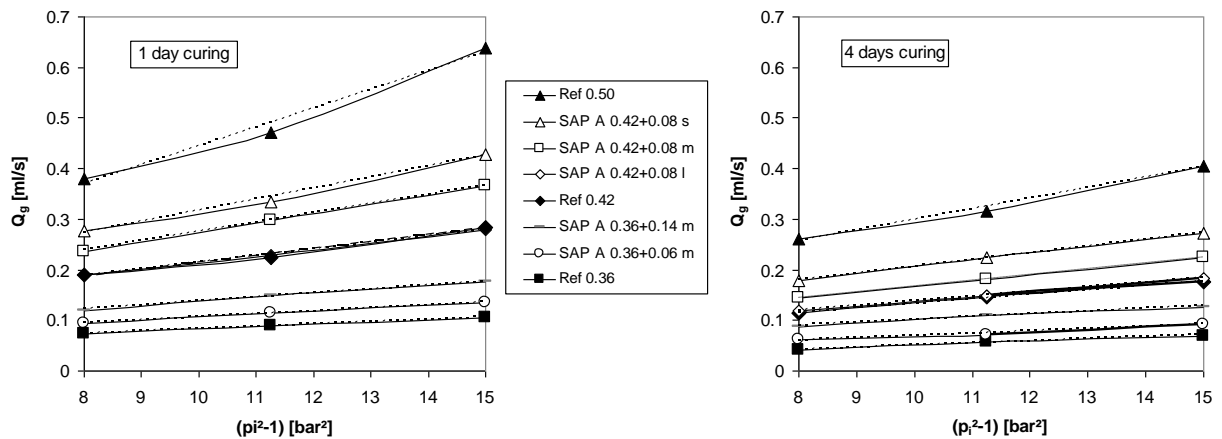


Figure A.9.2: Oxygen flow of samples cured 1 day (left) and 4 days (right) in water in dependence on inlet pressure (p_i^2-1) .

Fractional pore volume

Figure A.9.3 presents the total pore volume divided into the fractions of air pores, SAP pores and capillary pores.

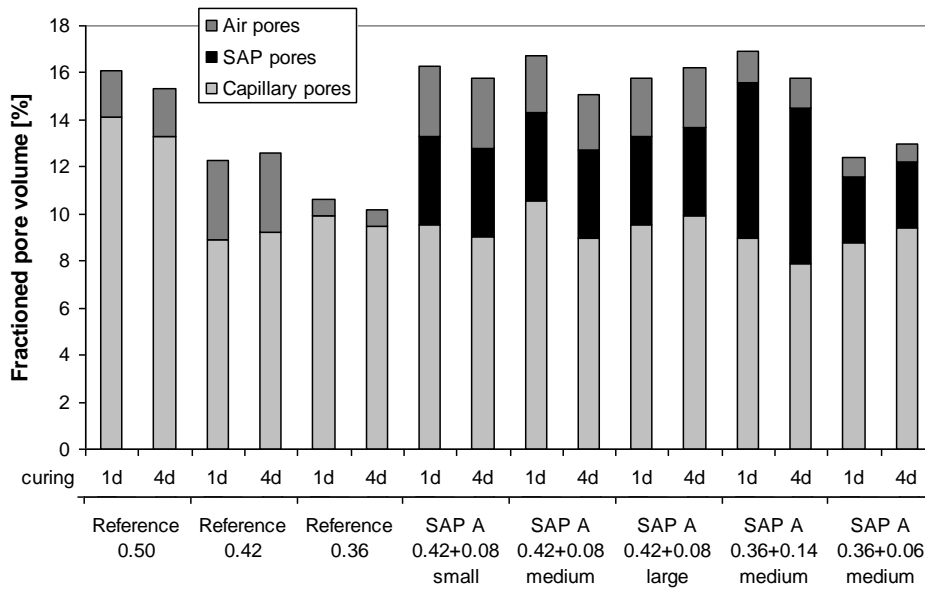


Figure A.9.3: Fractioned pore volume of concrete.

Relative pore size distribution

Figure A.9.4 shows the relative pore size distribution in correspondence with the cumulative pore size distribution presented in Figure 9.12 on page 136. The results were obtained from combining MIP results with results of pore counting according to [DIN EN 480-11 2005].

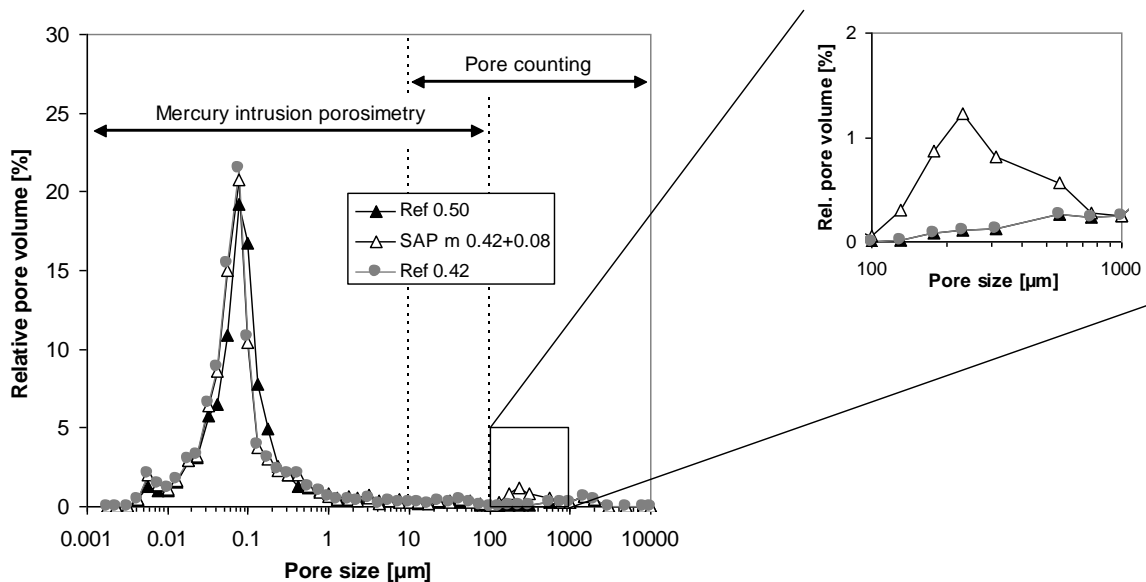


Figure A.9.4: Relative pore size distribution.

Appendix to chapter 10

Details on combined CDF-/CIF-test method

Figure A.10.1 presents the temperature curve of a CDF-test cycle (left) and the handling of specimen during combined CIF-/CDF-testing in a schematic manner (right).

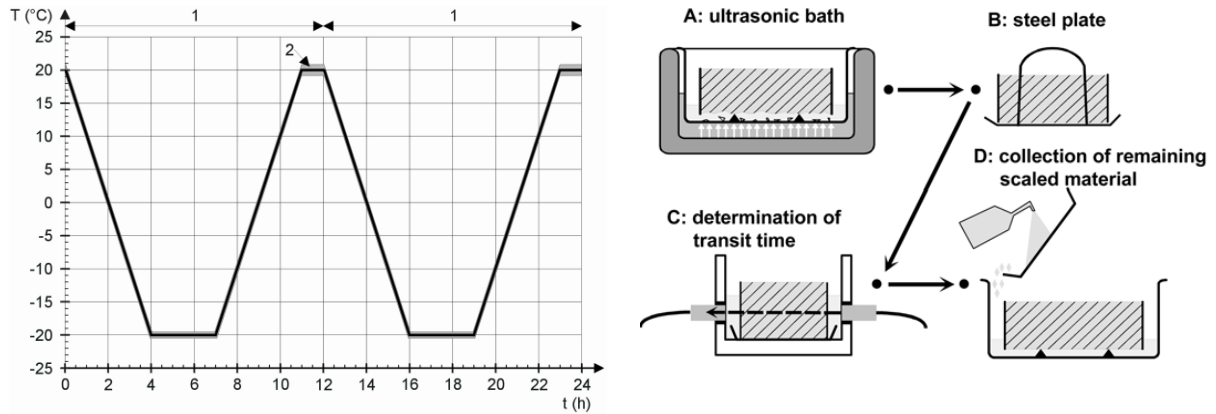


Figure A.10.1: Temperature as a function of time during two freeze-thaw cycles of CDF-testing [DIN EN 12390-9 2009] (left) and illustration of specimen handling during combined CDF-/CIF-testing [Rilem 2004] (right).

Grinding wheel method (Böhme)

Figure A.10.2 presents a schematic drawing of the wear test device using the grinding wheel in accordance to Böhme [DIN 52108 2010]. Length values are given in mm.

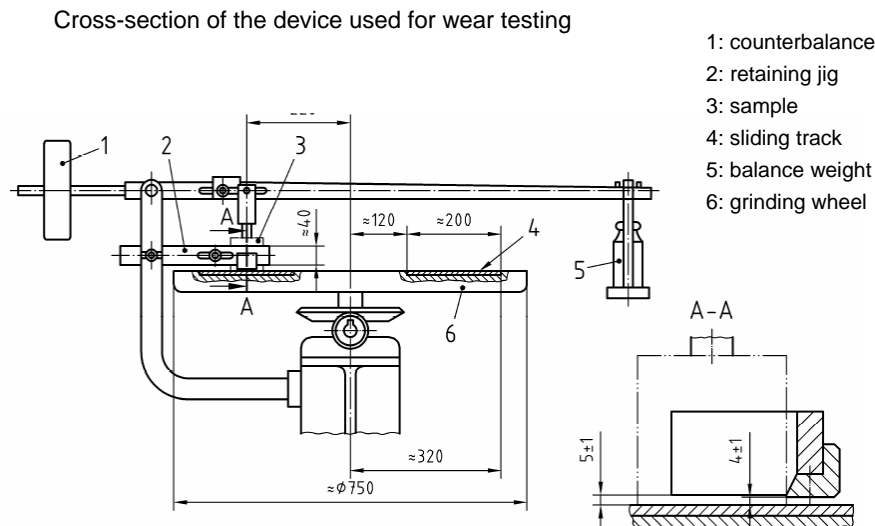


Figure A.10.2: Schematic drawing of the wear test device [DIN 52108 2010].

Note on CDF-testing results

Figure A.10.3 shows that samples of concrete Ref 0.40 with detached sealing (sample 2 to 5) possessed about 10% higher scaling compared to sample with intact sealing (sample 1).

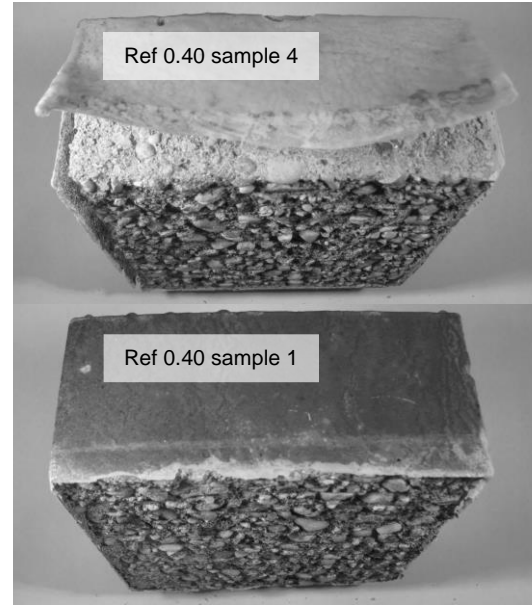
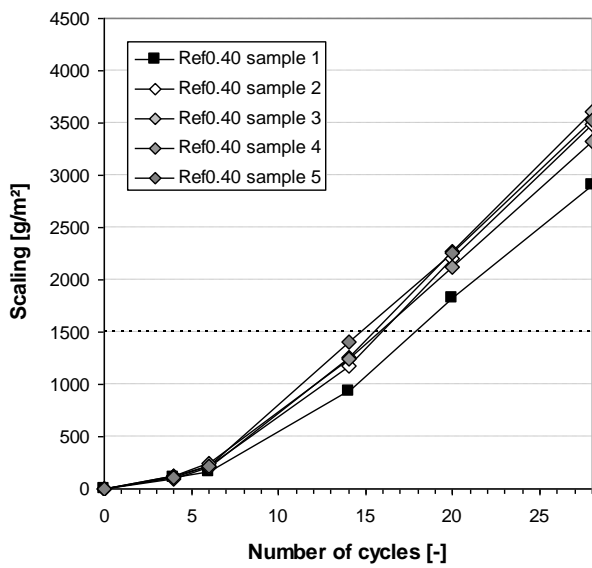


Figure A.10.3: Individual scaling of Ref 0.40 (left) and pictures of sample 4 with detached epoxy sealing (top right) and sample 1 with undamaged epoxy sealing (bottom right) after 28 freeze-thaw cycles.

Relative performance of concretes

Figure A.10.4 shows the relative performance of concretes with respect to strength, scaling, pore volume and abrasion. The best value among the concretes reached within each category is set to zero; the worst is set to one. Under the assumption that all properties are regarded as equivalent, the smallest surface described by the square indicates the best performance.

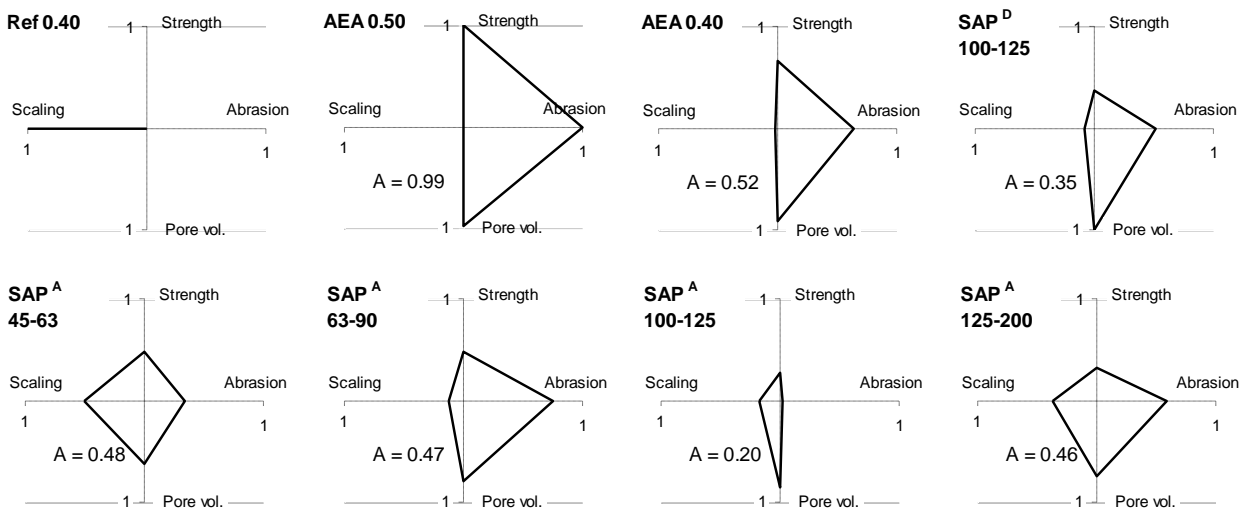


Figure A.10.4: Performance of concretes.

Curriculum Vitae

Persönliche Daten

Alexander Assmann
geboren am 27. April 1984
in Backnang

Schulbildung und Beruf

seit 01/2013	Laborleiter bei der BASF Construction Polymers GmbH in Trostberg
03/2008 - 12/2012	Wissenschaftlicher Mitarbeiter am Institut für Werkstoffe im Bauwesen der Universität Stuttgart
10/2003 - 02/2008	Studium des Bauingenieurwesens an der Universität Stuttgart
09/1994 - 06/2003	Max-Born-Gymnasium Backnang, Allgemeine Hochschulreife